MOPM

MEXICAN OPTICS AND PHOTONICS MEETING 2012

ACADEMIA MEXICANA DE ÓPTICA, A.C.

UNIVERSIDAD AUTÓNOMA DE SAN LUIS POTOSÍ

RIAO

Mexico Territorial Committee for Optics
Member Since 1972

Proceedings

San Luis Potosí, S. L. P., September 19-21, 2012

Proceedings of the Mexican Optics and Photonics Meeting 2012 (MOPM 2012)

www.amo-ac.mx

San Luis Potosí, S. L. P., September 19-21, 2012.

Edited by
Amalia Martínez García
Eric Rosas

Foreword

The **Mexican Optics and Photonics Meeting** is a new forum developed by the *Academia Mexicana de Óptica*, intended to provide the Mexican optics and photonics high impact scientific research and technological results, with an international visibility.

The **Mexican Optics and Photonics Meeting** is a three days conference, having the participation of world-wide recognized plenary speakers in the hot areas of optics and photonics.

The **Mexican Optics and Photonics Meeting** also includes a stringent selection of invited speakers, presenting their most recent and relevant research results, which altogether, constitute a genuine sample of the fields, quality and impact, the optics and photonics scientific research and technological development reached in Mexico.

In order to promote the integration of the current research groups in optics and photonics of Mexico, the **Mexican Optics and Photonics Meeting** will also have poster sessions with a selection of refereed voluntary contributions.

From today and ahead, the **Mexican Optics and Photonics Meeting** will become the place to learn of the hot Mexican optics and photonics.

Eric Rosas
Oracio C. Barbosa García

Organizing Committees

MOPM 2012 Director

Alfonso Lastras Martínez
Instituto de Investigación en Comunicación Óptica (IICO)
Universidad Autónoma de San Luis Potosí (UASLP)

MOPM 2012 Local Organizing Committee

Andrei Gorbatchev (IICO-UASLP)
Amparo Rodríguez Cobos (IICO-UASLP)
Luis Felipe Lastras Martínez (IICO-UASLP)
Raúl Balderas Navarro (IICO-UASLP)
Jorge Ortega Gallegos (IICO-UASLP)

MOPM 2012 Technical Committee

Carolina Arriola Necchi (CIO)
Maira Solís Arredondo (IICO-UASLP)
Angélica María Hernández Guzmán (IICO-UASLP)
José Ignacio Diego Manrique (CIO)
José Luis González Molina (CIO)
Elisa Villa Martínez (UGTO)

MOPM Organizing Committee

Oracio C. Barbosa García (CIO)
Eric Rosas Solís (CENAM)
Amalia Martínez García (CIO)
Ramón Rodríguez Vera (CIO)
Norberto Arzate Plata (CIO)
Julio César Gutiérrez Vega (ITESM)
Raúl Hernández Aranda (ITESM)

Organized by

ACADEMIA MEXICANA
DE ÓPTICA, A.C.

Academia Mexicana de Óptica

Mexico Territorial Committee for Optics
Member Since 1972

México Territorial Committee for Optics

RIAO

Red Iberoamericana de Óptica

Instituto de Investigación en Comunicación Óptica

UNIVERSIDAD AUTÓNOMA
DE SAN LUIS POTOSÍ

Universidad Autónoma de San Luis Potosí

Sponsored by

Centro de Investigaciones en Óptica

Centro de Investigación Científica y de Educación Superior de Ensenada

Instituto Nacional de Astrofísica, Óptica y Electrónica

The Optical Society

Satelsa

Program at a Sight

Time	Wednesday 19	Thursday 20	Friday 21
08h00	Registration	Registration	Registration
08h30	Opening Ceremony		
09h00	Plenary Talk 1 David Aspnes North Carolina State University, U. S. A. A Century of Plasmonics	Plenary Talk 2 Phil Bucksbaum Stanford University, U. S. A. Atomic and Molecular Physics at the LCLS X-Ray Laser	Plenary Talk 3 Luis Adolfo Orozco NIST-UM Joint Quantum Institute, U. S. A. Evanescent Fields in Nanofibers
10h15	Research Parallel Session. Invited Talks	Research Parallel Session. Invited Talks	Research Parallel Session. Invited Talks
11h00	Coffee Break	Coffee Break	Coffee Break
11h30	Research Parallel Session. Invited Talks	Research Parallel Session. Invited Talks	Research Parallel Session. Invited Talks
13h00	Lunch		Lunch
13h15		Plenary Talk 4 Francisco Ramos Gómez UNAM, Mexico. SISMENEC: A Meeting Place for Industry, Consumers and Academia	
14h00		Lunch	
15h00	Posters Session. Selected Contributions & Coffee Break		Posters Session. Selected Contributions & Coffee Break
15h30		Plenary Talk 5 Ricardo Benjamín Ávila Suárez Industrias Tonali, Mexico. Linking Academia & Business: The Experience of "Industrias Tonaly"	
16h15		Coffee Break	
16h30	Luis Felipe Lastras IICO, UASLP, Mexico. Modulated Spectroscopies Short Course	Research Parallel Session. Invited Talks	Andrei Gorbatchev IICO, UASLP, Mexico. Semiconductor diodes lasers Short Course
17h15		Outreach Parallel Session. Invited Talks	
18h00	AMO XXV Anniversary Ceremony Honor Wine	AMO General Assembly / OSA & SPIE Student Chapters Meeting	Closing Ceremony
20h00		Gala Dinner	

Wednesday, September 19, 2012.

08h30-09h00	Opening Ceremony	
09h00-10h00	David Aspnes North Carolina State University, U. S. A. A Century of Plasmonics Session Chair: Alfonso Lastras Martínez	
10h15-11h00	Session Chair: Amalia Martínez García	Session Chair: Amparo Rodríguez Cobos
	Daniel Malacara Hernández CIO Design of Schmidt-Cassegrain Aplanatic Telescopes S1O	Wolf Luis Mochán Backal UNAM Macroscopic Properties and Photonic Propagation in Metamaterials S1F
11h00-11h30	Coffee Break	
11h30-12h15	Eduardo Tepichín Rodríguez INAOE Objective Performance of a Set of Uncorrected 20/20 Normal Eyes: Clinical Reference S2O	Eduardo Gómez García UASLP Precision Measurements Using Cold Atoms in Optical Traps S2F
12h15-13h00	Fernando Mendoza Santoyo CIO 3D Digital Holographic Interferometry: Biomedical Applications S3O	Eugenio Rafael Méndez Méndez CICESE Goos-Hänchen Shifts with Random Fields S3F
13h00-15h00	Lunch	
15h00-16h30	Posters Session SM1 MOPM-2012-OP-01 to MOPM-2012-OP-20 MOPM-2012-PH-01 to MOPM-2012-PH-20 Session Chair: Norberto Arzate Plata	
16h30-18h00	Short Course SFA Luis Felipe Lastras UASLP Modulated Spectroscopies	
18h00-20h00	AMO XXV Anniversary Ceremony Honor Wine	

Thursday, September 20, 2012.

09h00-10h00	Phil Bucksbaum Stanford University, U. S. A. Atomic and Molecular Physics at the LCLS X-Ray Laser Session Chair: Ramón Rodríguez Vera	
10h15-11h00	Session Chair: Raúl Balderas Navarro	Session Chair: Luis Felipe Lastras Martínez
	Diana Tentori Santa Cruz CICESE Polarization Performance of Twisted Erbium-Doped Fibers S4O	Jorge Alberto Gaspar Armenta USON Interaction of Light with Metallic Cylinders S4F
11h00-11h30	Coffee Break	
11h30-12h15	Jorge Ojeda Castañeda UGTO Tunable Depth of Field with High Resolution S5O	José Luis Maldonado Rivera CIO Research and Applications of Plastic Optoelectronics and Photonics S5F
12h15-13h00	Gustavo Rodríguez Zurita BUAP Modulation of Polarization in Phase-Shifting Interferometry S6O	Manuel Fernández Guasti UAM Energy Content of Ultrafast Chirped Pulses S6F
13h15-14h00	Francisco Ramos Gómez UNAM, Mexico. SISMENEC: A Meeting Place for Industry, Consumers and Academia Session Chair: Eric Rosas	
14h00-15h30	Lunch	
15h30-16h15	Ricardo Benjamín Ávila Suárez Industrias Tonali, Mexico. Linking Academia & Business: The Experience of "Industrias Tonaly" Session Chair: Oracio Barbosa	
16h15 - 16h30	Coffee Break	
16h30-17h15	Session Chair: Julio César Gutiérrez Vega	Session Chair: Luis Felipe Lastras Martínez
	Kurt Bernardo Wolf Bogner UNAM 40 Years in Linear Canonic Transforms Development S7O	Roberto Ortega Martínez UNAM Ultra Short Laser Pulse Characterization Techniques S7F
17h15-17h45	Enrique Rivera Garibaldi Grupo SISA, Mexico. CALIPO – GRUPO SISA: Experience in a High-Tech Business in México S1V	Jorge Raymundo Loredo Murphy UANL, Mexico. Triple Helix Links S2V
18h00-19h00	AMO General Assembly Auditorium	OSA & SPIE Student Chapters Meeting Room 7
20h00-24h00	Gala Dinner Hotel Panorama	

Friday, September 21, 2012.

09h00-10h00	Luis Adolfo Orozco NIST-UM Joint Quantum Institute, U. S. A. Evanescent Fields in Nanofibers Session Chair: Eric Rosas	
10h15-11h00	Session Chair: Oracio Barbosa	Session Chair: Andei Gobatchev
	Carlos Gerardo Treviño Palacios INAOE Millimeter-Teraherz Instrumentation S8O	Bernardo Mendoza Santoyo CIO Optical Coherent Current Control at Surfaces: Theory of Injection Current and Spin Generation S8F
11h00-11h30	Coffee Break	
11h30-12h15	Julio César Gutiérrez Vega ITESM Pancharatnam-Berry Phase for Optical Systems S9O	Nikita Pikhtin Ioffe Institute, Russia. High Power CW and Pulsed Diode Lasers based on Separate Confinement Quantum Well Double Heterostructures S9F
12h15-13h00	Luis Vidal Ponce Cabrera IPN Laser Ablation for Thorns Removal of Opuntia S10O	Raúl Rangel Rojo CICESE Nonlinear Optical Properties of Anisotropic Metallic Nanocomposites S10F
13h00-15h00	Lunch	
15h00-16h30	Posters Session SM2 MOPM-2012-OP-21 to MOPM-2012-OP-44 MOPM-2012-PH-21 to MOPM-2012-PH-31 Session Chair: Raúl Hernández Aranda	
16h30-18h00	Short Course SFA2 Andrei Gorbatchev UASLP Semiconductor Diodes Lasers	
18h00-18h30	Closing Ceremony	

CONTENTS

POSTERS CONTRIBUTIONS

A Century of Plasmonics

D. E. Aspnes

Department of Physics, North Carolina State University, Raleigh, NC 27695-8202 USA
Department of Physics, Kyung Hee University, Seoul 130-701, Republic of Korea

ABSTRACT

Considerable attention has recently been given to plasmons, which are resonant solutions of Maxwell's Equations that occur for inhomogeneous configurations (materials or structures) independent of an external driving field. This attention has been driven partly because plasmons can be highly localized, and thus are a potentially useful means of transmitting information with excitations of dimensions much smaller than photons, and partly because they provide a means of generating very high local fields, which makes them attractive for applications such as surface enhanced Raman scattering (SERS). However, the main driving force is our recently developed capability of engineering nanostructures to specification, which allows them to be designed for particular applications.

The recent activity in the field tends to obscure the fact that plasmonics is not a new topic. It has a long history in describing and analyzing inhomogeneous materials and their structure, beginning with Maxwell Garnett's 1904 work explaining the deep red color of glass containing dispersions of gold nanospheres, and continuing through many years of papers on effective medium theories and their use in determining the compositional and structural properties of nanoscopically inhomogeneous materials. Here, I discuss these and more general aspects. I begin by considering solutions of equations for configurations such as the parallel-plate capacitor, the two-phase (substrate-ambient) Fresnel reflectance expression for p-polarized radiation, and the standard entry-level electrostatics problem of the dielectric sphere in a dielectric medium where no external field is applied. These solutions yield bulk, interface, and structural plasmons in a simple way. I then consider applications that are less well known from the plasmonics perspective, including effective-medium theory, the limit theorem on average internal fields, and how this identifies the structure maximizing the average field. . I conclude with a discussion of recent advances and applications. Many aspects of plasmonics are well illustrated by reflectance data on transition-metal oxide films, for which behavior can be varied over a wide range by thickness and doping [1].

[1] C. Rhodes et al., J. Appl. Phys. **103**, 093108 (2008).

Atomic and Molecular Physics at the LCLS X-ray Laser

P. H. Bucksbaum

PULSE Institute, Departments of Physics, Applied Physics, and Photon Science, Stanford University, and SLAC National Accelerator Laboratory, 2575 Sand Hill Road, Menlo Park, CA 94025, USA
phbuck@stanford.edu

ABSTRACT:

The Stanford Linac Coherent Light Source (LCLS) at the SLAC National Accelerator Laboratory is the world's first hard x-ray free electron laser. It is approximately one billion times brighter than any previous laboratory source of multi-kilovolt x rays (*1*). It produces millijoule pulses of sub-100 fsec coherent radiation, which have been focused to intensities in excess of 10^{18} W/cm^2. This places the LCLS in the class of the world's most intense laser sources.

Early atomic and molecular physics experiments at LCLS have concentrated on studies of fundamental processes of photoionization and subsequent relaxation (*2*-*8*). The significant dynamical time scales involved are on the order of a few femtoseconds. Several strong-field and nonlinear effects have now been documented, and I will review the early results as well as the status of ongoing work. Findings to date have included new rapid sequential processes such as multi-photon multiple core-hole formation, as well as studies of coherent x-ray multiphoton processes. Some of this work has also involved preparation of molecules with intense ultrafast optical laser pulses which are then probed by x rays, and the opposite: preparation of molecules by x rays followed by probes with ultrafast lasers. The pump-probe timing critical to these studies will also be reviewed.

Acknowledgments: This work was supported by the AMOS program within the Chemical Sciences, Geosciences, and Biosciences Division of the Office of Basic Energy Sciences, Office of Science, U. S. Department of Energy.

References

1. P. Emma *et al.*, *Nature Photonics* **4**, 641 (2010).
2. J. P. Cryan *et al.*, *Journal of Physics B: Atomic, Molecular and Optical Physics* **45**, 055601 (2012).
3. J. P. Cryan *et al.*, *Phys. Rev. Lett.* **105**, 083004 (2010).
4. G. Doumy *et al.*, *Phys. Rev. Lett.* **106**, 083002 (2011).
5. J. M. Glownia *et al.*, *Opt. Express* **18**, 17620 (2010).
6. M. Hoener *et al.*, *Phys. Rev. Lett.* **104**, 253002 (2010).
7. L. Young *et al.*, *Nature* **466**, 56 (2010).
8. E. P. Kanter *et al.*, *Physical Review Letters* **107**, 233001 (2011).

Evanescent fields in nanofibers

Luis A. Orozco

Joint Quantum Insititue
Department of Physics
University of Maryland and NIST
College Park, MD 20742 United Sates
lorozco@umd.edu

ABSTRACT:

I will present results of our nano fiber fabrication facility. We can reliable produce conical profiles and control the waist down to a diameter of 500 nm. By controlling the geometry of the conical region in an adiabatic way, we can minimize loses of propagation. The transmission at 780 nm of the fibers is greater than 99% for the fundamental mode. For higher order vectorial modes, it can reach 80% with interesting propagation dynamics.

Interfacing atomic and superconducting qubits in a hybrid system is a promising option for quantum information processing. To build this system, drastic experimental conditions must be met: the techniques used to trap and control atoms with light should be implemented in the cryogenic environment necessary for working with superconducting qubits. To limit the heating induced by light trapping, we are implementing trapping atoms in the evanescent fields of nanofibers.

Work done in collaboration with J. A. Grover, J. E. Hoffman, S. RavetsK. D. Voigt, U. Chukwu, I. Schoch, A. K. Wood Z. Kim, J. Lee, J. R. Anderson, M. Hafezi, C. J. Lobb, S. L. Rolston, J. M. Taylor, and F. C. Wellstood. Work supported by the National Science Foundation of the United States through the Physics Frontier Center of the Joint Quantum Institute, by the Multi University Research Initiative of the Airforce Research Office in Atomtronics, and the Fulbright foundation.

OCIS: 060.0060, 060.2280, 020.7010

MEXICAN OPTICS AND PHOTONICS MEETING
19 al 21 de septiembre del 2012
San Luis Potosí, México

SISMENEC: a meeting place for industry, consumers and academia

Francisco Ramos Gómez

Facultad de Ciencias, UNAM
framos@unam.mx

ABSTRACT:

The lack of impact of academic research on industry and consumers is one of the most frequent complaints we hear in Mexico. Although the problem has been diagnosed for a long time, the strategies to deal with it have rendered limited if any results.
One reason for this lack of impact may be found in the absence of meeting places between the scientific community –usually restricted to academic spaces- and other sectors of society, industry and consumers included. The result of this is that the scientific capabilities to attend society problems are usually unknown or under appreciated. In fact, frequently there is not even a common language through which those sectors can truly communicate.
In this presentation we argue that the so called "Sistema de Metrología, Normalización y Evaluación de la Conformidad (**SISMENEC**)", offers one of the best and least used opportunities to bring together social segments that need to know each other, such as: industry, commerce, basic products providers, consumers and academy.
As we shall explain, the **SISMENEC** rests on technical standards (also known as norms), which are legal instruments that establish the specifications to be comply by products offered to consumers. By law, these tools must be prepared by comities that include the participation of all relevant sectors. This allows the exchange of points of view among these sectors, which is important to obtain an unbiased technical standard. We are convinced that these comities also represent a space where the academic bodies and other social sectors can get to know each other, discover their needs and capabilities, and learn how obtain the best of them.

MOPM
MEXICAN OPTICS AND PHOTONICS MEETING
19 al 21 de septiembre del 2012
San Luis Potosí, México

Linking Academia & Business: The experience of "Industrias Tonaly, S. A. de C. V."

Ricardo Benjamín Ávila Suarez

Industrias Tonaly, S. A. de C. V. Zitácuaro, Mich.
itonaly@prodigy.net.mx

ABSTRACT

Most of the goods and services industry in Mexico is made up of micro and small companies. According to INEGI data, there are approximately 4 million 15 thousand business units, of which, 99.8% are micro, small and medium enterprises ("MIPYMES"), generating 52% of GNP and 72% of employment in the country, and the rest are large national and foreign companies, i.e., a very small number.

Foreign or multinational companies conduct research and technology development at their home venues, so, in terms of percentage, they do very little linkage in Mexico with national institutions. It is therefore interesting to look at the linkage experience of a small Mexican technology company. Linking schemes and support management systems for Science and Technology in Mexico are designed for medium and large companies; hence the difficulty for micro and small companies to gain access to such aids. Yet, the vast majority of companies operating in the country - even those considered the most advanced - limit themselves to using these resources to make administrative improvements aimed at servicing their customers.

Linking and scientific innovations do not take place in a void; we must take into account the macroeconomic conditions of the country. The economy of Mexico is not only stagnant, but it has also had very severe crises for over 30 years; hence, there is limited access to credit, low tax collection and public spending on science is of only 0.44 per cent of gross domestic product, whereas the United Nations recommended minimum is of at least 1 percent.

Tonaly has filled these gaps with creative efforts to achieve concrete results with the little support received. Among its most notable achievements is the recognition by CONACYT by naming two of Tonaly's technological development projects as successful cases, and the nomination by Philips to the Gold Supplier Award in 1999.

Recently, the company successfully developed a prototype parabolic solar concentrator and a 100 watt range type Stirling engine for S. T. C. Metro (Mexico city's subway system), and, in tandem with the "Instituto Politécnico Nacional (IPN)", is competing in the 2012-02 CONACYT-Mexico City Government call for projects in order to gain funds for a specific demand project for the scaling of these technologies.

Tonaly has innovation and technological development projects of practical application for Mexican Industry and Agro-Industry, and it takes advantage of its links with research centers belonging to the SEP-CONACYT system in order to develop them for the benefit of small farmers, as in the case of optical equipment for bean color selection, among others.

MEXICAN OPTICS AND PHOTONICS MEETING
19 al 21 de septiembre del 2012
San Luis Potosí, México

Design of Schmidt-Cassegrain aplanatic telescopes

Daniel Malacara Hernández

Centro de Investigaciones en Óptica, A. C.
León, Gto. México
dmalacara@cio.mx

ABSTRACT:

The Schmidt-Cassegrain aplanatic astronomic telescopes had been used with great success for more than 50 years and many different designs had been proposed. An aplanatic system is one in which the spherical aberration as well as the coma had been corrected. The spherical aberration in a two mirror system can be corrected if the primary mirror is a paraboloid and the secondary mirror is a hyperboloid, both with rotational symmetry. This is the basic Cassegrain telescope, which has the disadvantage that the coma is not corrected and so, it is not aplanatic. To make this system aplanatic we need that both, the primary mirror as well as the secondary mirror is hyperboloids with rotational symmetry. Unfortunately, the solution makes the system more difficult to construct and it is called a Ritchey-Chretien.

For many years astronomers and opticians have been looking for alternative solutions simpler to manufacture. The telescopes proposed by Baker had been considered many times. The limitations of these designs are that there are quite difficult to construct and the spherical aberration has to be corrected with the Schmidt corrector plate, which is highly aspheric. Besides this aspheric plate, in order to correct the coma, at least one, but frequently both mirrors, had to be aspheric.

Here we will describe these telescopes and a new design proposal will be presented that do not need aspheric mirrors, making them simpler.

MEXICAN OPTICS AND PHOTONICS MEETING
19 al 21 de septiembre del 2012
San Luis Potosí, México

Macroscopic properties and photonic propagation in metamaterials

W. Luis Mochán,[1] José Samuel Pérez,[1,2]
Guillermo Ortiz[3] y Bernardo Mendoza[4]

[1] Instituto de Ciencias Físicas, UNAM, México
[2] Posgrado en Ciencias Físicas, UNAM, México
[3] Universidad Nacional del Nordeste, Argentina
[4] Centro de Investigaciones en Óptica, México

We present a very general and efficient formalism to calculate the macroscopic electromagnetic properties of periodic metamaterials made of inclusions embedded within a host. Our formalism can be expressed concisely as $\hat{\mathcal{W}}_M^{-1} = \hat{\mathcal{W}}_{aa}^{-1}$, where $\mathcal{W}$ is the microscopic wave operator, the subindices aa denote the average-average projection of the corresponding operator and the subindex M denotes the macroscopic operator. The geometry of the inclusions is arbitrary and may be obtained from digitized photographs or drawings that may be manipulated with image processing tools. The composition of the inclusions and the host is also arbitrary, and may correspond to either insulators or conductors, dissipationless or dissipative, non-dispersive or dispersive. In the long-wavelength regime, the dependence on the composition and frequency may be decoupled from the dependence on the geometry, which allows an acceleration of the computations by several orders of magnitude with respect to other schemes. As an application, we design extremely anisotropic systems that behave as almost perfect absorbers or reflectors according to the polarization direction within an easily tunable energy range, and we obtain an explanation of the extraordinary transmission of metallic films perforated by nanometric holes without invoking surface plasmons explicitly. For example, the figure shows the reflectance of a square array of elliptical dielectrical cylinders (excentricity $e = 0.83$, $\epsilon = 4$)within an Au host. For polarization along a direction y the reflectivity is similar to that of Au, while for the orthogonal polarization x the reflectivity has a deep minimum that may be tuned along a wide energy range by rotating the cylinders by an angle θ. When the wavelength becomes comparable to the unit cell size, the macroscopic response becomes strongly spatially dispersive. When we fully take spatial dispersion into account, our macroscopic formalism is able to reproduce the photonic bands of the system.

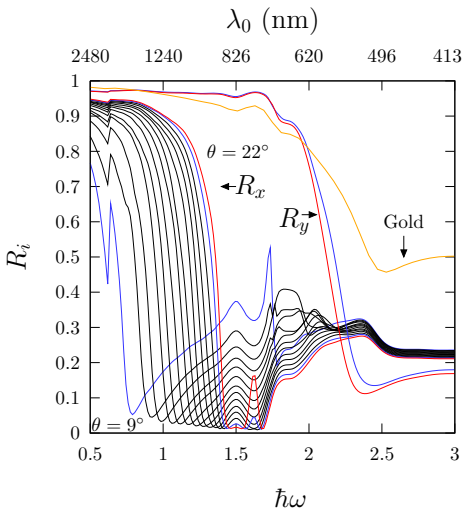

MEXICAN OPTICS AND PHOTONICS MEETING
19 al 21 de septiembre del 2012
San Luis Potosí, México

Objective performance of a set of uncorrected 20/20 normal eyes: Clinical Reference

Eduardo Tepichín Rodríguez

Departamento de Óptica, Instituto Nacional de Astrofísica, Óptica y Electrónica.
Calle Luis Enrique Erro No. 1, Sta. Ma. Tonantzintla,
Puebla, 72840, Pue., México;
tepichin@inaoep.mx

ABSTRACT:

We have been working in the characterization of the objective average performance of a set of uncorrected human eyes with a 20/20 visual acuity. The resultant performance has been described mainly as the resultant average wavefront aberration function (WA), point-spread function (PSF), modulation transfer function (MTF), and power refractive maps, which describes the so called "Normal Mexican Eye" (NME). The NME has been used as a clinical reference to compare and measure the objective performance of pre-operated, and post-operated eyes with different laser refractive surgery techniques. We also expand the scope of our clinical reference by including the objective performance of 20/30 an 20/40 human eyes, which, despite of the increase in the visual acuity, does not need any refraction correction. We describe the results that we have been obtaining with the application of our clinical reference in different clinical situations.

Keywords: emmetropic eyes; clinical reference; objective performance; refractive surgery.

MEXICAN OPTICS AND PHOTONICS MEETING
19 al 21 de septiembre del 2012
San Luis Potosí, México

Precision measurements using cold atoms in optical traps

Eduardo Gomez

Institute of Physics, UASLP

ABSTRACT:

The measurement of small forces requires a good understanding of the probe used. Isolated atoms are ideal in this sense, since we understand very well their response and there are techniques to manipulate them with extreme precision. We have implemented a laser cooling system that produces a sample of atoms at a temperature of 30 μK confined in a region smaller than 1 mm. We plan to use the atoms to measure the interaction force between an atom and a surface. The interaction is dominated by the Casimir-Polder force at distances between 1 to 10 microns which is the range of study. To measure the force we use a quantum transport phenomena called Bloch oscillations that appears with atoms moving in a periodic potential. The frequency of oscillation is directly proportional to the acceleration and can be used to measure the force after subtracting the gravitational contribution. We produce the periodic potential with two counter-propagating lasers of the same frequency that produce a standing wave. From the measurement we will set improved limits about the existence of new short range forces that correspond to physics beyond the Standard Model.

To implement the Magneto-Optical Trap we developed a rapidly tunable laser system with high output power. The system uses an acousto-optic modulator in double pass configuration to generate fast yet controlled frequency changes. The output goes through a tapered amplifier in double pass and we obtain 1 W out with a 1 mW input. A second acousto-optic modulator gives us control over the intensity we send to the atoms and opens the possibility of having additional independent beams that we use for example to do absorption imaging. We transfer the atoms from the Magneto-Optical Trap to a purely Optical Trap that produces a conservative potential for the atoms and allows for coherent measurements. The Optical Trap, once retro-reflected creates the periodic potential that we need for the measurement of the Casimir-Polder force. We send the trapping laser through an amplifier to have high power (1 W). The amplifier increases the seed power but it produces fluorescence at other frequencies that is enough to interact resonantly with the atoms and kick them out of the Optical Trap. To solve the problem we filter the undesired frequencies with a heated rubidium cell. The power of the laser beam is controlled with a piezo-electric actuator based shutter designed in the laboratory that is capable of blocking the beam with a precision 1000 times better than commercial shutters. We have demonstrated with the complete system Optical Trapping of rubidium atoms putting us one step closer to our scientific goals.

MEXICAN OPTICS AND PHOTONICS MEETING
19 al 21 de septiembre del 2012
San Luis Potosí, México

Digital Holographic Interferometry, Biomedical Applications

Fernando Mendoza Santoyo

Centro de Investigaciones en Óptica, A.C.
Loma del Bosque 115, Colonia Lomas del Campestre
León, Guanajuato37160
fmendoza@cio.mx

ABSTRACT:

Digital Holographic Interferometry (DHI) is an optical non-invasive technique that has proven to be a very important tool to measure displacement data from a quite large number of objects from an impressively number of diverse fields. For over 25 years DHI has helped design and modeling engineers and scientists to corroborate their theoretical and practical work with the results that stem from experimenting with DHI. More recently researchers have turned their attention to the application of DHI as an alternative tool to measure displacements from biomedical objects, with one of the main objectives being the rendering of precise quantitative data that may be used to better the diagnosis in the more common qualitative assessment performed in some biomedical areas. This presentation will deal with the underlying optical mechanisms employed to set-up a 3D DHI system, where three object-illumination beams are used to independently measure the x, y and z displacement components. Results that were obtained for the first time to measure 3D micro-deformations on the tympanic membrane (TM), plotted on its optically found contour, preliminary results showing the surface displacement of the vocal chords, and a comparison study on the wings' in-flight displacements of five different Mexican butterflies will be presented. A thorough discussion on the implication of all results will be encouraged.

Deformation overlaid on the tympanic membrane contour in its normal direction. The shape of the object is given in mm. The color bar scale amplitude is in μm.

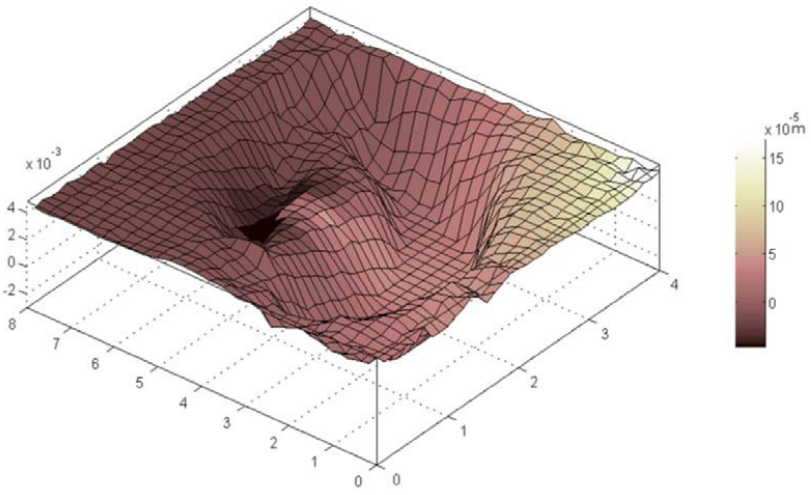

MEXICAN OPTICS AND PHOTONICS MEETING
19 al 21 de septiembre del 2012
San Luis Potosí, México

Goos-Hänchen shifts with random fields

Eugenio R. Méndez, Sergio de la Cruz, and Héctor M. Escamilla

División de Física Aplicada, Centro de Investigación Científica y de Educación Superior de Ensenada, B. C., México
emendez@cicese.mx

ABSTRACT:

The lateral displacement of a totally reflected light beam from the position expected by geometrical optics has been known for some time. The effect, which is relevant in the theory of dielectric optical waveguides, is known as the Goos-Hänchen shift. It may be understood by considering the phase change acquired, upon reflection at the interface, by the plane waves in the angular spectrum representation of the incident field. Under some circumstances, the intensity maximum of the reflected beam, resulting from the sum of all the reflected plane waves, is laterally shifted with respect of the position predicted by geometrical optics. In this work, we study the reflection of random fields from dielectric and metallic interfaces. The theory is applicable to both, speckle and partially coherent fields. We find that, in similarity with the effect that is well known for beams, random fields can also present lateral shifts in reflection experiments.

MOPM
MEXICAN OPTICS AND PHOTONICS MEETING
19 al 21 de septiembre del 2012
San Luis Potosí, México

Polarization performance of twisted erbium-doped fibers

Diana Tentori

Departamento de Óptica, División de Física Aplicada
Centro de Investigación Científica y Educación Superior de Ensenada, B.C.
Carretera Ensenada-Tijuana 3918, Playitas, Ensenada, B.C. 22860
diana@cicese.mx

ABSTRACT:

Due to various imperfections, such as core ellipticity and internal stresses, single-mode optical fibers are birefringent. In general, the magnitude and orientation of this unwanted birefringence is considered to vary randomly along the fiber. Therefore, statistical models and polarimetric techniques based on long length samples have been developed and validated for the characterization of fiber communication links. However, most fiber devices are built with short fiber lengths (< 50 m), and for such lengths, it can be considered that any non-polarization-maintaining fiber exhibits a uniform residual birefringence. Under this scope, classical polarimetric techniques should be adequate for the polarization characterization of single-mode fibers. But, since residual birefringence is highly sensitive to stresses induced by external fields (electric, magnetic, mechanical, thermal), several authors have developed measurement procedures in which one of these perturbations is the test probe. Although it is correct to assume that a finite birefringence induced by a certain external field can dominate over the unintentional birefringence introduced during the fabrication process, it is evident that the results of such an assessment do not provide precise information of residual birefringence. Since there is no previous characterization of the birefringence induced by the applied external field, the analysis of the results obtained by different authors using different measurement procedures created a large amount of unclear information leading to the idea that single-mode optical fibers have complicated polarization characteristics.

Due to residual birefringence, single-mode fiber lasers operate in two polarization modes with slightly different resonant wavelengths. Power exchanges between the two polarization modes limit their use as light sources in optical communications. For this application it is necessary to ensure single frequency as well as single polarization operation. Furthermore, the existence of both polarization modes makes such devices attractive as polarimetric fiber sensors. Changes in the birefringence of the laser cavity in response to external perturbations, directly translate into changes in the frequency separation between the two modes. It has been shown that under certain circumstances twist induced birefringence can be used to force single-polarization-mode operation or to tune the sensitivity of some polarimetric sensors. In this work I present the results of the investigation on twist-induced birefringence in erbium-doped fibers (EDFs) and discuss how this information can be used to understand the polarization performance of lasers and sensors built with EDFs.

The present work on birefringence characterization of optical fibers has been developed under the assumptions that: 1) short length fibers possess a uniform residual birefringence and 2) classical polarization optics can be applied to optical fibers. A polarimetric method is used since these procedures do not require *a priori* knowledge of the fiber polarization performance. The specification of a light polarization state demands the definition of a fixed reference frame; therefore, an important aspect of the reported polarization measurement is the use of a set up in which the reference frame is the same at the fiber input and output. In regard with the measurement signal, it is linearly polarized. This is an easily controllable polarization state that offers an additional degree of freedom to elucidate the birefringence response of fibers and fiber devices. The polarization states are represented graphically using Stokes parameters and mapping their evolution on the Poincare sphere.

OCIS: 060.2270, 060.2300, 060.2370, 060.2400, 060.2410, 060.2420, 060.3510

Interaction of light with metallic cylinders

Jorge A. Gaspar Armenta

Departamento de Investigación en Física
Universidad de Sonora
Apdo. Postal 5-088, Hermosillo, Sonora 83190
jgaspar@cifus.uson.mx

ABSTRACT:

The electromagnetic modes of metallic cylinders with a circular cross section have been studied extensively about forty years ago[1]. More complex systems formed by metallic covered dielectric cylinders were studied later because their use as sensors and as part of microscopes[2]. Their study has increased in the last two decades as components of photonic crystals, metamaterials, and plasmonic devices.

An interesting characteristic of the surface plasmon modes is the behavior as a function of the radius of the cylinder for different values of the azimuthal number or angular dependence about its axis. For small radius the surface modes acquires unique characteristics. There are several branches according to the number m in the angular part of the solutions, exp(i m ϕ) [1]. The real modes exist only for wave vectors along the axis larger than the wave vector in the surrounding medium. However, when this condition is not fulfilled, still there are surface resonances named virtual modes. These resonances are important since there are several situations when light propagates in a plane that is perpendicular to the axis of the cylinder and may produce structure in the scattering factor, for example, a metal-dielectric photonic crystal in two dimensions. For cylinder with large radius compared to the surface plasmon wavelength, the virtual modes can be approximated as the surface plasmon winding along the cylinder. For very small radius all the virtual modes converge to the plasma frequency when absorption is neglected. The only mode that apparently survive is the one corresponding to m=1 in such a way that for very small radius, the mode of the metallic cylinder behaves as a dipole with a frequency given by the plasma frequency divided by the square root of 2.

The excitation of the virtual modes are explored using finite difference time domain computer program. It is found that for very small radius, for an incident plane wave, only the m=1 mode is excited and observed in the scattering coefficient.

References.
1.-“Surface polaritons in a circularly cylindrical interface: Surface plasmons”, C. A. Pfeiffer and E. N. Economou, K. L. Ngai, Phys. Rev. B, vol. 10, pags. 3038-3051 (1974).
2.-“Light propagation in a cylindrical waveguide with a complex, metallic, dielectric function”, L. Novotny and C. Hafner, Phys. Rev. E, vol. 50, pags. 4094-4106 (1994).

OCIS: 050.1755, 050.6624, 240.6680, 240.6690, 260.3910, 260.5740

MEXICAN OPTICS AND PHOTONICS MEETING
19 al 21 de septiembre del 2012
San Luis Potosí, México

Tunable Depth of Field with High Resolution

Jorge Ojeda-Castañeda
University of Guanajuato, Salamanca, 36885, Guanajuato, México

Electronics Department, University of Guanajuato
Palo Blanco, Salamanca 36885, Guanajuato, México
jorge_ojedacastaneda@yahoo.com

ABSTRACT:

We present a tunable, complex amplitude mask that reduces the influence of focus errors, on the modulation transfer function, as well as spurious oscillations associated to the use of filters that extend the depth of field. We show that phase-space representations provide suitably tools for describing the performance of this device.

1. Introduction

Several authors have identified phase filters that extend the depth of field of an optical system. These types of filters reduce the impact of focus errors on the transfer function (MTF). However, the MTF exhibits unwanted oscillations around a tendency line[1-3]. Here, we discuss a complex amplitude filter for controlling, in a tunable fashion, the influence of focus errors, as well as for reducing unwanted oscillations of the MTF.

2. Phase-Space description

For implementing a phase-space representation of a 1-D optical signal, u(x), it is convenient to generate an intermediate 2-D signal, $p(x, y) = u(x + y/2)\, u^*(x - y/2)$, here denoted as the product space[4]. We show that this intermediate representation is well- suited for describing the optical features of the tunable spatial filters. Furthermore, the 2-D Fourier transform of the product space is the product spectrum, $P(\mu, \nu)$,which is useful for discussing the behavior of the MTF as one changes the amount of focus error[4]. We exploit the advantages of the ambiguity function for illustrating the features of our proposed device.

3. References

1. J. Ojeda-Castañeda, J. E. A. Landgrave and C. M. Gómez-Sarabia, Applied Optics, **47**, 22, E99 - E105 (2008)
2. J. Ojeda-Castañeda and C. M. Gómez-Sarabia, Proceedings of the International Conference on Trends in Optics and Photonics (Kolkata, India, 2011) ISBN 978-81-908- 188 1-0
3. J. Ojeda-Castañeda et al., US Patent, US2011/0292516 A1 (Dec 1, 2011)
4. M. Testorf, M. B. Hennelly and J. Ojeda-Castaneda, "Phase-Space Optics Fundamentals and Applications" (McGraw-Hill Professional, 2010)

Research and applications of plastic opto-electronics and photonics

J. L. Maldonado

Grupo de Propiedades Ópticas de la Materia (GPOM)
Centro de Investigaciones en Óptica (CIO) A.P. 1-948, CP 37000 León, Gto., México.
jlmr@cio.mx

ABSTRACT:

Organic semi-conducting molecules and polymers are of great importance for many fields, including physics, chemistry, optics, material sciences, and engineering.[1-12] These novel materials combine exceptional characteristics such as an easy processing, low cost, mechanical flexibility, and room temperature deposition on a variety of substrate materials. Additionally, these organic materials can be designed in virtually an infinite variety of forms to optimize any of their mechanical, electrical and optical properties.[6,7,11] For these reasons, it is expected that, in the near future, organic semi-conducting compounds will find widespread use in many technological devices. Some examples of plastic opto-electronic devices include light emitting diodes (OLEDs), photoreceptors for xerography, photovoltaic cells (OPVs), photorefractive (PR) materials for light manipulation, sensors, and more. These plastic compounds are also used for photonic applications: plastic waveguides, all polymeric integrated circuits, ultra-fast all optical correlators using third order non-linear effects, solid-state lasers, and other applications in a growing list. The advances in the developing of organic materials with better mechanical, electrical, and optical (linear and non-linear) characteristics are of a great importance for this area. In this talk is presented the research on some of these topics carrying out in the **Group of Optical Properties of Materials (GPOM)** from Centro de Investigaciones en Óptica (CIO), in collaboration with Chemistry Departments of different institutions. Basic optical characterization is performed through several techniques such as *TOF*,[4] *FWM* and *TBC*,[3,5,10] *THG Maker Fringes*,[6,11,12] *Z-scan*,[12] and *TPA*.[8,9] Additionally, some applications, such as cell imaging through two-photon excited fluorescence (TPEF),[8,9] reversible holography by using photorefractive polymers,[3,5,10] and OPVs cells[1,2] will be discussed. Particularly, in the GPOM we have got TPA cross sections up to 9000 GM and organic solar power conversion efficiency of 2.2 %.

GPOM references

[1] C. Salto *et al.*, *Synthetic Metals,* **161**, 2412–2416 (2011)
[2] J.F. Salinas *et al.*, *Solar Energy Materials and Solar Cells* **95**, 595-601 (2011)
[3] M. Rodríguez, *et al.*, *Spectrochim. Acta A* **79**, 1757-1761 (2011)
[4] Z. Zhao *et al.*, *Chem. Commun*. **47**, 6924-6926 (2011)
[5] V. Herrera-Ambriz *et al.*, *J. Phys. Chem*. *C* **115**, 23955–23963 (2011)
[6] G. Ramos-Ortíz *et al.*, *Polymer* **51**, 2351-2359 (2010)
[7] M. Rodríguez *et al*., *Dyes and Pigments* **87**, 76-83 (2010)
[8] Y. Wan *et al.*, *J. Phys. Chem. B* **114**, 11737-11745 (2010)
[9] R. Castro-Beltrán *et al.*, *Appl. Phys. B* **97**, 489–496 (2009)
[10] J.L. Maldonado *et al.*, *J. Phys. D: Appl. Phys.* **42**, 075102 (2009)
[11] M. Rodríguez *et al.*, *New J. Chem.* **33**, 1693–1702 (2009)
[12] M. Rodríguez *et al.*, *Synthetic Met.* **159**, 1281-1287 (2009)

MEXICAN OPTICS AND PHOTONICS MEETING
19 al 21 de septiembre del 2012
San Luis Potosí, México

Modulation of Polarisation in Phase-Shifting Interferometry

Gustavo Rodríguez-Zurita

Facultad de Ciencias Físico-Matemáticas
Benemérita Universidad Autónoma de Puebla
Sn. Claudio y Río Verde s/n, Ciudad Universitaria, San Manuel
72570, Puebla; Pue.
gzurita@fcfm.buap.mx

ABSTRACT:

One of the main problems in interferometry consists of extracting the phase distribution in a plane on the basis of interferograms. Since the decade of 1970s, a number of techniques have been developed by introducing given amounts of phase into an interfering wave to obtain appropriate modifications in the interferograms of the same situation. For example, continuously increasing linear phase changes or sinusoidal time-varying phase changes, give rise to the possible generation of electric signals whose phase relation maintains the unknown optical phase. Thus, very precise electronic measurements can be used to obtain the optical phase (heterodyne interferometry). As a second example, the introduction of a spatial carrier results equivalent to an introduction of a spatial phase. This can be carried out with a tilt in one of the interfering waves for instance and the procedure leads to the possibility of extracting the phase by filtering in the Fourier plane of one interferogram (method of Takeda, MT). A third technique consists of introducing at least N=3 known phases to obtain the same number N of interferograms to construct an appropiate system of equations to solve for the tangent function of the phase. This can be done with N-1 phase shifts (Phase-shifting interferometry, PSI). PSI has been very successfully adapted in electronic interferometers such as the ones based on the speckle phenomena. These methods overcome many drawbacks of the previous interferometric techniques. Almost all of these methods require of a component to perform the needed shift. With the remarkable exception of the MT, a sequence to generate the N interferograms demands of a static phase distribution during measurements. Efforts to develop single-shot PSI systems has been reported for N=4 by the end of the 1990s. In one of them, a modulation of polarisation was reported as an important stage of this system's performance.

Among the several possible shifters for PSI, the modulation of polarization seems to have important advantages in connection with calibration as well as a very good adaptability to a variety of interferometric systems. To emphasize these properties, in this talk the development of two-windows common-path interferometers using phase gratings or phase grids and polarisation controls is reviewed. It is shown that the diffractive element makes the multiplexing task of complex amplitude fields, while the modulation of polarisation is accomplished with adequate polarisers on each field replica. Some examples are presented showing how cyclic interferometers are able to produce the two windows which are needed in the interferometric systems under consideration with precise adjustment of their mutual separation. A further case within the realm of holographic interferometry is also shown. Another illustrative example deals with interferometry using optical vortices. This can give rise to the appearance of spiral fringes whose orientation, in turn, prompts about the sign of the phase, thus removing an ambiguity which has to be dealt with in traditional PSI. Finally, the possibility of using PSI with several wavelengths to obtain linear dispersion curves of isotropic refractive indexes is briefly discussed.

OCIS: 120.3180, 050.1950, 050.5080, 260.5430, 050.1960, 090.2880, 050.4865,260.2030

MEXICAN OPTICS AND PHOTONICS MEETING
19 al 21 de septiembre del 2012
San Luis Potosí, México

Energy content of ultrafast chirped pulses

M. Fernández Guasti

Lab. de Óptica Cuántica, Depto. de Física,Universidad A. Metropolitana – Iztapalapa,
09340 México D.F., Ap. postal. 55-534, MEXICO
e-mail: mfg@xanum.uam.mx, url: http://luz.izt.uam.mx

ABSTRACT:

Conservation equations for electromagnetic fields are evaluated with the complementary fields formalism[1]. This description involves the dynamic energy exchange between two co-existing fields. The energy and flow assessed in this way, do not differ (except for constants) from the average Poynting's theorem calculations for electromagnetic waves with adiabatic temporal envelope. However, when the pulse envelope becomes comparable with the carrier frequency, these two formulations differ quantitatively and qualitatively.

The complementary fields approach is used to calculate the energy content of ultrafast chirped pulses with Gaussian envelope. A quadratic phase chirp produces a wave packet with linear time dependent frequency. The energy content turns out to be dependent on the chirp parameter in the time domain as well as the frequency domain.

An asset of this formulation is that it does not require a temporal averaging in order to obtain meaningful results. This procedure has also been successfully exploited to evaluate the energy content of femtosecond pulse trains produced in Ti:Sa oscillators[2].

These results are compared with the field energy evaluated via: i) Poynting's theorem, ii) the Wigner distribution function[3], and iii) the density and flux radiometric quantities developed by Walther, Marchand and Wolf[4] (WMW) for scalar fields.

OCIS: 260.2110 Electromagnetic optics, 260.2160 Energy transfer, 260.7120 Ultrafast phenomena.

1 M. Fernández-Guasti. Complementary fields conservation equation derived from the scalar wave equation. J. Phys. A: Math. Gen., 37:41074121, 2004.
2 M. Fernández-Guasti, E. Nava, F. Acosta and R. Chandrasekar, "Physical processes behind a Ti:Sa femtosecond oscillator", in Optics and Photonics 2011 vol. 8121, (SPIE, 2011)
3 M. A. Alonso, "Wigner functions in optics: describing beams as ray bundles and pulses as particle ensembles ", Adv. Opt.Phot. 3 (2011), pp. 272-365.
4 E. W. Marchand and E. Wolf, "Radiometry with sources with any state of coherence", Opt. Soc. Am. 64, 9 (1974), pp. 1219-1226.

40 years of development in linear canonical transforms

Kurt Bernardo Wolf

Instituto de Ciencias Físicas
Universidad Nacional Autónoma de México
Av. Universidad s/n, Cuernavaca, Morelos 62210
bwolf@fis.unam.mx

ABSTRACT:

The discovery and development of the theory of Linear Canonical Transforms (LCTs) was motivated by work in two very different physical systems: paraxial optics and nuclear physics. This occurred almost simultaneously during the early 70s and in two distinct environments . The LCT integral kernel was proposed as a descriptor of light propagation in the paraxial regime of wave optics by Stuart A. Collins Jr., who worked in a laboratory of the electrical engineering department at the State University of Ohio at Columbus. On the other hand, Marcos Moshinsky and his postdoctoral associate Christiane Quesne, theoretical physicists at the Instituto de Física of UNAM (the Mexican national unviersity), who worked among other problems the alpha decay in radioactive nuclei, were interested in LCTs in quantum mechanics as a problem in basic science, which we now understand to be the conservation of information and of uncertainty.

Almost three decades elapsed before the authors of the two research lines knew of each other's work. Since mathematics yields more results than are useful in the laboratory, the 40-year history of LCTs present an interesting case study on the intertwining of basic and applied research. We have found radial and hyperbolic LCTs, complex extensions, and faithful realizations in infinite discrete systems. We propose that the appropriate framework to understand the various incarnations of LCTs is in the context of the theory of unitary representations of the symplectic groups. In its simplest case this is the `2+1' Lorentz group, all of whose representation matrices and integral kernels are known.

During the last few years there has been increasing interest in analyzing discrete and finite sets of data, since only such can be addressed by sensor and computing devices in laboratories. And here again we see evidence of a bifurcation of interests, between those that develop efficient algorithms, and those of us who look for the symmetry behind appearances.

OCIS: 000.2850, 000.3860, 070.2025, 070.2465, 070.2590, 070.4560, 080.4298

MEXICAN OPTICS AND PHOTONICS MEETING
19 al 21 de septiembre del 2012
San Luis Potosí, México

Ultrashort laser pulse characterization techniques

Roberto Ortega-Martínez

Centro de Ciencias Aplicadas y Desarrollo Tecnológico, Universidad Nacional Autónoma de México.
Ciudad Universitaria, Coyoacan, D.F. 14020, México.
roberto.ortega@ccadet.unam.mx

ABSTRACT:

There are several competing techniques for the characterization of ultrashort laser pulses. These techniques use the autocorrelation or crosscorrelation of the signals. The spectral properties of almost-Gaussian functions were applied for the second-order approximation of the coefficients of Hermite-Gaussian functions that described almost perfect pulses. Other techniques are discussed such as the real-time spectral phase interferometry for direct-field reconstruction (SPIDER), frequency-resolved optical-gating (FROG), which is a time-dependent intensity and phase of the laser pulse, the sonogram of an ultrashort pulse using a two-photon detector which is sensitive and robust. Finally, the Ambiguity-Wigner functions properties were applied for the characterization of ultrashort pulses.

OCIS Codes: 070.6770, 320.0320, 320.2250.

Millimeter-Terahertz Waves Instrumentation

Carlos Gerardo Treviño Palacios

Coordinación de Óptica, Instituto Nacional de Astrofísica, Óptica y Electrónica.
Calle Luis Enrique Erro No. 1, Sta. Ma. Tonantzintla,
Puebla, 72840, México
carlost@inaoep.mx

ABSTRACT:

We present the advances on an imaging setup by using submillimeter detectors and terahertz laser source. Terahertz radiation, known as T-rays, falls in the far infrared region of the electromagnetic spectrum close to the microwaves and fraction of millimeter wavelengths. These T-rays are ideal candidates for medical imaging because the wavelength is long enough to be dispersed by molecular structures and sufficient small to produce images with a reasonable resolution, in a non-ionizing way. The millimeter detectors used in this proposal are being developed in parallel to the detectors used in the large Millimeter Telescope (LMT/GTM). Using the non-ionizing water absorption to terahertz radiation by different tissues we study the absorption difference between healthy and tumors in spite of the large absorption by water present in the body.

Keywords: Terahertz sources, submillimeter detectors.

MEXICAN OPTICS AND PHOTONICS MEETING
19 al 21 de septiembre del 2012
San Luis Potosí, México

Optical coherent current control at surfaces: theory of injection current and spin generation

Bernardo Mendoza Santoyo

Centro de Investigaciones en Óptica, A. C.
León, Gto. México
bms@cio.mx

ABSTRACT:

We present a study of optical coherent control of injection currents and spin generation at surfaces. First we show that the injection current is a new optical effect that will serve as a surface sensitive probe of fundamentally and technologically important cubic semiconductors with both bulk inversion symmetry, (such as cubic diamond 6 m2 or 6, and non-centrosymmetric systems, (such as zinc-blende symmetry 43m). In crystals with any of these symmetries this effect vanishes in the bulk, but it is allowed in surface regions due to the breaking of the bulk symmetry there. We present the results of ab initio calculations for injected currents at prototypical clean and Sb-covered GaAs(110)(1x1) and clean Si(111)(2x1) surfaces, which have well understood and experimentally reproducible reconstructions. The effects are shown to be essentially sensitive to surface structure, and the injected currents can be interpreted in terms of the surface electronic structure. Calculated magnitudes indicate that the currents should be easily observable, and the calculated spectra of all of the surfaces demonstrate interesting behavior as a function of the energy of the incident light. Finally, layer-by-layer analysis provides detailed access to the surface properties through explicit separation of the contributions coming from different layers.
Second, we present a study of electron spin-generation onto several semiconductor surfaces due to optical excitation above the direct band gap with circularly polarized light. The chosen examples are the As and In covered Si(111) surfaces, and the clean and Sb covered GaAs(110) surfaces. As in the previous case, we use a full-band electronic structure scheme to calculate the rate of spin and carrier generation, and then calculate the degree of spin polarization up to energies well above the surface modified band gap. Again a “layer-by-layer” analysis of the spin-generation is implemented; the model accounts for the coherences excited in a semiconductor with spin-split bands. We show that the spin-generation could be almost 100% for the As covered Si(111) surface and 90% for the clean GaAs(110) surface. For comparison, in bulk Si and GaAs, the maximum polarization calculated is only 30% and 50%, respectively. The degree of spin polarization for all of the surfaces shows a large signal and an interesting behavior as a function of the photon energy.

MEXICAN OPTICS AND PHOTONICS MEETING
19 al 21 de septiembre del 2012
San Luis Potosí, México

Pancharatnam-Berry phase for optical systems

Julio César Gutiérrez-Vega

Centro de Óptica, Tecnológico de Monterrey
Garza Sada 2501, Monterrey, N. L. México 64849
juliocesar@itesm.mx

ABSTRACT:

We present simple closed-form expressions for evaluating the overall and the Pancharatnam-Berry phase introduced by an optical system with either orthogonal or non-orthogonal eigen-polarizations. The formulas are useful in interferometric measurements with vector beams and provide meaningful connection with the Pancharatnam-Berry phase associated to non-closed paths on the Poincare sphere.

High Power CW and Pulsed Diode Lasers based on Separate Confinement Quantum Well Double Heterostructures

N. A. Pikhtin, I. S.Tarasov, S. O. Slipchenko

Ioffe Physico-technical Institute, Russian Academy of Sciences, 194021 St. Petersburg, Russia,
e-mail: nike@hpld.ioffe.ru

ABSTRACT

The concept of high power semiconductor lasers (λ = 800-1800 nm) based on MOCVD-grown separate-confinement double heterostructures with quantum wells will be presented. Output characteristics of ridge waveguide 100μm-aperture diode lasers reaching 20W room temperature (RT) continuous wave (CW) optical power at 1060 nm wavelength will be considered in detail. Temperature stability of such devices in 20 – 140°C range will be analyzed for different heterostructure designs. Physical and technologic factors limiting RT optical output power in CW and pulsed (100ns/1kHz) regimes will be discussed.

Reasons of external differential quantum efficiency drop with CW and pulsed pump current increase will be analyzed. Experimental results of spontaneous and stimulated emission spectra, internal optical loss and internal quantum efficiency measured in wide temperature (20 – 140°C) and pump current (0-150 A) ranges will be used for optical power saturation analysis. Band structure engineering and chip geometry construction will be also considered for effective pulsed and CW diode laser operation.

Epitaxially-integrated tunnel-junction laser heterostructure design will be proposed as an effective way of pulsed optical power increase in single-element diode lasers. Experimental data will be presented.

MEXICAN OPTICS AND PHOTONICS MEETING
19 al 21 de septiembre del 2012
San Luis Potosí, México

Laser ablation for thorns removal of opuntia

L. Ponce, M. Arronte, E. de Posada, T. Flores.
Centro de Investigaciones en Ciencia Aplicada y Tecnología Avanzada del Instituto Politécnico Nacional.
Km 14,5 Carretera Tampico-Puerto Industrial, Altamira 89600, Tamps, México.
lponce@ipn.mx

J. Cabrera, O. Cruzata, B. Lambert
IMRE-Universidad de La Habana. Vedado 10400, C. Habana, Cuba.

ABSTRACT:
A new method that eliminates the thorns from food products like Opuntia (nopalitos) by using laser pulses is presented. Looking for wavelength that should be absorbed selectively by the the parts to be removed, an optical characteristics in the 400 to 1200 nm spectral range were studied. The energy and duration of the most appropriate pulses were empirically determined, the key criterion being to achieve the highest ablation efficiency while causing minimal damage to the surrounding area. The pulsed photo-acoustic technique (PILA) and dynamic reflectance measurement were used for interactively monitoring the thorn removal process. Lastly, the morphology of the samples was analyzed by several techniques in order to guarantee the quality of product after de-thorning. There were demonstrated the advantages of laser process avoiding the losses caused by manual de-thorning and also the increment of product life. Finally a brief description of laser machine for Opuntia processing is presented.

MEXICAN OPTICS AND PHOTONICS MEETING
19 al 21 de septiembre del 2012
San Luis Potosí, México

Nonlinear optical properties of anisotropic metallic nanocomposites

Raúl Rangel Rojo,[1] Bonifacio Can Uc,[1] Israel Rocha-Mendoza,[1] Luis Rodríguez-Fernández,[2] and Alicia Oliver[2]

[1]*Departamento de Optica, Centro de Investigación Científica y de Educación Superior de Ensenada, Carretera Ensenada-Tijuana No.3918, Zona Playitas, 22860, Ensenada, Baja California, México*
[2]*Instituto de Física, Universidad Nacional Autónoma de México, Circuito de la Investigación Científica S/N, Ciudad Universitaria, Distrito Federal, México*
rrangel@cicese.mx

ABSTRACT:

The nonlinear optical properties of nanostructured materials composed of metal nanoparticles have attracted much attention in recent years due to the possibility of using them as photonic nanodevices and in plasmonic circuitry. Recently, we have started the study of the optical third-order nonlinearity of randomly placed, elongated silver nanoparticles (Ag-NPs) which are aligned in a preferential direction, embedded in silica [1].

In this work, we present a study of both the second-order, and third-order nonlinear response of composites materials containing such elongated and aligned silver NPs. The second-order nonlinear processes were probed by means of a study of the polarization dependence of second harmonic generation with nonresonant femtosecond pulses [2]. The third-order nonlinear response was studied using the z-scan technique with the same femtosecond laser source. The use of the z-scan technique allowed us the resolution of the refractive and absorptive contributions to the response. The same measurements were made in a sample containing spherical silver NPs for comparison.

The spherical silver nanoparticles (Sp Ag-NPs) were produced by a single ion implantation process, as described in ref. [1], from which a film containing spherical-like silver nanoparticles, of around 6 nm in diameter, at around 1 μm depth inside the silica matrix was obtained. The elongated silver nanoparticles (El Ag-NPs) were obtained by means of a second ion implantation process, with Si ions, over the initial SpAg-NPs samples. They were irradiated at an angle of 45^o with respect to the sample surface obtaining a 0.5 μm thick layer containing randomly placed elongated nanoparticles. The El Ag-NPs were actually shaped as prolate spheroids with an average minor axis diameter of 5 nm and an aspect ratio of 1.7. The resulting sample is highly anisotropic.

We acknowledge financial support from PAPIIT-UNAM *IN*103609; from CONACyT through grant 102937, from ICyT-DF through grant PICCT08-80, and (I. Rocha-Mendoza) from UC-MEXUS/CONACyT under collaborative research programs.

[1] R. Rangel-Rojo, *et. al.*, "Anisotropy in the nonlinear absorption of elongated silver nanoparticles in silica, probed by femtosecond pulses," *Opt. Commun*., 282, 1909–1912 (2009).
[2] I. Rocha-Mendoza, *et. al.* "Second-order nonlinear response of composites containing aligned elongated silver nanoparticles, " *Optics Express* 19(22), 21575-21587 (2011).
[3]G. Bachelier, *et. al.*, "Origin of optical second-harmonic generation in spherical gold nanoparticles: Local surface and nonlocal bulk contributions," *Phys. Rev. B,* 82 (23), 235403 (2015).
OCIS: 000.2850, 000.3860, 070.2025, 070.2465, 070.2590, 070.4560, 080.4298

MEXICAN OPTICS AND PHOTONICS MEETING
19 al 21 de septiembre del 2012
San Luis Potosí, México

CALIPO – GRUPO SISA:
Experience in a High-Tech Business in México

Enrique Rivera Garibaldi
Technical Director GRUPO SISA, Ensenada, B. C.
erivera@gruposisa.com

ABSTRACT
In accordance with the decree that created the "Centro de Investigación Científica y de Educación Superior de Ensenada (CICESE)", in the eighties, a group of researchers[1] and students[2] of the Division of Applied Physics (Optics Department) initiated works in technological development aimed at having social and economic impact on the community. Then, the Optics Department started to be recognized as a leader in technological projects in the areas of fine and precision mechanics, development of ophthalmic glass, growth of optical crystals, manufacture of plastic lenses and development of polarizing devices. In order to spread the main results and implications of these developments, this talk will present a brief history of the evolution of a scientific research project that was transformed into a technological development project that led to the creation of "Calipo, S. A. de C. V." (now called "Crystal Opto de Mexico S. A. de C. V."), which is part of "Corporativo de Sistemas y Servicios Ambientales, (GRUPO SISA)", a parent company specializing in environmental systems and services. In 26 years of business work, one of the founding scientists of Calipo has established a vision of working outside academia, where the following can be highlighted:

1. Personal commitment
   - The dedication, commitment and training required for technological development projects.
2. The current status of research in Mexico, which highlights:
   - The low investment in science and technology due to their not having had any impact on society.
   - The lack of knowledge among the business and research sectors.
   - The divergent interests between industry and research centers.
   - National fostering policies and their disassociation from national problems.
   - Technology as an important element, but not sufficient, for the success of technology companies or specialized service providers.
   - The need for the spread and management of research results among high-ranking government officers and businesses so that the benefit of using them is duly appreciated.
3. The elements inhibiting linkage between research centers and industry due to:
   - Resistance to change in research centers.
   - Differences between projects and business plans.
   - Knowledge of markets and definition of product and services.
   - Inadequate incentives to researchers in Mexico; the interface between doing basic and applied science lends itself to surviving in the system with little social commitment.
   - The urgency for scientists to cultivate, along with a strong academic background, a major business vision for development.
4. Lack of business training
   - Business training to minimize the risks of a business (market, personal, financial and accounting risks, legal obligations and tax payments, logistics, technological horizon, etc.)
   - The importance of business and social sciences as complementary to technical activities.
   - The importance of information technologies in a business; management systems are necessary to be competitive in the market.

1.- Dr. Romeo Mercado, Dr. Luis Enrique Celaya, Dr. Marco Machado, Dr. Martin Celaya, Dr. Roberto Machorro, Dr. Diana Tentori, Dr. Enrique Mitrani, Fis. Narayana Varanasi, Ing. Manuel Yamada.
2.- Dr. Alfonso García Weidner, Dr. Enrique Rivera, Dr. Heriberto Márquez

MOPM
MEXICAN OPTICS AND PHOTONICS MEETING
19 al 21 de septiembre del 2012
San Luis Potosí, México

Triple helix links

Jorge. R. Loredo Murphy
Facultad de Ingeniería Mecánica y Eléctrica
Universidad Autónoma de Nuevo León, México

ABSTRACT

The need of collaboration between Government, Industry and Academia has revealed itself as a trigger of activities and achievements in innovation and technological development, as a new path to the traditional worries for networking, and there are economic indications that at least partially show some of the implications. Recent results seem to come out from government efforts to stimulate investment in research and development, and whereas specific data might not yet be available, it seems worthwhile to review some facts, among them the creation of the "Parque de Innovación y Transferencia de Tecnología", PIIT, a Research Park in the State of Nuevo Leon, Mexico, that brings together a series of Research and Development Centers, National, as well as Private and Academic, Mexican and International, including CONACYT Centers. A quick overview is presented.

MEXICAN OPTICS AND PHOTONICS MEETING
19 al 21 de septiembre del 2012
San Luis Potosí, México

MODULATED SPECTROSCOPIES

L. F. Lastras-Martínez

Instituto de Investigación en Comunicación Óptica, Universidad Autónoma de San Luis Potosí, Álvaro Obregón 64 CP 78000, San Luis Potosí, SLP, México

ABSTRACT

Reflectance Modulated (RM) spectroscopies constitute very powerful tools for the study and characterization of the physical properties of semiconductor materials. In such techniques, either a physical parameter of the sample under study or a parameter of the probing light is modulated periodically. Among the EM techniques we can mention ellipsometry, photoreflectance, reflectance difference (RD) and photoreflectance difference spectroscopies. One of the important features of RM spectroscopies is that they can be used in air or under vacuum conditions. EM spectroscopies provide complementary information. In this course, we will discuss the basic principles of the EM spectroscopies and their applications. Specifically we will give a discussion of RD spectroscopy and the physical mechanisms that originate the line shape of the spectra. Additionally, we will extend the discussion of RD spectroscopy to a microscopic regime, illustrating the potential of the technique.

MEXICAN OPTICS AND PHOTONICS MEETING
19 al 21 de septiembre del 2012
San Luis Potosí, México

Short Course: Semiconductor Laser Diodes

Andrei Gorbatchev

Universidad Autónoma de San Luis Potosí, Instituto de Investigación en Comunicación Óptica, Av. Karacorum 1470, Col. Lomas 4ª Sec., CP 78210 San Luis Potosí, México
andre@cactus.iico.uaslp.mx

Abstract

The course deals with the basic aspects of the physics of semiconductor lasers. In addition to theoretical knowledge, participants will get elementary skills in the characterization of devices based on laser diodes. The course is aimed at graduate students who are specialized in the area of photonics, semiconductor materials and devices, it last 2 hours and consists of 2 parts.
In the first part of the course, a brief introduction will be given to the theory of the optical model of the laser, the basic aspects of the mechanism of charge carriers injection in the structures on the basis of p-n junctions. Types and constructions of the laser diodes with horizontal and vertical resonators, their main electro-optical characteristics and applications will be presented.
The second part of the course is experimental. The students will get practical experience on the work with semiconductor structures, laser diodes, and devices on their basis. The studies include measurements of the emission spectra, Current-Voltage (I-V) and Optical power-Current (P-I) characteristics.

MEXICAN OPTICS AND PHOTONICS MEETING
19 al 21 de septiembre del 2012
San Luis Potosí, México

Method for Breast Cancer Detection: Calcification & Mass Malignant

R. Guzmán-Cabrera, J.R. Guzmán-Sepúlveda, M. Torres Cisneros, J. Ruiz Pinales and O.G. Ibarra Manzano

División de Ingenierías del campus Irapuato-Salamanca, Carretera Salamanca-Valle de Santiago Km 3.5+1.8 Km Comunidad de Palo Blanco, C.P. 36885 Salamanca, Gto. Tel. +52 (464) 64 7 99 40.

Corresponding author email: guzmanc@ugto.mx

ABSTRACT:

Breast cancer is the most common cause of death in women and the second leading cause of cancer deaths worldwide. Typical signatures of this disease, such as masses and micro-calcifications appearing on mammograms, can be used to improve early diagnostic techniques, for which several Computer-Aided Diagnosis schemes have been developed to support radiologists and internists on their diagnosis. In this paper, we propose an approach to optimize the analysis of digital mammograms by using texture segmentation for discriminating masses and micro-calcifications from the background tissue based on Morphological Operators and extracting them through machine learning techniques and clustering algorithms for intensity-based segmentation.
Key words: Cancer Detection, Micro calcification, Tumor

REFERENCES AND LINKS

[1] Lei Zheng and Andrew K. Chan, "An artificial intelligent algorithm for tumor detection in screening mammogram," IEEE transactions on medical imaging, vol. 20, no. 7, July, 2001.
[2] M. Heath, K. Bowyer, D. Kopans, R. Moore, and W. P. Kegelmeyer, "The Digital Database for Screening Mammography", Proceedings of the Fifth International Workshop on Digital Mammography, M.J. Yaffe, ed., pp. 212-218, Medical Physics Publishing. (2001)
[3] M. Heath, K. Bowyer, D. Kopans, W. P. Kegelmeyer, R. Moore, K. Chang, and S. MunishKumaran, "Current status of the Digital Database for Screening Mammography", Digital Mammography, pp. 457-460, Kluwer Academic Publishers (1998), Proceedings of the Fourth International Workshop on Digital Mammography.

1. Introduction

The proposed technique uses feature extraction through texture analysis for the identification and discrimination of suspicious areas related to cancer and benign tumors, as well as micro-calcifications. Since texture-based analysis methods characterize texture in terms of the extracted features, segmentation depends not only on the images under study but also on the purpose for which the image texture analysis is used [1]. The proposed algorithm deals with 8-bit gray-scale hand-labeled images obtained from the Digital Database for Screening Mammography (DDSM) [2-3], which are 16-bit gray-scale images stored with lossless JPEG compression.

2. Method and Principle of Operation

The main goal of this work is to optimize the parameters of the proposed technique to achieve the best performance in the identification and extraction of previously identified suspicious regions. The predominant parameters of the proposed technique are the reference gray-level of the texture to be found (i.e. gray-level of the pixels in the abnormality region), and the reference regions size for "small" areas to be removed from the binary texture image of

the suspicious and background textures. Fig. 1 shows the performance of the algorithm for three different reference gray-level, it can be noticed the high sensitivity of the algorithm to this parameter.

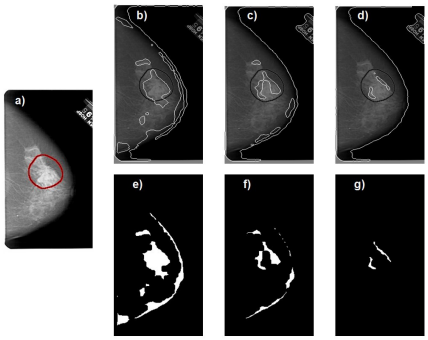

Figure 1. a) Original Image. b-d) Segmentation and e-f) extraction results for reference gray levels 0.77, 0.80, and 0.83, respectively. Volume 11 – Case 1236 – Right CC, [9-10]

3. Optimization: Experiments and Results

Since the algorithm can result in successful or unsuccessful detection of the abnormality, an optimization process is proposed for the parameters mentioned above. The filter-like response of the correlation coefficient between the detected and labeled regions, which is shown in Fig. 2, suggests that there are specific gray-levels for which greater similitude between the processed and labeled images is achieved. The insets in Fig. 2 show the surface of the correlation coefficient as a function of the reference areas, which allows selecting the most adequate input parameters resulting in order to obtain the highest correlation coefficient. Fig. 2a shows the correlation for micro calcifications, while Fig. 2b shows the correlation for the mass; by comparing them it can be seen a different behavior in the slope of the correlation curve for the case of micro calcifications and masses.

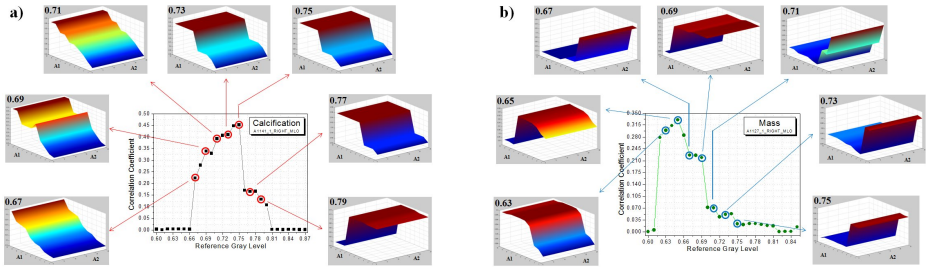

Figure 2. Correlation between the detected area and labeled image for different level of gray in a) micro-calcification and b) mass.

4. Conclusion

The exhibited behavior of the correlation coefficient is directly related with the size of the reference area for the small regions to be removed after segmentation, in the case of micro-calcifications, it can be clearly noticed that the correlation coefficient increases when large areas are removed, which means that the information corresponding to small areas, including those where the calcifications are located, still remain in the picture; on the other hand, in the case of mass, the correlation coefficient increases when small areas are removed, which means that the information corresponding to large areas remains in the picture and can be then discriminated. This difference can be used not only to determine the best conditions of the input parameters but also for differentiating between micro-calcification and mass, resulting in an effective image analysis for convenient assistance to the medical diagnosis.

MOPM
MEXICAN OPTICS AND PHOTONICS MEETING
19 al 21 de septiembre del 2012
San Luis Potosí, México

A rotation invariant correlation using an adaptive methodology

Alfredo Solís Ventura, Josué Álvarez Borrego

Centro de Investigación Científica y de Educación Superior de Ensenada.
asolis@cicese.edu.mx, josue@cicece.mx

ABSTRACT:
Distortions of an object due to displacement or rotation, adds difficulty or makes impossible the identification of the object. A low computational cost digital algorithm was developed to recognize images even when these images appear rotated, displaced and immersed in noise. Vectorial signatures are generated from binary masks of concentric rings when this is multiplied by the modulus of the Fourier transform of the image. In this application, vectorial signatures are compared using nonlinear correlations. It was possible to get the identification of the 26 alphabet letters, where each of these were rotated degree by degree from 0^o to 359^o generating 9360 different images. Results with a 100% confidence level in the identification of the 26 alphabet letters are shown.
Key words: Image recognition, nonlinear correlation, rings mask, one-dimensional signatures, Fourier transform.

REFERENCES AND LINKS

[1] G. Lendaris, G. Stanley, "An opticalogical self-organizing recognition system" *Opt. Electro-Opt. Inf. Proc*., Ch. 29, 535-550 (1965).

[2] A. Fares, A. Bouzid, M. Hamdi, "Rotation invariance using diffraction pattern sampling in optical pattern recognition" *J. Mic. and Optoelec*., 2, 33-39 (2000).

[3] S. Solorza, J. Álvarez-Borrego, "Digital system of invariant correlation to position and rotation" *Opt. Commun*. 283(19), 3613-3630 (2010).

[4] G. Chaparro-Magallanez, J. Álvarez-Borrego, S. Solorza. "Invariant correlation to position, rotation and scale using one-dimensional composite filters". *Proc. of SPIE* 8011(801171) (2011).

[5] S. Solorza, J. Álvarez-Borrego, "Digital system of invariant correlation to position and scale using adaptive ring masks and unidimensional signatures". *Proc. of SPIE*. 8011(801172) (2011).

[6] V. K. Vijaya-Kumar and L. Hassebrook, "Performance measures for correlation filters," *Appl. Opt*. 29(20), 2997–3006 (1990).

1. Introduction.

Recognition of images in real time is not an easy issue because the object to recognize can be displaced and to have distortions from rotation or from different kinds of noise. Therefore it is necessary the development of specific techniques to recognize the same object with invariance to a concrete distortion or a set of these. Since 60's, the binary masks are used to take frequency samples from the diffraction pattern and to get the invariance to position [1]. The rotation invariance is achieved using a binary mask of concentric rings [2]. Recent investigations have used adaptive rings mask, getting a robust one-dimensional vectorial signature, taken only the most important frequencies from the image diffraction pattern. A k-law nonlinear filter is used to realize the digital invariant correlation that gives us information on the similarity between different images [6].

1. Methodology.

The digital algorithm proposed generates an adaptive binary rings mask from the real part of the Fourier transform (FT) of the image. The mask takes samples of the most important frequencies from the modulus of the Fourier

transform of the image to generate a one-dimensional vectorial signature. Signatures are compared using an adaptive k-law nonlinear correlation.

2.a. **Binary rings mask of the image.** The construction of the binary rings mask starts taking the positive and real part of the FT associated to a target image. From this reference, adaptive concentric rings mask are generated. Next, a point to point product with the rings mask and the modulus of the Fourier transform (|FFT|) of the target image was done. From this product, concentric rings with sampled values from |FFT| are calculated. The next step is to compute the sum of the intensity values in each ring and to obtain a one-dimensional vectorial signature. This signature represents a target image with invariance to rotation and position. Same procedure is made for the problem image (image to be recognized or classified).

2.b. **Nonlinear correlation.** In order to recognize the target, the signature of the problem image (PI) is compared with the signature of the target image (TI) using the non linear correlation, C_{NL1},

$$C_{NL1}(PI,TI) = PI \otimes TI = FFT^{-1}\left(\left|FFT(PI)\right|^{k} e^{i\phi_{PI}} \left|FFT(TI)\right|^{k} e^{-i\phi_{TI}}\right), \quad (1)$$

where $\otimes$ means correlation, $i=\sqrt{-1}$, ϕ_{PI} and ϕ_{TI} are the phase of the Fourier transform of the problem image and the target image signature, respectively, $0 < k < 1$ is the non linear coefficient factor [10].
The area value of an image can be used as invariance to rotation; this invariance is obtained because even if the image is rotated this value will be conserved [9]. In this case, the mean value of the images as parameter invariant to rotation was used. In order to increase the discrimination between the target and the problem image, a ratio of the mean values of the images is introduced to Eq.(1).

$$\text{IF } mean(PI) < mean(TI),\ ratio = mean(PI)/mean(TI) \text{ ELSE } ratio = mean(TI)/mean(PI), \quad (2)$$

Then the Eq.(2) ratio is introduced to Eq.(1), and has a new adaptive nonlinear correlation, C_{NL2},

$$C_{NL2}(PI,TI) = PI \otimes TI = FFT^{-1}\left(\left|FFT(PI)\right|^{ratio\cdot k} e^{i\phi_{PI}} \left|FFT(TI)\right|^{k} e^{-i\phi_{TI}}\right), \quad (3)$$

2. **Results.**
An optimal value of k (ratio-k) to use in Eq.(3) in the presence of additive Gaussian noise and salt and pepper noise was found. The 26 alphabet letters were analysed, each of these images in Arial font type was rotated degree by degree from 0^o to 359^o generating 9360 different images in black and white format, size of 128 x 128 pixels. 360 different correlations to each letter were computed. The mean value of these correlations are represented in a box plot, at two standard errors (±2SE), the confidence level was 95.4%. If the correlation of different letters mean correlation values don't overlap, then we get a confidence level of 100%. In all the cases the identification of the target images was a success with a confidence level of 100%. The computer time per image is about 0.2 sec.

4. **Conclusion.** The proposed adaptive methodology is able to extract the necessary information from an image to get a one-dimensional vectorial signature invariant to position and rotation; and using the aid of a novel proposed variant of a k-law nonlinear correlation to achieve an adaptive version of nonlinear correlation, this methodology is able to represent a target image with success and excellent results even when the problem image is immerse in noise. It was possible to get the identification of the 26 alphabet letters, with a confidence level of 100% and using a minimal time of computational cost in all the cases.

Acknowledgements

This document is based on work partially supported by CONACyT under Grant No. 102007.

MEXICAN OPTICS AND PHOTONICS MEETING
19 al 21 de septiembre del 2012
San Luis Potosí, México

Pattern recognition in digital images by binary concentric rings optimal masks

Reconocimiento de patrones en imágenes digitales mediante máscaras óptimas de anillos concéntricos

Selene Solorza [(1)], Josué Álvarez-Borrego [(2)],

1. Facultad de Ciencias, Universidad Autónoma de Baja California.
2. División de Física Aplicada, Centro de Investigación Científica y de Educación Superior de Ensenada
Corresponding author email: josue@cicese.mx

ABSTRACT:

In this work a new non-linear correlation digital system invariant to position, rotation, scale and resolution based on optimal masks and the one-dimensional signatures methodology is presented.

Key words: Optimal mask, one-dimensional signature, non-linear correlation.

RESUMEN:

En este trabajo se presenta un nuevo sistema digital de correlación no lineal invariante a posición, rotación, escala y resolución que se basa en máscaras óptimas y en la metodología de firmas uni-dimensionales.

Palabras clave: Máscara óptima, firma uni-dimensional, correlación no lineal.

REFERENCES AND LINKS

[1] S. Solorza, J. Álvarez-Borrego y G. Chaparro-Magallanez, Pattern recognition of digital images by one-dimensional signatures, Chapter 13, Fourier Transform-Signal Processing, Intech (2012).

[2] R.E. Guerrero-Moreno y J. Álvarez-Borrego, "Nonlinear composite filter performance", *Opt. Eng.* **48**, 06720 (2009).

1. Introduction

Recently, digital systems invariant correlation to position, rotation and scale are utilized in the pattern recognition field [1]. Such invariants are made by the Fourier and Fourier-Mellin transforms in conjunction with non linear filters (*k*-law filter). The non linear filters have advantages compared with the classical filters (POF, BAPOF, VanderLugt, CHF) due to their great capacity to discriminate objects, the maximum value of the correlation peak is well localized, and the output plane is less noisy [2]. In order to have a new non-linear correlation digital system

invariant to position, rotation, scale and resolution in this work a new methodology based on one-dimensional signatures of the images is presented. This new algorithm uses optimal masks to obtain resolution invariant.

2. The digital system

2.a.- The optimal masks

The masks associated of a given square image *I* of size *N*X*N* are built by taking the real and imaginary parts of its *2D*-Fourier transform (*FT(I)*). Results of both images are filtered by a mask of a binary disk of diameter equal to *N*. After that, *180* profiles with length *N* are obtained for each Fourier plane image. These profiles pass for the centre of the image (*c*,*c*) and they ending in the disk's border. The profiles are separated by 1 deg, sampling of this way the entire circle. The next step is to compute, for the real part, the addition of the intensity values in each profile and select the profile whose sum has the maximum value; it is called the optimal profile f_{FR}. Analogously for the imaginary part, the optimal profile f_{FI} is calculated. From f_{FR} two binary functions are built by

$$Z_{P}^{FR}(x)=1 \text{ if } f_{FR}(x)>0 \text{ and } 0 \text{ if } f_{FR}(x)\le 0. \quad Z_{NP}^{FR}(x)=1 \text{ if } f_{FR}(x)\le 0 \text{ and } 0 \text{ if } f_{FR}(x)>0, \tag{1}$$

where *x=1,… N*. For f_{FI} only the binary function Z_{P}^{FI} is obtained as eq. (1). This three binary function are symmetric in *x=c*. Taking *x=c* as the rotation axis, the graph of Z_{P}^{FR}, Z_{NP}^{FR} and Z_{P}^{FI} are rotated 180 degrees to obtain three optimal masks, M_{FRP}, M_{FRNP}, M_{FIP}, of concentric rings with different widths and centred in (*c*,*c*) associated to the images *I*. Based on these optimal masks, three one-dimensional signatures are computed using the Fourier-Mellin transform like [1]. The average of them is called the average-signature of the image *I*.

2.b.- The pattern recognition

Let *A* the set of *n* reference image (*RI*). Then, *n* average-signatures are computed as section 2.a. If a problem image (*PI*) will be classified, its average-signature is build using the M_{FRP}, M_{FRNP}, M_{FIP}, of $RI_K \in A$. If the maximum value of the magnitude for the non-linear correlation [2] are significant, that is similar to the autocorrelation maximum value, hence the *PI* contains the RI_K, otherwise are different. Moreover, the *PI* could had a different resolution of that images in *A* and the digital system classified it. The resolution invariant is achieved by the uses of the same three optimal masks of the RI_K to make the average-signature of the *PI*.

3. Conclusions

This work presents a low computational cost algorithm invariant to position, rotation, scale and resolution. The digital system was tested using a database of BW Arial font letter and it presents an excellent performance, a confidence level of 95.4% or greater.

Acknowledgements

This work was partially supported by CONACyT under grant No. 102007 and 169174.

MEXICAN OPTICS AND PHOTONICS MEETING
19 al 21 de septiembre del 2012
San Luis Potosí, México

Some statistical properties of surface slopes from glitter patterns considering a non-Gaussian probability density function.

Josué Álvarez-Borrego [(1)], Beatríz Martín Atienza[(2)]

1. División de Física Aplicada, Centro de Investigación Científica y de Educación Superior de Ensenada
2. Facultad de Ciencias Marinas, Universidad Autónoma de Baja California.

Corresponding author email: josue@cicese.mx

ABSTRACT:

Relationships to obtain information concerning some statistical properties of surface slope from statistical properties of the image intensity in remote sensed images, considering a variable detector line of sight angle, are shown. Considering the assumption that all the ocean waves are moving along a single direction and that the observer and the sun are both in the vertical plane containing this direction, a new expression between the mean and the variance of the intensity in the image and the variance of the surface slopes is derived considering a non-Gaussian statistics where the skewness and kurtosis moments are taken into account. The one-dimensional case is considered and the results are presented graphically.

Key words: Sunglint, Random Processes, Glitter Pattern.

REFERENCES AND LINKS

[1] J. Álvarez-Borrego and B. Martín-Atienza, "An improved model to obtain some statistical properties of surface slopes via remote sensing using variable reflection angle," IEEE Tran. Geos. Rem. Sens., vol. 48, pp.3647-3651, October 2010.

[2] C. Cox and W. Munk, "Slopes of the sea surface deduced from photographs of sun glitter," Scripps Inst. Oceanogr. Bull, vol. 6, pp.401-488, September 1956.

[3] W. Munk, "An inconvenient sea truth: spread, steepness, and skewness of surface slopes," Annu. Rev. Mar. Sci., vol. 1, pp.377-415, January 2009.

---

1. Introduction

Recently an improved model to obtain some statistical properties of sea surface slopes via remote sensing using variable reflection angle was considered [1]. In that case, a Gaussian probability density function was considered.
The idea in this work is to derivate new relationships between the mean and the variance of the intensity in the image of the sea surface (taken by a CCD camera) and surface slopes for different incidence angles, but considering a more realistic probability density function like was discussed in several papers before [2-3].
The brightness distribution in sunlight reflected from the ruffled sea surface is related to the joint probability distribution of the two components of surface slope. A one-dimensional section through the brightness distribution provides values of the joint distribution along a line through the joint distribution.

2. Relationships among the variances of the intensities in the image and surface slopes

The mean of the image intensity μ_I may be written as [1]:

$$\mu_I = \langle I(x) \rangle = \frac{1}{N} \sum_{i=1}^{N} \int_{-\infty}^{+\infty} B(M_i)\, p(M_i)\, dM_i , \tag{1}$$

where $B(M_i)$ is the glitter function defined by [1]. $p(M_i)$ is the probability density function, where a non-Gaussian function is considered in one dimension:

$$p(M_i) = \frac{1}{\sigma_M \sqrt{2\pi}} \exp\left(-\frac{M_i^2}{2\sigma_M^2} \right) \bullet \left[1 + \frac{1}{6} \lambda_M^{(3)} \left\{ \left(\frac{M_i}{\sigma_M} \right)^3 - 3\left(\frac{M_i}{\sigma_M} \right) \right\} + \frac{1}{24} \lambda_M^{(4)} \left\{ \left(\frac{M_i}{\sigma_M} \right)^4 - 6\left(\frac{M_i}{\sigma_M} \right)^2 + 3 \right\} \right] \tag{2}$$

where $\lambda_M^{(3)}$ is the skewness, $\lambda_M^{(4)}$ is the kurtosis and σ_M is the standard deviation of the surface slopes.

The variance of the intensities in the image σ_I^2 is given by

$$\sigma_I^2 = \frac{1}{N} \sum_{i=1}^{N} \left\{ \begin{array}{l} \left[erf\left(\frac{b_i}{\sqrt{2}\sigma_M} \right) - erf\left(\frac{a_i}{\sqrt{2}\sigma_M} \right) \right] \bullet \left[\frac{1}{2} + \frac{1}{8} \lambda_M^{(4)} \left(1 - 3\sigma_M^2 \right) \right] + \\ + \exp\left(-\frac{a_i^2}{2\sigma_M^2} \right) \bullet \left[\frac{\lambda_M^{(3)}}{6\sqrt{2\pi}\sigma_M^2} \left(a_i^2 - \sigma_M^2 \right) + \frac{\lambda_M^{(4)} a_i}{24\sqrt{2\pi}\sigma_M^3} \left(a_i^2 - 3\sigma_M^2 \right) \right] + \\ + \exp\left(-\frac{b_i^2}{2\sigma_M^2} \right) \bullet \left[\frac{\lambda_M^{(3)}}{6\sqrt{2\pi}\sigma_M^2} \left(\sigma_M^2 - b_i^2 \right) + \frac{\lambda_M^{(4)} b_i}{24\sqrt{2\pi}\sigma_M^3} \left(3\sigma_M^2 - b_i^2 \right) \right] \end{array} \right\} - \tag{3}$$

$$\frac{1}{N^2} \left[\sum_{i=1}^{N} \left\{ \begin{array}{l} \left[erf\left(\frac{b_i}{\sqrt{2}\sigma_M} \right) - erf\left(\frac{a_i}{\sqrt{2}\sigma_M} \right) \right] \bullet \left[\frac{1}{2} + \frac{1}{8} \lambda_M^{(4)} \left(1 - 3\sigma_M^2 \right) \right] + \\ + \exp\left(-\frac{a_i^2}{2\sigma_M^2} \right) \bullet \left[\frac{\lambda_M^{(3)}}{6\sqrt{2\pi}\sigma_M^2} \left(a_i^2 - \sigma_M^2 \right) + \frac{\lambda_M^{(4)} a_i}{24\sqrt{2\pi}\sigma_M^3} \left(a_i^2 - 3\sigma_M^2 \right) \right] + \\ + \exp\left(-\frac{b_i^2}{2\sigma_M^2} \right) \bullet \left[\frac{\lambda_M^{(3)}}{6\sqrt{2\pi}\sigma_M^2} \left(\sigma_M^2 - b_i^2 \right) + \frac{\lambda_M^{(4)} b_i}{24\sqrt{2\pi}\sigma_M^3} \left(3\sigma_M^2 - b_i^2 \right) \right] \end{array} \right\} \right]^2$$

which is the required relationship between the variance of the intensities in the image σ_I^2 and the variance of the surface slopes σ_M^2 when a non-Gaussian probability density function is considered.

3. Conclusions

We derived the mean and the variance of the surface slopes from the variance of the intensities of remote sensed images for different H values, considering a glitter function given by [1] in the one-dimensional case. In addition, it is possible to observe the effect of skewness and kurtosis of the sea surface slope distribution in an optical image. When we have a sea surface slope with a Gaussian distribution, there are a number of bright points in the optical image originated by the non-linear slope band, due to the variation of $(\theta_d)_i$ with respect to each *i* point of the surface. Then, when the statistics of the sea surface slope distribution is non-Gaussian (considering the skewness and kurtosis) the number of bright points will be reduced or increased (depending on the skewness (negative or positive) and kurtosis values) in the optical image because the probability density function is not more an even function.

Acknowledgements
This work was partially supported by CONACYT under grant No. 102007.

MEXICAN OPTICS AND PHOTONICS MEETING
19 al 21 de septiembre del 2012
San Luis Potosí, México

Angle Reduction of the object wave in digital holography

Gilbert F. Pérez-García, J. M. Flores-Moreno, Amalia Martínez-García, J. A. Rayas

Centro de Investigaciones en Óptica, A. C., León Gto.
gilbert@cio.mx

ABSTRACT:

A method is described in which object angle are optically reduced, allowing the recording and numerical reconstruction of larger objects compared with the CCD size. The holograms are recorded by phase-shifting technique and by using an in-line setup. Experimental results are presented

Key words: Digital holography; Numerical reconstruction, imaging angle, phase-shifting.

REFERENCES AND LINKS

[1] T. Kreis, *Handbook of Holographic Interferometry*, Wiley-VCH, Weinheim, (2005).

[2] U. Schnars, T. Kreis and W. P. O. Jüptner, "Digital recording and numerical reconstruction of holograms: reduction of the spatial frequency spectrum", *Opt. Eng*. 35(4), 977–982 (1996).

[3] J. Mundt and T. Kreis, "Digital holographic recording and reconstruction of large scale objects for metrology and display", *Opt. Eng*. 49(12), 125801-1- 125801-6 (2010).

1. Introduction

Digital holography is an optical method for digital recording and numerical reconstruction of holograms. This method allows to obtain amplitude and phase data of distorted wave fronts. In digital holography, some parameters need to be considered in the geometry of the holographic setup. The most important might be the spatial frequency of the interference pattern which sets a restriction on the object angle [1], defined as the angle between rays from the edge points of the object and the normally impinging reference wave. In most practical applications of metrology it is necessary to analyze objects larger than CCD dimensions. Hence it is essential reduce imaging angle to increase spatial resolution of the hologram from a large object. By modifying the holographic configuration by introducing either a diverging or converging imaging lenses [2, 3], it is possible reconstruct numerically objects larger than CCD dimensions.

2. Analytical equations for calculating the reduction of the imaging angle

In the arrangement depicted in Fig 1, there are two very important distances to consider which are S_1 and S_2. By using the lens equation (Eq. 1:$\frac{1}{f} = \frac{1}{S_1} - \frac{1}{S_3}$), the equation sets the limit value to imaging angle (Eq. 2:$\theta < \frac{\lambda}{2\Delta\zeta}$), and from geometry of the optical system (Eq. 3:$S_2 = \frac{-d_1 f}{(S_1 - f)2\tan\theta} + \frac{fS_1}{S_1 - f}$), the reconstruction's distance is obtained (Eq. 4:$d = S_2 + S_3$). The details can be found in reference [1]. For practical applications we have to fix the arrangement of the object, lens, CCD by selecting an optimal choice of S_1 and S_2.

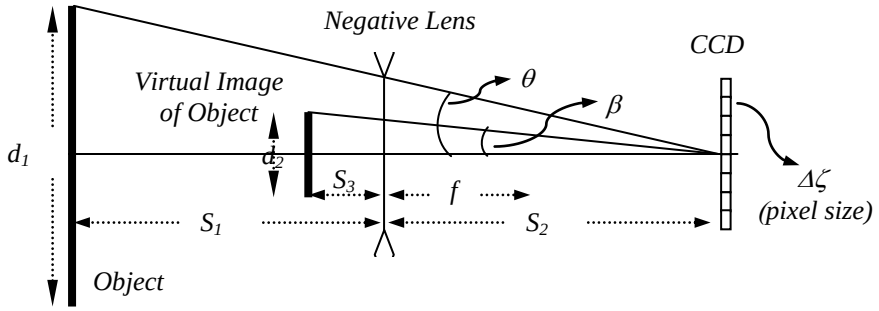

Fig. 1. Reduction of the object angle by using of a divergent lens.

3. Results

The optical arrangement for the reduction of the imaging angle is shown in Fig. 2. We used a laser with λ= 532nm, it is split through a beam splitter (BS) to obtain the reference and object beams which are coupled to optical fibers (length=2m, core=3μm). The beam scattered by the object impinges on the diverging lens ($f = -8cm$). The object wave field impinging onto the CCD target (which has a resolution of 1280 x1024,$\zeta = 6.7\ \mu m$) seems to come from the small virtual image of the object and not from the large object itself. The hologram is reconstructed through a complex image formed by phase stepped images every $\frac{\pi}{2}$ radians. The hologram reconstructed is depicted in Fig. 3. The parameters used are:$d_1 = 6cm$,$S_1 = 50cm$, and$S_2 = 6cm$. The height of object is 5cm.

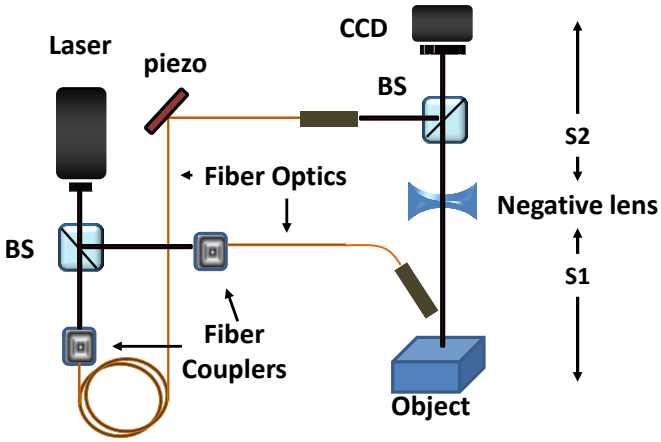

Fig. 2. An optical setup to reduction of the object angle.

Fig. 3. Numerical reconstruction of object.

4. Conclusions

The main advantage of the numerical reconstruction of holograms is to develop a very simple interferometric arrangement without imaging formed components, by using robust algorithms and computing hardware; besides, with a reduction of the imaging angle it is possible to record objects larger than CCD size

MEXICAN OPTICS AND PHOTONICS MEETING
19 al 21 de septiembre del 2012
San Luis Potosí, México

Quantification of Corrosion Products Formation onto a Cupper Sample by Digital Holographic Microscopy.

J. A. Marbán Salgado, J. Uruchurtu Chavarín, D. Mayorga Cruz.
Centro de Investigación en Ingeniería y Ciencias Aplicadas, UAEM. Avenida Universidad 1001, colonia Chamilpa, C.P. 60209, Cuernavaca Morelos, México.
Corresponding author email: darwin@uaem.mx

ABSTRACT:

In this work an application of digital holographic microscopy as a tool for oxide layer growth monitoring onto a cupper sample, as well as determination of velocity of corrosion products formation and type of corrosion taking place (localized corrosion or uniform corrosion) is here presented.

Keywords: Digital Holography, Holographic Microscopy, Corrosion.

REFERENCES

[1] A. Mendoza J., G. Llongueras. *Más Allá de la Herrumbre*. Colección La Ciencia desde México, No. 9: FCE-SEP-CONACYT; 1986.

[2] K. Habib, "Holographic Interferometry in Predicting Cathodic Deposition of Metals in Aqueous Solution", Proceedings of SPIE, 1230, 293-296, 1990.

[3] D. Mayorga, J. Uruchurtu, O. Sarmiento, P. A. Marquez, "Estimation of corrosion parameters in electrochemical system using Michelson interferometry". Proceedings of SPIE 6046, 60460J (2006) pp. 115-120.

[4] V. Micó, C. Ferreira, Z. Zalevsky and J. García, *Basic principles and applications of digital holographic microscopy, Microscopy: Science, Technology, Applications and Education*. ©FORMATEX 2010.

1. Introduction

Corrosion, defined as degradation of a metal caused by its interaction with environment, is one of the most investigated natural phenomena, mainly due to the material and economical loss originated, as 3% of GDP of USA approximately [1]. This last has given rise to resurgence of electrochemistry as the scientific discipline dedicated to investigation of corrosion causes and its different specialties. The electrochemical methods, based on Faraday law are vital to understand these phenomena; however almost all of them are commonly contactive, i.e. destructive techniques. On the other hand, one of the main advantages of optical metrology methods, is precisely its non-contactive nature, and this is the reason why interesting proposals for corrosion experimental investigation based on holographic interferometry or Michelson interferometry have been developed, as they have been applied to aluminum corrosion monitoring by optical interference fringes counting and its relation with metal degradation caused by electrochemical action [2, 3]. Here an application of Digital Holographic Microscopy [4] is presented to perform optical monitoring of corrosion, as it allows a quantification of corrosion products formation rate as depending of time.

2. Experimental setup

The experimental setup shown at Fig. 1 is based on a modified Mach-Zehnder interferometer; an amplified and collimated optical beam emitted from a low power He-Ne laser is divided in two equal intensity beams (i.e. reference

and object signals). The object signal is focused with a lens and a 4X objective onto the metallic sample, which reflected surface image is recaptured by the objective and focused in the CCD sensor. On the other hand the reference signal is directed by some mirrors and focused also to the camera; a digital optical hologram obtained by the interference between the two beams is stored in a PC. As in this particular case the image is focused in the camera sensor plane there is no need to perform numerical propagation at different planes, and only numerical reconstruction is required to obtain a phase-map in order to get the 3D reconstruction at different moments; then the variation of the oxide layer thickness formed on the cupper sample as a function of time is obtained. The optical monitoring is here performed on the sample dampened with a saline solution and exposed to the environment, as holograms were captured during 18 hours.

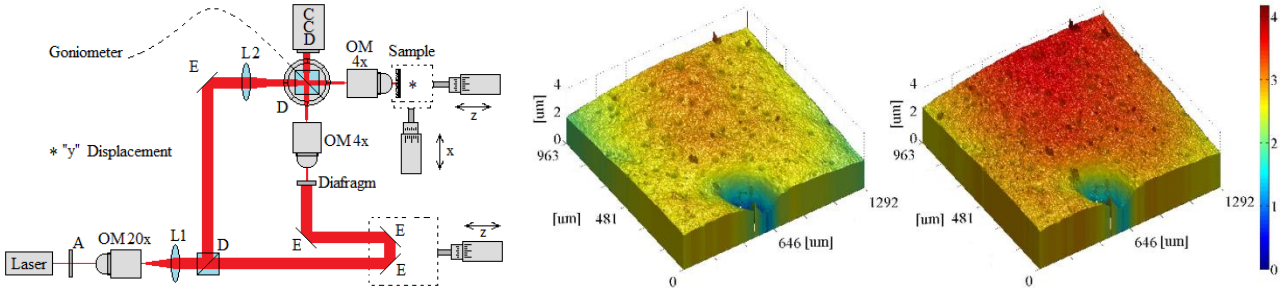

a) b) c)

Figure 1. A) Experimental setup, b) 3D digital reconstruction at the beginning of test, c) Digital reconstruction at the end of test.

3. Results

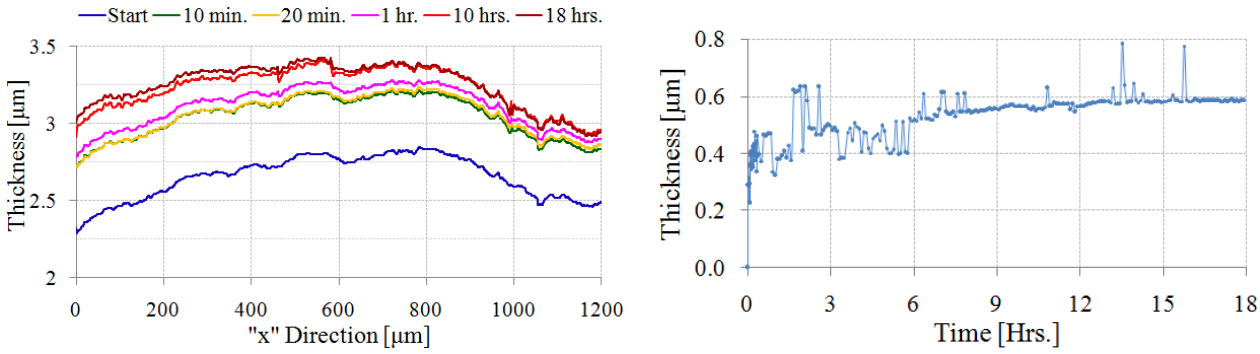

a) b)

Figure 2. Lateral profiles obtained from the digital topographic reconstruction at different moments. b) Oxide layer growth as a function of time.

4. Conclusions

An application of Digital Holographic Microscopy as a tool for optical monitoring of the oxide layer growth on a cupper sample has been presented; it also shows the potentiality of these optical methods when they are used as complementary methods for the investigation of dynamic physical-chemistry processes as metallic corrosion.

MEXICAN OPTICS AND PHOTONICS MEETING
19 al 21 de septiembre del 2012
San Luis Potosí, México

Theoretical and Experimental Characterization of Optical Spatial Solitons in Liquid Crystals

E. Ordoñez-Flores[(1)], A.A. Rodríguez-Rosales[(1)], C.J. Román-Moreno[(1)], J. Garduño-Mejia[(1)], O.G. Morales-Saavedra[(1)] and, R. Ortega-Martínez[(1)].

CCADET-UNAM, Apdo, Postal 70-186, C.P. 04510. Coyoacán, Cd. Universitaria, México D. F.
Corresponding author email: arrosales@prodigy.net.mx

ABSTRACT:

This contribution gives a brief overview of the principles inherent in the generation and modeling of spatial optical solitons (SOS) observed in nematic liquid crystals. In our case we used the MBBA and 5CB nematic liquid crystals doped with methyl red at 1% wt. We propose an experimental technique for the generation and characterization of SOS generated in the liquid crystalline system. The analyses of obtained images support the results.

Key words: Spatial optical soliton, nonlinear optics, reorientational nonlinearity, Liquid Crystals.

REFERENCES AND LINKS

[1] A. A. Rodríguez-Rosales, O. G. Morales-Saavedra, C. J. Román and R. Ortega-Martínez, "*Variations of nonlinear refractive index in Dye-doped liquid crystals by local and nonlocal mechanisms*". *Optical Materials*, 31,(2), pp. 350-360, 2008.

[2] Lui Lam, Jacquest Prost, *Solitons in Liquid Crystals*, Springer-Verlag, 1992

[3] Y. S. Kivshar, G. P. Agrawal, *Optical Solitons: From Fibers to Photonic Crystals*, Academic Press, 2003.

[4] G. R. Cathy,A. A. Minzoni, "*Large-amplitude nematicon propagation in liquid crystals with local response*", *J. Opt. Soc. Am*., 23, 2551, 2006.

1. Introduction

In this work we present the experimental characterization of spatial optical solitons (SOS) generated in liquid crystals (LCs) doped with nematic MBBA and 5CB and methyl red organic dye at 1% by weight [1]. It's well accepted that a spatial soliton full filled the next two conditions: 1) the energies that they transport are finite, continuous, bounded and localized in space [2], and 2) are beams that remain confined in the transverse directions orthogonal to the direction of propagation [3]. The evolution of polarized light cause a local reorientation of the director in a nematic liquid crystal, this leads to change the refractive index and self focusing trough the beam propagation in the nematic cell [3], [4]. Thus, the aim of the experimental setup is to search for this kind of nonlinearly induced beams within the nematic cell.

2. Solitons in liquid crystals

The nonlinear Schrödinger equation is used for explaining the behaviour of optical solitons, in the case of liquid crystalline materials, it is necessary to take into account the physical characteristics of these complex systems, the director vector, birefringence, nonlinear refractive index and nonlinear absorption coefficient. The envelope of the

electric field E satisfies the Foch-Leontovich equation (eq. 1) [4] and the angle ψ of the director vector of the nematic molecules (eq. 2), p a factor related with static electric field applied and v with the Franck constants of the LC.

$$i\frac{\partial E}{\partial z}+\frac{1}{2}\nabla^2 E-\cos(2\psi)E=0 \tag{1}$$

$$v\nabla^2\psi+2p\sin(2\psi)+2|E|^2\sin(2\psi)=0 \tag{2}$$

3. Experimental Setup

The LC cell consists of two glass plates glued together, with a controlled gap spaced 20 μm between the plates. The cell is filled with the nematic liquid crystals MBBA and 5CB doped with methyl red (MR) at 1% wt [1]. Linear polarized laser light at 632nm impinges on the sample. The beam propagation in the cell is detected by a CCD camera attached to a microscope (20X) due to scattering induced by the LC.

4. Results

We present some results for the diameter of the beam in two different regimes: one for low input powers (< 1mW) and other for high input powers (> 1.5mW). We can observe that for the lower regime the diameter don't change his value over a distance of 4 to 6 Raleigh ranges (1a) and natural diffraction takes place. On the other hand, within the high power regime, we found that this diameter don't change his value in distances over 10 Raleigh ranges (1b).

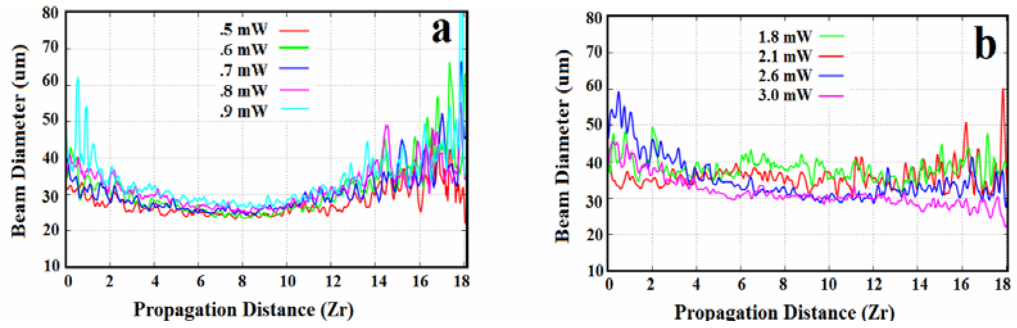

Fig. 1 Beam Diameter as a function of the propagation distance (in Raleigh ranges), a) "low" input power regime (less than 1mW), b) "high" input power regime (over 1.5 mW).

5. Conclusions

It can be concluded that spatial optical solitons can be generated within the liquid crystals MBBA over 10 Raleigh ranges. The aim of this work is to maximize this propagation distance of the beam inside of the sample, clearly identifying the diffraction, scattering and soliton phenomena. Future experimental work a bias voltage applied to the sample will improve the soliton production.

Acknowledgements

The authors gratefully acknowledge sponsorship to BID-UNAM #98-B3-C-DGP-L0034-1077, UNAM-PAPIIT: IN104597, IN108900, IN075710, IN113809-3, CONACyT-Mexico: 131746, 4480-A9409, 34921-E, U-49846-F and IACOD-I1100611.

MEXICAN OPTICS AND PHOTONICS MEETING
19 al 21 de septiembre del 2012
San Luis Potosí, México

Fringe projection profilometry system using a cyclic shear interferometer

Analía Sicardi-Segade[1], Amalia Martínez García[1], N.I. Toto-Arellano[2], J. A. Rayas[1]
1. Centro de Investigaciones en Óptica, A. C. León Guanajuato, México.
2. Universidad Tecnológica de Tulancingo, Hidalgo, México.
analia@cio.mx

ABSTRACT:

In this work, we present a fringe projection technique generated by using a cyclic shear interferometer (CSI) to obtain the three-dimensional surface information of an object. The experimental results were compared with the obtained from the coordinate measuring machine (CMM).

Key words: Optical metrology, projected fringes, cyclic shear interferometer.

---

[1] S. S. Gorthi and P. Rastogi, "Fringe Projection Techniques: Whither we are?", Opt. Lasers Eng. 48(2), 133-140 (2010).
[2] A. Martínez, J. A. Rayas, H. J. Puga, K. Genovese, "Iterative estimation of the topography measurement by fringe-projection method with divergent illumination by considering the pitch variation along the x and z directions", Opt. Lasers Eng. 48, 877-881 (2010).
[3] M. I. R. B. Zainal A., G. L. M. Jie, M. Wee, T. Lai, Y. Fu, H.M. Shang, "A Simple Laboratory Set-up For The Fringe-Projection Method", Proc. SPIE Vol.4588 (2002).
[4] J. C. Estrada, M. Servin, and J. A. Quiroga, "Noise robust linear dynamic system for phase unwrapping and smoothing", Opt. Express Vol.19 No. 6 (2011).

---

1. INTRODUCTION

During the last years, the use of fringe projection technique for generating three-dimensional (3D) surface information has become one of the most active research areas in optical metrology [1]. The retrieval of the three-dimensional shape of an object is an issue of great interest for a wide range of applications such as heritage protection, industrial, technical and medical applications [2].

Coordinates measurement machines (CMMs) are well established and widely accepted in many applications. However, CMMs possess some limitations such as a high cost, a low measurement speed and the sparseness of the measurement points [2]. Common optical methods for surface profiling include the use of moiré and holographic interferometry, fringe projection and others [3]. Among them, the fringe projection method is perceived as the simplest one because optical fringes can be generated and projected easily with a Michelson interferometer. But the use of the Michelson interferometer requires stringent vibration-free testing conditions, thereby confining its applications to laboratory environment [3]. In this paper we present a cyclic shear interferometer (CSI) to generate projected fringes. This has the advantage of generating stable fringes with little vibration isolation.

2. EXPERIMENTAL SETUP USING A CYCLIC SHEAR INTERFEROMETER TO GENERATE PROJECTED FRINGES

In Figure 1, we show the CSI to a fringe projection system where the shear is generated by moving the mirror M by a small distance Δs. A Verdi laser with a wavelength of *532 nm*, was expanded and spatially filtered using a 60× microscopic objective and 20 μm diameter pinhole. The used power was of 20 mw. Light goes through the first linear polarizer placed at 45 degrees with respect to the polarized light transmission axis from laser. When the light beam passes through the polarized beam-splitter (PBS) and is divided in two beams, one is transmitted with a horizontal polarization and the other one is reflected with a vertical polarization. Both beams are reflected in the two mirrors. When both beams get outside the beam-splitter, one beam polarization is perpendicular to the other one and a polarizing linear filter P_0 is needed in order to make that both beams components interfere. The fringe pattern can then be seen in a reference plane. By moving the mirror

M the fringes

pitch can be adjusted.

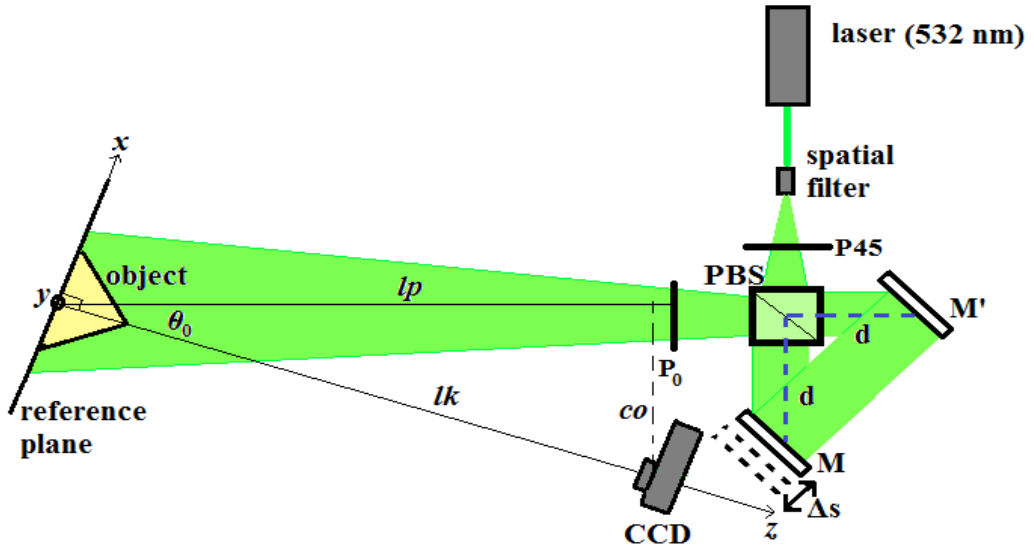

Figure 1. Fringe projection system using a CSI. (M and M ': Mirrors, PBS: Polarized Beam-Splitter, P45: polarizer placed at 45 degrees with respect to the polarized light laser., P_0 : polarizing linear filter in order to make that both beams components interfere.)

3. RESULTS

The object that we used was a pyramid with *48 mm* high and *89 mm x 89 mm* base. To retrieve the object by using the CMM method we measured 41 points and we extrapolated and interpolated the others. Figure 2a shows the topography of the object using CMM. Figure 2b shows the topography by using the optical method described in this work. A maximum difference of *4.5%* is found between the corresponding z coordinates of two 3D maps. The wrapping phase was calculated using the Fourier method and to calculate the unwrapping phase we used a noise robust linear dynamic algorithm [4].

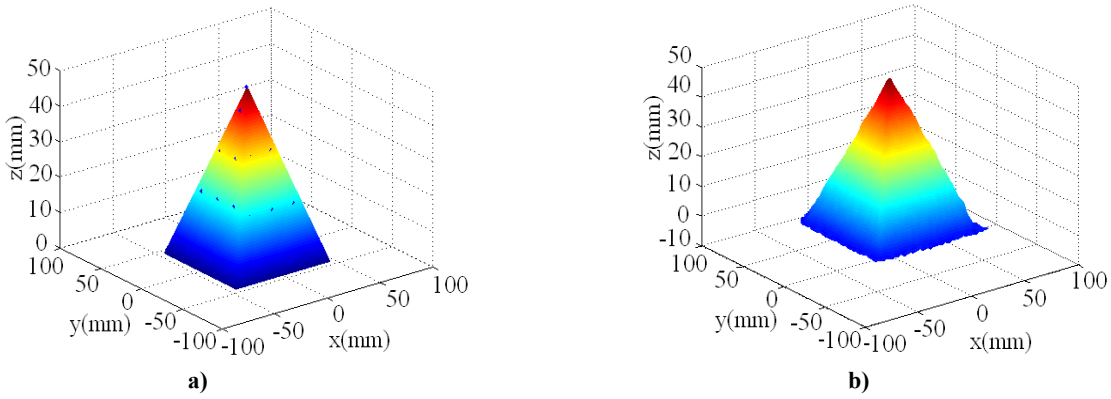

Figure 2. Shape of the object obtained by a) CMM and b) fringe projection technique.

4. CONCLUSIONS AND FUTURE WORK

In this work we proposed a cyclic shear interferometer to generate projected fringes. Being cyclic path this interferometer is quite stable. As a future work, we will analyze fringe visibility in function of the distance between object and projection system as a function of laser power.

MEXICAN OPTICS AND PHOTONICS MEETING
19 al 21 de septiembre del 2012
San Luis Potosí, México

Digital Post-Processing for Extended Depth of Field

E. Yépez-Vidal, E. García-Almanza, C. A. Rivera-Romero, M. Lopez-Ramirez, L. M. Ledesma-Carrillo, E. Cabal-Yepez, A. Garcia-Perez and J. Ojeda-Castañeda.

División de Ingeniería Campus Irapuato-Salamanca, Universidad de Guanajuato
Corresponding author email: ecabaly@gmail.com

ABSTRACT:

For extending the depth of field of an optical system, it is convenient to use an optical pre-processing mask, and a digital post-processing filter. Here, we analyse the performance of three different types of digital filters, which employ either the optical transfer function or the modulation transfer function of the pre-processing mask. Our numerical simulations are related to other image quality criteria.

Key words: Digital image processing, Image quality, Extended depth of field, Image restoration.

REFERENCES AND LINKS

[1] J. Ojeda-Castañeda, R. Ramos, and A. Noyola-Isgleas, "High focal depth by apodization and digital restoration," Appl. Opt. 27, 2583–2586 (1988)

[2] E. R. Dowski and W. T. Cathey, "Extended depth of field through wavefront coding", Appl. Opt. 34, 1859-1865 (1995)

[3] J. Ojeda-Castañeda, E. Yépez-Vidal and E. García-Almanza, "Complex amplitude filters for extended depth of field", Photonics Letters of Poland, Vol. 2, (2010)

1. Introduction

For extending the depth of field of an optical system, it is convenient to employ both an optical mask for pre-processing pictures, and digital filters for image post-processing [1-2]. It appears that the best option for pre-processing is the use of complex amplitude masks [3]. Here we are interested in selecting the best option for digital post-processing. To that end, we analyse the performance of three different types of digital filters, which act either on the optical transfer function (OTF) or on the modulation transfer function (MTF).

2. Pre-Processing Mask

In reference 3, the authors discuss the convenience of employing phase masks and a Gaussian apodizer for generating a MTF with low sensitivity to focus errors, and low oscillations around a tendency line. The complex amplitude transmittance, of the 1-D version of generalized pupil aperture, is

$$P(\mu;W;a;c)=e^{-\pi c\left(\frac{\mu}{\Omega}\right)^2}e^{j2\pi W\left(\frac{\mu}{\Omega}\right)^2}e^{j2\pi a\left(\frac{\mu}{\Omega}\right)^3}, \qquad (1)$$

In (1), μ denotes the spatial frequency variable. Its maximum value is the cut-off spatial frequency Ω. The parameter W represents the aberration coefficient for focus errors, in units of wavelengths. And the lower case letter

"*c*" denotes the attenuation factor of the Gaussian filter. By assuming the use of a cubic phase-mask, the parameter *a* represents the maximum value of optical path difference in the phase mask.

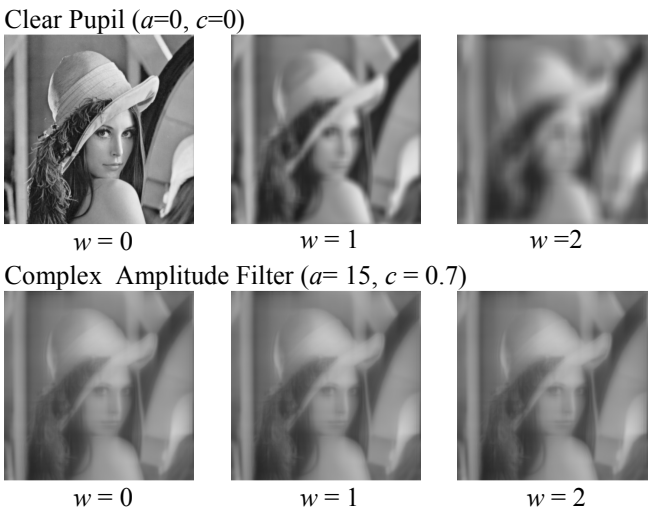

Figure 1 Pre-Processed Images

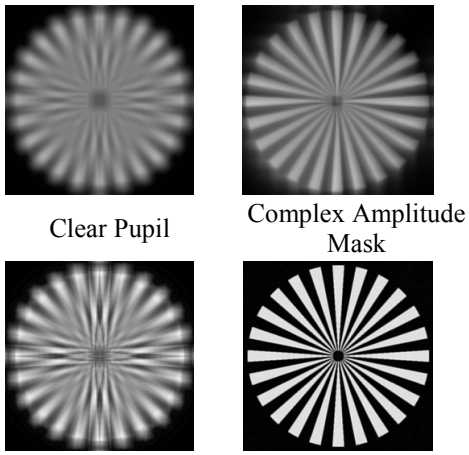

Figure 2 Image restorations using a Wiener filter

In Figure 1, we display the numerical simulations of six pictures. Along the first line of Figure 1, we show the irradiance distributions of an image taken by using a pupil clear pupil aperture (a=0, c=0), for three amounts of focus error, W=0, 1 and 2. Along the second line of Figure 1, we show the irradiance distributions of image taken by using the complex amplitude mask in reference 3, with a=15, c=0.7. The values of W are the same as those in Line 1. It is apparent from the second line of Figure 1 that the quality of the images is the same, independent of the amount of focus errors. In other words, complex amplitude mask is able to reduce the influence of focus errors. However, the modulation on the images is substantially reduced. Consequently, a digital post-processing operation is in order.

3. Post-Processing Digital Filters

By taking the inverse Fourier transform of Eq.(1) one can obtain the amplitude distribution of the coherent, impulse response. Its square modulus is the irradiance Point Spread Function (PSF). As is well-known the Fourier transform of the PSF is the OTF $H(\mu, w)$. The modulus of the OTF is the MTF. After evaluating the OTF, or the MTF, one can apply digital filters for image restoration. In Figure 2 we illustrate our proposal when using a Wiener filter, for W=2.8792. Along column one, we display the images obtained when using a clear aperture. Along column two, of Figure 2, we show the images obtained when using the complex amplitude mask in reference 3. It is relevant to comment that for the digital restoration, one needs the values of the OTF. Some distortions are introduced if one employs the MTF.

Furthermore, from column one, in Figure 2, we note that the Wiener filter is unable to restored the information lost due to focus errors. However, from column two in Figure 2, we observe that the Wiener digital filter is able to restore the losses in modulation.

4. Conclusions

From our numerical simulations, we show that digital post-processing works well, provide that there is a pre-processing operation. By using other image quality criteria is possible to show that the best option is to use the OTF, rather than the MTF, when applying the digital post-processing operation.

MEXICAN OPTICS AND PHOTONICS MEETING
19 al 21 de septiembre del 2012
San Luis Potosí, México

Analysis of a parabolic collector and its coupling with a plastic optical fiber

Guillermo Sánchez [(1)], Perla Viera [(1)], Victoria Navarro Franco [(1)], Gustavo Cárdenas Ortiz [(1)], Daniel Ceballos[(1)], Romeo Selvas[(1)].

1. Universidad Autónoma de Nuevo Leon, Facultad de Ciencias Físico-Matemáticas
Corresponding author email: guillermoesanchez@gmail.com

ABSTRACT:

In this work, we present the advances related to the fabrication of an inexpensive parabolic reflector and its coupling with a plastic optical fiber with the goal to introduce and propagate visible radiation trough the plastic fiber. For the fabrication of the cylindrical-parabolic solar collector we use an flexible acrylic mirror with high reflectivity, in this way, we can collect radiation from a light source within a plastic optical fiber at the focal point of the collector, The analysis of the coupling of both systems is performed and presented in this work .

Key words: Solar Collector, Plastic Optical Fiber, Cylindrical-parabolic

---

REFERENCES AND LINKS

[1] Pedro Fernández Díez (2000-09). "*Energías Alternativas*". Chapter 4 "*Colectores de Concentración de media Temperatura"*. From http://es.libros.redsauce.net/index.php?pageID=12.

[2] http://luces-led.com/Upl/tablaequivalenciasled.pdf

[3] http://www.sedoptica.es

---

1. Introduction

Nowadays the energy from non-renewable resources is increasing, so we have a strong interest in the use of renewable energies, in special from the sun, as a result, studies in solar concentrators have been of interest for diverse uses such as heating water, solar cells, interior lighting and others. There are different types of medium temperature solar concentrators: circular disc, parabolic disc, cylindrical parabolic disc and others which reach high temperatures depending on the dimensions, but under 1200°C, the cylindrical-parabolic is the concentrator which reaches the lowest temperature [1] and it's very used to heat water.

This paper shows the amount collected from a cylindrical-parabolic collector and transmitted by a plastic optical fiber, to indoor lighting.

2. Proposal and Experimental Results

As mentioned above, we have chosen the cylindrical parabolic collector due to temperatures reached are lower compared to other collectors reported in literature, allowing us to work safely with plastic optical fiber, because its melting temperature is 160°C. In this work we measured the width of the focus profile and the amount light transmitted by our fiber to measure the percentage transmitted. With this information we make a calculation of the amount necessary to match optical fibers within a luminaries, i.e. magnitudes of about 4100 lm [2].

We propose a cylindrical-parabolic collector shown in figure 1, which the focus gives us a 2.5 mm width of light.

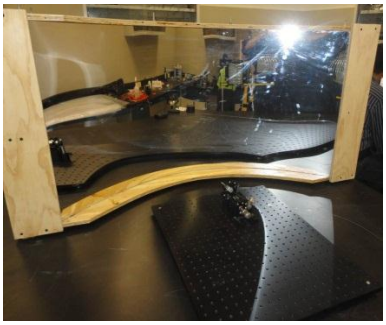

Fig 1. Cylindrical-parabolic collector

At the focal length we measured the intensity in lumens with a detector of 5.4x7.0mm, and we obtained 82,200 lumens, or 4356 lumens per square millimeter.

And then we measure the light transmitted with our arrangement trough a plastic optical fiber of 180cm length and 1mm of diameter. For this, we establish the fiber, you can see in the figure 2 the light in the fiber trough a diaphragm. We measure a total of 3279 lumens in the exit of the fiber with a background of 71 lumens (with lights off) and this give us a total of 4173 per square millimeter.

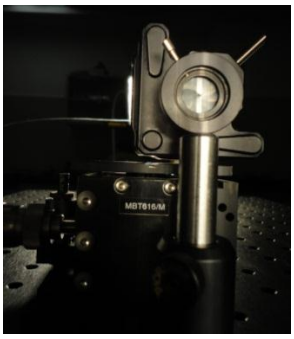

Fig 2. Arrangement of the optical fiber.

3. Conclusions

This works give us the quantity of light that can be transmitted with one cylindrical-parabolic collector. The main purpose of the collector is use it with the light of the sun, but we measure the intensity of the light in a controlled environment, in future works we are going to use the sun as our source of light, increasing the light collected and also the temperature.

Acknowledgements

The support of the Centre for Research in Mathematics and Physical Sciences at the Autonomous University of Nuevo Leon.

MEXICAN OPTICS AND PHOTONICS MEETING
19 al 21 de septiembre del 2012
San Luis Potosí, México

Optical nonlinearity of native collagen fibers and fibrils grown *in vitro*: A nonlinear optical microscopy and spectroscopy study

Cindy Fuentes Grethel Corona [(1)], Rebecca Younger [(2)].
Eric Olaf Potma [(2)] and Israel Rocha-Mendoza [(1)*]

1. Departamento de Óptica, CICESE, Ensenada, México
2. Department of Chemistry, University of California Irvine, Irvine, California, U.S.A.

Corresponding author email: irocha@cicese.mx

ABSTRACT:

We report our recent progress in the study of the optical 2nd and 3rd order nonlinearity of fibrillar collagen type I. We focus on the specific role of the methylene (CH_2) functional group in the optical nonlinear signals generated from both collagen fibrils grown i*n vitro* and native collagen fibers. We present and discuss our preliminary images and vibrational spectra taken of these samples using second harmonic generation (SHG), coherent anti-Stokes Raman scattering (CARS) and Raman scattering images (SRS) micro-spectroscopy.

Key words: Nonlinear Microscopy, Vibrational Spectroscopy Imaging, Collagen Fibrogenesis

REFERENCES AND LINKS

[1] I. Rocha-Mendoza, *et. al.,* "SFG-Vibrational Spectroscopy: The molecular origins of the optical 2nd order nonlinearity of collagen", *Biophysical Journal*, **93**, 433-444 (2007)

[2] M. Zimmerley, et. al, "Molecular orientation in dry and hydrated cellulose fibers: A CARS microscopy Study", *J. Phys. Chem. B*, 114, 10200-10208(2010)

[3] S. Bancelin, et. al., "In situ three-dimensional monitoring of collagen fibrillogenesis using SHG microscopy", *Biomed. Opt. Express*, **3**, 1446-1454 (2012)

[4] V. Raghunathan, *et. al.*, "Rapid vibrational imaging with sum frequency generation microscopy," *Opt. Lett*., **36**, 3891-3893 (2011)

1. Introduction

Collagen type I is the most abundant protein in human body. It forms more than 90% of the organic mass of bone and is the major constituent of tendon, skin, ligaments, cornea and many interstitial connective tissues. Collagen molecular structure, biosynthesis and assembly is important for understanding developmental pathological processes in tissues. In recent years, nonlinear micro-spectroscopy techniques have become a standard method for tissue imaging and studying molecular structure of fibrous proteins [1, 2]. For instance, the molecular origins of collagen second-order susceptibility has been elucidated using nonlinear vibrational sum frequency generation (SFG) spectroscopy, where the methylene (CH_2) group was assigned to be the main dipolar contribution [1], and just recently, SHG microscopy has been used to monitor the fibrogenesis *in vitro* [3]. To our knowledge, rapid vibrational imaging techniques such as CARS, SRS or SFG-spectroscopy [2, 4] have not been used for these purposes so far. While SHG imaging provides information on collagen sub-micron fibrils at the optical resolution limit, the information about the molecular groups that constitute the collagen molecular structure could directly be extracted using vibrationally sensitive microscopy [4]. In this work, we will present and discuss preliminary images and vibrational spectra taken of native collagen fibers and collagen fibrils grown *in vitro* using nonlinear SHG microscopy and nonlinear CARS and SRS spectroscopy.

2. Experiment and Results

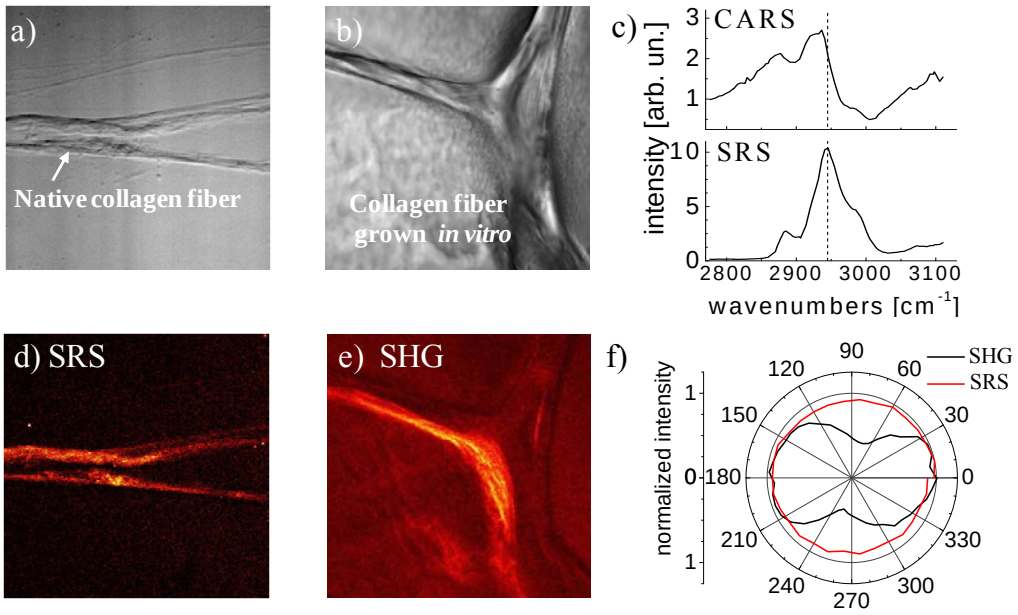

Figure 1. Transmission images, nonlinear microscopy images, vibrational spectra and polar dependence plots of both native collagen fibres and collagen fibres grown *in vitro* (see description in text).

Two types of collagen samples were used in our experiments. The first samples consisted on type I collagen fibres immersed in 1% agar and sandwiched between two microscope cover slips; the fibres were previously extracted from rat tail tendon fascicles and then washed with purified water. The second samples consisted of collagen fibres grown from collagen solution deposited over microscope cover slips; the solution was prepared by diluting 8 parts of 100μg/ml collagen solution with 1 part of 10× PBS and adjusting the PH at around 7.3 using 0.1 M NaOH to trigger collagen fibrogenesis. Transmission images of both samples are shown in Figs. 1(a) and (b), respectively. The image size is in Figs. 1 (a, b) and (d, e) is 50×50 μm^2.

The nonlinear vibrational spectra, images and polar dependence shown in Figs. 1(c-f) were taken using picosecond CARS/SRS micro-spectroscopy combined with femtosecond SHG microscopy as described in Ref. [2]. Fig. 1(c) shows the CARS (top) and SRS (bottom) vibrational spectra, taken at the CH_2 vibration mode of the collagen fibre indicated by the white arrow in Fig. 1(a); the CARS spectra is distorted due to the nonresonant CARS signal. Figs. 1 (d) and (e) show the SRS image at the CH_2 molecules and a typical SHG image of collagen fibres, respectively. Finally, Fig. 1 (f), show polarization dependence of the collagen fibers (black) and the CH_2 molecules (red) taken with SHG and SRS microscopy. Interestingly, the CH_2 molecules show isotropic dependence despite of knowing that they are the main sources of the 2nd order nonlinearity [1, 4].

3. Conclusions

Nonlinear microscopy images and vibrational spectra using SHG, CARS and SRS micro-spectroscopy were taken on both collagen fibers from native collagen and grown in vitro from solution. This data represent preliminary data towards studying chemical and structural changes in collagen during the fibrogenesis process. They also indicate that the 2nd and 3rd order optical nonlinearities of collagen originate from different molecular properties.

Acknowledgements
This work was funded by UC MEXUS/CONACYT collaborative programs and CONACyT (grant n. 155803).

MEXICAN OPTICS AND PHOTONICS MEETING
19 al 21 de septiembre del 2012
San Luis Potosí, México

Refractive index measurement of metallic and dielectric thin film using Surface Plasmon Resonance and Brewster-Abeles technique.

Y. M. Espinosa Sánchez*, D. Luna Moreno , E. Noé Arias , G. Garnica Campos

Centro de Investigaciones en Óptica AC, Apdo. Postal 37150 León, Gto. México.

essym@cio.mx

ABSTRACT:

We present a θ-2θ rotatory system illuminated with He-Ne laser with p-polarization, which can make real and complex refractive index measurements of optical thin film coating by use of the Brewster-Abeles and surface plasmon resonance techniques.

Key words: Surface Plasmon Resonance; Brewster´s Abeles technique; Refractive index measurement.

REFERENCES AND LINKS

[1] Homola J. Sinclair S. Y., Gauglitz G., "Surface Plasmon resonance sensors: review," Sensors and actuators B, vol. 54 (1999) 3-15.
[2] G. Hass, R. E. Thun, "Precision measurement in thin film optics," in: H. E. Bennet (Eds.), Physics of Thin Films, vol. 4, Academic Press, New York, 1967 (Chapter 1).
[3] Macleod H. A., Thin-Film Optical Filters, Third Ed., Bristol Philadelphia: Institute of Physics Publishing (2001).

1. Introduction

The Surface Plasmon Resonance (SPR) is a surface electromagnetic wave that exists in the interface between two medium with dielectric constants that have opposite signs [1]. The arrangement of the Attenuated Total Reflection in the Kretschmann configuration is shown in Fig. 1, part A) [1].
The Brewster-Abeles technique is a simple and fast measurement method to obtain the refractive index of a dielectric thin film [2].

2. Results

a) A prism was mounted on the experimental setup to measure the attenuated total reflection in the Kretschmann configuration, as is shown in Fig.1, part B). A *p*-polarized 632.8 nm He-Ne laser was used as light source, it was launched into a semicylindrical shaped prism with its flat face looking downward to validate normal incidence, mounted on a rotator stage with a sweep of θ degrees. The data acquisition system performs two tasks: the control of the stepper motors in the rotatory stage with a 0.01 degree resolution, and the measurement of the intensity of reflected light through the prism. The acquisition of the reflected light is performed by a photodiode. The main value measured by SPR-based devices at an angle θ_{sp}, corresponds to the minimal intensity of light. The refractive index and thickness calculation of the silver thin film was found by the fitting of the theoretical and experimental curves (Fig. 2 b), that were calculated from known optical constants for the materials made of three layer optical structure (Bk7, silver, air), using MathCAD ™ script based on the calculation of the Fresnel reflection coefficients for the structure using matrix formalism [3].

b) The experimental set up to measure the Brewster angle is shown in Fig.1 A). The used laser was the same as in a) part. The light was directed toward a surface (substrate) partially coated with the probe film of refractive index *n*.

The substrate was mounted on the same system as in a) .The incident light was reflected in the interface ambient/film toward an optical photodetector mounted in a second rotatory stage (rotatory system 2θ) synchronized with the first rotatory system to maintain the detector-signal aligned. For the substrate, the intensity of the signal reflected was diminished as function of the incident angle, being minimal when matches the Brewster angle. We made the measurement of the refractive index by the Abeles Brewster method [2], scanning the incident angle from 40 to 75 degree. The interception angle of the curves corresponds to the Brewster angle of the film, this because no light was reflected from the ambient-film interface, then the reflectivity of the film-covered substrate is the same as the an uncoated substrate at the Brewster angle θ_B. Thus, the refractive index of the film was calculated using the expression $n = \tan\theta_B$. In Fig. 2a is shown the reflectance curves of the SF6 coated and uncoated thin film of SiO_2.

2.a.- Figures

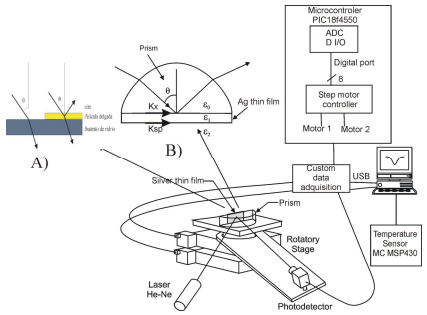

Figure 1. The experimental setup consist in a rotatory stage where it is mounted the prism for SPR measurement (B) or substrate uncoated and coated with dielectric thin film for Brewster angle measurement (A).

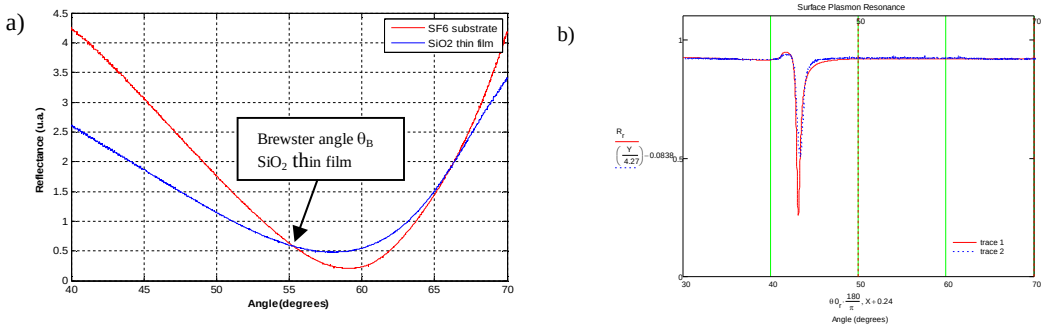

Figure 2.a) Reflectance curves of a SF6 substrate with uncoated and coated thin film of SiO_2, where θ_B=60.15, with n=1.7425. The interception angle of the curves was θ_B=55.26 , with n= 1.442. b) Best fitting of SPR curves obtaining a thickness of 55 nm and N=0.11-3.88i for a silver thin film.

3. Conclusions

This work describe the use of the p polarization in a rotatory system θ-2θ applying the SPR method to measure the complex refractive index of a silver thin film over a BK7 semicylindrical prism and applying the Brewster-Abeles methods to measure the real refractive index of a dielectric thin film of SiO_2 over a SF6 substrate. These measurements show the versatility of the θ-2θ system to measure metallic and dielectric thin films. The measurement is fast and simple and these experiments can be described with accuracy by using the Fresnel reflection coefficients.

MEXICAN OPTICS AND PHOTONICS MEETING
19 al 21 de septiembre del 2012
San Luis Potosí, México

Hybrid method reduces the spherical aberration in the human eye

J. F. Aguilar-Gutiérrez [(1)], M. L. Arroyo Carrasco [(1)], M. D. Iturbe-Castillo[(2)]

1. Facultad de Ciencias Físico Matemáticas, Benemérita Universidad Autónoma de Puebla, C.P. 72570, México
2. Instituto Nacional de Astro física, Óptica y Electrónica, C.P. , México

Corresponding author email: juanmath@gmail.com

ABSTRACT:

We studied an exact model to describe the propagation of rays in the human eye by considering spherical surfaces and radii of curvature, thickness and refraction index constants. By doing the exact ray tracing we found that the system exhibits spherical aberration, so to reduce it, we considered a gradient-index in the lens, and we calculated the propagation of rays in the full human eye with a combination of exact ray tracing and ABCD matrices, the hybrid method.

Key words: ABCD matrix, exact ray tracing, spherical aberration, human eye

REFERENCES AND LINKS

[1] J. A. Díaz, ABCD matrix of the human lens gradient-index profile: applicability of the calculation methods. (2008) Appl. Opt. Vol. 47, No 2.

[2] A. Gullstrand, Hemholtz's Handbuch der Physiologischen Optik, 3rd. ed., Vol. 1, Appendix II, pp. 302-358.

[3] Y. Huang and D. T. Moore " Human eye modelling using a single equation of gradient index crystalline lens for relaxed and accommodated states" Proc. SPIE 6342, 63420D (2006)

1. Introduction

In this work we model the human eye as an optical system formed by lens immersed in medium of constant index refraction Our model is exact because it satisfies the condition of having at least four refracting surfaces, the anterior and posterior cornea and the anterior and posterior lens, Then we apply exact ray tracing and ABCD matrices to study the rays propagation and the spherical aberration with different conditions over the human lens.

2. Hybrid method

We consider the human lens divided in vertical very thin slices, so we are able to apply the ABCD matrices to describe the propagation through this slices, ours results show that in this case the matrices gives the exact trajectory as in reference [1]. In the figure 1, we have considered the index refraction proposed by Gullstrand in 1909 [2] for the human lens and we compare with a human lens whose refraction index in each slice depend only in the height as in the formula (1), but this dependence is different from slice to slice, this idea allow us to reproduce the exact solution for the rays propagation , with the right number of slices in our case we found that 500 slices were sufficient. Our results are in perfect agreement with reference [1]

$$n(y)=n_0+\frac{n_0}{2L^2}y^2$$

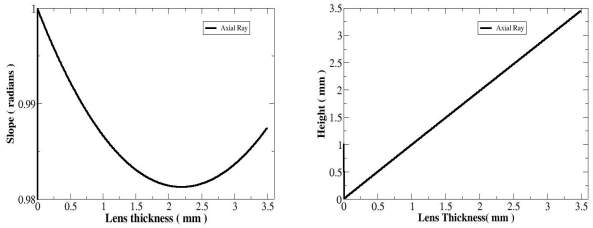

Fig. 1. The plot on the left show the slope of the axial ray and on the right hand the height of the axial ray through the human lens, both the behavior and values are in agreement with reference [1].

After we shown the efficiency of the slicing method, we applied it to the full human eye, so we used exact ray tracing until the lens an from there we used the ABCD matrices to find the complete trajectory of the rays

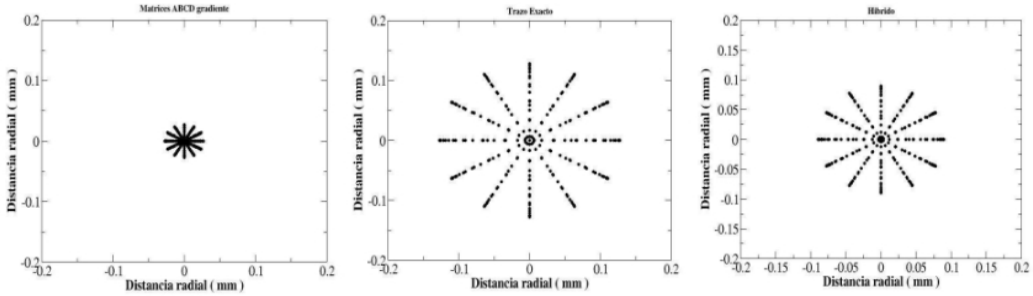

Fig. 2. We can compare the 3 spot diagram, from left to right, for ABCD matrices, for exact ray tracing and last one for our hybrid method, we can see that the hybrid method reduce the size of the spot diagram

Finally we compare the size of the spot diagram for the three cases figure 2, ABCD matrices, exact ray tracing and the hybrid method, under the same values for the different parameters.

3. Conclusions

When we combine the exact ray tracing and ABCD matrices to calculate the propagation of the rays in the human eye, we found that it is possible to reduce the spherical aberration even below to that obtained in the paraxial case. The right choice of values for the index refraction is sufficient to achieve this reduction.

MEXICAN OPTICS AND PHOTONICS MEETING
19 al 21 de septiembre del 2012
San Luis Potosí, México

Speckle interferometer based on a two aperture common-path interferometer.

Antonio Barcelata-Pinzon and Cruz Meneses-Fabian

Facultad de Ciencias Físico-Matemática, Benemérita Universidad Autónoma de Puebla, Apdo. Postal 1152, Puebla, Pue., México.
Corresponding author email: lafrecuenci@hotmail.com

ABSTRACT:

A very stable and robust schema for electronic speckle pattern interferometry configured to be sensible out-of-plane for studying phase objects is presented. It is based on a 4*f* imaging system, consisting of two windows in the object plane and a Ronchi ruling in the Fourier plane. The speckle effect is created by a ground glass diffuser placed in the object plane. Analytic explanation and experimental results are shown.

Key words: Speckle Interferometry, Phase shifting, Phase objects.

REFERENCES

[1] C. Meneses-Fabian, G. Rodriguez-Zurita, J. F. Vazquez-Castillo, C. Robledo-Sanchez, V. Arrizón," Common-path phase-shifting interferometer with binary grating" Opt. Comm., 264 (2006) 13-17.
[2] J. M. Huntley, "Automated analysis of speckle interferograms," in: P.K. Rastogi, Digital Speckle Pattern Interferometry and Related Techniques, John Wiley & Sons Ltd, England (2001) pp. 59-139.

1. Introduction

Speckle interferometry has been used primarily in a wide variety of applications for opaque objects that includes analysis of vibrations, strains, contour, deformations, but there are a few reports for phase objects studying. In this work, an electronic speckle pattern interferometry (ESPI) configured to be sensible out-of-plane is presented for studying phase objects by observing phase changes because of two object states.

2. Theoretical model

The theoretical background for this work can be split basically in two themes: two aperture common path interferometer (TACPI)[1] and speckle interferometry [2] for phase objects. TACPI is built on a $4f$ imaging system consisting of two apertures in the object plane and a Ronchi ruling in the Fourier plane. In one aperture a phase object is placed, attending as a probe arm, while the other one is left free of obstacles, attending as a reference arm [1]. If a ground glass is placed in the input plane the speckle effect appears because it is illuminated with a light laser. This technique measures the phase difference between two recorded objects positions or physical states that present the speckle effect showing an electronic interference pattern. The phase extraction is done by a perpendicular translation of the optic axis of the Ronchi ruling [1].

3. Experimental results.

We have done the arrangement implementation in Fig (1) in order to apply PSI technique for phase retrieval in an experimental implementation of the schema. We have mounted a ruling of $u_p = 12.7\mu m$ (2000 lines per inch) on a stage controlled by a vernier micrometer where its transversal translation is controlled manually with it having a nominal resolution of $\Delta u_d = 10\mu m$, then $u_d = k\Delta u_d$, and so $\alpha_k = k\Delta\alpha$ with α like a constant phase introduced and

u_d as a transversal displacement of the ruling. Each screw turned by each graduation step will generate a phase step of $\Delta\alpha = 2\pi\,\Delta u_d / u_p = 4.947 rad$. Therefore for $k = 0,1,2,3$, $\alpha_k = 0, 4.947, 9.895, 14.842$, the patterns g_0, g_1, g_2, g_3 for each phase-shift are obtained. Then the object phase ϕ can be calculated from [2]

$$\tan\phi = \frac{(g2-g0)(\cos\alpha 3-\cos\alpha 1)-(g3-g1)(\cos\alpha 2-\cos\alpha 0)}{(g2-g0)(\sin\alpha 3-\sin\alpha 1)-(g3-g1)(\sin\alpha 2-\sin\alpha 0)} \tag{1}$$

In order to verify the phase step $\Delta\alpha$ is considered to be unknown; in this paper we use the Carré's method [2] and another alternative method,

$$\tan\Delta\alpha_C = \sqrt{\frac{3(g1-g2)-(g1-g3)}{(g1-g2)+(g0-g3)}}\,; \qquad \cos\Delta\alpha_A = \frac{(g0-g1)+(g2-g3)}{2(g1-g2)}, \tag{2}$$

where the subscripts C and A indicate experimentally measured values of $\Delta\alpha$ by Carré and an alternative method. The average values were $\overline{\Delta\alpha_A} = 4.931$ and $\overline{\Delta\alpha_C} = 4.805$ .In the experiment, a bending acetate was collocated in the window B as a phase object, and a series of speckle fringes were obtained as explicated above for $N = 4$, $g_0 - g_3$. Fig. 2 (a,b,d,e) shows the four patterns, after of a routine processing, the fringes were computed for obtaining the wrapped phase (Fig. 2c), and the unwrapped phase (Fig. 2f) was computed by using a conventional phase integration algorithm.

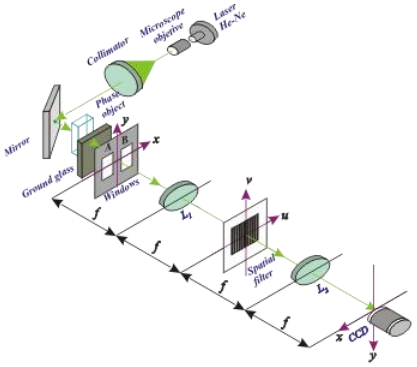

Fig (1)

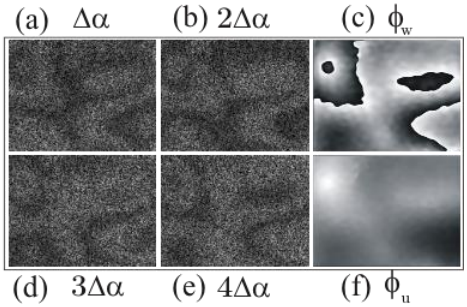

Fig (2)

3. Conclusions

We have presented a phase-shifting speckle interferometer configured to be sensible out-of-plane for phase objects studies, which was based on a TACPI, where the phase-step was done by turning a venier micrometer for $N = 4$ and validated by Carré and an alternative method, it results to be very practicable, stable and robust system, because of the reference and probe arms, travel together by the same optical elements, the mechanical vibrations are affected of equal form to both beams and the phase difference holds constant.

Acknowledgements

A. Barcelata-Pinzon appreciates the scholarship from Consejo Nacional de Ciencia y Tecnología (México) under grant 160211. This work was partially supported by Vicerrectoría de Investigación y Estudios de Posgrado of Benemérita Universidad Autónoma de Puebla under grant MEFC-EXC12-I and was experimentally carried out in the FCFM-BUAP laboratorio de interferometría facilities, which has been developing thanks to the grant CONACYT 124145.

MEXICAN OPTICS AND PHOTONICS MEETING
19 al 21 de septiembre del 2012
San Luis Potosí, México

Generating anaglyph images using spectral density functions

Yolanda Y. López D., Amalia Martínez García

Centro de Investigaciones en Óptica A. C. León Gto.
yanetld@cio.mx, amalia@cio.mx

ABSTRACT:

A projection method is presented to generate anaglyph stereoscopic images using the spectral absorption curves of the glasses, the spectral density functions of the display primaries and the colorimetric properties of the observer.

Key words: Three-dimensional effects, Anaglyph images, Stereoscopic images

REFERENCES AND LINKS

[1] E. Dubois, "A Projection method to generate anaglyph stereo images", IEEE Int. Conf. Acoustics Speech Signal Processing, **3**, 1661-1664(2001).

[2] G. Wyszecki and W.Stiles, *Color science: concepts and methods, quantitative data and formulas*. John Wiley& Sons, N. Y. (1967).

[3] D. Malacara, *Color vision and colorimetry: Theory and applications.* SPIE Press, USA, 2° Edition (2011)

[4] C. Poynton, *A technical introduction to digital video*. John Wiley & Sons, N. Y (1996)

1. Introduction

The anaglyph images are composed by two layers of colour, superimposed but moved slightly between them in order to obtain the perception of depth. In the basic method, the image contains two filtered images, one for each eye. Usually the left view is in red and the right view in blue or cyan. Both images are superimposed and when viewed through the anaglyph glasses, it will appear a three-dimensional image. There are many techniques for generating the anaglyph images, including software that works with colour anaglyph. In this paper we describe a method using the spectral absorption curves of the filters of the anaglyph glasses, in order to better perception of depth.

2. Metodology

In this process we need a stereo pair images ($V_{lj}(x)$ and $V_{rj}(x)$) [1] corresponding to the left and right view, where j=1, 2, 3 and correspond to the three channels of the *RGB* images. The spectral density functions of the *RGB* display are denoted by $d_j(x)$ and the spectral density of the light emanating from point *x* in the left and right view is given by:

$$Q_l(\lambda, x) = \sum_{j=1}^{3} V_{lj}(x) d_j(\lambda) \quad \text{and} \quad Q_r(\lambda, x) = \sum_{j=1}^{3} V_{rj}(x) d_j(\lambda) \tag{1}$$

The color-matching functions [2,3] $\bar{p}_k(\lambda)$ (from *RGB* to *XYZ*) are used to determine the color perceived at point *x* in the left and right images:

$$\tilde{V}_{lk}(x) = \int Q_l(\lambda, x)\ \bar{p}_k(\lambda) = \sum_{j=1}^{3} V_{lj}(x) \int \bar{p}_k(\lambda)\ d_j(\lambda)\ = \sum_{j=1}^{3} c_{kj} V_{lj}(x) \tag{2}$$

The $\bar{p}_k(\lambda)$ functions are tabulated in [3], and thus we obtain the *3x3* matrix C. The light from the display CRT passes through two filters $f_l(\lambda)$ and $f_r(\lambda)$ before arriving to the eyes of the human observer. Similarly as the previous equations, the spectral absorption function of the filtered glasses is required. Then, the matrix *A* is obtained.

$$[A_l]_{kj} = \int \bar{p}_k(\lambda)\ d_j(\lambda)\ f_l(\lambda)\mathrm{d}(\lambda) \text{ and } \quad [A_r]_{kj} = \int \bar{p}_k(\lambda)\ d_j(\lambda)\ f_r(\lambda)\mathrm{d}(\lambda) \tag{3}$$

$$R = \begin{bmatrix} A_l \\ A_r \end{bmatrix}$$

In both cases, the integral is over the wavelengths of the visible spectrum, in this case we use a 350 *nm – 700 nm* range. So, we can define the following equations:

$$\tilde{V}_l(x) = CV_l(x)\ ;\ \tilde{V}_r(x) = CV_r\ (x) \qquad \text{Where } [\mathrm{C}]_{kj} = c_{kj} \tag{4}$$
$$\tilde{U}_l(x) = A_l V_l(x)\ ;\ \tilde{U}_r(x) = A_r V_r(x)$$

A *1x6* matrix $\tilde{V}(x)$ is required, which contains the six images corresponding to the three channels of the left and right image. W is a *6x6* identity matrix used as an auxiliary to make the projection approach.
The resultant anaglyph is given by:

$$\tilde{V}(x) = [\tilde{V}_{l1}(x)\ \tilde{V}_{l2}(x)\ \tilde{V}_{l3}(x)\ \tilde{V}_{r1}(x)\ \tilde{V}_{r2}(x)\ \tilde{V}_{r3}(x)]^T = CV(x) \tag{5}$$
$$\hat{V}_{an}(x) = (R^T W R)^{-1} R^T W R \tilde{V}(x) = (R^T W R)^{-1} R^T W R C V(x) = PV(x)$$

3. Experiment

In figure 1 is showed the transmission curves for the two filters red and blue used in the anaglyph glasses used in this experiment. The figure 2 shows the generated anaglyph image.

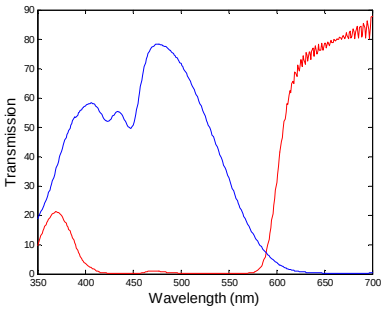

Fig.1. Transmission as a function of wavelength of two filters: Red and Blue

Fig.2. Example of a generated anaglyph image.

4. Conclusions

This method to generate anaglyph images is very effective due to that is obtained a better perception of three-dimensional view. Its effectiveness is due to being considered the spectral absorption curves of the glasses, the spectral density functions of the display primaries and the colorimetric properties of the human observer.

MEXICAN OPTICS AND PHOTONICS MEETING
19 al 21 de septiembre del 2012
San Luis Potosí, México

Phase-shifting interferometry by the modulation of the wave amplitude: The general case

Uriel Rivera-Ortega, Cruz Meneses-Fabian

Facultad de Ciencias Físico-Matemática, Benemérita Universidad Autónoma de Puebla. Apdo. Postal1152, Puebla, Pue., México.

Corresponding author email: mecatronica00@hotmail.com

ABSTRACT:

A new phase-shifting method for phase-shifting interferometry (PSI) based on the modulation of the electric field amplitude is presented; this modulation is based on the interference of three waves where the modulation is made in two of them named the reference beams. We show that if an arbitrary phase difference between these references is keeping constant, it can be modeled as an interference of two beams, where both an additional phase term and one of the beams are composed by the two references.

Key words: Interferometry, Phase shifting, Amplitude modulation

REFERENCES

[1] K. Creath, *Phase-Measurement Interferometry Techniques* (Progress in Optics. Vol. XXVI, E. Wolf, Ed., Elsevier Science Publishers, Amsterdam, 1988), p. 358- 365.

[2] C. Meneses-Fabian and U. Rivera-Ortega, "Phase-shifting interferometry by wave amplitude modulation", *Opt. Lett*. **36**, 2417-2419 (2011).

[3] C. Meneses-Fabian and U. Rivera-Ortega, "Phase-shifting interferometry by wave amplitude modulation: General case", *Opt. and Las. in Eng*. **50**, 905-929 (2012).

1. Introduction

In PSI, a series of interferograms are recorded where the phase of one of the two interfering beams is changed by a certain amount [1]. In PSI a fringe pattern obtained because of the interference of two waves is modeled by

$$I_k(x,y) = a(x,y) + b(x,y)\cos(\phi(x,y) + \psi_k), \tag{1}$$

where $\phi(x,y)$ is attributed to the object phase ψ_k, with $k = 0,1,...,N-1$ is the phase step generated to obtain N interferograms. If a system of $N \times 3$ is formed, a solution for the object phase can be obtained [1] .

2. Basic theory

Let us have three lineally polarized waves at the same plane traveling on z-direction, whose spatial part is

$$E_n(x,y) = A_n(x,y)\exp[i\phi_n(x,y)], \tag{2}$$

with $n = 1,2,3$. The superposition of these waves at any point (x,y) is the sum of the three fields. For simplicity their phases are considered to be, omitting coordinates

$$\phi_1 \neq 0;\ \phi_2 = \phi_1 + \Delta\phi_1 + \phi;\ \text{and}\ \phi_3 = \phi_1 + \Delta\phi, \tag{3}$$

where $\Delta\phi_1$ is a constant phase difference between the first and second wave, $\Delta\phi$ is a constant phase difference between the first and third wave. The resulting irradiance can be expressed by

$$I = A_r^2 + A_2^2 + 2A_r A_2 \cos(\phi + \Delta\phi_1 - \psi), \tag{4}$$

A_r is similar to a reference amplitude and ψ is an additional phase, both given by

$$A_r^2 = A_1^2 + A_3^2 + 2A_1 A_3 \cos\Delta\phi \quad (5.1); \qquad \tan\psi = \frac{A_3 \sin\Delta\phi}{A_1 + A_3 \cos\Delta\phi}, \tag{5.2}$$

where a typical expression for a fringe pattern of two beams as in Eq.1, has been deduced, indicating that both A_r and ψ depend on the variations of A_1, A_3 and of $\Delta\phi$. By multiplying Eq.(5.1) by $\sin^2\Delta\phi / A_r^2$, this can take the form of an ellipse whose amplitudes can be described in a parametric form by

$$A_1 = \frac{A_r}{\sin\Delta\phi}\sin(\Delta\phi_2 - \psi); \qquad A_3 = \frac{A_r}{\sin\Delta\phi}\sin\psi, \tag{6}$$

Fig.1 shows a section of a simulated ellipse corresponding to a value of $\Delta\phi = 2\pi/3$, while Fig.2 shows the simulated interference patterns shifted in phase with the respecting needed amplitude values for nine steps.

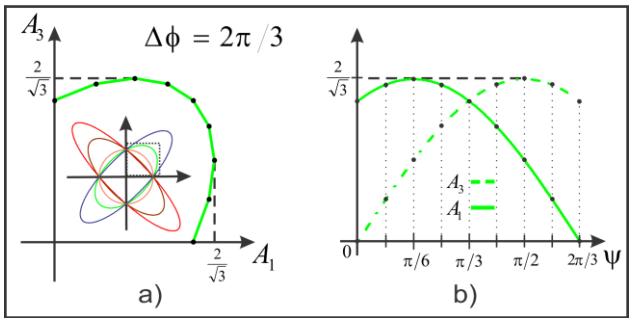

Fig. 1a) shows the segment of an ellipse at the first quadrant corresponding to $\Delta\phi = 2\pi/3$. In Fig. 1b) the phase-shift are indicated in x-axis while the values of the amplitudes needed to get a certain phase shift are located by the intersection of the vertical dotted lines with the parametric equations corresponding to A_1 and A_3.

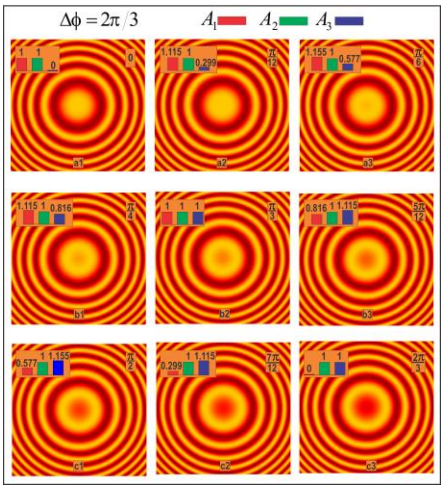

Fig. 2 Simulated interference patterns shifted in phase.

3. Conclusions

It has been shown by a mathematical analysis and a numerical simulation the feasibility to generate a phase-shifting [2-3] in a three beam interferometer by varying the amplitude of two of them which are considered as reference beams.

Acknowledgements

U. Rivera-Ortega appreciates the scholarship from Consejo Nacional de Ciencia y Tecnología (México) under grant 209494. This work was partially supported by Vicerrectoría de Investigación y Estudios de Posgrado of Benemérita Universidad Autónoma de Puebla under grant MEFC-EXC12-I

MEXICAN OPTICS AND PHOTONICS MEETING
19 al 21 de septiembre del 2012
San Luis Potosí, México

Polynomial representations of wavefront aberrations

Armando Gómez-Vieyra[1,*], Daniel Malacara-Hernández[2], Carlos A. Vargas[1], and Ricardo B. Flores-Hernández [2]

1. Laboratorio de Sistemas Complejos, Departamento de Ciencias Básicas, Universidad Autónoma Metropolitana, Unidad Azcapotzalco, Av. San Pablo 180, 02200 México, D. F., México
2. Centro de Investigaciones en Óptica A.C, Loma del Bosque 115, C.P. 37000, León, Guanajuato, México

Corresponding author email: agvte@correo.azc.uam.mx

ABSTRACT:

The wavefront aberration is the difference between the real wavefront and a spherical reference wavefront at the exit pupil of the optical system. This wavefront aberration can be analytically represented by different polynomial families or polynomial series. These polynomials have their own characteristics and applications. The physical interpretation is customarily done in terms of Seidel, Zernike, one proposed in our previous work and many other representations. In this article, we will compare and analyze these different representations pointing out their relative advantages or disadvantages. Furthermore, we extend our previous published proposal, for a new polynomial representation, originally valid only for systems with lateral symmetry about the y axis, to make it valid for systems without any symmetry.

Keywords: polynomial wavefront representation, wavefront aberrations, non-centered and non-symmetrical optical systems

---

REFERENCES AND LINKS

[1] Malacara, D., Z. Malacara (2004), Handbook of Optical Design. USA: Marcel Dekker.

[2] Mahajan, V.N. (1998), Optical Imaging and Aberrations: Part I Ray Geometrical Optics. SPIE Press Monograph Vol PM45. Bellingham, WA:SPIE.

[3] Gómez-Vieyra, A., and D. Malacara-Hernández, "Geometric theory of wavefront aberrations in an off-axis spherical mirror," Appl. Opt. **50** (2011).

[4] Malacara, D., DeVore, S.L., "Interferogram Evaluation and Wavefront Fitting" in Optical Shop Testing, D. Malacara, ed., John Wiley, New York, 455-499 (1992).

[5] Mahajan, V.N., "Zernike Polynomials and Wavefront Fitting" in Optical Shop Testing, D. Malacara, ed., John Wiley, New York, 498-546 (2007).

---

1. Wavefront aberrations representation given by non-centered and non-symmetrical optical systems.

In the general case, when the optical system is not symmetric and/or it is not centered, the wavefront aberration representations given in the Taylor and Seidel [1-5] are insufficient to describe this wavefronts, because non-symmetrical aberrations and non circular pupils could be present in these systems.

Zernike Polynomials

The Taylor general representation is not the most adequate for the analysis of an arbitrary optical system. A grouping of two or more monomial components is normally used to represent certain common wavefront deformations called optical aberrations. For example, a spherical wavefront deformation is called defocus, a toroidal or cylindrical deformation are called astigmatism and a rotationally symmetric aspheric deformation with a fourth power radial dependence is called primary spherical aberration and so on. Several other practical aspects have to be taken into consideration to define these aberrations, for example the following two: Are the different aberration terms to be orthogonal to each other? ; Where is the center of curvature of the reference sphere to be located?

There are several practical reasons why orthogonal polynomials are useful and desirable, for example, an easier numerical manipulation and an easier interpretation in interferometrical applications. If the wavefront aberration polynomials are designed to form an orthogonal (in a circular pupil with unit semi-diameter) set of polynomials, they are called the orthogonal Zernike polynomials [4], and recently, the orthonormal Zernike wavefront representation has been adopted as standard [5]. Both Zernike wavefront representations have the following properties:

The reference sphere has a radius of curvature determined only by the defocus term. This sphere represents the best least squares fit of the aberrated wavefront to a sphere. A consequence of this is that if the defocus term is simply removed, a plane surface would be the closest sphere to this aberrated wavefront without the defocusing term, in the least squares sense. The closest reference sphere for each of the Zernike aberration terms is a flat surface with no tilt. This is achieved during the orthogonalization procedure by adding to each Zernike term the proper linear combination of Zernike terms of lower order. In other words, the center of curvature of the reference sphere is not at the Gaussian image, but at a point close to the optimum image, located between the sagittal and tangential images. We can say that this center of curvature is close to the medium focus (waist of the caustic if only spherical aberration is present), but not exactly there, for two reasons:

There is a small axial displacement for the medium focus image, because it is defined for the best image considering paraxial transverse aberrations (sagittal and tangential), while in the Zernike polynomials it is the best image considering the minimum wavefront deformations for the whole aperture (This includes paraxial as well as marginal rays).

There is a small lateral displacement because the medium focus image is defined for paraxial rays, while the best focus for Zernike polynomials is for the whole aperture. The lateral displacement of the image is due to the presence of the odd aberrations, like coma.

On the other hand, the difference between the two Zernike representations is that the norm of the orthonormal representation is normalized. Zernike polynomials had become so popular that several types of orthogonal polynomials for non-circular pupils (ellipsoidal, hexagonal, square) based on Zernike family had been proposed by Mahajan [5].

The alternative proposal for non-centered and non-symmetrical optical systems

In a previous work [3], we proposed another wavefront representation whose centers of curvature of the reference sphere are near the circle of least confusion for the image, actually “the center of curvature of the reference sphere is located at the average focus, between the sagittal and tangential image [3]. However, this representation is not complete, so, it is necessary to include the remining asymmetric terms. That is, they form a base of symmetric and antisymmetric terms based on the previous conditions, with center of curvature at the medium focus, which is on the medium surface.

3. Conclusions

We have analyzed and compared different wavefront representations for systems.

MEXICAN OPTICS AND PHOTONICS MEETING
19 al 21 de septiembre del 2012
San Luis Potosí, México

Optofluidic system design for particles manipulation

Heriberto Carlos Ayala Cruz [(1)], Dr. Víctor Ruiz Cortés [(1)]

1. Depto. de Óptica, Div. Física Aplicada, Centro de Investigación Científica y de Educación Superior de Ensenada (CICESE), Ensenada, B. C. México

Corresponding author email:
vruizc@cicese.mx

ABSTRACT:

The objective of this work is the manipulation and sorting of particles inside an optofluidic device using a structured beam. With the help of a spatial light modulator we can design different field distributions in the confinement region starting with a plane wavefront. In this way we can manipulate several particles with a single beam.

Key words: optofluidic, trapping, microfluidic.

REFERENCES AND LINKS

[1] A. Ashkin, "Optical trapping and manipulation of neutral particles using lasers", Proc. Natl. Acad. Sci. USA, 94, 4853-4860 (1997).

[2] E. R. Dufresne, G. C. Spalding, M. T. Dearing, S. A. Sheets, and D. G. Grier, "Computer-generated holographic optical tweezer arrays", Rev. Sci. Instrum. **72**, 1810-1816 (2001).

[3] J. C. McDonald, D. C. Duffy, J. R. Anderson, D. T. Chiu, H. Wu, O. J. A. Schueller and J. M. Whitesides, "Fabrication of microfluidics systems in poly(dimethylsiloxane)", Electrophoresis **21**, 27-40 (2000).

[4] A. A. S. Bhagat, P. Jothimuthu and I. Papautsky, "Photodefinable polydimethylsiloxane (PDMS) for rapid lab-on-a-chip prototyping", Lab Chip **7**, 1192-1197 (2007).

1. Introduction

The project involves the design and manufacture of optofluidic devices to use them in particle manipulation. This manipulation is performed by using an optical tweezers system. The optical tweezers system used in this work is similar as the one proposed by Ashkin [1], we can accelerate, decelerate, deflect, guide and confine microparticles through the induction of pressure forces by the radiation of a highly focused laser beam, in this way, we can confine small dielectric particles in a small volume.

A spatial light modulator was added to the optical tweezers system, this was in order to modify the wavefront of the beam from a source, the modification is such that allow us to form a field distribution desired in the containment area, so we can achieve manipulate multiple particles simultaneously. The array of optical tweezers with spatial light modulator is called holographic optical tweezers [2]. A schematic diagram is depicted in Fig. 1 (a).

With a computer program the spatial light modulator (SLM) can change the wavefront of the light beam from a laser. The user will be able to design field distributions leading to the confinement of several particles at a time. An example of field distribution is shown in Fig. 1 (b):

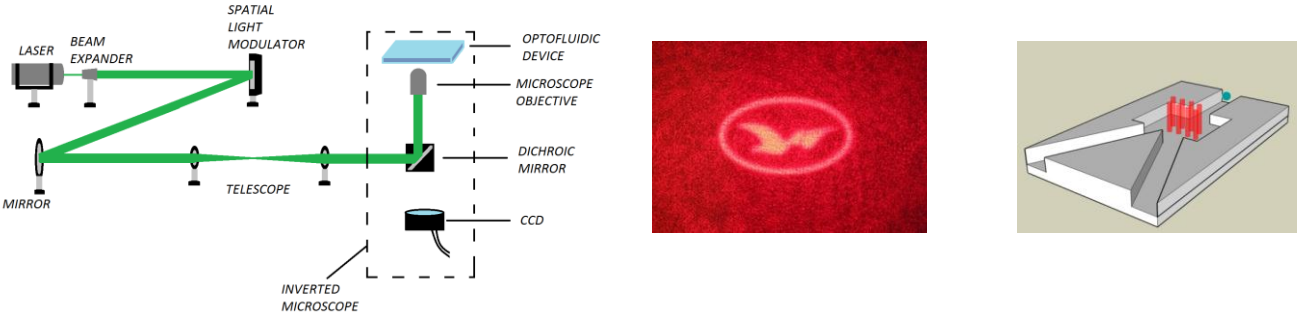

(a) (b) (c)

Fig.1. (a) Holographic optical tweezers system. (b) Image obtained from the SLM. (c) Optofluidic device with a focused confinement beam in the reservoir enclosure.

The benefits of this technology are the ability to use small amounts of samples and reagents, and carry out the sorting and detection of particles with high resolution and sensitivity [3], low cost and short time of analysis. The microfluidic offer fundamentally new capabilities in the control of molecules concentrations in space and time.

The design and construction of the optofluidic devices was carried out using PDMS (polydimethylsiloxane), a polymer which after preparation allow us to fabricate microchannels ranging from 50-200 micrometers deep or more [4]. The fluids and particles to be handled travel inside these microchannels, Fig. 1 (c).

To inject the fluid inside the microchannels a syringe pump was designed and constructed, this allowed the insertion of the fluid in a gradual and controlled way, in addition of not generating large amount of pressure to burst the channels.

2. Results

Particles classification was achieved for polystyrene particles of 5µm in diameter, this thanks to the suitable design of optofluídico devices and the implementation of holographic optical tweezers arrangement.

3. Conclusions

The holographic optical tweezers system is an excellent tool for carrying out particles classification by size. Also such a system can be implemented for tasks like separation of living particles from dead particles, cell sorting by refractive index, and several other tasks.

MEXICAN OPTICS AND PHOTONICS MEETING
19 al 21 de septiembre del 2012
San Luis Potosí, México

Testing a parabolic trough solar collector by using a single flat null screen

V.I. Moreno-Oliva [(1)], E. Román-Hernández [(1)], A. Castañeda Mendoza [(1)], M. Campos García [(2)]

1. Universidad del Istmo, Campus Tehuantepec, C.P. 70760, Oax., México
2. Universidad Nacional Autónoma de México, Centro de Ciencias Aplicadas y Desarrollo Tecnológico, Apdo. Postal 70-186, C.P. 04510, México, D.F.

Corresponding author email: vmorenofcfm@hotmail.com

ABSTRACT:

A novel approach based on null-screen testing is proposed for Parabolic Trough Solar Collector (PTSC) testing. Our proposal consists of a new configuration: a single layer perpendicular to the optical axis flat null-screen. We analyzed the light rays reflected on the PTSC surface in order to know where the caustic lies in terms of the optical system parameters. In this paper we describe the resulting null-screen shapes along with their singularities when are placed inside the caustic region. Our testing method is very similar to the one proposed at [1-2] where a two sided flat null-screen parallel to the optical axis is used. The fact of being necessary to use a two sided null-screen is disadvantageous because of an obscure region appears due to the separation between both null-screen sides. In another paper [3] people solve this problem by means of a "thick" null-screen, consisting of a perpendicular third null-screen placed between both of the original null-screens, allowing , this setting, to avoid the obscure region. This approach has been proved to be unpractical due to alignment problems and new experimental errors.

Key words: Optical testing, Null Screen, Caustics

REFERENCES

[1] Moreno-Oliva, V.I., Campos-García, M., Granados-Agustin, F., Arjona-Pérez, M.J., Díaz-Uribe, R., Avendaño-Alejo, M., "Optical testing of a parabolic trough solar collector by a null screen with stitching", in Modeling Aspects in Optical Metrology II, edited by Harald Bosse, Bernd Bodermann, Richard M. Silver, Proceedings of SPIE Vol. 7390 (SPIE, Bellingham, WA 2009) 739012

[2] Víctor I. Moreno-Oliva, Rufino Díaz-Uribe and Manuel Campos-García (2010). Shape Measurement of Solar Collectors by Null Screens, Solar Collectors and Panels, Theory and Applications, Dr. Reccab Manyala (Ed.), ISBN: 978-953-307-142-8, In Tech, Available from: http://www.intechopen.com/books/solar-collectors-and-panels--theory-and-applications/shape-measurement-of-solar-collectors-by-null-screens

[3] J. Beltrán-Madrigal, R. Díaz-Uribe, M. Campos-García, V.I. Moreno-Oliva, "Nuevos diseños de pantallas nulas para la prueba de un colector solar parabólico de canal", en Memorias en Extenso; Sesiones de Óptica (en CD-ROM), Agustín Santiago, ed. (DO-SMF/AMO, Puebla, Pue., México, 2010)

1. Preliminaries

The null-screen method for optical surface testing is an ongoing topic on research for its many advantages, like a simple experimental setting, and good results despite its simplicity. For the null-screen design an inverse ray tracing technique is used like that described in [1-3], where a parallel to the optical axis null-screen is used. Although this experimental setting is very simple, it does not allow the entire optical surface to be tested. To solve this, we propose a perpendicular to the optical axis null-screen. The inverse ray tracing calculations are done the same way, but this time the null-screen is at a different angle and position.

This novel approach for null-screen testing is being used for the surface of a PTSC. The complete setup for a simulation consists of the PTSC plus a CCD and a pinhole, this allow us to test how the real experiment will behave and solve problems associated with the caustic and the optical system parameters such as the CCD resolution and size and focal distances (PTSC and CCD). In our custom simulation software the CCD-pinhole par is seen as a structured point light source. Also a domain set (CCD pixels) consisting of an equally spaced grid is mapped on to a codomain set (null screen). Due to the reflected rays on the PTSC a caustic is created, when the null screen is inside the caustic the mapping stops being one to one for some points, thus being impossible to test the PTSC. Therefore, for a successful null-screen testing setup a caustic avoidance region must be calculated during the experimental setup design.

In order to calculate the caustic avoidance region, two par of marginal and paraxial rays reflected are used. Further caustic properties still being studied point to the fact that this method of calculation is not effective all of the time.

2. Conclusions

We proposed a novel approach based on null-screen testing for parabolic trough solar collector testing which allow us to avoid problems aroused in previous papers. Analytic calculations are done for the null-screen design in terms of the PTSC and optical system parameters. We also characterized and determined a caustic avoidance region allowing us to choose the better place for a perpendicular to the optical axis null screen.

Acknowledgments

This research has been supported by the Programa de Mejoramiento del Profesorado (PROMEP), under the project: 103.5/11/5266 (UNISTMO-PTC-066).

MEXICAN OPTICS AND PHOTONICS MEETING
19 al 21 de septiembre del 2012
San Luis Potosí, México

Phase changed and sensitivity in optical fiber when pressure is applied

Pulido-Navarro M. G., Alvarez-Chavez J. A.

Centro de Investigación e Innovación Tecnológica – IPN, Cerrada Cecati S/N Col. Santa Catarina 002250
Corresponding author email: jalvarezch@ipn.mx

ABSTRACT:

This work is focused in obtaining the sensitivity in optical fibers subjected to stress. Fiber propagation theory shows that when pressure is applied on the fiber, its refractive index changes and high order modes are radiated out due to the fact that the fiber diameter gets reduced.

Key words: sensitivity, refractive index, high order modes.

REFERENCES AND LINKS

[1] T. Elsarnagawy, "Investigating prospectives of using fiber optics based sensors".

[2] A. J. Rogers, "Distributed optical-fibre sensors for the measurement of pressure, strain and temperature", King's College London (1988).

[3] J. W. Berthold, "Design and Characterization of a high Temperature Fiber-Optic Pressure Transducer", Journal of Lightwave Technology (1987).

[4] W. hCuang, "Characterization of Pressure Response of Bragg Gratings in Grapefruit Microstructured Fibers", Journal of Lightwave Technology (2010).

1. Introduction

In the modern world, especially in structures it is of most importance to acquire a system capable of giving information about the physical state of them. The aim of structural health monitoring (SHM) is to monitor continuously the state of these structures. In this sense, today there exist many techniques but, the one that is proving to be one of the most efficient and cost effective is the one that exploit optical fibers. The reasons why they are the best choice is quite ample, to mention just a few: light weight, immune to electromagnetic interference, low cost in terms that the fiber itself can become the sensor mechanism as well as the communication channel, thus, saving money and weight in terms of avoiding complicated cabling along structures. Other advantages are that they can be embedded in new structures or be installed in old ones due to its nature of being non-destructive. Also the information they give is quite accurate and it can be in real-time giving us a great advantage over other techniques when time is of most importance. This work is focused in detecting changes in the fiber characteristics when it is exposed to different weights. When strain is induced in the fiber, its refractive index changes, this phenomenon is known as the elasto-optic effect [1]. The change in refractive index is due to the optical polarization direction that is parallel to the strain vector, relative to the orthogonal direction. The resultant difference in velocities for the two polarization directions is known as linear birefringence that leads to an optical phase difference between the two directions, per unit length of fiber, which is proportional to the magnitude of the strain [2,3]. The optical power in the fiber is attenuated in proportion to the distortion amplitude via coupling from propagation to radiating modes [4]. An optical fiber exposed to strain experiences both radial and axial pressure, where the actual axial strain is the sum of the two components

$$\varepsilon z,\text{core} = \varepsilon z,\text{radial pressure} + \varepsilon z,\text{axial pressure} \quad (1)$$

In order to obtain the refractive index profile, the photo-elastic effect is used along with the stress distribution:

$$nx = n0 - C1\sigma x - C2(\sigma y + \sigma z) \quad (2)$$

$$ny = n0 - C1\sigma y - C2(\sigma x + \sigma z) \quad (3)$$

where σx, , σy , σz are the stress components, C1 and C2 are stress-optic coefficients. C1 = 6.5 x 10-13 m2/N and C2 = 4.2 x 10-12 m2/N.

2. Experimental set-up

Initially, a static load is applied on the optical fiber. The signal from the fiber is converted into strain by using the Phase-Strain Sensitivity equation:

$$G = \frac{\Delta\phi}{\varepsilon L} = \frac{4\pi}{\lambda}.n\left[1 - \frac{1}{2}n^2((1-\nu)\rho_{12} - \nu\rho_{11})\right] \quad (4)$$

and

$$\varepsilon_z = ((2\nu - 1)P)/E \quad (5)$$

Where, n : refraction index; ν : Poisson's rate; ρ_{12}, ρ_{11} : elasto-optic coefficients; λ : wavelength; ε: stress; E : Young's module, P : applied pressure.

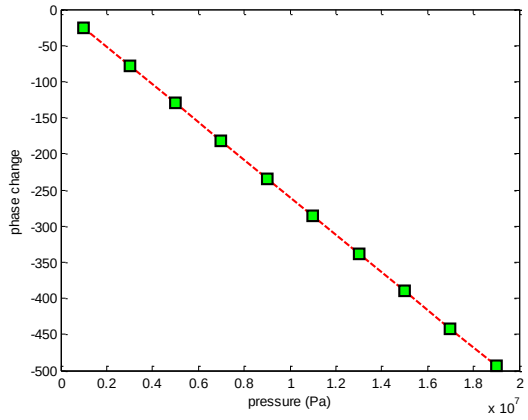

Fig.1. Phase Change.

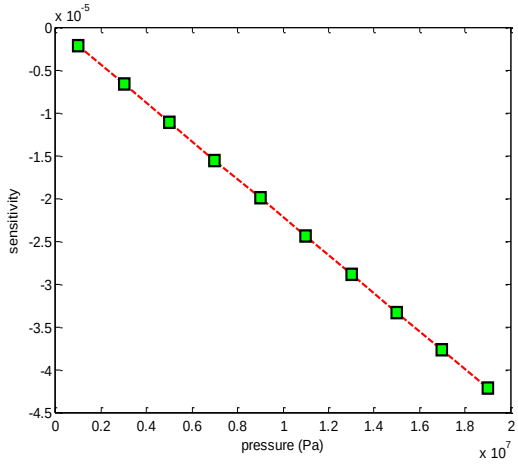

Fig2. Sensitivity.

3. Conclusions

As can be seen from the graphics the more pressure is applied to the fiber, the greater is the change in phase and sensitivity. This is because the change in the refractive index is more marked as the pressure increases and the higher order modes get radiated more efficiently.

Acknowledgements

The authors express their gratitude to CONACYT and IPN-CIITEC for the PhD scholarship and for the technical support.

MEXICAN OPTICS AND PHOTONICS MEETING
19 al 21 de septiembre del 2012
San Luis Potosí, México

An instantaneous phase shifting system for temperature fields measurements

David Serrano-García[1], Amalia Martínez-García[1], Noel Iván Toto-Arellano[2], J. A. Rayas[1], Gustavo Rodríguez-Zurita[3]

1. Centro de Investigaciones en Óptica, A. C., León Gto.
2. Universidad Tecnológica de Tulancingo, Hidalgo
3. Benemérita Universidad Autónoma de Puebla

david@cio.mx

ABSTRACT:

In this study, a measurement optical system based in a Michelson interferometer which is capable of grabbing three phase-shifted interferometric images simultaneously is developed for singular temperature fields measurements of a flame varying in time. The system constructed allows the three phase-shifted images to be grabbed by one CCD simultaneously.

Key words: Refractive index; temperature profile, phase shifting, polarization, interferometry.

REFERENCES AND LINKS

[1] Ch. Vest, *Holographic Interferometry*, Wiley, New York (1979).

[2] D. I. Serrano-García, N. I. Toto-Arellano, A. Martínez-García, G. Rodríguez-Zurita, "Radial slope measurement of dynamic transparent smples", *J. Opt. A-Pure Appl. Op.* **14**, 045706-7p (2012).

1. Introduction

In the past, stepping motor or piezoelectric transducers are normally used to move reference surface or rotate the polarizer to get interference fringe images of different phase. However, this kind of practice takes a long time and is susceptible to environmental effects such as ambient vibration or air turbulence which results in measurement errors. To facilitate the applicability of interferometric techniques for dynamic events measurement, the system that is capable to acquire several phase shifted images instantaneously or simultaneously is required. In order to reduce the influence of environment and increase the accuracy and stabilization, the instantaneous phase-shifting interferometry (IPSI) technique is introduced. In this study, a measurement system which is capable of grabbing three phase-shifted interferometric images instantaneously (or simultaneously) was developed for temperature measured in long period of time. A polarization phase-shifting interferometric system was designed and constructed. By the calibration and digital processing techniques we were capable of measure the phase data map in a single capture. Test of the system is demonstrated.

2. Analytical equations for the temperature measurement

The phase difference ϕ between two waves passing through the same point of the phase object of interest, one in the presence of inhomogeneous medium and the other in the air is given as [1] $\phi = \frac{2\pi}{\lambda}\int_0^{\Gamma}[n(x,y,z)-n_0]dx$.

where $n(x,y,z)$ is refractive index of the medium, n_0 is the refractive index of the air and Γ is the total length of the medium. In this equation the optical path difference provides the distortion of the wavefront. For an axisymmetric phase object $n(x,y,z) = n(r,z)$, where $r = \left(x^2 + y^2\right)^{1/2}$. Since the temperature distribution is axi-symmetric it can write

$\int_1^2 (n - n_0)dx = 2\int_y^\infty \frac{f(r)rdr}{\sqrt{r^2 - y^2}}$, where $f(r) = n(r) - n_0$. The solution to this is given by the Abel Transform. The density ρ can be found using $\rho = \rho_{ref} + \frac{f(r)}{K}$, where K is the Gladstone-Dale constant found for air for $\lambda = 632.8\,nm$ and $\rho_{ref} = 1.225\,\mathrm{kg/m^3}$ for air at standard temperature pressure. To find the temperature T, the equation of state used is $T = \frac{P}{\rho R}$, where $P = 101325 N/m^2$ and $R = 287\,J/kg\,K$.

3. Instantaneous phase-shifting interferometer

The instantaneous phase-shifting interferometer setup is shown in Fig. 1, where a QWP45° is 45 degree quarter-wave, BS is a no polarized beam-splitter; P0°, P60°, P90^0 and P120°, are polarizer with 0°, 60°, 90^0, 120° transmission axis, respectively. As the light emerges from a linear polarized He-Ne laser at 45°, passes through the spatial filter and lens L_1 becoming a collimated light beam. A 4-f system, using a high frequency Ronchi grating in the frequency plane, is coupled at the end of the Michelson interferometer to replicate the fringe pattern and introduce the phase shiftings by using of the polarizers at the output [2].

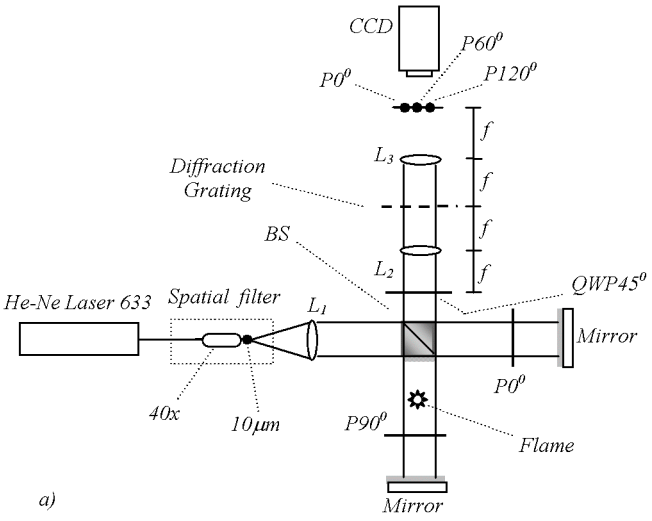

Fig.1. a) The setup of instantaneous polarized phase-shifting interferometer.

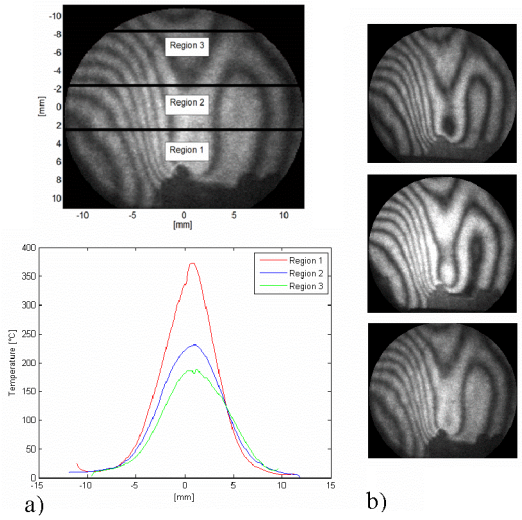

Fig. 2 a)Variation of temperature with distance from the center of the flame. b) Set of fringe patterns with a relative phase shifting of 2π/3 obtained in single capture

4. Conclusions

In this study, a Michelson interferometer together with a 4-f system using a high frequency Ronchi ruling grating were developed based on polarization phase shifting techniques. The main advantage is the capture of multiple fringe patterns, shifted in phase, in a single image in order to retrieve the phase data map using a CCD camera. Therefore, it can reduce the external environment effects and thus applicable to the dynamic measurement. Test of the system by a flame temperature measurement demonstrates the feasible of the developed system.

MEXICAN OPTICS AND PHOTONICS MEETING
19 al 21 de septiembre del 2012
San Luis Potosí, México

Measuring the speed of sound in crystal-violet/water dissolutions via photoacoustic technique

V. Torres-Zúñiga [(1)], R. Castañeda-Guzmán [(2)], S.J. Pérez-Ruiz [(2)], O.G. Morales-Saavedra [(2)]

1. Facultad de Ciencias, Universidad Nacional Autónoma de México, Circuito Interior, Ciudad Universitaria, 04360 México D.F., México
2. Centro de Ciencias Aplicadas y Desarrollo Tecnológico, Universidad Nacional Autónoma de México, CCADET-UNAM. Cd. Universitaria, A.P. 70-186 C.P. 04510 México D.F. México.

Corresponding author email: vicentz@gmail.com

ABSTRACT:

Speed of sound can be used as a cardinal acoustic parameter for quantitative characterization of organic systems. In this work, the relationship between the speed of sound and the concentration of crystal-violet (CV) in distillated water (DW) dissolutions is investigated. The speed of sound was measured by the pulsed-laser photoacoustic technique (PLPA), which consists in the generation of acoustic waves by the optical absorption of pulsed light incident on a material. The generated sound-waves traveling through the fluid are detected with two piezoelectric sensors separated by a known distance. An appropriate processing of the detected photoacoustic signals permits an adequate data analysis of the generated longitudinal waves, reflections and other types of waves generated within this system, allowing an accurate determination of the sound-speed as function of the CV concentration. An important advantage of the PLPA-method is that it can be implemented with poor or null optical transmitting materials.

Keywords: speed of sound, photoacoustics, concentration, density, organic fluid

REFERENCES AND LINKS

[1] V. Torres-Zúñiga, R. Castañeda-Guzmán, O.G. Morales-Saavedra, A.L. Pérez-Martínez, and T. Ogawa, "Monitoring molecular orientational order in NLO push–pull based polymeric films via photoacoustic measurements", *Opt. Lasers Eng.* **49**, 1413–1421 (2011).

[2] S.J. Pérez Rúiz, S. Alcántara Iniesta, P.R. Hernández, and R. Castañeeda-Guzmán, "Sound speed resolved by photoacoustic technique", *Rev. Mex. Fis.* **53**, 213–217 (2007).

1. Introduction

In recent works, the pulsed laser photoacoustic technique (PLPA) has been successfully used to study structural anisotropies in different dichroic organic samples [1]. In this communication, it is shown that the PLPA-methodology can be implemented in order to analyse the speed of sound as function of the concentration of an organic chromophore. The aim of this investigation is to obtain standard parameters in order to develop an analytical methodology and a PLPA-based device capable to analyze different physical properties in organic samples immersed in a liquid phase.

2. Experimental procedure and representative results

Fig. 1 shows the implemented experimental set-up. Here, a glass-cell (GC: ~2.3x1.3x0.2 cm^3) was filled with CV/DW dissolutions with increasing CV concentrations (CV-dye from Aldrich Inc.: 90% purity). Given that the CV-dye exhibits a high molar extinction coefficient around the laser excitation wavelength (λ_{ex} =532 nm), this dye

can be properly implemented as an adequate absorber compound in the photoacoustic experiments. In contrast, the DW and GC are highly transparent at λ_{ex} and produce negligible PLPA-signals. In this way, the CV/DW system was illuminated with a frequency doubled (@ λ_{ex}) Nd:YAG laser system (from Continuum Co. Minilite II) with light pulses of $\tau \approx 5$ ns (at 10 Hz repetition rate; Pulse energy: ~10.0 mJ/pulse). It is worth noting that the laser beam was not focused into the GC in order to avoid molecular degradation due to strong laser peak intensities. The chemical stability of the dissolutions was confirmed via UV-Vis-NIR spectroscopic measurements after PLPA-measurements.

The generated PLPA-signals were simultaneously monitored by means of two piezoelectric transducer (PZT/Lead-Zirconate-Titanate; Resonance Frequency: ~500 kHz) attached to the GC along the y-direction, see Fig 1. PLPA-signals were averaged, visualized, stored and partially analyzed on a digital oscilloscope. Finally, collected PLPA-signals were ready for numerical processing in a personal computer in order to obtain the representative root-mean-square (RMS) amplitude and the speed of sound [2] as functions of the CV-dye concentration, see results in Fig. 2A and 2B, respectively. In general, it is observed from our measurements that both the RMS-amplitude and the speed of the sound are linear functions of the CV-dye concentration at least within the 7.67-20.68 mg/L range.

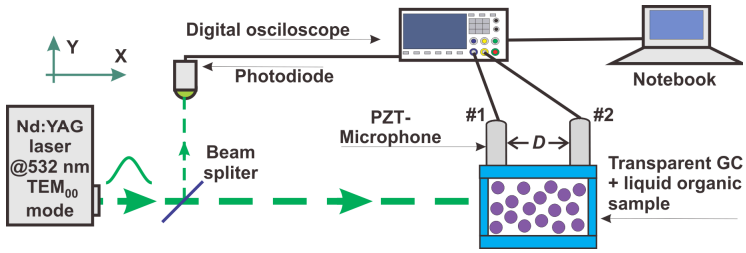

Fig.1. Schematic representation of the experimental set-up implemented for measuring the speed of sound using the photoacoustic technique.

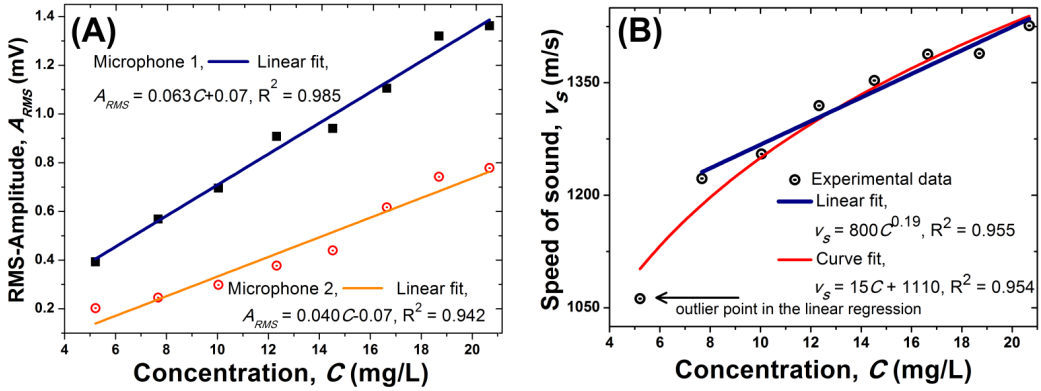

Fig.2. **(A)** RMS-Amplitude A_{RMS} analyses, and **(B)** Estimated speed of the sound v_s as function of the CV-concentration C in DW dissolutions based on PLPA-signals.

3. Principal conclusions

The PLPA-methodology was implemented as a nondestructive, easy to implement and accurate technique to analyze and quantify the chromophore concentration and the speed of sound in quasi- and fully opaque dye-based liquid samples. This is important since at the implemented CV-dye concentrations, conventional optical techniques such as UV-Vis spectroscopy, which is limited by the Beer-Lambert law, are inappropriate to perform accurate and trustable data analyses to determine several structural and photo-physical material properties in opaque samples.

MEXICAN OPTICS AND PHOTONICS MEETING
19 al 21 de septiembre del 2012
San Luis Potosí, México

Barker sequences as spatial filters: Null test

Pedro A. Cerna-García, A. Sauceda-Carvajal* and Jorge Ojeda-Castañeda.

División de Ingeniería Campus Irapuato-Salamanca, Universidad de Guanajuato
Corresponding author email: jorge_ojedacastaneda@yahoo.com

*Escuela de Ingeniería, Universidad de Ciudad Juárez, Chihuahua, México

ABSTRACT:

We present a spatial filter that employs a composed Barker code for implementing (with high light throughput) narrow passband filters, which works well even when the optical system suffers from focus errors. Numerical simulations display the potential use of this filter for setting null tests.

Key words: Spatial filters, Noncoherent Image Formation, Image Processing, Passband filters, Null Test

---

REFERENCES AND LINKS

[1] M. Harwit and N. J. Sloane, *"Hadamard Optics"* Academic Press (New York, 1979)
[2] T. F. Krile, M. O. Hagler, W. D. Redus and J. F. Walkup, ñMultiplex Holography with chirp-modulated binary phase-coded reference masksò, Appl. Opt. Vol. 18, 52-56 (1979)
[3] *",* J. Ojeda-Castañeda, L. Díaz-Santana and J. Piñataro, "*Pseudorandom gratings for noncoherent theta-decoders,"* Opt. Comm., Vol. 157, 209-217 (1998)

---

1. Introduction

There is a strong analogy between the use of pseudo-random sequences for digitally filtering signals, and the use of complex amplitude masks for shaping the point spread function (PSF) of an optical system [1-3]. Hadamard optical devices have high light throughput than pinholes and slits.

Here, for implementing a narrow passband filter, we use a mask whose complex amplitude transmittance is equal to a 13 *13 composed Barker code. By using numerical simulations, we show that this narrow band filter works well, even when the optical system suffers from focus errors.

2. Periodic input patterns

For the sake of clarity, we verify our proposal by employing a 1-D input pattern optical system, with the following irradiance distribution

$$I_0(x) = \frac{1}{2}\left[1 + cos(2\pi\sigma x)\right]. \qquad (1)$$

In Eq.(1), we denote the spatial frequency as ů=1/d. Now, a narrow passband filter allows passing the spatial frequency ů, and it rejects the spatial frequency $\sigma \pm \delta\sigma, with\ \delta\sigma \ll \sigma$.

3. Numerical simulations

Next, in Figure 1, we show the numerical evaluations of the out-of-focus *Optical Transfer Function* (OTF), associated to a pupil aperture that is covered with composed Barker code, 13*13.

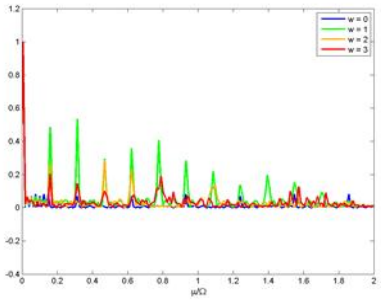

Figure 1 Out-of-focus OTFs

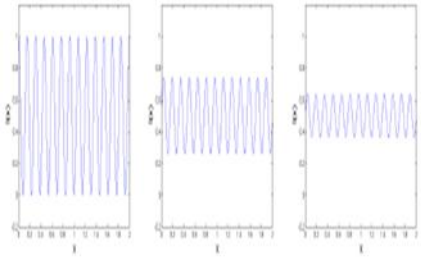

Figure 2 Output irradiance distributions

It is apparent from Fig. 1 that the OTF has several highly narrow, peaked windows at the spatial frequencies n ů , where ů= 26 pixels, and n = 1, é , 9. The cut-off spatial frequency is equal to 338 pixels. In Figure 2 we plot the output irradiance distribution, if ů= 26 pixels with focus error coefficients $W_{2,0} = 0, \lambda, and\, 2\lambda$. For visualizing the rejection bands, we plot the output irradiance distribution, if $\sigma - \delta\sigma = (52 - 8)\, pixels = 43\, pixels,$ with focus error coefficients $W_{2,0} = 0, \lambda, and\, 2\lambda$.

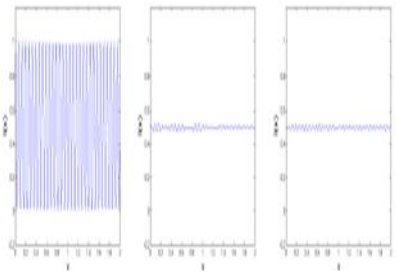

Figure 3 Output irradiance distributions

It is apparent from Figs. 2 and 3 that the OTF does work as a passband filter. The above results suggest the following. For an input with variable frequency, one can identify either the in-focus plane (as in Figure 3), or the spatial frequency of the input pattern, as in Figure 2. This procedure can be thought of as setting null tests.

2. Conclusions

We present the use of a composed Barker code for generating an optical transfer function that exhibits several narrow and highly peaked windows. The transmittance windows have the same location even when the optical system suffers from focus errors. Hence, one can apply these masks for identifying either spatial frequencies, or the in-focus plane. We note that the proposed filter has higher light throughput that if one uses either pinholes or narrow slits.

MEXICAN OPTICS AND PHOTONICS MEETING
19 al 21 de septiembre del 2012
San Luis Potosí, México

Effects of the optical path lengths in an optical fiber interferometer

Perla Viera-González [(1)], Guillermo Sánchez-Guerrero [(1)], Romeo Selvas-Aguilar [(1)], Daniel Ceballos-Herrera [(1)], Candelario Guajardo-González [(1)], Valentín Guzmán-Ramos [(1)], Carlos Martínez-Hernández [(1)]

1. Universidad Autonoma de Nuevo Leon
marlene.viera.gzz@gmail.com

ABSTRACT:

In this paper, we present the design of an all-fiber Mach-Zehnder interferometer configured as a sound detector. The setup consists in two 3dB couplers, a visible diode laser, and U-bench fiber coupler. The proposing of the U-bench coupler is to deviates the laser path and lengthens the optical path length of one of the arms. This free space signal laser interacts with sound waves and as a result this signal is modulated. The next step is launch the modulate beam into the optical fiber. Whereas the second arm is only used as a reference signal, at the second beam splitter both signals are recombined and form the interference. This work intended to study the equations that describe this effect. We made the study of the phase delay between the sensing and the reference arms analyzing the changes in the refractive index of the air due to the differences in the pressure caused by the sound in the environment. As results, we obtained the sensitivity of our microphone and to have a clear idea of what occurs in our experiment.

Key words: Mach-Zehnder Interferometer, Laser Microphone, Optical Path length, Phase Delay, Acoustic Pressure.

REFERENCES AND LINKS

[1] Ghatak, A. K. And Thygarajan, K. (1998). Single-mode optical fiber sensors. *An introduction to Fiber Optics* (397-403). Cambridge, United Kingdom: Cambridge University Press.

[2] Kirkendall & Dandrige, "*Overview of high performance fibre-optic sensing*", *Appl.Phys.* **37**,R197-R216 (2004).

[3] G. Sánchez, et al. "*Remote Ultra Sensitive Laser Microphone"*, SPIE Vol. **8133** (2011).

[4] Flores, A., et al, *"Undergraduate experiments in optics employing a fiber optic version of the Mach Zehnder Interferometer"*, SPIE Vol. **4588** (2002).

1. Introduction

Currently, the use of optical fibers in sensing applications has been growing due to these have some advantages above the electrical sensors [1]. Some of the sensing applications of optical fibers are the measurements of pressure, temperature, magnetic field, pH, and also, high performance sensing like surveillance systems, seismic systems and inertial navigation system [2]. In the literature, we can find optical fiber sensors based on Mach-Zehnder Interferometers that are used like sound detectors, because they have a section to catch sound and voice vibrations through a fiber optics. Most of these works use a membrane or other device like the receptive component but, are another that has the opportunity to increase the sensitivity because they use the free space instead of a material [3]. We analyzed the changes in the refractive index of the air due to pressure variations [4] considering the acoustic pressure, 2×10^{-5}Pa, that humans can hear [1].

2. Mathematical analysis

Like in our typical layout for a Mach Zendher Interferometer, we use fiber optic couplers instead of beam splitters, and we can use the coupling equations for obtain our intensity outputs [1]:

$$I_1 = I_0 cos^2\left(\frac{\Delta\phi}{2}\right), \quad (1)$$

Where $\Delta\phi$ is the phase delay $(\phi_2 - \phi_1)$ between the arms and I_0 is the intensity applied in the input of our system. Now, we consider how obtain the phase of the path in an arm [2]:

$$\phi_i = \frac{2\pi n_i L_i}{\lambda}, \quad (2)$$

Where n_i is the refractive index of the path, L_i is the length of the arm and λ is the wavelength of the system. At least, we must consider the relation of the refractive index of the air, the pressure and the temperature given by [4]:

$$(n-1)\times\left\{\frac{p[1+p(6.13-T)\times10^{-10}]}{96095.4(1+0.003661T)}\right\}\times 10^8 = 8324.13 + 240603(130-\sigma^2)^{-1} + 15997(38.9-\sigma^2)^{-1}, \quad (3)$$

Where n is the refractive index of the air, T and p are the temperature and the pressure of the environment respectively, and $\sigma = 1/\lambda$. We considerer $p = P_{base} + \Delta p$

TABLE I

Technical data

I_0	n_{FO}	n_{air} *(average)*	$L_{ref} = L_{sens}$	λ	T	P_{base}
5.25 mA	1.46	1	50.8 mm	633 nm	22° C	101300 Pa

Considering the typical arrangement for a Mach Zendher interferometer and some constants that we establish (Table I), we can then calculate the increases and decreases of the refractive index of the air using (3). If we don't have changes in pressure we will have a delay phase constant, in other cases, we can calculate the differences in the output (I_1) due this changes using (1) and (2).

3.- Results

According with the analysis we obtain the graph in Fig. 2 and we know that the sensitivity of our microphone is around:

$$\frac{\Delta I_1}{\Delta p} = -0.00112197\ Watts/Pascal \quad (4)$$

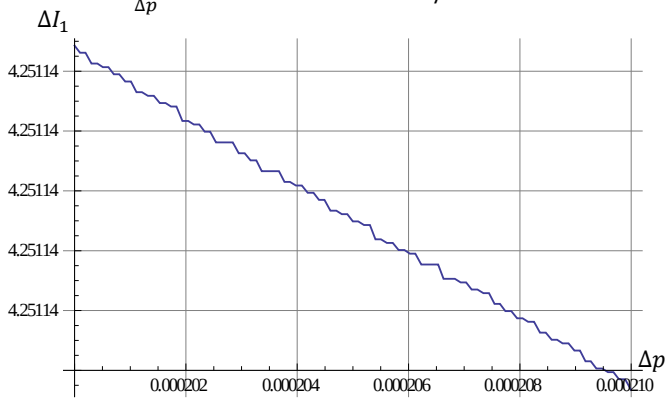

Fig.2. Pressure Variations vs. Output Intensity. In the y-axis the variations are in the order of nW.

4.- Conclusions

We obtained sensitivity around the order of 1 nW that can be measured for our photodiode, with this we can conclude that we had a device that can catch most of the sounds that the human voice can produce because it works very well in the range of pressure variations that we produce when we talk.

MEXICAN OPTICS AND PHOTONICS MEETING
19 al 21 de septiembre del 2012
San Luis Potosí, México

In grinding optical surfaces it was measured the dragging force as a function of relative velocity between glass and tool.

Alberto Cordero Dávila [(1)], Carina Gutiérrez Ojeda [(1),] Saldivia Gomez Elizabeth [(1)]
1. Facultad de Ciencias Físico- Matemáticas, B.U.A.P., C.P. 72570. Puebla, Pue.

acordero@fcfm.buap.mx
carina_gutierrezojeda@hotmail.com

ABSTRACT:

For grinding optical surfaces it was measured dragging force as a function of the relative velocity between glass and tool. We found that results are reproducible and we can conclude the friction force is independent of the angular velocity.

Key words: drag force, ground, airspeed, astigmatic surfaces, revolution surfaces

---

REFERENCES AND LINKS

[1] http://www.utm.mx/~mtello/Extensos/extenso160409.pdf
[2] Leonardo Téllez-Arriaga, Alberto Cordero-Dávila, Carlos Ignacio Robledo- Sánchez y Jorge Cuautle-Cortés, *"Correction of Preston equation for low speeds"*
[3] Camilo Valencia y Hernán Bedoya, *"Regresión y correlación de superficies tópicas de revolución en forma canoníca conocidos los radios de curvatura"*
[4] Ing. G. Pablo Lemus Alonso, tesis "*Medición de la fuerza de arrastre y su relación con la producción de superficies astigmáticas en el pulido*, (2011)

1. Introduction

The first work in establishing a model for the wear on the grinding optical surfaces was done by Preston [1]. It was established that the wear is proportional to the work done by the tool on the surface, equation 1; where *h* is the wear produced by a tool at the time (0, τ), μ is the coefficient of friction, f_N normal force and *v* the relative velocity between the glass and the tool. Preston supposed that μ is independent of the relative velocity, however in recent work [2] it has been found that frictional force depends of relative velocity.

In the grinding processes we have obtained experimental results of dragging force between glass and tool for several relative velocities. From which it can be concluded that frictional force is independent of the relative velocities.

2. Experimental set up and results

We did experiments in a R. Howard Strasbaugh Inc, model 6DE4 commercial polishing machine, see Figure 1. We measured dragging force between a rotating glass (30cm in diameter) in a fixed tool (4 cm in diameter). In order to change the relative velocity radial position of the tool was increased.

The obtained experimental results are reproducible ones as a function of the relative velocity between glass and tool, as you can see in the Table 1 and Figure 2, in which you can see a plot of the measured dragging force vs relative velocities.

By comparison of plot Figure 2 and results of Tellez Arriaga et al [2] we can conclude that frictional force does not depend of relative velocity

2. Data

2.a. Mathematical equation and models that describe the system

$$h = A\int_0^{\tau} \mu f_N v dt \qquad \text{equation (1)}$$

2.a. Tables

Velocity	Dragging force	Velocity	Dragging force	Velocity	Dragging force
0	0.06	23.03834613	0.405	58.64306287	0.565
0	0.03	25.13274123	0.62	62.83185307	0.66
0	0.04	29.32153143	0.58	69.11503838	0.66
0	0.04	31.41592654	0.59	73.30382858	0.715
0	0.04	31.41592654	0.55	75.39822369	0.565
6.28318531	0.56	37.69911184	0.66	87.9645943	0.705
10.4719755	0.49	37.69911184	0.58	92.15338451	0.67
12.5663706	0.7	41.88790205	0.12	94.24777961	0.715
14.6607657	0.515	43.98229715	0.565	113.0973355	0.705
18.8495559	1.23	46.07669225	0.605	115.1917306	0.53
18.8495559	0.515	52.35987756	0.58	138.2300768	0.69
20.943951	0.73	56.54866776	0.565		

Table1. It present the exactly behaviour of grinding force and de ground force

2.b.- Experimental assembly: Figures

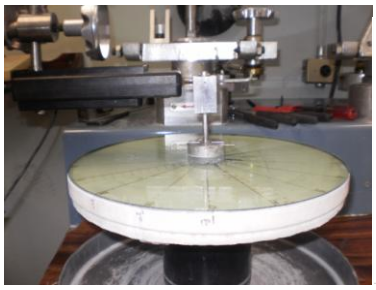

Fig.1.

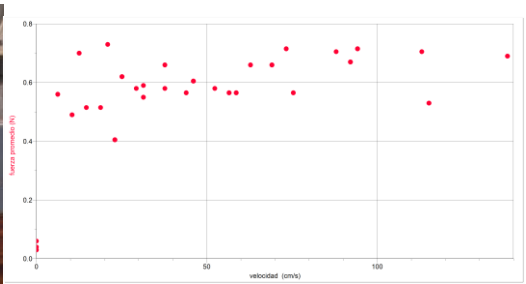

Fig.2.

Fig.1. Experimental setup with a disc 30cm in diameter (left)
Fig.2. Plot of variation of drag force versus relative velocity (right).

3. Conclusions

In grinding process the friction coefficient is independent of the relative velocity between glass and tool. in other words, it is a constant value.

Acknowledgements

Acknowledgements to Jorge Cuautle and Noé Cuautle in the optical workshop.

MEXICAN OPTICS AND PHOTONICS MEETING
19 al 21 de septiembre del 2012
San Luis Potosí, México

Tapered Er-doped ASE Fiber Source Design

G.G.Pérez-Sánchez [1], J.A.Alvarez-Chávez [1].

[1] Centro de Investigación e Innovación Tecnológica (CIITEC), Cerrada de Cecati S/N. Col. Santa Catarina Azcapotzalco, C.P. 02250, México D. F.

Corresponding author email: gret_hell@hotmail.com

ABSTRACT:

In the present work we analyze theoretically the use of a tapered Er^{3+} doped fiber section working in Amplified Spontaneous Emission (ASE) regime. Results on different pump and signal powers in forward and backward propagation direction with respect to fiber length.

Key words: ASE sources. Er^{3+}, tapered fibres

REFERENCES

[1] Hartmut Hillmer, Bernd Klepser., Low-Cost Edge-Emitting DFB Laser Arrays for DWDM Communication Systems Implemented by Bent and Tilted Waveguides, IEEE journal of quantum electronics, vol.40, No.10,october 2004.

[2] Emmanuel Desurvire, Jay R. Simpson. Amplification of Spontaneous Emission in Erbium-Doped Single mode Fiber, Journal of lightwave technology vol. 7 No. 5 1989

[3] E. F.Pinzón-Escobar, G.E. Sandoval-Romero, Theoretical and Experimental Results of Superluminiscent Fiber Optic Source,

1. Introduction

In the last few years efforts to improve the ITU-T channel generating sources in optical communications systems such as Dense Wavelength Division Multiplexing (DWDM) have been carried in the 1550nm region. Some examples include DFB sources, semiconductor lasers and arrays, etc. [1]. Appropriate ASE generation could lead to generate enough bandwidth for up to 240 channels as specified in ITU-T G.709.

Er^{3+}-doped fibre broadband sources have been proposed for ASE emission at around 1550nm, which in turn coincides with the lowest loss in fibres. On the other hand, a tapered fibre could improve the efficiency response for the signal vs. pump wavelength. Such improvements are included in this work.

2. Theoretical model

We used a modified version of the rate equation for three-state laser source considered in ASE regime [2] which describe the response of the pump and signal powers with respect to fibre length:

$$\frac{dP_p(z)}{dz} = -\gamma_p(z)P_p(z) \tag{1}$$

$$\frac{dP_s^{\pm}(z,\lambda_i)}{dz} = \pm\{G_e(z,\lambda_i)[P_s^{\pm}(z,\lambda_i) + P_0] - G_a(z,\lambda_i)P_s^{\pm}(z,\lambda_i)\} \tag{2}$$

Where $P_p(z)$ is the pump power propagating in z direction parallel to the doped optical fibre axis and $P_s^{\pm}(z,\lambda_i)$ is the output power in forward and backward direction, $\gamma_p(z)$ is the absorption coefficient, $G_e(z,\lambda_i)$ is the amplification of spontaneous emission, $G_a(z,\lambda_i)$ is the absorption coefficient of spontaneous emission and P_0 represents an equivalent input noise power:

$$P_0 = 2h\nu_s\Delta s \tag{3}$$

$$\Delta s = \left(\frac{c}{\lambda_s^2}\right) \Delta\lambda_s \tag{4}$$

When $P_p(z)>>P_p^{th}$ we can consider $\gamma_p(z)$ as a constant [3] P_p^{th} is the threshold power

$$P_p^{th} = \pi a^2 \frac{h\nu_p}{\sigma_p \tau} \tag{5}$$

In this work we present the comparative between untapered and tapered fibre. The taper function is the follow:

$$a = 2 * 10^{-6} - \left(0.5 * 10^{-6}\right) * \frac{L}{3} \tag{6}$$

2.a.- Theoretical results:

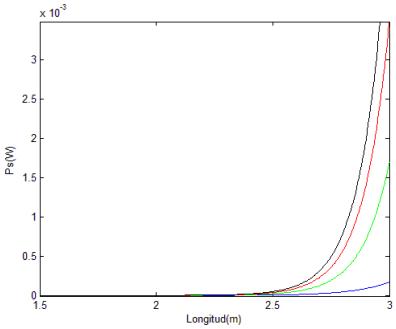

Fig 1.Forward output power vs. fiber length with Pp= 20, 30 40 and 50mW. untapered fiber.

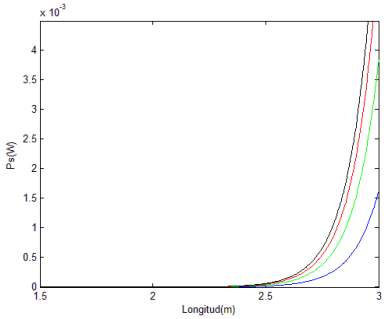

Fig 2. Forward output power vs. fiber length with Pp= 20, 30 40 and 50mW tapered fiber.

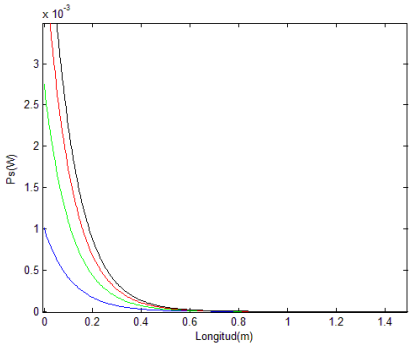

Fig 3.Backward output power vs. fiber length with Pp= 20, 30 40 and 50mW. untapered fiber.

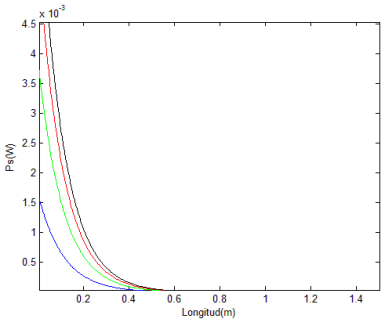

Fig 4. Backward output power vs. fiber length with Pp= 20, 30 40 and 50mW. tapered fiber.

3. Conclusions

We can observe the advantage of use a tapered section to increase the output signal power in forward and backward propagating direction. We suppose the possibility to use this kind of fibres to design DWDM sources. We also found that efficiency increase with tapered fibre.

Acknowledgements

G. G. Perez Sanchez thanks CONACYT for PhD studentship, J.A. Alvarez-Chavez is grateful towards Instituto Politecnico Nacional, CIITEC-IPN and CONACYT Ciencia Basica for funding their project 50265.

MEXICAN OPTICS AND PHOTONICS MEETING
19 al 21 de septiembre del 2012
San Luis Potosí, México

Identification of acrylic fibers: differentiation of methyl acrylate and vinyl acetate comonomer by polarized Raman spectroscopy

R. González-Mota[(1)], C.M. Rodríguez-Cuéllar [(1)], C. Frausto-Reyes[(2)] , J.J Soto-Bernal[(1)] , I-Rosales-Candelas[(1)], E. I. Muñoz-Campos[(1)]

1. Instituto Tecnológico de Aguascalientes, Ags. México
2. Centro de Investigaciones en Óptica,Unidad Aguascalientes, Ags. México

Corresponding author email: rgmota73@yahoo.com.mx

ABSTRACT:

The ability to accurately identify fibres is of importance in the textile industry, but this can prove problematic when dealing with fibres which possess similar chemistry and microstructure, acrylic fibers are particularly challenging in this regard due to the use of comonomers. Conventional techniques such as microscopic examination, flame probe, measurement of fiber widths and the use of the twist test, will often prove unreliable. This research has concentrated on use polarized Raman spectropscopic technique in order to differentiate two fiber types of acrylic fiber, with MA and VA comonomers.

Key words: Acrylic, vinyl acetate, methyl acrylate, polarized Raman spectroscopy

REFERENCES AND LINKS

[1] Lewis Menachem, Ed. *Handbook of fiber chemistry*, CRC press, Boca Raton Fl (2007).
[2] P. Garside and P. Wyeth "Identification of cellulosic fibres by FTIR spectroscopy: differentiation of flax and hemp by polarized ATR FTIR", Studies in Conservation. **51**, 205-211 (2006).
[3] Li-Ling Cho. "Identification of textile fiber by Raman microspectroscopy", Forensic Science Journal. **1**, 55-62 (2007)

1. Introduction

The term ''acrylic fiber,'' specifically refers to a fiber containing at least 85% acrylonitrile (AN) comonomer. The effect of comonomers on the morphology of acrylic fiber has been the subject of several investigations. In all cases, addition of comonomer reduces the crystallinity and crystalline perfection. The changes in the structure caused by addition of the comonomer are not uniform over the entire range of composition, but instead a critical comonomer level is reached where the characteristic PAN morphology begins to rapidly disappear. methyl acrylate (MA) and Vinyl acetate (VA) are the most commun comonomers used; they are of similar in size and both are larger than the methacrylonitrile group, hence expected to be more effective in disrupting the crystalline morphology [1].
Conventional methods used to characterize textile fibers such as microscopy and spectroscopy can be used to investigate the morphology and chemistry of a sample, but reveal little about its microstructure. Combining Raman spectroscopy with a polarizer allows both the nature and orientation of chemical bonds within the sample to be explored, thus yielding vital microstructural information [2].

Raman spectroscopy is a rapid, nondestructive and noncontact technique. Raman microspectroscopy provides no sample preparation or little preparation to analyze fiber sample. Fibers can be taped directly to glass microscope slides or shiny side of aluminum foil covering microscope slides. Most of the fibers can obtain Raman spectra

directly from glass slide mount in order to obtain polymeric identification of undyed fibers. No additional sample preparation was required after visual light microscopy [3]. The purpose of this article is to show acrylic fibers with different VA and MA comonomers can be analyzed by polarized Raman spectroscopy.

2. Experimental and Results

2.a. Experimental Method

Two samples of acrylic fibre were considered in the study, chosen to represent the types of fibre typically encountered in acrylic textile artefacts: acrylic with MA and acrylic with VA. The samples were not subjected to any preparative treatment, and were analysed under ambient conditions.

Raman spectra were taken with a Renishaw model 1000 Raman spectrometer (excitation wavelength of 830nm) for all samples fitted with a Polarization Accessory. The polarizing filter was aligned such that the electric vector of the polarized radiation was oriented perpendicular or/and parallel to the plane of beam path.

2.b.- Results and Discussions

Figure 1 shows the Raman spectra of the acrylic fiber obtained with AM and AV in parallel and perpendicular to the incident radiation beam in which identifies the variations due to the type of comonomer used in the preparation of the acrylic fiber . In region 1, 1500 to 2000cm^{-1}, the spectrum of the AV acrylic fiber has absorption bands, unlike the spectrum of the AM acrylic fiber which does not present band in this region. Region 2, about 1100cm^{-1}, presents a band, which, besides the difference in intensity of the band, shows a peak bifurcation for the AV fiber whereas for AM fiber, this band does not present bifurcation.

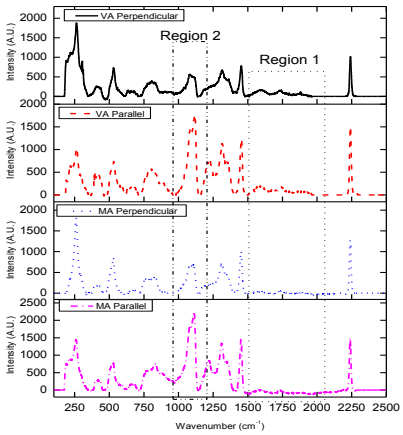

Fig. 5. Raman Spectrum of MA and VA acrylic fiber.

3. Conclusions

The identification of AV and MA comómeros used in the preparation of the acrylic fiber can be made using polarized Raman spectroscopy and setting the fibers in parallel and perpendicular to the incident radiation beam. When the spectrum is taken with the fibers perpendicular to the incident radiation beam, gives information about the functional groups in the branches of the chains, which are due to the comonomers present. When measurements are performed in parallel position to the incident radiation beam, get information about the functional groups of the polymer backbone.

MEXICAN OPTICS AND PHOTONICS MEETING
19 al 21 de septiembre del 2012
San Luis Potosí, México

Phase Diagram for Tin-Lead Soldering Irradiated With CO2 Laser

J. Mascorro-Pantoja [1,2], J.J. Soto-Bernal [2], M. Nieto-Pérez [1], R. González-Mota [2], I. Rosales-Candelas [2], A. Cardoza-Rodríguez [2]

1CICATA Querétaro. Cerro Blanco No. 141. Col. Colinas del Cimatario, Querétaro, Qro., México, C.P. 76090;
2Instituto Tecnológico de Aguascalientes, Av. A. López Mateos 1801 Ote, Aguascalientes, Ags., México, 20256.

ABSTRACT:

In recent years, laser beam welding has become an emerging welding technique; the use of laser in welding area is a high efficiency method. In this work is showed a phase diagram for tin-lead soldering irradiated with CO2 Laser. There is a direct relation between solder wire temperature and laser ratio and time interaction, considering the energy absorption of material, it is necessary so select a proper distance between laser beam and material to get optimal area of interaction and optical absorption graph.

Key words: Solder, laser, Phase diagram, absorption, heat.

REFERENCES AND LINKS

[1] Mashkov, P. Pencheva, T. Popov, D. Gyoch, B. Apparatus and Method for Soldering Electronic Components to Printed Circuit Boards

[2] Lyndell Kelly, Lynne Reid and Neal I. Walker Repair of Pig Dura in Vivo Using Temperature Controlled Co2 Laser Soldering

[3] R. Vanzetti, A.C. Traub Eliminating Electronic Component Stresses Through Controlled Laser Soldering

[4] Beckett, P.M. Fleming, A.R. Gilbert, J.M. Whitehead, D.G. Practical Application of Laser Soldering in Electronics Assembly

1. Introduction

The metals absorbs radiation in some parts of the electromagnetic spectrum, the amount of absorption depend directly on the wavelength, the amount of absorbing material in the radiation path and the absorption characteristic of that material at that wavelength[1].

The absorbance of the laser energy is defined by the percent of photonic energy transformed into the metal by converting to heat, versus energy reflected away. The absorption affect occurs when the electric field of a electromagnetic wave interacts with absorbing atoms in an oscillating dipole interaction, when the radiation is absorbed then the atoms is placed in an excited state, this process occurs only at resonant wavelengths, in this case a part of energy is dissipated as heat [1]. In this case the CO2 laser was used to irradiate a specific alloy No. 112 (ISO 9453:2006). The wavelength of 10600 nm produced by CO2 lasers is very absorptive in organic material like rosin used to deoxidize surfaces and flowing agent in solder process[2].

Heat Timing

As has just been implied, full power of the laser cannot be used. There is a practical limit of around 400 milliseconds of heating time for even the most ideal laser soldering applications because it takes time for all the surfaces to heat

the alloy to spread. Most point to point laser reflow applications will have laser on-time between 500 and 1500 milliseconds. The key features of lasers as a heating method is the non-contact, precision of location and amount of heat applied [3,4]. The controlling factors are: thermal load of components, mass of solder paste, distance to wet, joint geometry and thermal sensitivity

2. Phase diagram

2.a. Equations

Equation 1 describes energy absorptivity as a function of change in temperature over time when a certain amount of laser energy is applied to a particular metal.

$$A = \frac{\text{absorbed energy}}{\text{laser energy}} = \frac{\sum_i m_i c_{pi}}{P} \frac{\Delta T}{\Delta t} \qquad (1)$$

Where A is the absorptivity, m_i is the mass, and c_{pi} the specific heat of each heated component $_i$ (in case of solder paste each component used in the alloy), ΔT is the difference in temperature achieved over time Δt by introduction of power P.

2.b.- Figures

From equation 1, energy absorbance is directly proportional to specific heat c, which is measure of energy required to increase temperature of a given amount of material by one degree. Therefore the absorbance rate of laser energy at a given wavelength may differ one alloy to another.

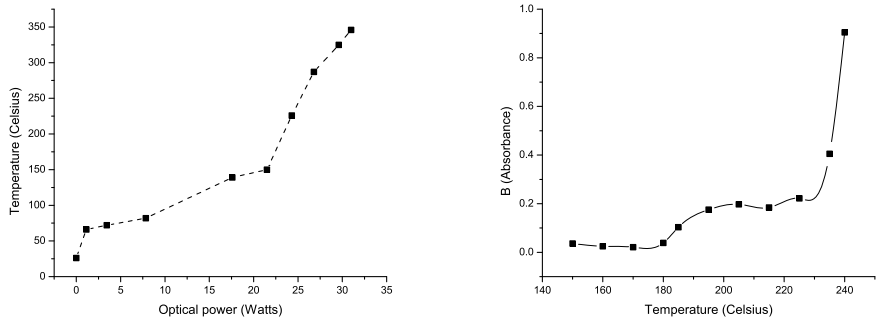

Fig.1. a) Temperature over optical power b) Temperature over absorbance.

The energy density distribution of laser beam generated remains uniform through the width of the spot regardless of its size. As consequence, laser energy is equally spread over the target area (Fig 1).

3. Conclusions

The product features that make laser heating an attractive option have been defined. Comparatively with other heating methods laser welding is a very efficient method which solve a product heating requirement. For those applications that can benefit from laser heating the remaining question is which type to use.

MEXICAN OPTICS AND PHOTONICS MEETING
19 al 21 de septiembre del 2012
San Luis Potosí, México

Reducing the impact of focus errors with multiple-frame photography

E. Yépez-Vidal, E. García-Almanza and Jorge Ojeda-Castañeda.

División de Ingeniería Campus Irapuato-Salamanca, Universidad de Guanajuato
Corresponding author email: jorge_ojedacastaneda@yahoo.com

ABSTRACT:

One can reduce the influence of focus errors, on the optical transfer function, by superimposing a series of snapshots taken with a conventional camera, which is axially displaced. Here, we analyse this optical technique as well as its relationship to the procedure of taking a single snapshot, with a camera that has an optical pre-processing mask.

Key words: Image synthesis, Image Processing, Extended Depth of Field.

REFERENCES AND LINKS

[1] M. Mino and Y. Okano, "Improvement in the OTF of a Defocused Optical System Through the Use of Shaded Apertures," Appl. Opt. 10, 2219-2225 (1971)

[2] J. Ojeda-Castañeda, L. R. Berriel-Valdos, and E. L. Montes,"Line-Spread Function Relatively Insensitive to Defocus," Opt. Lett. **8**, 458-460 (1983)

[3] J. Ojeda-Castañeda, E. Yépez-Vidal and E. García-Almanza, ñComplex Amplitude Filters for Extended Depth of Fieldò, Photonics Letters of Poland 2, 162-164 (2010)

[4] Gerd Haeusler, ñA method to increase the depth of focus by two step image processingò, Optics Communications, Vol. 6, 38-42 (1972)

1. Introduction

There are several techniques for extending the depth of field, of an optical system that uses noncoherent illumination [1-4]. These techniques usually have two stages. In the first stage, an optical system acquires one image or several images. At the second stage, the acquired images are manipulated for generating a final image. Typically, in the first stage, one acquires a single image with an optical system that employs a pre-processing mask [1-3]. However, several years ago, Hauesler has proposed to record several images, while moving axially the optical system [4].

Here we analyse the similarities and the differences between the technique that uses a series of snapshots, and the technique of taking a single snapshot.

2. Averaging the optical transfer function

For the sake of clarity, we consider a 1-D optical system, with a rectangular pupil aperture. If one considers that the generalized pupil aperture has a focus error term, then the optical transfer function (OTF) is

$$H(\mu;W) = rect\left[\frac{\mu}{4\Omega}\right]\left(1-\left|\frac{\mu}{\Omega}\right|\right) sinc\left[\left(1-\left|\frac{\mu}{\Omega}\right|\right) 4W\frac{\mu}{\Omega}\right] \qquad (1)$$

In Eq.(1), we dente as μ the spatial frequency. Its maximum value is the cut-off spatial frequency 2q . The letter W represents the focus error coefficient, in units of wavelength. Next, we define the average OTF as follows

$$\langle H(\mu)\rangle = \int_0^{W_{max}} H(\mu; W)\, dW = \frac{\Omega}{4\mu}\, Si\left[\frac{4\pi\mu}{\Omega}\left(1 - \left|\frac{\mu}{2\Omega}\right|\right) W_{max}\right]. \quad (2)$$

It is apparent from Eq.(2) that the average OTF is a non-monotonic curve.

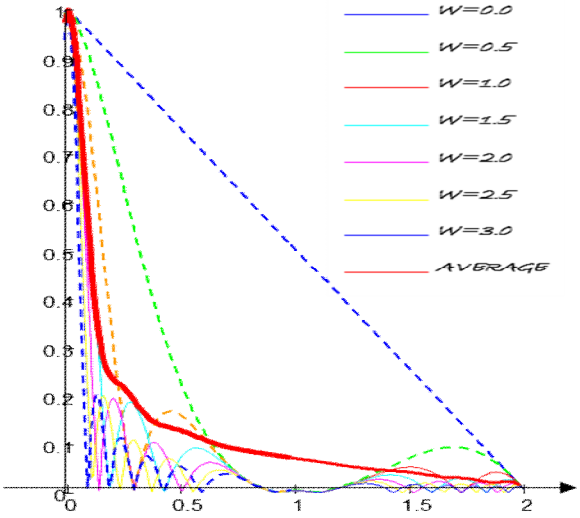

Figure 1 Average OTF in full line

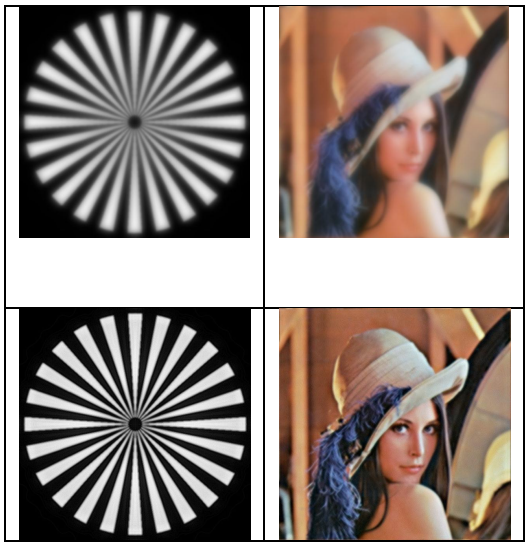

Figure 2 Final images

In Figure 1 we plot as broken lines several OTFs, with variable values of W. In full line, we plot the numerically evaluated average OTF. We note that the average OTF is non- monotonic curve. In reference 3, by using the least-squares method, we identify the following tendency MTF

$$|H(\mu)| = 0.4174\, e^{-0.0181\mu} + 0.6126\, e^{-0.1925\mu}. \quad (3)$$

This is a monotonic curve. Along line one, of Figure 2, we illustrate our numerical simulations, which result from averaging ten, out-of- focus images, with W_{max}ÒB. Along line two, of Figure 2, we show the final images of a single snapshot, with optical pre-processing and digital post-processing. It is apparent that the average image, along line one, exhibit a ñsoft-focusò effect, as expected from a non-monotonic curve.

3. Conclusions

On the one hand, by taking a series of snapshots, with conventional optics, one can obtain an average OTF. This later function is a non-monotonic curve. On the other hand, the single snapshot technique requires a pre-processing filter, as well as post-processing filters. It generates a tendency MTF that is monotonic curve.

MEXICAN OPTICS AND PHOTONICS MEETING
19 al 21 de septiembre del 2012
San Luis Potosí, México

Experimental synchronization between dragging force and glass rotation can explain astigmatic surface production?

Cordero Dávila Alberto [(1)]
Saldivia Gomez Elizabeth [(1)]
Carina Gutiérrez Ojeda [(1)]

1. Facultad de Ciencias Físico-Matemáticas, B.U.A.P 72570, Puebla pue.
201000388@fcfm.buap.mx
acordero@fcfm.buap.mx

ABSTRACT:
For grinding processes we measured the dragging force applied from a rotating glass to tool as a function of time. We found there is a synchronization between dragging force and glass rotation. This result is independent of the radial position and angular velocity of the tool, and then astigmatic surface production can be explained from this effect.

REFERENCES AND LINKS

[1] L. Tèllez- Arriaga, A. Cordero- Dávila, C. Robledo - Sanchez, and J. Cuautle - Cortés "Correction of the Preston equation for low speeds", Appl. Opt.46, 1408-1410 (2007)
[2] F. W. Preston, "theory and design of plates glass polishing machines," J. Soc. Glass Technol. 11,214-256 (1927).
[3] R .Resnick and D .Halliday " Fìsica ", parte 1 pp 110 (1980)
[4] E. Rabinowicz, "Stick and Slip," Sci.Am. 194,109-118 (1956).

1. Introduction

The grinding process is used to approximate the real to ideal surface within 5 microns. This is done by rubbing glass and tool, and between them it is deposited emery (aluminium oxide of 5 microns).
Preston [1] found that in grinding and polishing processes the total wear *h* is proportional to the work carried out for the frictional force between the glass disk and the tool (1).We measured dragging force (which is the sum of the frictional forces) for a rotating glass and we found this last is a periodic function. The periods of rotating glass and dragging force are equal ones independently of the rotating velocities of the glass and radial position of the tool.

2. Development

We used a glass disk of 30 cm in diameter placed, Figure 1, on a polishing machine (R. Howard Strasbaught Inc 6DE4). A tool of 4cm in diameter was used in dragging force experiment; measurements were made with a PASCO Scientific CI 6537 force sensor also, we used a water suspension of aluminium oxide of 5 microns, whose density was kept a constant value.
We measured the dragging force between glass and tool as a function of time for different relative speeds; this was done by changing the radial position of the tool center. Then a Fourier analysis was applied to each one of the obtained experimental results, from which fundamental frecuency was evaluated. In Fig 2 it is plotted experimental fundamental period of the dragging force vs period of the glass rotation; as you can see the in the slope of fitted line is equal to one. Therefore in all cases dragging force frecuency is kept a constant value equal to the glass frecuency

2.a. Equations

$$h = A\int_0^{\tau} \mu f n v dt \quad (1)$$

2.b.- Figures: Experimental Setup

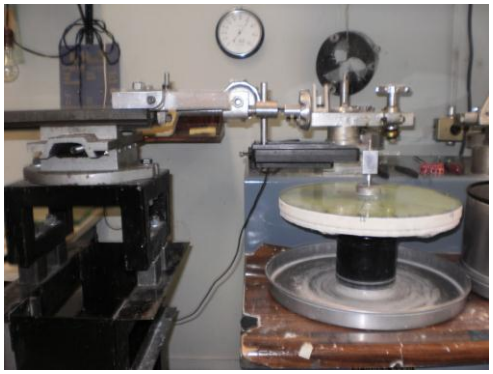

Fig1. System installed in the commercial polishing machine .

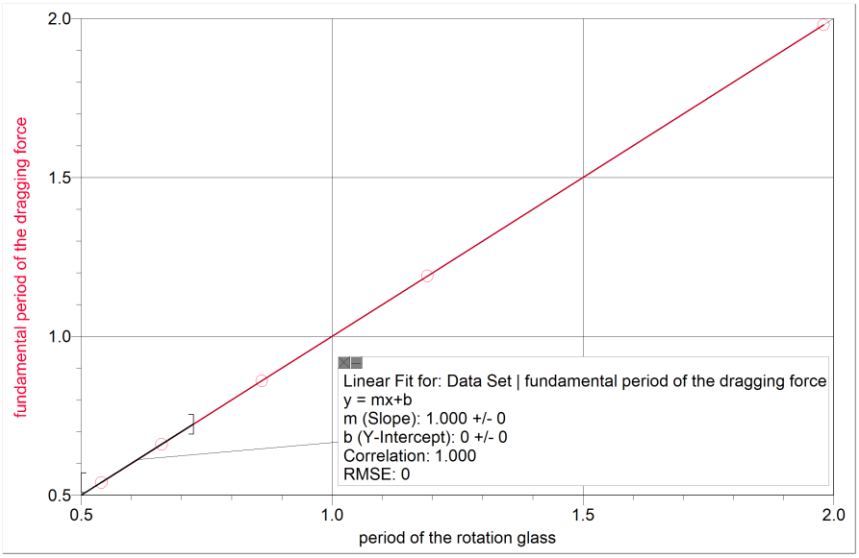

Fig 2. fundamental period of the dragging force vs the period of the rotating glass

3. Conclusions

In grinding process dragging force is a periodic function synchronized with glass rotation. This means that friction force is periodic too and then wear will be a function of the angular position. Therefore astisgmatic surfaces are produced in grinding process.

Acknowledgements

Thank the support staff of the optical testing laboratory of the Facultad de ciencias físico matemáticas, BUAP. and Dr Alberto Cordero Davila for his advice.

MEXICAN OPTICS AND PHOTONICS MEETING
19 al 21 de septiembre del 2012
San Luis Potosí, México

Evaluation of the principal radius of curvature of a convex surface with the null-screen method

Manuel Campos-García [(1)], Amílcar Estrada-Molina [(1)], Rufino Díaz-Uribe [(1)]

1. Centro de Ciencias Aplicadas y Desarrollo Tecnológico, Universidad Nacional Autónoma de México, Circuito Exterior S/N, Ciudad Universitaria, A. P. 70-186, Delegación Coyoacán, C.P. 04510, México D. F. Mexico
Corresponding author email: manuel.campos@ccadet.unam.mx

ABSTRACT:

The null-screen method has been used to test aspheric surfaces. This geometrical method measures the slope of the test surface and from these measurements it is possible to calculate the principal radius of curvature. Sagittal radius is obtained from the surface normals and the meridional radius is calculated from a function fitted to the derivative of the sagittal curvature.

Key words: Null screen, Optical testing, Aspherics, Surface measurements, Radius of curvature

REFERENCES AND LINKS

[1] R. Díaz-Uribe, M. Campos-García, "Null screen testing of fast convex aspheric surfaces", Appl. Opt. 39, 2670-2677 (2000).

[2] M. Campos-Garcia, R. Diaz-Uribe and F. Granados-Agustın, "Testing fast aspheric con- vex surfaces with a linear array of sources," Appl. Opt. 43(34), 6255-6264 (2004).

1. Introduction

In a previous work [1], we proposed a null screen method to test fast aspheric convex surfaces. The method consists of drawing a set of spots on a cylinder in such a way that by reflection on the test surface, the image consists of a perfect pattern of radial or square arrangement of circles or lines, as long as the test surface is perfect. Here the whole surface is tested at once.This method measures the shape of the test surface from slope measurements.

2. Radius of curvature from normals data

To calculate the surface normals $\mathbf{N}= (n_x, n_y, n_z)$ on each point on the test surface, we perform a three-dimensional ray trace to find the direction of the reflected $\mathbf{r}_r$ and the incident ray $\mathbf{r}_i$ [2]. From reflection law, the surface normal **N** can be obtained according to

$$\mathbf{N} = \mathbf{r}_r - \mathbf{r}_i , \tag{1}$$

From the normals measurements the sagittal radius of curvature can be obtained from

$$r_{sag} = -\left(x^2 + y^2\right)^{1/2} \left\{ x^2 + y^2 + \left(x\frac{n_x}{n_z} + y\frac{n_y}{n_z} \right)^2 \right\}^{1/2} \Big/ \left(x\frac{n_x}{n_z} + y\frac{n_y}{n_z} \right), \tag{2}$$

And the meridional radius of curvature is calculated from

$$r_{mer} = r_{sag} + \frac{\left\{r^2 - k\left(x^2 + y^2\right)\right\}^{3/2}}{k\left(x^2 + y^2\right)}, \tag{3}$$

where r is the vertex radius of curvature, k is the conic constant, and can be obtained by fitting

$$\eta \equiv \left(\frac{n_x}{n_z}\right)^2 + \left(\frac{n_y}{n_z}\right)^2 = \frac{x^2 + y^2}{\left\{r^2 - (k+1)\left(x^2 + y^2\right)\right\}^{1/2}}, \tag{4}$$

Eqs. (2) and (3) shows that from measurements of the normal to the test surface we can calculate the principal radius curvature. In Fig. 1 we show the principal radius of curvature of the steel ball (r = 6.375 mm) against the radial distance. The variations of the principal radiuses around the design radius of curvature value r are evident.

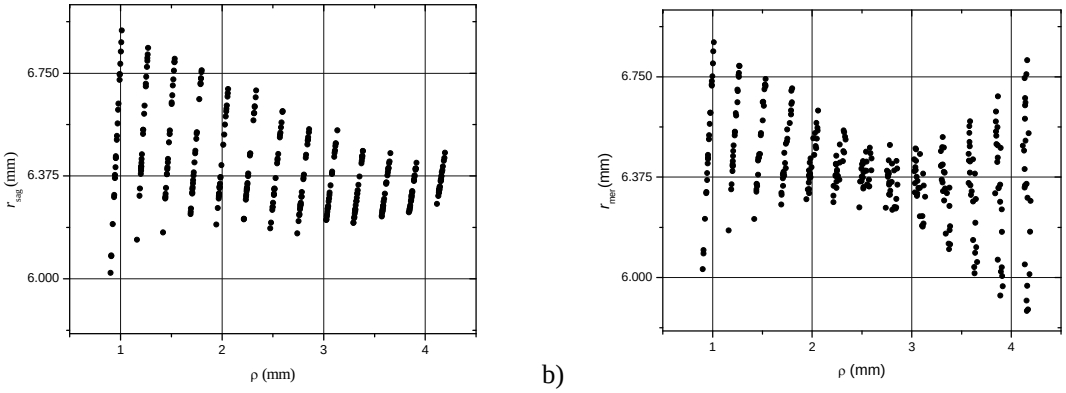

a) b)

Fig.1. a) Sagittal, and b) Meridional radius of curvature of the steel ball against the radial distance.

3. Conclusions

We have proposed a procedure to compute the principal radius of curvature for a convex surface. Sagittal radius was calculated with the data raw from the surface normal. In order to reduce the numerical errors in the evaluation of the meridional radius we proposed fit an analytic function to the derivative of the sagittal radius instead of performing the numerical derivative of the sagittal radius directly.

Acknowledgements

This research was supported by the Dirección General de Asuntos del Personal Académico, Universidad Nacional Autónoma de México (DGAPA-UNAM) under project Programa de Apoyo a Proyectos de Investigación e Inovación Tecnológica (PAPIIT) no. IN114110-2 and no. IT101912.

MEXICAN OPTICS AND PHOTONICS MEETING
19 al 21 de septiembre del 2012
San Luis Potosí, México

Ronchi-test visibility as a function of illumination source size and duty cycle of the ruling.

Alberto Cordero Dávila [(1)], Javier Álvarez Jiménez [(2)]

1. Benemérita Universidad Autónoma de Puebla
2. Benemérita Universidad Autónoma de Puebla

acordero@fcfm.buap.mx
200718756@alumnos.fcfm.buap.mx

ABSTRACT:

We report visibility of ronchigrams (computed with exact tracing), as a function of two variables: linear source size and duty cycle. We started from a computer program used to simulate ronchigrams with point source at any position [1] and a cosinusoidal ruling [2] for analyzing the wave front reflected on a spherical mirror. The program was modified in order to include a linear source, oriented along transversal direction of the ruling lines. We also simulate the case in which the ruling was placed after the linear extended source. We show the graph of visibility as a function of the size source and the duty cycle of the Ronchi-ruling.

Key words: Ronchi-test, visibility, duty cycle.

REFERENCES AND LINKS

[1] Cordero-Dávila A., [Dificultades de la aplicación del método de mínimos cuadrados en la evaluación tradicional de interferogramas], PhD Thesis, (Instituto Nacional de Astrofísica, Óptica y Electrónica, México, 1991)

[2] Kantún-Montiel J. R., [Estimación del error en una superficie óptica mediante simulación de ronchigramas con una rejilla cosenoidal, splines cúbicos y algoritmos genéticos], Masters Thesis, (Benemérita Universidad Autonoma de Puebla, México, 2011)

---

1. Introduction

Experimentally, it is well known that by placing a ruling in front of the light extended source the ronchigram visibility increases. We have used a computer program to calculate the visibility of ronchigrams simulated with an extended linear source and with/without ruling in front of this.

2. Numerical simulation

In Figure 1a they are shown graphs of visibility vs. size of the linear source for several periods of the Ronchi ruling. It can be seen that the drop speed of the visibility, υ, depends on ruling period. Nevertheless, if we use the period of the ruling as measure unity for the source size L, then the entire visibility graphs match, as you can see in Figure 1b.

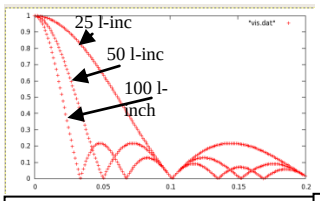

Figure 1a. Graphs of visibility as a function of source size for rulings with 25, 50 and 100 lines per inch.

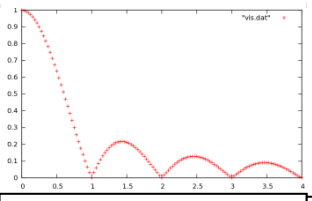

Figure 1b. Graph of visibility as a function of source size measured in one ruling period unities.

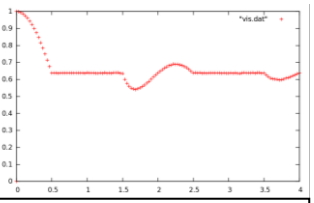

Figure 1c. Graph of visibility as a function of source size, case with ruling after the source.

It was added to the computer program the option of include the ruling immediately after the source. This Ronchi ruling had the same period and orientation than test ruling. In Figure 1c it is shown a graph of υ as a function of L, we can see that visibility improves substantially, which reproduces experimental results.

We will use the known variable:

$$dc = \frac{ab}{T} \tag{1}$$

where ab and T correspond to the transparent width and to the period of Ronchi ruling respectively.

By placing punctual sources at the center of transparent areas of illumination ruling, dc=0, we obtained visibility 1. Therefore it is equivalent to place a punctual source at the center of the illuminated area of the ruling to place some sources at the centers of transparent areas of the ruling, with the difference that the intensity is increased.

We calculate υ vs. Source size (L) and duty cycle (dc). In figure 2 it is shown the respective plot.

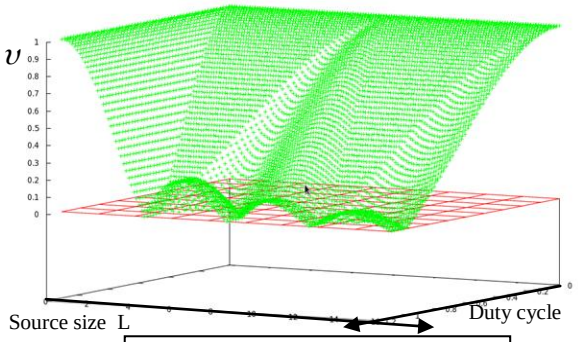

Figure 2. Graph of L, dc and V.

We can see from Figure 2 that visibility improves in two situations: when the size of the source is small and when dc tends to cero, however en the second case some intensity is lost.

3. Conclusions

In this work we obtained, from the geometrical point of view, an analysis of the visibility vs. linear source size and duty cycle of the Ronchi ruling. Then it can be calculated the visibility of any ronchigram for any linear source size and any duty cycle.

MEXICAN OPTICS AND PHOTONICS MEETING
19 al 21 de septiembre del 2012
San Luis Potosí, México

Generation of spiral optical vortices in a Mach-Zehnder interferometer

Areli Montes-Pérez [(1)], Gustavo Rodríguez-Zurita [(2)], Cruz Meneses-Fabián[(2)], Carlos Robledo-Sánchez [(2)], Amalia Martínez-García [(1)], Noel-Ivan Toto-Arellano[(2)]

1. Centro de Investigaciones en Optica A.C. Léon, Gto.
2. Benemérita Universidad Autónoma de Puebla, Facultad de Físico-Matemáticas
Corresponding author email: ylehra@hotmail.com

ABSTRACT:

In the field of interferometry, there is a property related with optical vortices, which is the subject of this paper, is the possibility of obtaining interference patterns that have information about the sign of the phase. This information is recognizable in the direction of the rotation of the spiral strips in the neighborhood of the vortex. The spiral strips are the result of the superposition of a wavefront with vortices and a spherical wave. In this paper, we show the experimental and numerical results of the generation of optical vortices with a SLM (spatial light modulator) in a Mach-Zehnder interferometer.

Key words: Interferometry, phase spirals, phase modulators, spatial light modulators, optical vortices.

REFERENCES AND LINKS

[1] S. R. Cooper, D. W. Tomkins, and M. Petty, *Surface-relief diffraction gratings recorded by multiple-beam coherent phase exposure,* Optics Letters, **22**, 357-359 (1997)
[2] Khonina S. N., Kotlyar V. V., Shinkaryev M. V., Soifer V. A. and Uspleniev G. V., *The phase rotor filter, J. Mod. Opt.,* **39,** 1147–1154 (1992)

1. Introduction

The problem of the formation of optical vortices has been subject of research during the last 25 years [1], due to their wide scope of applicability in the generation of microscopic regions of null intensity, with a random phase for the enclosure of non-charged bodies, in order to use these kind of regions as “optical tramps” or “optical pincers” to manipulate them [1].

The Laguerre-Gaussian modes can be created with a spiral phase plate (SPP) created with holograms appropriately with a spatial light modulator (SLM). The hologram generates a common lattice with a dislocation. If it is hit with a laser beam, the hologram generates optical vortices with a topological charge that increases with the diffraction order. The zeroth-order is purely Gaussian and the vortices have an opposite topological charge on one side or the other of the zeroth-order. The number of dislocations is directly related with the topological charge of the first order of diffraction. As is usual in holography, instead of using an amplitude lattice, a phase lattice is used, the efficiency is increased. The SLM are optoelectronic devices that can create dynamic vortices, sets of vortices or other

types of beams. Thus, it is possible to generate spiral optical phase vortices in a Mach-Zehnder interferometer using the field that is the result of the interference of a vortex wave and a spherical wave, which conserves the phase sign.

2. Experimental results

In Figure 1, the experimental Mach-Zehnder scheme is shown, as well as the experimental results of the spiral-type optical vortices.

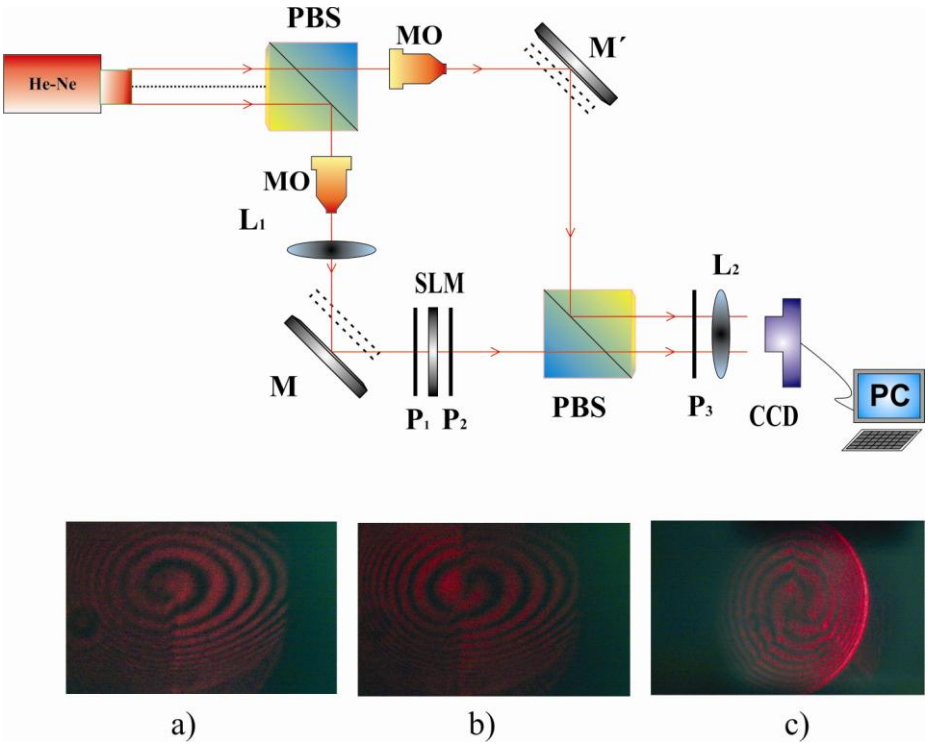

Fig.1. Experimental setup. PBS: polarizing geamspliter, MO: microscope objective, P_1 ,P_2, $P_{3:\ polarizer's,}$ SLM: spatial light modulator, L_1, L_2: lens, CCD: camera color digital. Vortex a) first order, b) second order and c) third order.

3. Conclusions

The experimental method is presented in order to generate optical phase vortices of the field that is the result of the interference of a vortex wave and a spherical wave, showing the phase signs in the structure of the spiral vortices. These interference patterns present this phase sign, opening the possibility of the elimination of the ambiguity of the interferometry in conventional beams. In this context, it is possible to define an optical system with a central vortex impulse effect. This can be done with an azimuthal-phase variation pupil.

Acknowledgements

Author AMP grateful ocucupies a postdoctoral position at CIO and G. Rodriguez Zurita and C. Robledo Sánchez is also acknowledged.

MEXICAN OPTICS AND PHOTONICS MEETING
19 al 21 de septiembre del 2012
San Luis Potosí, México

Visual interface in LabVIEW for measurement of stokes parameter in scalar and vector field.

Gildardo-Pablo Lemus-Alonso, Cruz Meneses-Fabian, Rosaura Kantun-Montiel

Benemérita Universidad Autónoma de Puebla, Facultad de Ciencias Físico Matemáticas (México)
Corresponding author email: cmeneses@fcfm.buap.mx

Abstract
In this work an ellipsometer for measuring the polarization state of a scalar and vector optical field is discussed. It is developed in LabVIEW programming language, and it is based on measuring the Stokes parameters of full field. Because of this the polarization state can be measured in each point of the optical field and so it is possible to measure the polarization state of a vectorial field. Experimental results of measurement in several optical fields are shown.

Key words: Measuring polarization, ellipsometer, Stokes Parameter.

References

[1].- Harland G. Tompkins, William A. McGahan; Spectroscopic Ellipsometry and Reflectometry; John Wiley & Sons, (1999).
[2].- Harland G. Tompkins, A user's guide to Ellipsometry; Academic Press,(1993).
[3].- R.Azzam, N.Bashara, Ellipsometry and polarized light; Oxford, (1977).
[4].- E.Hetch, Óptica, Addison Wesley 3a Edición (2000).
[5].- http://www.ni.com/labview/whatis/esa/

Introduction
It is known that the polarization is a property of transverse waves that describes the orientation of their oscillations, which is described by the amplitudes relation and their phase difference between the field components, they are described mathematically

$$E_x = E_{0x} e^{i(kz-\omega t)}, \tag{1}$$

$$E_y = \left(E_{0y} e^{i\alpha}\right) e^{i(kz-\omega t)}, \tag{2}$$

where E_{0x} , E_{0y} are the amplitudes of components x and y respectively, and α is phase difference between them, with the above, we can deduce the equation of a curve that it does not depend of position and time, this is

$$\left(\frac{E_x}{E_{0x}}\right)^2 + \left(\frac{E_y}{E_{0y}}\right)^2 - 2\left(\frac{E_x}{E_{0x}}\right)\left(\frac{E_y}{E_{0y}}\right)\cos(\alpha) = \sin^2(\alpha), \tag{3}$$

it is known like the general equation of the polarization ellipse, with an inclination angle ψ given by

$$\tan 2\psi = \frac{2E_{0x}E_{0y}}{{E_{0x}}^2 - {E_{0y}}^2}\cos\alpha, \tag{4}$$

and with an ellipticity angle ε

$$\sin 2\varepsilon = \frac{2E_{0x}E_{0y}}{E_{0x}^2 + E_{0y}^2}\sin\alpha\,. \tag{5}$$

There are two types of ellipsometer, the annulment and photometric ellipsometer. The first consists in rotating lenses that modifies the polarizer and analyzer angles until finding a null angle. The second is based directly on measurement of the light intensity [1-4].
Sir George Gabriel Stokes[4] proposed a method for determining the polarization state of a beam, based in the fact that the polarization can be described in terms of experimental observations in the irradiance of the optical field. These observations are known as the Stokes parameters, which are given by:

$$\begin{aligned} S_0 &= \mathrm{I} = I(0°) + I(90°) = \mathrm{E}_{0x}^2 + \mathrm{E}_{0y}^2 \\ S_1 &= \mathrm{Q} = I(0°) - I(90°) = \mathrm{E}_{0x}^2 - \mathrm{E}_{0y}^2 \\ S_2 &= \mathrm{U} = I(45°) - I(-45°) = 2\mathrm{E}_{0x}\mathrm{E}_{0y}\cos\varepsilon \\ S_3 &= \mathrm{V} = I_{\frac{\pi}{2}}(45°) - I_{\frac{\pi}{2}}(-45°) = 2\mathrm{E}_{0x}\mathrm{E}_{0y}\sin\varepsilon \end{aligned} \quad , \tag{6}$$

where the parameter I is the total intensity of the field and the valor of parameter Q, U and V determinate the coordinates of a point on the Poincaré sphere and this is associated with the polarization state.

The ellipsometer is constructed using the mathematics of the Stokes parameters and with the help of LabView. We were chosen LabVIEW platform because is a comprehensive development environment that provides scientists and engineers unprecedented hardware integration and broad compatibility [5]. It is also possible using this programming environment automate the measurement of the polarization state through the use of servomotors in some optical devices.

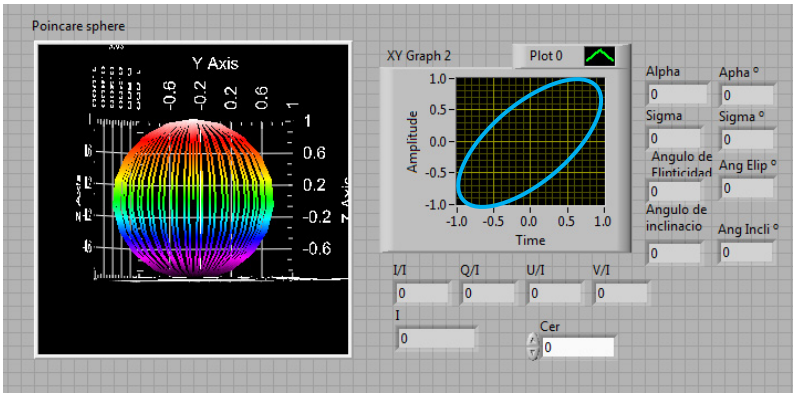

Fig. 1.- Interface Visual programmed in LabVIEW

MEXICAN OPTICS AND PHOTONICS MEETING
19 al 21 de septiembre del 2012
San Luis Potosí, México

Phase-shift interferometry for optical elements characterization

Rosaura Kantun-Montiel, Cruz Meneses-Fabian, Gildardo-Pablo Lemus-Alonso

Benemérita Universidad Autónoma de Puebla, Facultad de Ciencias Físico Matemáticas (México)
Corresponding author email: cmeneses@fcfm.buap.mx

Abstract

A characterization of typical optical elements in polarimetry by using a two aperture common-path interferometry is presented. In the input plane of the interferometer two apertures are considered, where one is left free assisting as a reference and in the other a test object is placed assisting a prove beam. The evaluation in phase of this object is carried out by phase-shifting interferometry, which is achieved by translation of Ronchi ruling at Fourier plane of the interferometer. Some test object such as polarizers, retarders, neutral density filters, among others, are considered. In this work, theoretical analysis and experimental results are shown.

REFERENCES

[1] V. Arrizón and D. Sánchez-de-la-Llave, "Common-path interferometry with one-dimensional periodic filters", Opt. Lett. 29, 141(2004)

[2] C. Meneses-Fabian, G. Rodriguez-Zurita, and V. Arrizon, "Optical tomography of transparent objects with phase-shifting interferometry and stepwise-shifted Ronchi ruling", J.Opt. Soc. Am. A 23, 298 (2006)

[3] Bruning J. H. "Digital Wavefront Measuring Interferometer for Testing Optical Surfaces and Lenses", Appl. Opt. **13**, 2693-2703 (1974).

[4] Horst Schreiber y John H. Bruning, "Phase Shifting Interferometry", en Optical Shop Testing, D. Malacara, ed., Wiley, New York, 1992, pp. 547-656.

[5]Carre´ P. '' Installation et utilisation du comparateur photoe´lectrigue et Interferentiel du Bureau International des Poids ek Measures,'' Metrologia, 1, 13-23 (1966).

A two-aperture common-path interferometer (TACPI) [1,2], as shown in Figure 1, consists of two apertures in the object plane and a grating in the Fourier plane. The object under test is placed in the B window serving as a test beam, while the A window is keep free of obstacles serving as a reference beam. Note that in general the test and reference beams travel together through the same optical elements, resulting to be very high stable to mechanical vibration. If a linearly polarized monochromatic beam traveling on the z direction with a plane wavefront illuminates this system, the optical transmittance function leaving of the windows is described by

$$t_A(x,y) = w_A(x+\frac{1}{2}x_0,y)A_1(x+\frac{1}{2}x_0,y) + w_B(x-\frac{1}{2}x_0,y)A_2(x-\frac{1}{2}x_0,y)e^{i\phi(x-\frac{1}{2}x_0,y)} \quad (1)$$

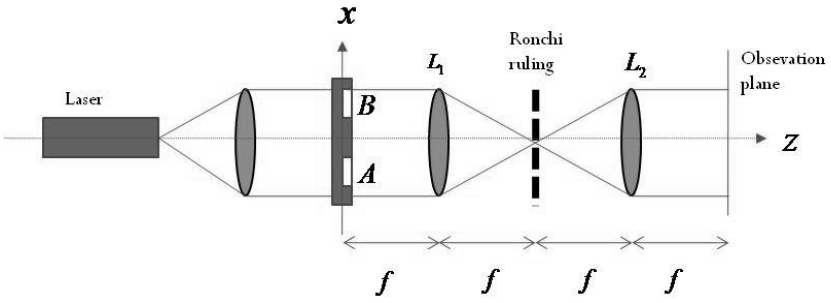

Figure 1. Two aperture common path interferometer array

when $w(x,y)$ is a window function in the input plane and $\phi(x,y)$ is the object phase. By adjusting the separation of the windows x_0 with the separation of diffraction orders $\lambda f / u_p$ at the image plane, which is

due to the grating, with fill factor of 1/2, in the Fourier plane, $x_0 = \lambda f / u_p$, where λ is the wavelength of the light used, f is the focal length of the lenses and u_p is the ruling period, the interference effect from the windows A and B can be successfully carried out. For the orders 0 and +1 from the windows w_A and w_B respectively, it can be proved that [2-4]

$$I(x, y, \alpha_k) = I'(x, y) + I''(x, y)\cos[\phi(x, y) + \alpha_k], \tag{2}$$

where $I' = A_1^2/4 + A_2^2/\pi^2$ is the background light, $I'' = A_1 A_2/\pi$ is the modulation light, and $\alpha_k = 2\pi k \Delta u_d / u_p$ is phase step, where $u_d = k\Delta u_d$ is the transversal displacement of Ronchi ruling in the Fourier plane, with k=0,…, N-1, and N indicates the number of steps. In order to evaluate the phase step and phase object, a modification of Carré algorithm [5] is used for four equal displacements with $k = 0,1,2,3$, we have

$$2\cos\Delta\alpha = \frac{I_2 - I_3}{I_1 - I_2} + \frac{I_0 - I_1}{I_1 - I_2} \tag{3}$$

$$2\sin\Delta\alpha\cot(\phi + \frac{3}{2}\Delta\alpha) = \frac{I_2 - I_3}{I_1 - I_2} - \frac{I_0 - I_1}{I_1 - I_2} \tag{4}$$

We have developed a computer program under Labview platform in order to assess the optical components quality (polarizers, retarders, filters, amplitude, etc.) that have been used in the laboratory to create and measure different polarization states.

As a first object, we have evaluated a solid polymer film retarding the value of delay between components is indicated is $\lambda/4$. In the experimental array we used a Ronchi ruling with period of 2000 lines per inch, a wavelength of 532nm, the focal distance L_1 and L_2 are of 40cm and 30cm, respectively. At first place, the computer program shots the interferogram images without test object in the B window, after four phase shifts are obtained, the obtained phase is called "reference phase" as shown in Figure 2a. At second place, the object under test is placed at the B window and then four interferograms shifted in phase are captured, the phase object and reference phase are retrieval and as it is showed in Figure 2b. At third place, the subtraction of phases computed in two back cases is realized in order to obtain phase object under test, which is shown in Figure 2.c. These phase representation founds corresponds to retarder oriented at a transmission axis, for recovering the delay value should be found the phase difference between the two transmission axes.

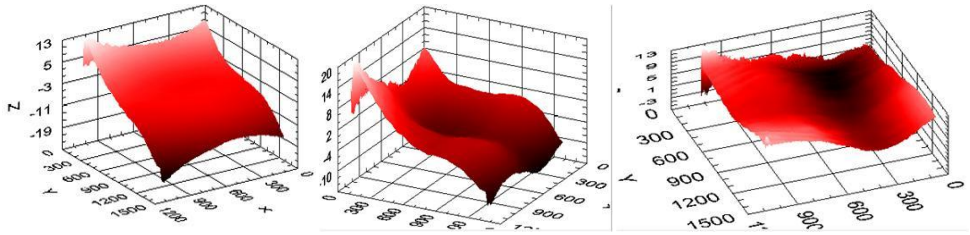

a) b) c)

Figure2.a) reference phase obtained, b) object phase obtained c) object pure phase of retarder film.

The phase that we are looking is the one shown in Figure 2c, it is necessary to clarify that it is analyzing only a retarding film region of $1.6\times1.6cm$. It is clear to note that the analyzed retarded have a very low quality because it is not introducing a space constant phase. The phase variations go from -1.7π to 3.9π being very large and undesirable differences.

The phases spatial changes have been found in the optical components analyzed are an important source of error in creating and measuring homogeneous polarization states. In this work also discusses, polarizing and neutral density filters of amplitude.

MEXICAN OPTICS AND PHOTONICS MEETING
19 al 21 de septiembre del 2012
San Luis Potosí, México

Approximate determination of the maximum power stored in Stokes lines generated in silica fibers

L. de la Cruz-May*[1], J. A. Álvarez-Chávez[2], M. May-Alarcón[1], F. Méndez[1], M.L. Estrella-Rosas[1], M. J. Vázquez-López[1], P. Mollinedo[1],

[1]Universidad Autónoma del Carmen, Facultad de Ingeniería, Av. Central S/N, Fracc. Mundo Maya, C.P. 24115, Ciudad del Carmen, Campeche México.

[2]Centro de Investigación e Innovación Tecnológica del IPN, Cerrada CECATI S/N Col. Sta. Catarina, C.P. 02250, México D.F. México.

*ldelacruz@pampano.unacar.mx

ABSTRACT:

This work presents a methodology for estimating the maximum power stored in 1, 2,..., N-orders Stokes. The analysis of the solution of the equations that governing the stimulated Raman scattering has been fundamental in the development of a novel mathematical relationship, which estimates with great approximation the maximum power stored in Stokes lines.

Key words: fiber optics, Raman effect, Raman amplifiers, Raman fiber lasers

REFERENCES AND LINKS

[1] G. P. Agrawal, *Nonlinear Fiber Optics*, Elsevier Academic Press, San Diego, (2007).

[2] A. S. Kurkov, E. M. Dianov, V. M. Paramonov. et. al., "High-power fibre Raman lasers emitting in the 1.22–1.34-μm range", *Quantum Electron*. **30**, 791-793 (2000).

[3] J. AuYeung, A. Yariv, "Theory of cw Raman oscillation in optical fibers", *J. Opt. Soc. Am*., **69**, 803-807, (1979).

[4] L. de la Cruz-May, J.A. Álvarez-Chávez, E.B. Mejía, A. Flores-Gil, F. Méndez-Martínez, S. Wabnitz, "Raman threshold for nth-order cascade Raman amplification", *Opt. Fiber Technol*., **17**, 214-217, (2011).

1. Introduction

The Raman scattering is a nonlinear effect that occurs when a monochromatic light beam propagates along the optical fiber, the majority of the beam power is transmitted without change, but a small quantity (typically 10^{-6}) is scattered with a new frequency (Stokes component) [1]. The SRS in the spectral region from 1.1-1.7 μm is of great importance in developing of several applications such as optical fiber communications, materials processing, signal processing, laser spectroscopy and medicine [2]. Equations for the behaviour of the Raman amplification have been described [1], [3] and solutions have been proposed [3], [4]. Despite these advances, there are parameters such as maximum power stored in the Stokes signals that have not been described.

2. Theory

To find an equation that provides an approximate measure of the maximum power stored in the Stokes lines, we find the Raman threshold for first Stokes. Consequently, we find the Raman threshold for the second Stokes. Both results are related to a constant number ~16, we take this number to obtain equality between the two equations, which leads to a new equation which determines approximately the scaling of the Raman gain coefficient given by[4];

$$g_{r2} = \frac{\lambda_P}{\lambda_S}\frac{L_{eff}}{L_{eff\,2}}\frac{A_{eff\,2}}{A_{eff}}g_r \qquad (1)$$

Where L_{eff}, L_{eff2}, λ_p, λ_s, and A_{eff}, A_{eff2} are: effective fiber lengths, wavelengths, and effective areas for the pump and first Stokes, respectively. Under physical considerations and taking into account the equation (1), we deduce an equation that estimates the pumping power required for the signal reaches the maximum value of storage given by:

$$30 \approx \frac{g_r}{A_{eff}} P_{Max}^{1} L_{eff} \tag{2}$$

The mathematical relationship is generalized in order to predict the maximum power stored in N-order Stokes before generating the N+1-order Stokes line.

$$P_{0N}^{Max} \approx 30 \frac{A_{eff}}{g_r L_{eff}} [1 + \frac{\lambda_S}{\lambda_{S1}} + \frac{\lambda_{S2}}{\lambda_{S3}} + ... + \frac{\lambda_{N-1}}{\lambda_N}] \tag{3}$$

Where P_{0N}^{Max} represents the maximum power stored in N-order Stokes. λ_s is the wavelength of the first Stokes.

2. Results

The mathematical equation developed is subject to rigorous experimental tests using a LEAF fiber. The experimental configuration used is versatile and known as free running because there is no feedback. We used an ytterbium laser operating at 1064nm, the beam emitted by is coupled to the LEAF fiber, at the output end of the fiber is placed a power meter to calculate the average power transmitted, and an optical spectrum analyzer for determining the shape of the spectrum. With these data are prepared figures showing the maximum power stored in the output signals.

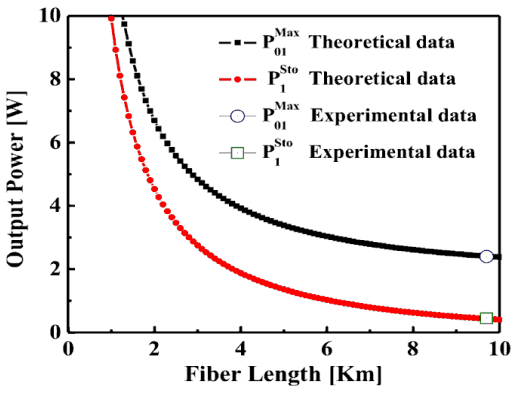

Figure 1. Comparison of numerical simulations with two experimental points.

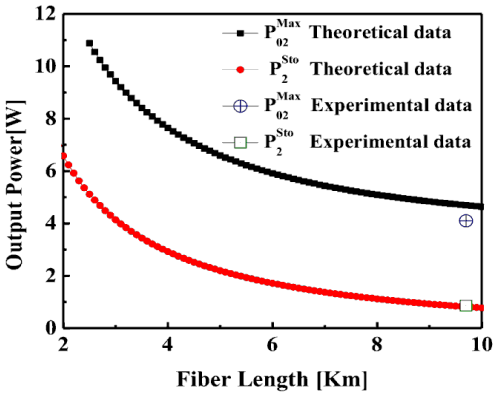

Figure 2. Maximum output power curves versus fiber length.

The numerical simulations are tested experimentally for 9.6 km LEAF fiber. The theoretical maximum pumping powers for the first and second Stokes are 2.43 W and 4.6 W, while experimentally are 2.4 W and 4.1 W, respectively. The proximity of these results proof the consistency of the mathematical formula here proposed.

3. Conclusions

An equation to predict the pumping power for maximum energy stored in the first, second and subsequent Stokes, to the best of our knowledge has not been reported. There is a strong correspondence between the simulated and experimental values for the first Stokes, however, that for the second Stokes the error in estimating the maximum power is 9%. The equation reported here is a powerful tool for designing efficient Raman lasers and amplifiers.

Acknowledgements

We thank the UNACAR widely through the project DAIT/2012/09.

MEXICAN OPTICS AND PHOTONICS MEETING
19 al 21 de septiembre del 2012
San Luis Potosí, México

All-fiber modal interferometer based on a single fiber taper

G. Salceda-Delgado, A. Martinez-Rios, D. Monzon-Hernandez

Centro de Investigaciones en Optica A. C., Loma del Bosque 115, col. Lomas del Campestre, Leon, Gto. 37150, Mexico
Corresponding author email: salceda@cio.mx

ABSTRACT:

The fabrication and characterization of a single taper optical fiber interferometer is presented. The taper has a fixed 10µm waist diameter and the spectrum transmission characteristics of the interferometer (visibility, period and losses) can be tailored by the proper selection of the fiber taper profile during the fabrication. The fabrication process is highly repeatable and only takes few minutes. All these characteristics make this device very attractive for optical fiber sensor technology.

Key words: Optical fiber devices, fiber taper fabrication, coupling modes, modal interferometer

REFERENCES AND LINKS

[1]. J. M. López-Higuera, ed., *Handbook of Optical Fiber Sensing Technology* (Wiley, 2002).

[2] Rui Yang, Yong-Sen Yu, Yang Xue, Chao Chen, Qi-Dai Chen, and Hong-Bo Sun, "Refractive index sensing based on Mach-Zender interferometer formed by three cascaded single-mode fiber tapers", APPLIED OPTICS / Vol. 50, No. 11 / 10 April 2011

[3] T. A. Eftimov and W. J. Brock, J. Lightwave Technol. 11, 2150 (1993).

1. Introduction

Fiber optic interferometer structures have recently been intensively studied since they exhibit extraordinary qualities for sensing [1]. They have been successfully used to measure physical, chemical or biological parameters, such as temperature, strain, refractive index (RI), gas phase concentrations, etc., due to their high resolution, high sensitivity, fast response, good stability, and repeatability [2]. These structures are attractive to the sensor community for several reasons, including small size and deployment flexibility, as well as the presence of a reduced thermal sensitivity in view of the usually small difference of the thermo-optic coefficients of the fiber modes of concern [3].

2. Optical fiber modal interferometer

2.a. Fabrication and working principle of the modal interferometer

We use a processor glass system "Vytran" model GPX-3400 to fabricate the tapers. This computerized system used the well-known heating and pulling process to produce a taper. The system allows us to control the fiber taper shape (Fig. 1), in particular, the two taper transitions and the waist. The working mechanism of the interferometer can be described as follows: in the down-taper transition the fundamental core mode is coupled to the higher order modes of the tapered fiber, this modes will propagates along the taper waist where they will acquire a phase delay difference, at the up-taper transition the higher order modes will be coupled to the fundamental core modes where they will be interfere producing a wavelength modulated spectrum.

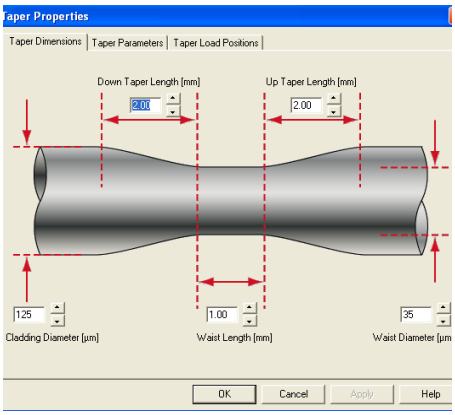

Figure 1. The computer window where the user can select the optical fiber taper profile parameters: down and up taper length, initial cladding and final waist diameter, and waist length.

2.b.- Results

Some results are summarized in the figure 2 where we can appreciate that the visibility and period of the interference pattern increases when the taper transition length decreases.

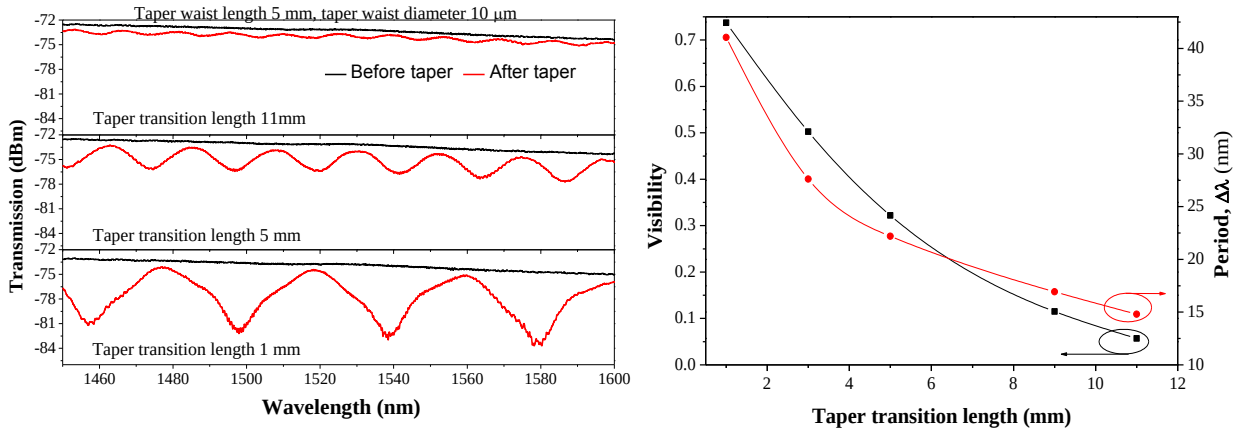

Figure 2. (Left) Optical fiber transmission before (black line) and after (red line) tapering. The taper waist length and diameter of all the samples were 5 mm and 10 µm, respectively, and the taper transitions length was 11 mm (top), 5 mm (middle), and 1 mm (bottom). (Rigth) Effect of the taper transition length on the visibility and period of the interference fringe.

3. Conclusions

In conclusion we demonstrated the fabrication of an optical fiber modal interferometer using a single fiber taper. The proper selection of the taper parameters allows us to control the characteristics of the transmitted interference pattern. The unique characteristics of this device can be used to construct novel sensors or comb filters for one particular application.

Acknowledgements

G. Salceda-Delgado would like to thank Consejo Nacional de Ciencia y Tecnologia (CONACYT) for the scholarship granted to him.

MEXICAN OPTICS AND PHOTONICS MEETING
19 al 21 de septiembre del 2012
San Luis Potosí, México

Objects recognition by using identity vectors signatures

Claudia Fimbres-Castro[(1)], Josué Álvarez-Borrego[(2)]

Universidad Autónoma de Baja California[1],Centro de Investigación Científica y de Educación Superior de Ensenada[2]
Corresponding author: josue@cicece.mx

ABSTRACT:
In this work we present a new methodology to recognize objects by using identity vectors signatures (I_s) obtained for both the target and the problem image. In this application, (I_s) is obtained by means of a simplification of the main features of the original image in addition of the properties of the Fourier transform. Identity vectors signatures are compared using a nonlinear correlation. This new methodology recognizes objects with a confidence level above 95.4% and it has a low computational cost.
Key words: Image recognition, nonlinear correlation, rings mask, one-dimensional signatures, Fourier transform.

REFERENCES AND LINKS

[1] A.V. Lugt, "Signal detection by complex spatial filtering," *IEEE Trans. Inf. Theory*. 10(2), 139-145 (1964).
[2] D. Casasent, A. Iyer and G. Ravichandran, "Circular-harmonic function, minimum average correlation energy filters," *Appl. Opt*. 30(35), 5169-5175 (1991).
[3] S. Solorza and J. Álvarez-Borrego, "Digital system of invariant correlation to position and rotation," *Opt. Commun*. 283(19), 3613-3630 (2010).
[4] J. Álvarez-Borrego and E.J. Fájer-Ávila. "Identification of Platyhelminth parasites of the Wild Bullseye Pufferfish (Sphoeroides annulatus) using an invariant digital color correlation," *Rev. Biol. Mar. Oceanogr.* 41(1): 129-139 (2006).
[5] S. Solorza , J. Álvarez-Borrego. "System of digital invariant correlation to rotation applied to identify car models," *Digital Scientifica and Technological Journal, e-Gnosis* . ISSN 1665-5745 (2009).
[6] J. Lerma-Aragón, J. Álvarez-Borrego. "Vectorial signatures for invariant recognition of position, rotation and scale pattern recognition." *JMO*. 56: 1598-1606. (2009).
[7] A. Coronel-Beltrán, J. Álvarez-Borrego. "Comparative analysis between different font types and styles letters using a nonlinear invariant digital correlation," *JMO.* 57(1): 58-64. (2010).
[8] B.V.K Vijaya-Kumar, L. Hassebrook . "Performance measures for correlation filters," *Appl. Opt.* 29: 2997–3006. (1990).

1. Introduction.

Pattern recognition is an expanding field in optical and computer research since the first appearance of the classical matched filter [1]. In recent years, different methods have been proposed for objects identification which have been used in several areas where the main objective of these methods is the correct identification regardless of the image variations may occur [2-7]. In this work we present a new method to recognize objects by using identity vectors signatures which is used to recognize radiolarians, but it can be used for the recognition of other objects.

2. Methodology.

The procedure used in this work uses the original image statistical properties as well as the Fourier transform properties and provides a significant reduction of the image information of size *m x n* to one-dimensional vector of 1 *x 256* consequently with low computational cost.

Identity vectors signatures are compared using a k-law nonlinear correlation.

2.a. Identity vectors signatures.

First, the image to be recognized is denoted by $f(x,y)$. In the step 1, a vector of 256 elements is created and denoted by $h(m)$, which represents the values in grayscale of the image with a range of values from 0 to 255 (histogram). Thus, when the vector $h(m)$ is created, the rotation invariance is obtained. Then, in step 2, the identity vector is calculated by

$$id_{vec}(m) = \frac{h(m)}{pixel_{num}} \cdot m \ , \tag{1}$$

where $pixel_{num}$ is the number of pixels of the object, in this step the scale invariance is obtained. Then, the modulus of Fourier transform is calculated in order to obtain the identity vector signature which is denoted by I_S and it is obtained as (step3)

$$I_S(w) = \left| \Im\{id_{vec}(m)\} \right| \ , \tag{2}$$

where $\Im$ represents the Fourier transform of the function id_{vec} and |*| represents the modulus.

2.b. Nonlinear correlation.

A nonlinear correlation between the target and the problem image is used. In general a nonlinear filter is defined by [8]

$$NF = \left|F(u,v)\right|^k e^{-i\varphi(u,v)}, \quad 0<k<1, \tag{3}$$

where $|F(u,v)|$ represents the modulus value of the Fourier transform of the image, k is the nonlinear strength factor that takes values between zero and one and $\varphi(u,v)$ is the phase of the Fourier transform. We can manipulate the discriminate capacities of the nonlinear processor changing the k values in this interval and therefore determine the best k of the nonlinear filter. In this system k=0.3 was used.

3. Results.

To evaluate the performance of this digital system, 20 test images of different species of radiolarians were used. The results in all the cases presented a confidence level of at least 95.4% . In terms of computational cost, this new methodology takes about 0.02 s per image.

4. Conclusion.

The results show that identity vectors and their respective signatures are an efficiently methodology to identify objects and provide the necessary information to identify the object despite the significant reduction of information. This methodology has a confidence level of at least 95.4% and it has a low computational cost.

Acknowledgement

This document is based on work partially supported by CONACyT under Grant No. 102007. Claudia Fimbres-Castro is a student in the PhD program MYDCI offered by Universidad Autónoma de Baja California and supported by CONACyT's scholarship.

MEXICAN OPTICS AND PHOTONICS MEETING
19 al 21 de septiembre del 2012
San Luis Potosí, México

Nonlinear correlation by using vectorial signatures to recognize objects embedded in inhomogeneous illumination

Claudia Fimbres-Castro[1], Josué Álvarez-Borrego[2]

Universidad Autónoma de Baja California[1],Centro de Investigación Científica y de Educación Superior de Ensenada[2]
Corresponding autor: josue@cicece.mx

ABSTRACT:
In this work a nonlinear correlation methodology to recognize objects is presented. Vectorial signatures are obtained through several mathematical transformations such as Scale and Fourier transform. Vectorial signatures in addition to being invariant to position, rotation and scale, they are tested in environments with inhomogeneous illumination. In this application, vectorial signatures are compared using nonlinear correlations. This new methodology recognizes objects with a confidence level above 95.4% and it has a low computational cost.
Key words: Object recognition, nonlinear correlation, vectorial signatures, inhomogeneous illumination

REFERENCES AND LINKS

[1] S. Solorza , J. Álvarez-Borrego. "System of digital invariant correlation to rotation applied to identify car models," *Digital Scientifica and Technological Journal, e-Gnosis* . ISSN 1665-5745 (2009).

[2] J. Lerma-Aragón, J. Álvarez-Borrego. "Vectorial signatures for invariant recognition of position, rotation and scale pattern recognition." *JMO*. 56: 1598-1606. (2009).

[3] A. Coronel-Beltrán, J. Álvarez-Borrego. "Comparative analysis between different font types and styles letters using a nonlinear invariant digital correlation," *JMO.* 57(1): 58-64. (2010).

[4] M.A. Bueno-Ibarra, M.C. Chávez-Sánchez and Josué Álvarez-Borrego," K-law spectral signature correlation algorithm to identify white spot syndrome virus in shrimp tissues". *Aquaculture* ,318: 283-289 pp. (2011).

[5] G. Cristóbal, L. Cohen, "Image filtering and denoising through the scale transform" , *International Symposium on Time-Frequency and Time-Scale Analysis, Proceedings of the IEEE-SP* , 617–620. (1998).

[6] B.V.K Vijaya-Kumar, L. Hassebrook . "Performance measures for correlation filters," *Appl. Opt.* 29: 2997–3006. (1990).

1. Introduction.

Object recognition systems have emerged for identifying of distorted objects, e.g. the object can be rotated, scaled, immersed in a noise background and so on [1-4]. Furthermore, some works are focused on decrease of the computational cost. In this work, we use vectorial signatures as a tool of identification when the image has an inhomogeneous illumination. The system was tested with 10 different species of fossils diatoms but it can be used for the recognition of other objects.

2. Methodology.

This digital system has a low computational cost to achieve a significant reduction of processed information by using vectorial signatures. The invariant vectorial signatures are obtained from the information from both the target image as well as problem image. In this way, each image has its rotational and scale vectorial signature obtained through several mathematical transformations such as scale and Fourier transform. In addition, this method uses the great capacities from the non-linear filters to discriminate between similar objects. Vectorial signatures are compared using non-linear correlation.

2. a. Nonlinear correlation by using vectorial signatures

Figure 1 shows the algorithm used in this work. Step 1 and 2 follow the methodology described in Lerma-Aragón and Álvarez-Borrego[2]. This system is invariant to position, rotation and scale. The scale transform is given by [5]

$$D(c_\lambda, c_\theta) = \frac{1}{\sqrt{2\pi}} \int_0^\infty \int_0^{2\pi} e^{\lambda/2} f(\lambda, \theta) e^{\left[-j(\lambda c_\lambda + \theta c_\theta)\right]} d\lambda\, d\theta \quad , \tag{1}$$

where $\lambda = \ln r$ (r is the radial coordinate).

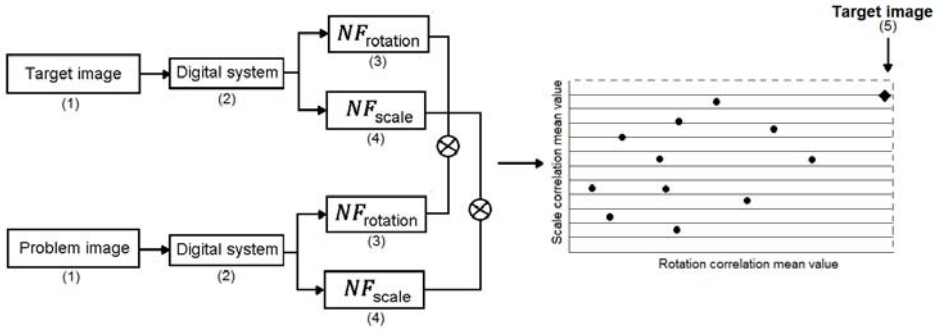

Figure 1. Output bidimensional correlation plane.

A nonlinear correlation between the target and the problem image is used. In general a nonlinear filter is defined by [6]

$$NF = |F(u,v)|^k e^{-i\varphi(u,v)}, \quad 0<k<1, \tag{2}$$

where $|F(u,v)|$ represents the modulus value of the Fourier transform of the image, k is the nonlinear strength factor that takes values between zero and one and $\varphi(u,v)$ is the phase of the Fourier transform. $k=0.3$ was used.

2. b. Inhomogeneous illumination

To evaluate the performance of the digital system, 10 different kind of fossil diatoms were used. Each one of the 10 different species of diatoms was exposed to 9 different ways of variations in the illumination (inhomogeneous). Figure 2 shows an example of the variations in the inhomogeneous illumination of the diatom called *Actinocyclus ingens*. In addition, each variation was rotated 180 deg in increments of 1deg and scaled from 75% to 125% in increments of 1%. Each species of diatom has 2079 variations. An image bank of 20790 was obtained.

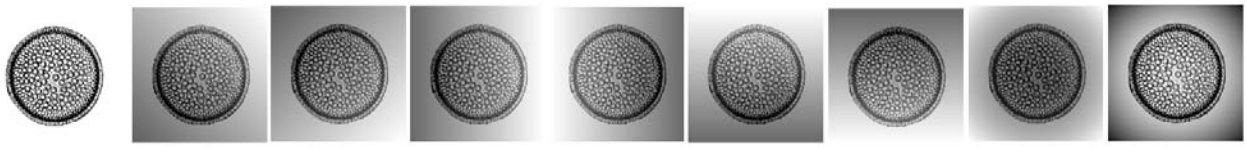

Figure 2. Variations in the inhomogeneous illumination (9 different ways).

3. Results.

To evaluate the performance of this digital system, 10 test images of different species of diatoms were used. The results in all the cases presented a confidence level of at least 95.4% (results are not shown).

4. Conclusion.

The results show that vectorial signatures can be recognized even if the image has different ways of variations in illumination. This methodology has a confidence level of at least 95.4% and it has a low computational cost.

Acknowledgement. This document is based on work partially supported by CONACyT under Grant No. 102007. Claudia Fimbres-Castro is a student in the PhD program MYDCI offered by Universidad Autónoma de Baja California and supported by CONACyT's scholarship.

MEXICAN OPTICS AND PHOTONICS MEETING
19 al 21 de septiembre del 2012
San Luis Potosí, México

Invariant correlation using a binary mask applied to binary and gray images

Josué Álvarez-Borrego[(1)], Selene-Solorza[(2)], Mario Alonso Bueno-Ibarra[(3)]

Centro de Investigación Científica y de Educación Superior de Ensenada[1], Universidad Autónoma de Baja California[(2)], Instituto Politécnico Nacional[(3)]
Corresponding author: josue@cicece.mx

ABSTRACT:

More alternative ways to generate the binary ring masks are studied and a new methodology is presented when in the analysis the image come with some distortion due to rotation. This new algorithm requires low computational cost. Signature vectors of the target so like signature vectors of the object to be recognized in the problem image are obtained using a binary ring mask constructed in accordance with the real or the imaginary part of their Fourier transform analyzing two different conditions in each one. In this manner, each image target or problem image will have four unique binary ring masks. The four ways are analyzed and the best is chosen. In addition, due to any image with rotation include some distortion, the best transect is chosen in the Fourier plane in order to obtain the best signature through the different ways to obtain the binary mask. This methodology is applied to two cases: to identify different types of alphabetic letters in Arial font and to identify different fossil diatoms images. Considering the great similarity between diatom images the results obtained are excellent.

Key words: Spectral image recognition, nonlinear correlation, binary masks.

REFERENCES AND LINKS

[1] S. Solorza, J. Álvarez-Borrego, Digital system of invariant correlation to position and rotation. Optics Communication 283, (2010), pp. 3613-3630.

1. Introduction

Recently, a digital system of invariant correlation to position and rotation was presented [1]. In that methodology a binary ring mask was constructed using the real part of the Fourier transform of the reference image. Different image sets were compared, for example different alphabetical Arial font letters and different species of diatoms using these binary masks and nonlinear correlations. However, in their paper they gave a small review of different correlation systems invariants to rotation and position [1].

In this paper we studied more alternative ways to generate the binary ring masks and we present a new methodology when in the analysis the image come with some distortion due to rotation.

2. Methodology

2.a The signature of the image

The objective is identifying a specific target no matter the position or the angle of rotation presented on the same plane. In order to have an invariance rotation we used the binary mask (step 1 in Fig. 1a). So, the modulus of the Fourier transform of the image is multiplied by the binary mask to sampling the frequencies pattern of the object (steps 2 and 3 in Fig. 1a). Finally, the modulus of the Fourier transform in each ring is summed and then assigned to the corresponding ring index to obtain the signature of the image (step 4 in Fig. 1a). The first ring begins from the

center of the image in Figure 1a (step 3). Figure 1b shows the comparison of the four signatures of the image when four different ways for calculating the binary mask are used.

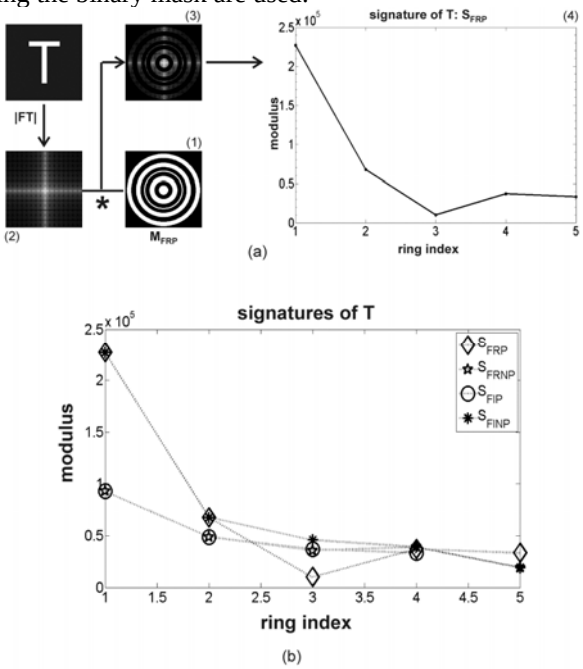

Fig. 1 Different four signatures obtained from the image T.

3. Results.

As a first step we analyze alphabet letters (binary images) and like a second step we used real images (diatoms). Anyway the method can be tested using any kind of images. If we consider the results presented in [1], we will analyze the nonlinear correlation results only. The mean value ± 2SE (two standard error) was calculated and outliers values were considered in the analysis. We can obtain a better result for the letter analysis when the real part of the Fourier transform is used. When the diatoms were analyzed good results were obtained using any of the four different ways for calculating the binary mask.

4. Conclusion.

In this deeper analysis, we find four different ways to obtain the binary mask. Binary images (letters) and gray real images (diatoms) were analyzed in order to know the best way to go in the correlation process. Nonlinear filters were used. In all the cases, composite filters f_{10} and f_{18} were used and they had the best performance with α =0.1-1.0 . In addition, using the f_{10} composite filter we have a less cost computational. In the particular examples presented in this paper, the correlation digital system shows an excellent performance, a confidence level of 95.4% or greater.

Acknowledgement
This document is based on work partially supported by CONACyT under Grant No. 102007 and 169174.

MEXICAN OPTICS AND PHOTONICS MEETING
19 al 21 de septiembre del 2012
San Luis Potosí, México

Design of Digital Odometer Using Optical Sensors for Uses in Teaching Automotive Mechanics

Gilberto Sánchez Mares[(1)], Norman Andrés Herrera Hernández[(1)]

1. Universidad Politécnica de Aguascalientes

e-mail: gilberto_gsm@hotmail.com, norman_andres09@hotmail.com

ABSTRACT:

The odometer is a device that indicates the distance traveled by car or other vehicle. The automobiles that use digital odometers employ a metal toothed wheel which is installed at the transmission output and a magnetic sensor gets a boost each time through one of the metal teeth of the wheel. In this article we´ll discuss about the design of a digital odometer for to be used in the automotive mechanics laboratories of the Universidad Politécnica de Aguascalientes.

Key words: Automotive Mechanic, Control Stage, Digital Odometer, Optical Sensors.

REFERENCES AND LINKS

[1] L. Casanova, *Medición de Distancias*, Artech House, Boston (1999).

[2] G. A. Londoñon, "Prototipo PIG intelligent", *Universidad Nacional Manizales.* 7-8 (2003).

[3] http://www.tefesur.com/fichas/sensores.pdf

1. Introduction

The odometer is a device that indicates the distance traveled by car or other vehicle. The odometers have long to exist in its mechanical form, and recently, digital devices have begun to replace them because are quick and easy to use [1]. Since the modern digital to the oldest have a very similar principle: a wheel rolls activating a series of gears that calculates the distance travelled [2].

In older cars, the odometers could only indicate up to value of 99, 999; in the early days of the automotive industry this was adequate. With continuous improvements, modern vehicles now survive to travel several hundreds of thousands of miles/kilometres. In 100.000 the odometer would restart from zero, this is known as odometer "rollover". New cars have odometers that can indicate to a value of 999,999 [3].

2. Development

2.a. Sensing Section

Include a board with optical sensors CNY70, the Opamp 358N and the 10kΩ potentiometers are to vary the sensitivity (Fig. 1).

The wheel have black and white section for the sensing, where the optical sensor detect forward or backward.

2.b. Control Stage

In this stage the PIC 18f542 is used for programing and LCD screen, which displays the forward or reverse (Fig. 2).

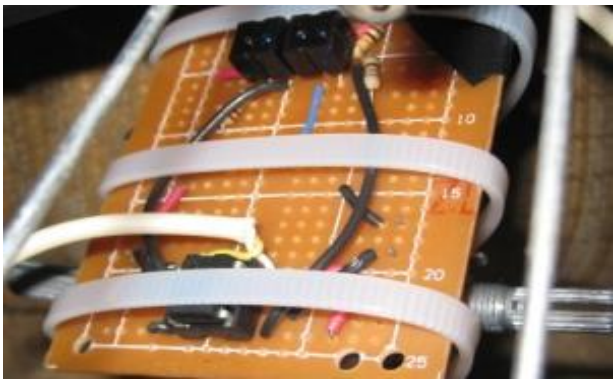

Fig.1. Sensing Section.

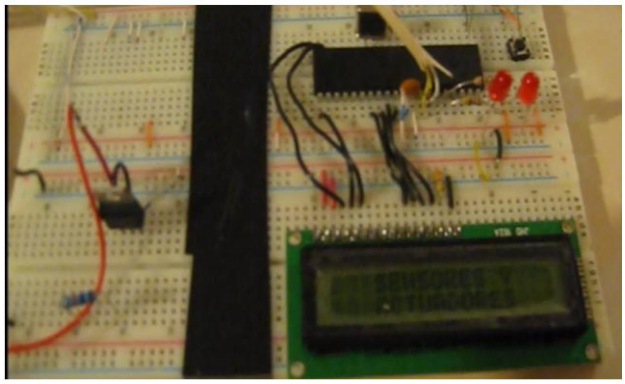

Fig.2. Control Stage.

2. Results

Once the sensing circuit placed in the tire, start working, pulses to the PIC, which due to its programming will tell us which way will the wheel; the way in which we can see the order as the sensor are activated, may be observed in the LEDs Section. This made possible the separation attached to the rim, all symmetrically arranged around the same for them once they turn in a certain order the LEDs will tell us whether it increases or decreases (Fig. 3) and this distance measurement is displayed on the LCD screen (Fig. 3 and 4).

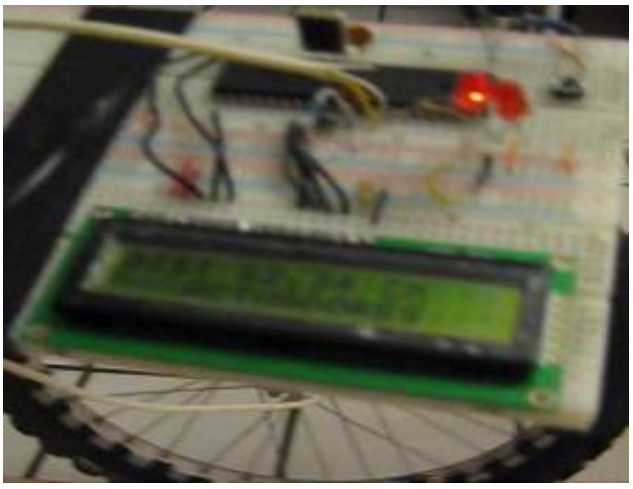

Fig.3. LED indicating the decrease and LCD showing values.

Fig.4. Distance measured in one meter with an error of 5.24.

4. Conclusions

The design and the successful use of a digital odometer to form part in automotive mechanical engineering teaching is the first pass to create a new laboratory, with the finality of continue building a variety of digital devices used by cars and with low cost.

MEXICAN OPTICS AND PHOTONICS MEETING
19 al 21 de septiembre del 2012
San Luis Potosí, México

CHARACTERIZATION OF THE SENSITIVITY OF FIBER BRAGG GRATINGS BY TEMPERATURE CHANGES.

M. May-Alarcón *(1), W. A. Silva-Martínez (1), J. A. Cobá Ramos (1), F. Méndez-Martínez (1), L. de la Cruz-May (1), R.A. Vázquez-Sánchez (2), H.H. Cerecedo-Núñez (3),

1. Universidad Autónoma del Carmen
2. Universidad de Ciencias y Artes de Chiapas. UNICACH
3. Universidad Veracruzana, UV

*mmay@pampano.unacar.mx,

ABSTRACT:

In this paper is presented the characterization of fiber Bragg gratings subjected to temperature changes, in order to study their behavior as sensors of all-fiber type. To characterize the sensitivity of the fiber Bragg grating is used the amplified spontaneous emission from an Optical Fiber Laser and reflection from the fiber Bragg grating, which is near to the wavelength of 1548.85nm and represents the point of maximum reflectivity, at the time that we change the temperature to the fiber Bragg grating we found a movement of the wavelength and is use to determine the sensitivity of the grating to changes in temperature. This paper presents the results of submit a fiber Bragg grating at different temperatures found a sensitivity of 12.5 pm/°C which is within the parameters reported in the literature.

Keywords: Fiber Sensors; Temperature changes; Fiber Bragg gratings; Fiber laser.

REFERENCES AND LINKS

[1] A. Ping ZHANG, Shaorui GAO, Guofeng YAN and Yinbing BAI. Advances in Optical Fiber Bragg Grating Sensor Technologies, Photonic Sensors (2012) Vol. 2, No. 1: 1–13

[2] S. A. Babin, A. A. Vlasov, and I. S. Fiber-Optic Sensors Based on Bragg Gratings, High Energy Chem. B., 2008, Vol. 42, No. 7, pp. 535–537

[3] H.H. Cerecedo-Núñez, L.A. Zenteno-Sánchez. Caracterización de rejillas de Bragg en fibra óptica, Rev. Mex. Fis. B., 45 (4) (2009), pp.364-369.

[4] Raman Kashyap. Fiber Bragg Gratings, Second Edition, USA. Academic Press (2009) pp. 444-445.

1. Introduction

An important property of the fibers is the photo sensitivity [1] or the inherent ability to change its refractive index by the action of UV radiation. This effect makes possible to construct a light control device directly into the fiber core; an example is the Fiber Bragg Grating (FBG), which has a structure with periodic refractive index [2]. FBG based sensors take advantage of the properties provided by fiber optics, which are: low transmission loss, immunity to electromagnetic interference, electrical insulation and low weight. These characteristics make them attractive for use in harsh environments where electrical currents could be dangerous. Furthermore, the intrinsic advantage of the FBG itself must also be considered as high signal to noise, compact size, high linearity, high sensitivity, and immunity to electromagnetic fields, low noise (resulting from the encoding of information in the wavelength domain). In this paper is presented the characterization of FBG subjected to changes in temperature, in order to study their behavior as sensors of any fiber type. The basic principle used in this system is to register the displacement of the Bragg

wavelength reflected by the FBG with temperature changes, so the measurement is encoded in terms of wavelength, which is not affected parameter by changes in the intensity of radiation, characteristic which makes these sensors useful in remote measurements. In this work using the Optical Fiber Laser [3] as a source of amplified spontaneous emission (ASE), thus determine the point of maximum reflectivity, also called Bragg wavelength and determining the spectral shift can be characterized the sensitivity of the Bragg grating to be used for other experimental tests, for determinate de sensitivity of the FBG this equation [4] is used.

$$Sensitivity = \Delta\lambda_B / \Delta T \quad \textbf{(1)}$$

Where, $\Delta\lambda_B$ = Wavelength change,

ΔT = Temperature change.

2. Results

At a temperature of 26 °C the ASE has a valley to the wavelength of 1548.8 nm as shown in Figure 1, this point represents the maximum reflectivity, as it was by changing the temperature showed a spatial displacement of this point. In Figure 2, we see the ASE spectrum for each of the experimental measurements which were performed to compare the different wavelengths and its temperature as it show in the Optical Spectrum Analyzer in the range of 1548.6 nm to 1550 nm. Based in these shifting produced by temperature changes and using the equation (1) the sensitivity of the FBG is 12.5 pm/°C

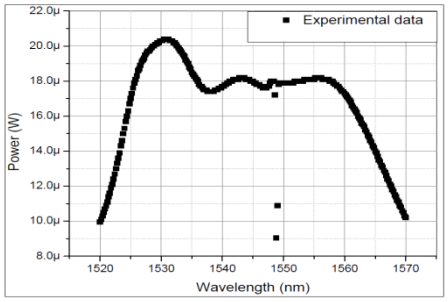

Figure 1. Amplified spontaneous emission spectrum at room temperature, where valley at 1548.8 nm is shown.

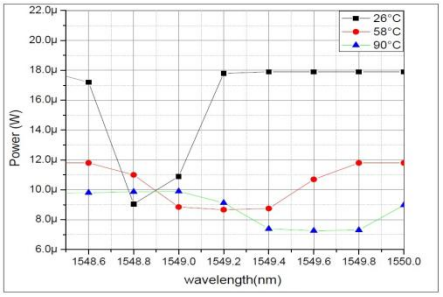

Figure 2. Amplified spontaneous emission spectrum for different temperatures

3. Conclusions

This paper presents the results of subjecting a Fiber Bragg grating at different temperatures and register the displacement of the Bragg wavelength, the temperature was changed with a Peltier device and was able to preserve stable for better measurement. A measure of the sensitivity of the FBG consistent with that reported in the literature was obtained.

Acknowledgements

Walter Ariel Silva Martínez and Jesús Alberto Cobá Ramos were supported by grant number 256855 and 256856 CONACyT respectively.

MEXICAN OPTICS AND PHOTONICS MEETING
19 al 21 de septiembre del 2012
San Luis Potosí, México

Dynamic Phase Profile of phase objects

N.I. Toto-Arellano [1], D. I. Serrano-García [2], A. Martínez-García[2], G. Rodríguez-Zurita[3], A. Montes-Pérez[3], J. M. Miranda-Gómez[1], G. Resendiz-López[1], A. González Rosas[1] and L. García Lechuga[1]

1. División de Fotónica, Área de Electromecánica Industrial de la de la Universidad Tecnológica de Tulancingo
2. Centro de Investigaciones en Óptica A.C.
3. Posgrado en Óptica de la Benemérita Universidad Autónoma de Puebla

ivantotoarellano@hotmail.com

ABSTRACT

This communication describes some details of modulation of polarization which are useful in phase-shifting interferometry applied to the study of phase objects. As an application, the case of a two-beam phase-grating interferometer is discussed on the grounds of polarization analysis as an example. This system does not use a double window, and generates two beams whose separation can be varied according to the characteristics of the grid used. Experimental results are also given.

Key words: Interferometry, Phase shifting, Polarization, Phase objects

REFERENCES AND LINKS

[1] M. Novak, J. Millerd, N. Brock, M. North-Morris, J. Hayes and J. Wyant, Analysis of a micropolarizer array-based simultaneous phase-shifting interferometer *Appl. Opt.* **44**, 6861-6868(2005)

[2] G Rodriguez-Zurita, N-I Toto-Arellano, C Meneses-Fabian, et al 2009 Adjustable lateral-shear single-shot phase-shifting interferometry for moving phase distributions *Meas. Sci. Technol.* **20** 115902.

1. Introduction

In this paper, we propose a Quasi Common-Path Interferometer based on a Mach Zehnder (MZ) configuration using simultaneous phase shifting interferometry modulated by polarization that shows insensitivity against external vibration. Due to the fact that an MZ system is capable of obtaining two beams, it can be used to implement a quasi-common path interferometer that allows the measurement of dynamic events with high accuracy. The configuration presented does not require items such as micro-polarizers [1], but only conventional polarizers, nor does it need additional software to eliminate noise caused by vibration, as the two beam interferometer is stable. Unlike previously proposed interferometers [2], this system does not use a double window (which should also have a separation x0 given by the characteristics of the grid used), but it generates two beams whose separation can be varied according to the characteristics of the grid used to obtain the interference patterns. A combination of a quarter-wave plate Q and a linear polarizing filter P_0 generates linearly polarized light oriented at ±45° entering the MZ system from a YVO_3 laser operating at 532 nm (see figure 1). This configuration generates two symmetrically displaced beams by moving mirrors *M* and *M*', enabling one to change the spacing x_0 between the beam centers. Retardation plates with mutually orthogonal fast axes (Q_L and Q_R) are placed in front of beams to generate left and right nearly-circular polarized light respectively. The transparent sample is collocated on B, and A is used as a reference beam. A phase grid carefully constructed by superposing two commercially available phase gratings with their respective grating vectors at ±90° is placed at the system's Fourier planes as the pupil. As shown in figure 1, placing a grating of spatial period $d=\lambda f/x_0$ on the Fourier plane, the corresponding transmittance is given by $G(\mu,\upsilon)$.The image $O'(x,y)$ formed by the system consists basically of replications of each window at distances X_0;

that is, the convolution of $O(x,y)$ with the Fourier transform of the phase grating. By selecting the diffraction term of order qr, after placing a linear polarizing filter with the transmission axis at an angle ψ, P_ψ, its irradiance results as being proportional to [2]

$$I = \left[\left(J_q J_r\right)^2 + \left(J_{q+1} J_r\right)^2 + 2 J_q J_r^{\,2} J_{q+1} \cdot \cos\left[2\cdot\psi - \phi(x',y')\right]\right] \tag{1}$$

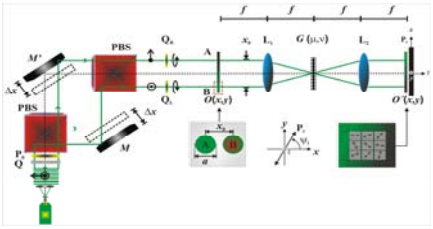

Figure 1. Simultaneous phase shifting quasi-common path interferometer with modulation of polarization.

2. 2-D Interference patterns generated by diffraction.

The interference patterns are obtained from the interference between the replicas of each beam, centered around each diffraction order. Figure 2(a) presents the replicas of beam **A,** with right circular polarization**,** and the replicas of beam **B ,** with left circular polarization; each order is superposed depending on separation x_0 of the beams at the output of the MZ system. Figure 2(b) presents the interference pattern generated by the interference of contiguous orders.

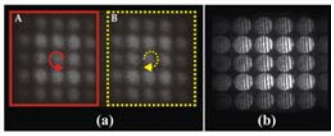

Figure 2. (a) Replicas of beams A and B. (b) Interference pattern

3. Experimental results

In order to automate image capture and process the phase, we developed a program called Dynamic Phase V.1 using Labview 8.5. Figure 4 shows the DynamicPhase V.1 platform based on a Labview structure. The program allows dynamic phase measurements by imaging the four shifted interferograms in a single capture. In this case, we present the temporal phase evolution of a thin flame candle. These results show that dynamic phase objects can be analyzed with the optical system used.

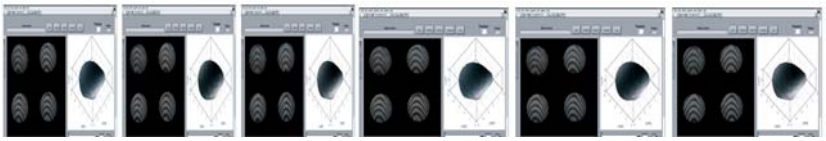

Figure 4. Dynamic Phase profile (Representative frames).

3. Conclusions

The experimental set-up for a simultaneous phase shifting quasi-common-path interferometer based on a Mach Zehnder system has been described to obtain the 4D phase profiles of phase objects using phase shifting techniques. One of the primary characteristics of the system presented is the adjustable beam separation, this characteristic optimizes the interferometric system used and allows the analysis of static and dynamic phase objects by using an automated phase data processing platform briefly introduced.

MEXICAN OPTICS AND PHOTONICS MEETING
19 al 21 de septiembre del 2012
San Luis Potosí, México

Class and grade Steel classification by Laser-induced Breakdown Spectroscopy (LIBS) and Principal Component Analysis (PCA)

U. Contreras [(1)], M.A. Meneses-Nava[(1)], J. Robles-Camacho [(2)], Gabriel Ramos-Ortiz [(1)], J.L. Maldonado [(1)] , O. Barbosa-García [(1)]

1. Grupo de Propiedades Ópticas de la Materia (GPOM); Centro de Investigaciones en Óptica A. C., Loma del Bosque 115, 37150 León, México
2. Laboratorio de Arqueometría de Occidente (LARQUEOC), Insituto Nacional deAntropología e Historia; Centro INAH Michoacán, Madero Oriente 799, 58000, Morelia, México

Corresponding author email: ulises@cio.mx

ABSTRACT:

Nowadays there exist more than 100 000 different types of steels according to their chemical and physical properties. Nevertheless there is not a unique method capable to identify or classify any sample of steel according to its class or grade. In this work it is described a method capable to identify and classify steels due to the chemical composition determination. The proposed method is based in the analysis of atomic spectra by Laser Induced Breakdown Spectroscopy (LIBS) and Principal Component Analysis (PCA). For steels from different classes it is possible to discriminate them due to their chemical composition. For steels from the same class but different grade, the information on the spectra is not sufficient for a satisfactory discrimination because of the relatively low difference in composition (<0.5%); however, discrimination of all analyzed samples is possible using PCA.

Key words: LIBS, PCA, Multivariate analysis, Laser ablation, Steel

REFERENCES AND LINKS

[1] C. Aragon, J.A. Aguilera, J. Campos, *"Determination of Carbon Content in Molten Steel Using Laser-Induced Breakdown Spectroscopy"*, Applied Spectroscopy 47(1993).

[2] V. Sturm, J. Vrenegor, R. Noll, M. Hemmerlin, *"Bulk analysis of steel samples with surface scale layers by enhanced laser ablation and LIBS analysis of C, P, S, Al, Cr, Cu, Mn and Mo"* J Anal. At. Spectrom. 19 (2004).

1. Introduction

Laser induced Breakdown Spectroscopy (LIBS) has been developed as a technique capable to determine the elemental composition of any sample either in solid, liquid or gaseous phase. Based LIBS elemental analysis of steel is reported for molten steel [1], as well as solid steel alloys and stainless steel samples. The interest in steel work analysis is a cost-effective analytical method, the simple or no sample pretreatment, quickness in acquisition results and the in-situ analysis [2]. LIBS has also been used as an online method of characterizing coatings on sheet steel on

a production line. In this work it is described a method capable to identify and classify steels due to the chemical composition determination by LIBS and multivariate methods such as Principal Component Analysis (PCA).

2. Experimental Array

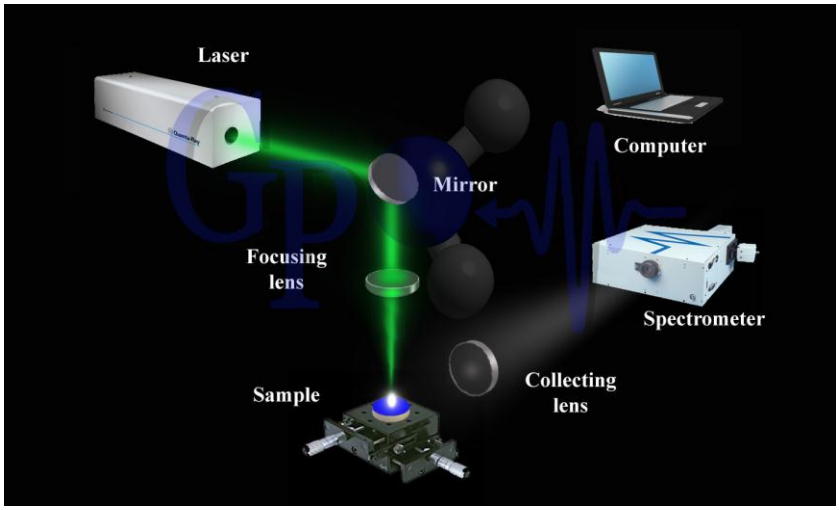

Fig.1. Experimental set up.

3. Conclusions

The LIBS technique together with multivariate analysis allows the multi-elemental characterization of steel samples and the classification according to their grade and class in a quick and practically non-destructive way. It is possible, with an adequate database containing all grades and steel classes, to implement a methodology capable to identify and classify any steel that can be used in laboratory and in the industry. It is also possible to use a methodology based on LIBS to monitor the quality control on steel alloys industry at real time.

MEXICAN OPTICS AND PHOTONICS MEETING
19 al 21 de septiembre del 2012
San Luis Potosí, México

Photonic band structure of a dynamic medium whose permittivity and permeability are modulated periodically in time

O. M. Becerra-Fuentes and P. Halevi
Instituto Nacional de Astrofísica, Óptica y Electrónica, Tonanzintla, Puebla

ABSTRACT
We have studied a bulk dynamic medium whose permittivity $\varepsilon(t)$ and permeability $\mu(t)$ are both periodic functions of time, modulated at the same frequency, however with an arbitrary phase difference. The dispersion relation turns out to be a band structure with forbidden bands for the propagation vector. These band gaps can be tuned by varying the modulation strengths and/or phase difference. We expect that, in practice, the same behavior can be obtained in the microwave regime by means of a dynamic "low pass" transmission line whose dynamic capacitance $C(t)$ and inductance $L(t)$ per unit length are given, respectively, by $\varepsilon(t)$ and $\mu(t)$.
Keywords: time-periodic permittivity, time-periodic permeability, temporal photonic crystal.

REFERENCES
[1] J. R. Zurita-Sánchez, P. Halevi and J. C. Cervantes-Gónzalez, *Phys. Rev. A* **79**, 053821 (2009).
[2] J. R. Zurita-Sánchez and P. Halevi, *Phys. Rev. A* **81**, 053834 (2010).
[3] P. Halevi, U. Algredo-Badillo and J. R. Zurita-Sánchez, *Proc. SPIE* **8095**, 809501 (2011).

1. Introduction

Recently, Zurita et al [1] have explored the idea of a "temporal photonic crystal (TPC)", namely, a uniform medium whose permittivity $\varepsilon(t)$ is a periodic function of time. This resulted in a band structure that is periodic in frequency and exhibits band gaps in the propagation vector. Subsequent investigation by Zurita and Halevi [2] showed that a slab of such a dynamic-periodic medium gives rise to resonant reflection and transmission under appropriate conditions for the slab thickness and the modulation frequency. Further, Halevi et al [3] demonstrated that such a TPC can be realized in practice in the microwave regime by means of a "low pass" transmission line whose capacitors are replaced by varactors with periodically modulated capacitance $C(t)$. In the present study we generalize ref. [1] case that the permeability $\mu(t)$ of the medium, as well as its permittivity $\varepsilon(t)$ are being modulated in time at the same frequency, however not necessarily in phase.

2. A bulk dynamic medium

2a. Dispersion relation

We consider a bulk, uniform, isotropic and nondispersive medium with relative permittivity $\varepsilon_r(t)$ and a relative permeability $\mu_r(t)$, both functions are assumed to be periodic and hence can be expanded in Fourier series as:

$$\varepsilon_r(t) = \sum_l \varepsilon_l e^{il\Omega t} \qquad \mu_r(t) = \sum_m \mu_m e^{im\Omega t} \tag{1}$$

Free charges being absent, the current density J and the charge density ρ vanish. Then, the wave equation for the electric field is found from the combination of Faraday's law and Ampere-Maxwell's law. This equation has plane-wave solutions. Using the Bloch-Floquet theorem the electric field is written as:

$$E(x,t) = E(t)e^{i(kx-\omega t)} \tag{2}$$

where $E(t) = \sum_n e_n(\omega)e^{in\Omega t}$ is a periodic function having the same periodicity as $\varepsilon_r(t)$ and $\mu_r(t)$. Substituting (1) and (2) into the wave equation for the electric field the following eigenvalues problem is obtained:

$$\sum_n \sum_m \left[\mu_{l-m}\varepsilon_{m-n}(\omega - m\Omega)(\omega - l\Omega) - k^2c^2\delta_{l,n}\delta_{m,0}\right]e_n(\omega) = 0 \qquad l,m,n = 0,\pm1,\pm2,\ldots \tag{3}$$

Here $\delta_{l,n}$ and $\delta_{m,0}$ are the Kronecker-delta functions and c is the speed of light in vacuum. Eq. (3) is an infinite set of linear equations where the unknowns are the amplitudes $e_n(\omega)$ of the electric-field harmonics and theirs coefficients are given by the square brackets. This eigenvalue problem has nontrivial solutions when the determinant of the coefficients vanishes. This condition leads to the eigenvalues, namely the propagation vectors $k(\omega)$. It turns out that an infinite number of wave vectors $k_1(\omega), k_2(\omega), \ldots$ are valid solutions for a given frequency, so that eq. (2) is generalized to read:

$$E_p(x,t) = \sum_p \sum_n e_{pn}(\omega) e^{i\left(kx-(\omega-n\Omega)t\right)} \tag{4}$$

2b. Numerical Simulations

In this section we show the band structure for some particular cases. Here, the relative permittivity and relative permeability are assumed to vary sinusoidally. Moreover, we allow $\mu_r(t)$ to have an arbitrary phase advance θ with respect to $\varepsilon_r(t)$:

$$\varepsilon_r(t) = \bar{\varepsilon}_r\left[1 + M_\varepsilon \sin(\Omega t)\right] \qquad \mu_r(t) = \bar{\mu}_r\left[1 + M_\mu \sin(\Omega t + \theta)\right] \tag{5}$$

Here $\bar{\varepsilon}_r(t)$ and $\bar{\mu}_r$ are, respectively, the average relative permittivity and permeability and, in this example, both have the value 5.25. In eq. (5), M_ε and M_μ are the "strengths of modulation". Furthermore, a normalized frequency and a normalized wave vector are introduced:

$$\tilde{\omega} = \omega/\Omega \qquad \tilde{k} = kc\Big/\left(\Omega\sqrt{\bar{\varepsilon}_r\bar{\mu}_r}\right) \tag{6}$$

Expressing (5) as (1) and substituting it in (3), the aforementioned eigenvalues are found. The normalized dispersion relations (or band structures) $\tilde{\omega}(\tilde{k})$ are plotted below.

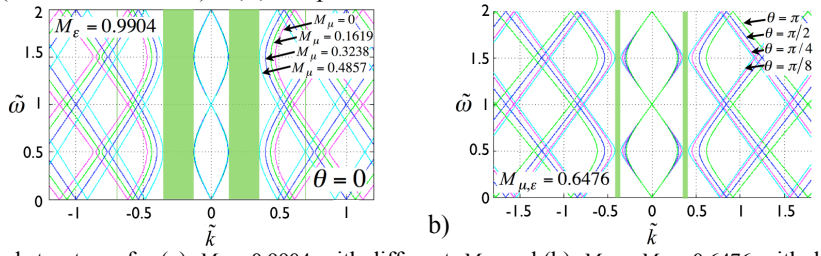

Fig.1. Band structures for (a) $M_\varepsilon = 0.9904$ with different M_μ and (b) $M_\mu = M_\varepsilon = 0.6476$ with different θ

Fig. 1a shows that, the larger the difference between the modulations, the wider the forbidden gap is for $\theta = 0$. Fig. 1b displays the band structure for $M_{\mu,\varepsilon} = 0.6476$ with $\theta = \pi/8$(cyan line), $\theta = \pi/4$(magenta line), $\theta = \pi/2$(blue line) and $\theta = \pi$(green line). Here it is demonstrated that, the larger the phase difference, the wider the forbidden gap is. Finally, the green regions illustrate complete forbidden bands for the propagation vectors in the cases that $M_\mu = 0.4857$ in fig. 1a and $\theta = \pi/4$ in fig. 1b.

3. Conclusions

The dispersion relation for dynamic media with both the permittivity and permeability varying periodically with time was obtained using the Bloch-Floquet theorem. The band structures for the case where both functions are sinusoidal were shown in fig. 1. Here, it is demonstrated that, the width of the forbidden band could be changed by modifying the modulations (M_μ, M_ε) or the phase difference. Fig. 1a illustrates that in the case where $\theta = 0$, the larger the difference between the modulations, the wider the forbidden gap is. It was also shown that, the larger the phase difference θ, the wider the forbidden gap is (fig. 1b). We expect that a dynamic-periodic "low-pass" transmission line with capacitance per unit length given by $\varepsilon_0\varepsilon_r(t)$ and inductance per unit length given by $\mu_0\mu_r(t)$ will give rise to the very same band structures, provided that $ka << 1$, where a is the size of the unit cell. In future work, we also plan to extend the study of resonances predicted in ref. [2] to a dynamic slab with periodic modulation of both $\varepsilon(t)$ and $\mu(t)$.

MEXICAN OPTICS AND PHOTONICS MEETING
19 al 21 de septiembre del 2012
San Luis Potosí, México

Residual birefringence cancelation in an optical fiber pump multiplexer (980nm/1550nm) working at 20°C

Rodríguez García Jorge Arturo [(1)], Tentori Santa Cruz Diana [(2)], Farfán Sánchez Miguel [(3)]

Centro de Investigación Científica y de Educación Superior de Ensenada
jrodrigu@cicese.edu.mx[(1)], diana@cicese.edu.mx[(2)], mfarfan@cicese.edu.mx[(3)]

ABSTRACT:

In this work we present a pump wavelength division multiplexer (WDM) in which the effect of birefringence on the polarization state of the light signal has been minimized for 20°C operation. The equalization of the state of polarization of the input and output signals can be used to preserve the information transmitted by pump WDMs.

REFERENCES AND LINKS

[1] A.M. Smith, "Automated birefringence measurement system" J. Phys. E **12**, 927-930, 1979.

[2] S. Lacroix, M. Parent, J. Bures, J. Lapierre, "Mesure de la biréfringence linéaire des fibres optiques monomodes par une méthode thermique," Appl. Opt. **23**, 2649-2653, 1984.

[3] ¨High-Gain, Polarization-Preserving, Y doped fiber amplifier for low duty cycle pulse amplification¨, LLE Review, volume 106.

[4] Xinhuan Feng, Hwa-yaw Tam, and P.K.A. Wai ¨Stable and uniform multiwavelength erbium doped fiber laser using nonlinear polarization rotation¨, Optics Express 8205 vol 14, No 18, 2006.

[5] Takaaki Matsura, Takuhiro Nakamura, Kenji NIshiwaki, Norihiro Momotsu, Kenichiro Asano, Hideyuki Hosoya, Sock Cheng Tan, Hui Li y Kok Siong Tan ¨Polarization maintaining optical device with low polarization crosstalk and high stability for temperatures¨ Fukiyura Technical Review, 2002

1. Introduction

Real fibers present various internal perturbations, such as core ellipticity and internal stress that cause characteristic differences of the propagation constants of the orthogonal polarization modes [1]. Since residual anisotropy is introduced during the manufacturing process, polarization modes can vary along the fiber length. Nevertheless, for short distances, the polarization properties of single-mode fibers can be considered as uniform [2].

The presence of this optic anisotropy reduces the performance of optic fiber devices in which it is required to control the polarization state of the light, such as polarization maintaining fiber amplifiers (PMFA), erbium doped fiber lasers (EFLs), as well as polarization multiplexed communication systems where it is needed fidelity in the information propagation and pulse stability [3:5].

In this research pump WDMs are used in erbium-doped fiber amplifiers (EDFAs), EFLs and sensors, to combine pump and signal waves. In this research two helical coils were prepared with the signal fiber arm, to reduce their birefringence effect and maintain the signal's state of polarization (SOP). We propose that helical windings induce a dominant birefringence and used them to equalize the state of polarization (SOP) of the signal at the WDM input and output ports.

2. Experiment

To evaluate the signal's SOP before and after the pump WDM, we used a polarimetric set up that kept the same framework in both cases. The light source was a tunable laser diode. To control the input polarized signal a polarization controller and a prism polarizer were used. SOPs were measured with a polarization analyzer.

After incorporating the pump WDM with two coils in the input arm, and equalizing the SOP of the emerging signal with that of the input signal, a 360 degrees scanning of the azimuth angle of the prism polarizer was performed. As result, the SOP of the input signal evolved along the equator of the Poincaré sphere (loci of linear SOPs) and the output SOP depicted the trajectory shown in figure 1, for a 1550nm signal.

Since temperature can produce significant changes of the SOP of light, it is important to evaluate its influence on the polarization control of the pump WDM here investigated. The WDM was placed inside a Dewar and a temperature controller was used to vary and stabilize the inside temperature. We increased temperature from 20 to 40 Celsius degrees and performed a scanning of the azimuth angle of the input signal at each 5°C step. Figure 2 shows the evolution of the output signal SOP (1550nm).

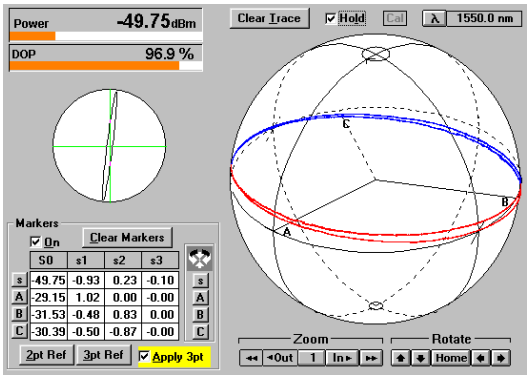

Figure 1.- Evolution of the output SOP for a 1550nm signal, -6dbm. Obtained scanning 360° the azimuth angle of the input SOP (2° step).

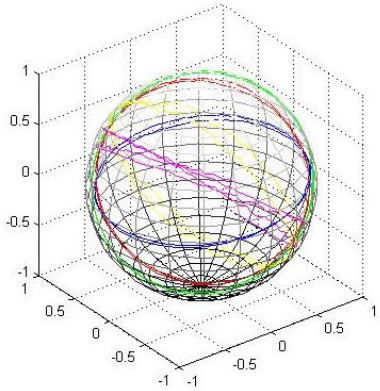

Figure 2.- Trajectories depicted by the emerging signal SOP (1550nm with -6dbm), for different temperatures (in °C): 20(blue), 25(red), 30(green), 35(yellow), 40(purple).

The trajectories in Fig. 2 are major circles of the Poincaré sphere with different ellipticity angles. They varied monotonically from 4.39° for 20°C to 16.44° when the temperature was 40°C. These results show the direct effect temperature had on birefringence and the information propagation along the fiber. The results we obtained for 1550nm show that double helical coils fix and reduce the effect of birefringence and can be used in systems working at 20°C that require a precision of 2.5° (Poincaré sphere is a 2-sphere). They can be used in exterior systems if the precision needed is below 8.5°.

3. Conclusions

The method here proposed for the pump WDM reduced and fixed the effect of birefringence on the output signal. Its polarization performance was tested at 20°C environmental temperature. For a 360° scanning of the input polarization along the Poincaré sphere equator, the major circle depicted by the ellipticity angle of the output SOP varied less than 5° (2.5° real angle). There was a shortcoming, when ambient temperature was raised to 40°C, accuracy was reduced since the maximum ellipticity angle increased to 17° (8.5°, real angle).

MEXICAN OPTICS AND PHOTONICS MEETING
19 al 21 de septiembre del 2012
San Luis Potosí, México

Femtosecond pulse compression in a hollow-core photonic bandgap fiber by tuning its cross section

N. González-Baquedano [1,*], N. Arzate [1], I. Torres-Gómez [1], A. Ferrando [2], D. E. Ceballos-Herrera [2], C. Milián [3]

1. Centro de Investigaciones en Óptica A.C., León, Guanajuato, México
2. Departamento de Óptica, Universidad de Valencia, Valencia, Spain
3. Instituto de Instrumentación para Imagen Molecular (I3M), InterTech, Universidad Politécnica de Valencia, Valencia, Spain

[*]Corresponding author email: noegb@cio.mx

ABSTRACT:

We present a numerical study of soliton pulse compression in a seven-cell hollow-core photonic bandgap fiber. We analyze the enhancement of both the compression factor and the pulse shape quality of 360 nJ femtosecond pulses at the wavelength of 800 nm by tuning the cross section size of the fiber. We use the generalized non-linear Schrödinger equation in order to modeled the propagation of light pulses along the fiber. Our numerical results show that output compressed pulses can be obtained, in a propagation length of 31 cm, with a compression factor of 6 and pulse shape quality of 77 % for a reduction of 4.5% of the cross section size of the fiber. The predicted compression factor is 3 times larger than that experimentally obtained in such propagation length of the pulse in a hollow-core photonic bandgap fiber.

Key words: Hollow-core fiber; Pulse compression; Soliton

References

[1] N. González-Baquedano, N. Arzate, I. Torres-Gómez, A. Ferrando, D.E. Ceballos-Herrera, C. Milián, "Femtosecond pulse compression in a hollow-core photonic bandgap fiber by tuning its cross section", *Photon Nanostruct: Fundam Appl*, (2012),http://dx.doi.org/10.1016/ j.photonics.2012.05.007.

[2] D. G. Ouzounov, F. R. Ahmad, D. Müller, N. Venkataraman, M. T. Gallagher, M. G. Thomas, J. Silcox, K. W. Koch, A. L. Gaeta, "Generation of Megawatt Optical Solitons in Hollow-Core Photonic Band-Gap fibers", *Science* **301**, (2003).

[3] F. Luan, J. C. Knight, P. St. J. Russell, S. Campbell, D. Xiao, D. T. Reid, B. J. Mangan, D. P. Williams, P. J. Roberts, "Femtosecond soliton pulse delivery at 800 nm wavelength in hollow-core photonic bandgap fibers", *Opt. Express* **12**, 835–840(2004).

[4] D. G. Ouzounov, C. J. Hensley, A. L. Gaeta, N. Venkateraman, M. T. Gallagher, K. W. Koch, "Soliton pulse compression in photonic band-gap fibers", *Opt. Express.* **13**, 6153–6159 (2005).

[5] F. Gêrome, K. Cook, A.K. George, W.J. Wadsworth, J.C. Knight, "Delivery of sub-100fs pulses through 8m of hollow-core fiber using soliton compression", *Opt. Express* **15**, 7126–7131 (2007).

MEXICAN OPTICS AND PHOTONICS MEETING
19 al 21 de septiembre del 2012
San Luis Potosí, México

1. Introduction

Non-linear optical effects in hollow-core photonic bandgap fibers (HC-PBGFs) are an active research topic [1, 2]. Recently have been used to deliver and compress high-intensity pulses due to the nature of their air core, which presents low non-linearity. These characteristics make HC-PBGFs efficient non-linear tools to be used as soliton fiber compressors [3, 4, 5]. We perform a numerical study of the compression of femtosecond unchirped pulses in HC-PBGFs. We study numerically the effects of tuning the cross section size of a HC-PBGFs on the modal parameters in order to have a fiber structure which promotes pulse compression. We will quantify this tuning by means of what we call the tapering factor, which is defined as the percentage of reduction of the cross section size of the fiber with respect to its original value. All the studied fiber structures have their fundamental guided mode at 800 nm.

2. Results

In order to evaluate the best option of optical fiber for pulse compression, it is necessary to take into account both features, the compression factor and the pedestal energy of a propagating pulse. The better choices for pulse compression are those fibers with tuning factors of 4.5% and 5%. However, the best choice is that fiber structure characterized by a tapering factor of 4.5%, since in that structure the pulse has the greatest pulse shape quality (or lower pedestal energy) along with the highest compression factor.

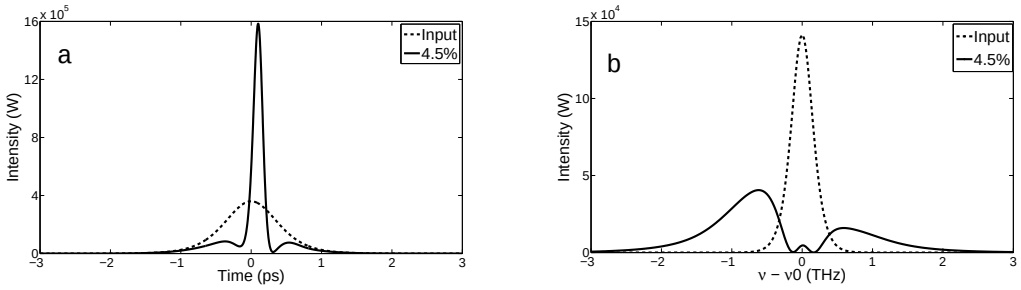

Figure 1: (a) Temporal [1] and (b) Spectral pulse shape of the optimun compressed pulse for a fiber with tapering factor of 4.5%. The compression factor predicted is 5.7 at a propagation distance of 31 cm.

Fig. 1, shows both temporal and spectral pulse shapes of the input and optimum compressed pulses. The corresponding compression factor has the value of 5.7 and it has a pedestal energy value of $E_{pedestal} = 23\%$. Such a compression factor is reached only after the pulse has been propagated through a distance of 31 cm.

3. Conclusions

We have studied numerically the influence of tuning the cross section size of a seven-cell HC-PBGF on both the pulse shape quality and the compression factor for unchirped pulses of 500 fs. It was found that a tuning of the cross section size of the fiber with a tapering factor of 4.5% improves both features. Our numerical results indicate a maximum compressed pulse with a compression factor of 5.7 with a temporal FWHM of 153.8 fs. The pulse reaches a peak power of 1.5851 MW with 77% of pulse shape quality. The length fiber at which the compressed pulse is reached is of 31 cm.

Acknowledgements We acknowledge CONACYT with grant number 106764 (CB-2008-1). NGB acknowledges CONACYT for the scholarship and the InterTech Group from the UV and UPV for allowing him to work with them. The work of AF and CM was partially supported by the MICINN TIN2006-12890 and TEC2010-15327 projects.

MEXICAN OPTICS AND PHOTONICS MEETING
19 al 21 de septiembre del 2012
San Luis Potosí, México

Photoreflectance anisotropy of low dimensional structures

J. V. González-Fernández [1], R. E. Balderas-Navarro [1], A. Lastras-Martínez [1], L. F. Lastras-Martínez [1], T. Mozume [2], S. Gozu [2], J. Ortega-Gallegos [1] and I. Lara-Velázquez [1].

1. Instituto de Investigación en Comunicación Óptica, Universidad Autónoma de San Luis Potosí, San Luís Potosí, SLP, 78210, México
2. National Institute of Advanced Industrial Science and Technologies (AIST), 2-1 Tsukuba Central, 1-1-1 Umezono, Tsukuba, Ibaraki 305-8568, Japan

Corresponding author email: fanogf@hotmail.com

ABSTRACT:

We report on measurement of photoreflectance-anisotropy (PRA) spectroscopy of two nanostructured semiconductor systems, namely coupled double quantum wells (CDQWs) and quantum dots lasers (QDLs). PRA spectra of CDQWs with 2 and 3 ML of AlAs coupling barriers super-lattice, show a clear and sharp peaks corresponding to inter-band transitions from the heavy-hole sub-bands to the conduction bands. Also we used PRA spectroscopy as an optical probe for the characterization of QDL with an active region consisting of InAs quantum dots embedded in a series of three stacked In0.15Ga0.85As quantum wells. PRA spectroscopy has the ability to detect and differentiate low dimensional structures. This technique can be an attractive tool for the characterization of buried interfaces in nanostructured devices at room temperature.

Key words: Photoreflectance anisotropy, super-lattice, coupled double quantum wells, quantum dot laser.

REFERENCES AND LINKS

[1] T. Mozume, "Molecular beam epitaxy and characterization of InGaAs/AlAs/AlAsSb coupled double quantum wells with extremely thin coupling barriers", *J. Vac. Sci. Technol.* **B 28(3)**, C3C25-C3C28 (2010).

[2] J. V. González-Fernández, "Dots-in-a-Well InGaAs Based Laser Probed by Photoreflectance-Anisotropy Spectroscopy", *IEEE* **978-1-4244-6029-8/09**, 8-12 (2009).

[3] E. M. Lopes, "Exciton behavior in GaAs/AlGaAs coupled double quantum wells with interface disorder", *J. of Lum.* **130**, 460-465 (2010).

[4] A. Lastras-Martínez, "Model for the linear electro-optic reflectance-difference spectrum of GaAs(001) around E1 and E1+Δ1", *Phys. Rev.* **B 59**, 10234-10239 (1999).

1. Introduction

Recently, systems based on an active area of coupled double quantum wells (CDQWs) and quantum dots (QD) have been extensively used for the fabrication of lasers, modulators, photodetectors and other optoelectronic devices [1].

In this work, we use photoreflectance anisotropy (PRA) spectroscopy for low dimensional structures characterization in order to study their optical anisotropies. PRA relies on the difference between two photoreflectance spectra, one

measured with non-polarized and the other with light polarization along [110] (or [1-10]) for (100)-oriented zinc-blende symmetry structures [2].

The CDQW configuration is fabricated using the quantum tunnelling effect between two quantum wells (QWs) separated by a thin barrier, the thickness barrier allows the overlapping of their wave-functions [3]. The residual strain in the border of each QW layer causes some anisotropy that we can detect by PRA.

The QD-based laser active area consists, in this case, of three stacked 110 Å-thick, In0.15Ga0.85As QWs with embedded 2.4 monolayers of InAs QDs. The PRA signal of the QDL is originated in the built in electric field extending across the heterostructure. This electric field breaks down the cubic symmetry of the InGaAs QWs through a piezoelectric effect, changing it to orthorhombic and thus leading to an optical anisotropy [4]. The QD morphological structure leads anisotropies along [110] and [1-10] crystallographic directions and this can be measured by this technique.

2. Figures

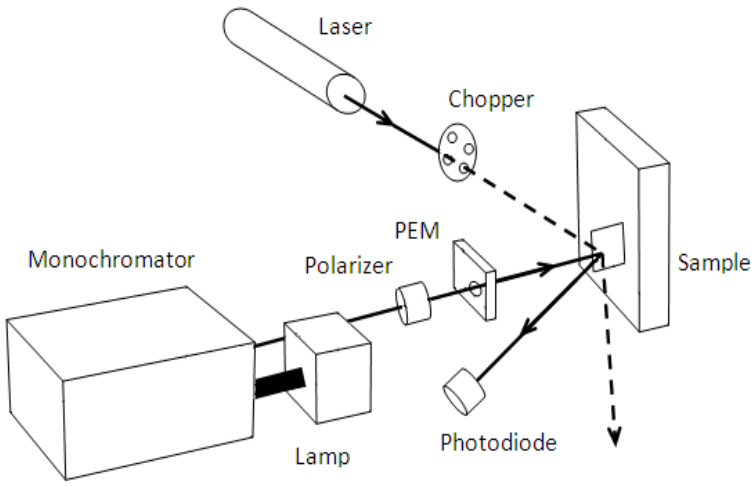

Fig.1. Experimental setup of photoreflectance-anisotropy spectroscopy.

3. Conclusions

We have used PRA to measure electro-optical anisotropies of a low dimensional hetero-structures. PRA spectra clearly provides useful information from CDQWs and QDLs structures at room temperature. This makes PRA spectroscopy an attractive optical tool for testing the energy level structure in complex quantum confinement systems.

Acknowledgements

The authors are grateful to B. E. Torres-Loredo, J. Ramírez-Rodríguez, and E. Ontiveros-Hernández for technical support. This work was supported by Consejo Nacional de Ciencia y Tecnología through grants 23962, CB2007 (79635) and CB2007 (81316), and FAI-UASLP.

MEXICAN OPTICS AND PHOTONICS MEETING
19 al 21 de septiembre del 2012
San Luis Potosí, México

High speed femtosecond pulse characterization based on Spectral Interferometry

G. Castro-Olvera [(1)], J. Garduño-Mejía [(1)], C. J. Román-Moreno [(1)] and R. Ortega-Martínez [(1)].

CCADET-UNAM, Apdo. Postal 70-186, C.P. 04510. Coyoacán, Cd. Universitaria, México D. F.
Corresponding author email: jesus.garduno@ccadet.unam.mx.mx

ABSTRACT:

In this work, we present spectrum and spectral phase retrieval of femtosecond pulses at 74 Hz refresh rate by a Spectral Interferometry technique. Different spectral phase designs including linear, quadratic and high order chirp are measured with this technique and generated with a pulse shaper based on a micro-machined deformable membrane mirror (MMDM).

Keywords: ultrafast optics, pulse characterization, femtosecond pulse shaping.

REFERENCES AND LINKS

[1] A. Weiner, "Programmable Shaping of Femtosecond Optical Pulses by Use of 128-Element Liquid Crystal Phase Modulator". *IEEE JQE* 28, (4), pp. 908-920, 1992.

[2] F. Verluise, V. Laude, Z. Cheng, Ch. Spielmann, and P. Tournois, "Amplitude and phase control of ultrashort pulses by use of an acousto-optic programmable dispersive filter: pulse compression and shaping". *Optics Letters*, 25, (8), pp. 575-577, 2000.

[3] J. Garduño-Mejía, A. H. Greenaway and D.T Reid, "Designer femtosecond pulses using adaptive optics". *Optics Express*, 11, (17), pp. 2030-2040, 2003.

[4] J. Garduño-Mejía, E. Ramsay, A. Greenaway and D.T. Reid, "Real time femtosecond optical pulse measurement using a video rate FROG system". *Review of Scientific Instruments*, 74, (8), pp. 3624-3627, 2003.

[5] T. M. Shuman, M. E. Anderson, J. Bromage, C. Iaconis, L. Waxer and I. A. Walmsley, "Real-time SPIDER: ultrashort pulse characterization at 20 Hz" *Optics Express*, 5, (6), pp. 134-143, 1999

[6] C. Dorrer and F. Salin, "Characterization of spectral phase modulation by classical and polarization spectral interferometry". *J. Op. Soc. Am. B*, 15, (8), pp. 2331-2337, 1998.

1. Introduction

Femtosecond pulse shaping is typically achieved by different techniques which involve a phase or intensity modulator such as a liquid-crystal display (LCD) array [1], acousto-optic programmable dispersive filters (AOPDF) [2] and micro-machined deformable membrane mirrors (MMDM) [3].
A main limitation in the convergence speed on pulse shaping is related with the pulse characterization speed itself. Reported convergence refresh rates of pulse characterization are between 1-20 Hz applying different techniques [4, 5].
A suitable option to improve the refresh rate, sensitivity with a simple setup for femtosecond pulse characterization is Spectral Interferometry. This method is very sensitive since does depends on a linear response with the only

condition that we must provide a reference pulse. The technique consists on resolve, in the frequency domain, the interferogram generated by the pulse to be characterized and its delayed (fixed) reference pulse in a spectrometer. Actual spectral phase information is retrieved by a Fourier Transform, side band filtering and phase unwrapping process. To complete the computation, actual spectral phase of the reference pulse is subtracted. If the pulse reference is Bandwidth Limited (BL), spectral phase calculation of a shaped pulse is then a straight forward process.
In the present work we present a high speed femtosecond pulse characterization, based on Spectral Interferometry technique [6], with a refresh rate of 74 Hz, to measure pulses from a shaper based on a MMDM.

2. Experimental Setup

Experimental setup involves a Mach-Zender interferometer where a pulse is divided in two replicas: one is sent to the shaper and the other one is delayed and characterized with a SHG-FROG [4] to provide a reference pulse. At the output both pulses are recombined collinearly in a spectrometer (Ocean Optics HR2000+ series).
The pulse shaper is based on a dispersionless design incorporating a 1200 lines/mm diffraction-grating and arranged in a *2f* configuration with a deformable mirror situated at the Fourier plane of a 500 mm focal length concave mirror. Near BL pulses from a self-mode-locked 200 femtosecond Ti:sapphire laser with a FWHM of 7 nm and centered at 826 nm (Coherent MIRA 900), were coupled into the shaper and dispersed to form a line spectrum extending across most of aperture of the mirror. Programming a chosen curvature onto the mirror surface produced a change in the spectral phase across the pulse spectrum. Data acquisition and interface were performed with LabVIEW.

3. Results

Different spectral phase designs including linear, quadratic and high order chirp generated with a pulse shaper were measured with Spectral Interferometry. In figure 1 an example of spectrum and spectral phase retrieval is presented.

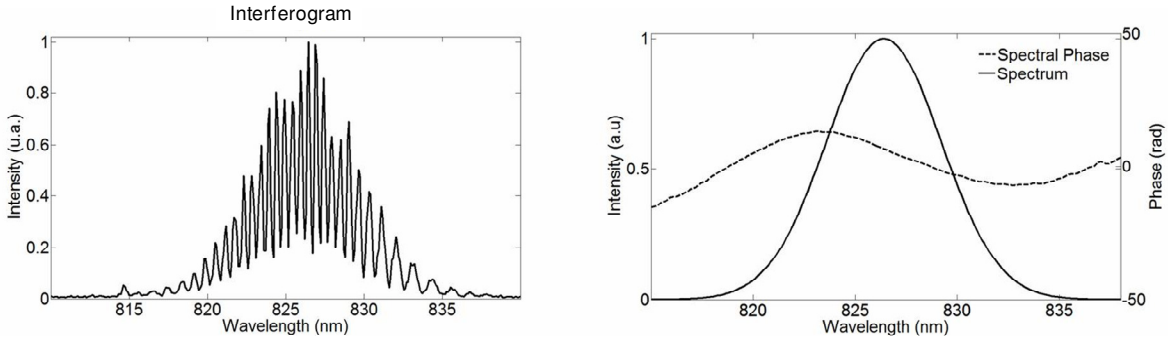

Figure 1. Interferogram, spectral phase and spectrum retrieved with Spectral Interferometry.

5. Conclusions

In the present work we demonstrates a high speed femtosecond pulse characterization, based on Spectral Interferometry technique, with a high speed refresh rate of 74 Hz, to measure pulses designed with a shaper based on a MMDM. This characterization method is very sensitive since does depends on a linear response, easy to setup with the only drawback that we must provide a reference pulse. Nevertheless, depending on the femtosecond laser source, reference pulse could remains constant for long periods of time and then its characterization should be performed couple of times during a day. This method represents a good alternative to be integrated in a closed loop femtosecond pulse shaper.

Acknowledgements

The authors gratefully acknowledge sponsorship of this work by DGAPA-UNAM. PAPIIT project: IN113809, IB101212, IACOD-I1100611, CONACyT-Mexico project CB 131746.

MEXICAN OPTICS AND PHOTONICS MEETING
19 al 21 de septiembre del 2012
San Luis Potosí, México

A 32-channel rapid reflectance-difference spectrometer

O. Núñez-Olvera, R.E. Balderas-Navarro, J. Ortega-Gallegos, L.E. Guevara-Macías, L.F. Lastras-Martínez, A. Lastras-Martínez
Instituto de Investigación en Comunicación Óptica
Universidad Autónoma de San Luis Potosí. México
Av. Karakorúm 1470. Lomas 4ª. Secc. 78210. San Luis Potosí, SLP, México.

ABSTRACT

We report on a 32-channel reflectance-difference spectrometer with 0.2 s spectrum acquisition time. To demonstrate the spectrometer performance we carried out RD dynamical measurements of (001) GaAs surfaces in molecular beam epitaxy conditions. The spectrometer is capable measuring spectra with an acquisition time of 0.2 s and amplitudes in the range within 10^{-4}.

INTRODUCTION

Reflectance difference spectroscopy (RDS) constitutes a powerful tool for the surface characterization of cubic semiconductors. RDS relies on the measurement of the difference of surface optical reflectance for two mutually orthogonal linear polarizations that arises due to the breakdown of the cubic symmetry in the near-surface region. RDS is a polarization-contrast, surface-specific technique that enhances surface spectral features against the dominant (isotropic) bulk reflectance component.

Its surface specificity makes RDS particularly well suited for the *in situ* characterization of the epitaxial growth dynamics in, both, ultra high vacuum and vapor-phase growth systems. The measurement of time-resolved reflectance-difference (RD) spectra as demanded by this application, nevertheless, poses some challenges. For one thing, the typical magnitude for the $\Delta R/R$ RDS signal lies in the range from $10^{-2} - 10^{-4}$. For another, the characterization of the epitaxial growth dynamics demands of sub second spectra acquisition times that ruled out the use mechanical scanning, single-channel spectrometers. RD spectrometers intended for the study of epitaxial growth dynamics should then rely on multichannel spectra acquisition.

Here we report on a 32-channel RD spectrometer with a spectra acquisition time of 100 ms. The spectrometer is based on 1) a photo-elastic modulator to modulate the polarization of the probing radiation, 2) a 32-channel photomultiplier (PM) array to detect light and 3) a lock-in amplifier to process the RD signal.

INSTRUMENT DESCRIPTION

The optical layout of the RD spectrometer reported here follows the design by D.E. Aspnes.[1] In figure 1 we show the corresponding electrical layout. For signal processing, the 32 outputs of PM array (Hamamatsu H7260) are multiplexed into the input of a lock-in amplifier (Stanford Research SR530). Channel multiplexing is carried out with two 16-channel analog multiplexor cards (MAXIM MAX306CPI). Both the analog input (R) and the analog output (ΔR) of the lock-in amplifier are digitized by a 16-bit data acquisition card (National Instruments NI-PCI 6221). The instrument is attached to the growth chamber of a molecular beam epitaxy system (Riber 32P). A stress-free 2” quartz window provides a perpendicular, unobstructed view of the epitaxial substrate in growth position.

RESULTS

To demonstrate the performance of the RD spectrometer we carried out *in situ* real time RD measurements of GaAs (001) surfaces under various conditions. In figure 2a we show the evolution of the RD spectrum of GaAs (001) surface at 500 ^{o}C after shutting off the As flux. In each case spectra acquisition time was 0.5 s. Under As flux the RD spectrum shows the typical line shape corresponding to a c(4x4) surface reconstruction. After As shut off, as the surface migrates into a less As-rich phase, the deep minimum observed at an energy around 2.6-2.7 eV begins to fade out. After about two minutes this minimum almost disappeared and the RD spectrum showed little optical structure. Next we annealed the GaAs surface at 500 ^{o}C for about one minute under As-deprived conditions, and then opened the Ga shutter and deposited an amount of Ga equivalent to 2 ML at a rate 0.2 Ml/s. In figure 2b we show the corresponding evolution of the RD spectrum. As it can be seen, after Ga deposition the RD spectrum gradually develops a deep minimum around 2.8 eV.

CONCLUSIONS

We demonstrate the performance of a 32-channel rapid RD spectrometer based on a PEM. The spectrometer is capable measuring RD 32-channel spectra with an acquisition time of 0.2 s and amplitudes in the range within 10^{-4}. The developed instrument allows for the real time study of epitaxial growth processes.

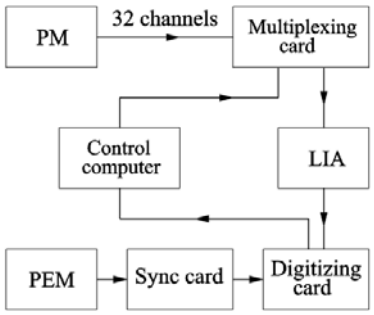

Figure 1. Electrical layout of the RD multichannel spectrometer. PM, LIA and PEM stand, respectively, for photomultiplier, lock-in amplifier and photo-elastic modulator.

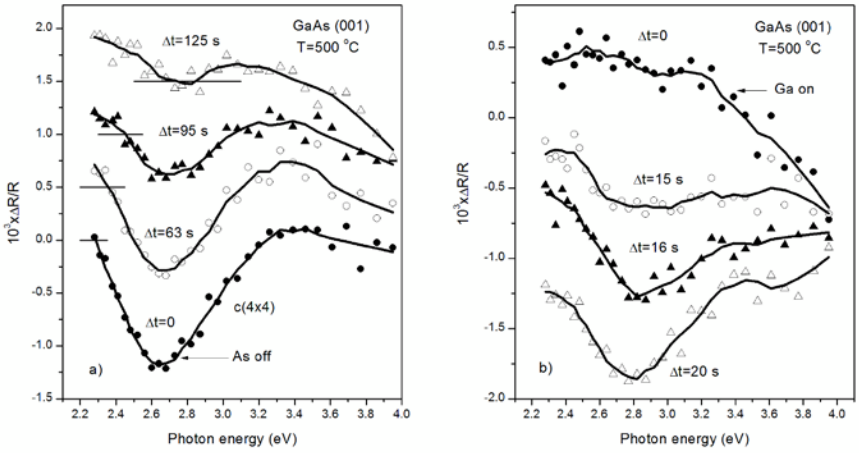

Figure 2. a) evolution of the RD spectra of the c(4x4) reconstructed, GaAs (001) surface) after shutting off the As flux. b) Evolution of the GaAs (001) surface annealed for three minutes at 500 ^{o}C under As-deprived conditions, after depositing Ga atoms to an amount equivalent to 2 ML. Continuous lines correspond to local polynomial fittings to experimental points For the sake of clarity, spectra for Δt=16 and Δt=20 s are displaced downwards for $3x10^{-4}$ and $7x10^{-4}$, respectively.

REFERENCE

[1] D. E. Aspnes, J. P. Harbison, A. A. Studna, and LT. Florez, J. Vac. Sci. Technol. A 6, 1327 (1988).

MEXICAN OPTICS AND PHOTONICS MEETING
19 al 21 de septiembre del 2012
San Luis Potosí, México

Raman spectroscopy and multivariate analysis for the determination of raw material provenance of archeological travertine objects

M.A. Meneses-Nava[1*], J. Robles-Camacho[2], O. Barbosa-García[1], J.L. Maldonado[1], G. Ramos-Ortiz[1]

1. Centro de Investigaciones en Óptica, A.P. 1-948, 37150 León, Gto., México. Fax number: +52 (477) 4414209
2. Laboratorio de Arqueometría del Occidente. Centro INAH Michoacán. Instituto Nacional de Antropología e Historia. Av. Madero oriente No. 799, Centro, 58000 Morelia, Mich., México. +52 (443) 3128838
*Corresponding author email: tono@cio.mx

ABSTRACT:

The use of Raman spectroscopy for the characterization of archeological objects has been widely used in recent years because it is an optical non-destructive technique and it provides compositional information without any sample preparation. In this work seven geological samples of travertine (Mexican onix) from Tecali de Herrera, Puebla, one from Magdalena Apasco, Oaxaca, one from Magdalena Tequisistitlán, Oxaca and one from Xicotlán, Puebla, have been used as the training set for SVM classification. Powder samples of nine archeological objects made from travertine, has been classified and the results show that almost all the samples belongs to the Tecali region. Although more samples are needed for a much better analysis, these results open up the possibility to use both tools for geological provenance determination of materials used in Mesoamerican lapidary.

Key words: Spectroscopy, Raman, Archeology, Minerals, Multivariate

REFERENCES AND LINKS

[1] Weerd, V.D. J., Smith, G., Firth, S., and Clark, R.J.H., Journal of Archaeological Science 31, 1429-1437 (2004).

[2] Vandenabeele, P., J. Raman Spectrosc; 35: 607–609 (2004).

1. Introduction

Archeometry is a new research field where the principal objective has been the mineral and chemical characterization of cultural objects, with the ultimate goal to establish the provenance of the analyzed sample's raw material. One of the promising technique used in archeometry is Raman spectroscopy (RS) [1], because it is a non-destructive technique, where no sample preparation is needed. To accomplish the determination of provenance of raw material, RS along is not capable to do so, because the measured spectra can be complex and changes from sample to sample very often are imperceptible that visual inspection is not suitable. In order to manage all the experimental data available and focus only on those relevant features that are critical for classification, multivariate analysis is employed. In particular Principal Component Analysis (PCA) is used to reduce the dimension of observations and support vector machine technique for classification.

2. Methodology.

All samples were grinded with an agate mortar and were measured without further preparation. When a CW green laser is used as excitation for Raman spectroscopy, fluorescence emission overwhelm the Raman signal, making

impossible the classification analysis. For this reason Time Resolved Raman Spectroscopy (TRRS) was used and almost all fluorescence suppressed using a gate windows of 5 ns. After acquisition the spectra were smoothed and background corrected. For multivariate analysis spectra were normalized using the standard normal variate normalization.

3. Results.

The multivariate analysis by PCA of ten geological travertine samples from Puebla and Oxaca, are described by the first two components, which explain 98% of the variance. Figure 1 shows the grouped samples together with their confidence ellipses, where a clear distinction between travertine from Xicotlan, Puebla is evident. Figure 2 shows the classification of the nine archeologically samples by the SVM algorithm.

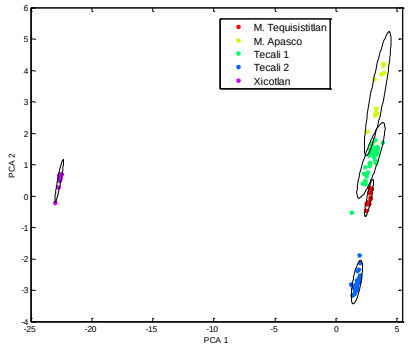

Fig.1. Groups of geological samples by PCA.

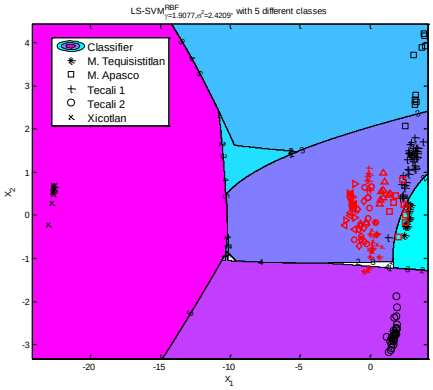

Fig.2. Classification by SVM of archeological samples.

3. Conclusions

PCA multivariate analysis and SVM classification, together with Raman spectroscopy show the possibility to group travertine minerals according to their outcrops, although more samples are needed for a much better analysis, these results open up the possibility to use both tools for geological provenance determination of archeological material.

MEXICAN OPTICS AND PHOTONICS MEETING
19 al 21 de septiembre del 2012
San Luis Potosí, México

White LEDs spectral mismatch correction factor dependence on the photometric detector spectral responsivity

A. Estrada-Hernández [1], E. Rosas [1], L. P. González-Galván [1], N. Vidal-Medina [1], R. González-Mota [2]

1. Centro Nacional de Metrología, km. 4.5 carretera a Los Cués, 76246, El Marqués, Querétaro.
2. Instituto Tecnológico de Aguascalientes, Adolfo López Mateos 1801, 20256, Aguascalientes, Aguascalientes.

Corresponding author email: aestrada@cenam.mx

ABSTRACT:

Here we present the initial results on the effect the photometric detector's spectral responsivity has on the spectral mismatch correction factors determination, for high intensity white LEDs; which highly impact the total luminous flux measurements and luminous efficacy determinations.

Key words: Solid-state lighting, led emitted color, spectral mismatch correction factors, photodetector responsivity.

REFERENCES AND LINKS

[1] N. Vidal, E. Rosas, J. B. Hurtado Ramos, *Illuminance spatial distribution based total luminous flux determination for white LEDs*, Proceedings of SPIE, **8011**(80111Z), Bellingham, USA, (2011).

[2] A. Estrada-Hernández, L. P. González-Galván, E. Rosas, *New paradigms in LED photometry and colorimetry*, Proceedings of SPIE, **7499**(74990L), Bellingham, USA, (2009).

[3] A. Estrada-Hernández, L. P. González-Galván, C. H. Matamoros-García, *Mediciones en LEDs de alta intensidad*, Centro Nacional de Metrología, **SM2008**-S4B1-1015, Santiago de Querétaro, México, (2008).

[4] A. Estrada-Hernández, L. P. González-Galván, H. Zárate-Hernández, R. Cardoso, E. Rosas, *Luminous flux and correlated color temperature determination for LEDs sources*, Proceedings of SPIE, **6422**(64220O), Bellingham, USA, (2007).

[5] Commission International d'Eclairage, *The measurement of luminous flux*, Technical Report No. 84, Vienna, Austria, (1989).

[6] Commission International d'Eclairage, *CIE 1988 2° spectral luminous efficiency function for photopic vision*, Technical Report No. 86, Vienna, Austria, (1990).

[7] Commission International d'Eclairage, *Colorimetry*, Technical Report No. 15, Vienna, Austria, (2004).

---

1. Introduction

It has been shown that a high accuracy measurement of the high-intensity white LEDs total luminous flux requires the application of several correction factors [1-4], such as the spectral mismatch correction factor, which is due to the mismatch the photometric detector spectral response has with respect to the CIE photopic observer [5, 6]; specially when measuring LEDs which emission spectrum highly differs to that of the standard source, normally a CIE standard illuminant A [7].

2. Results

The spectral mismatch correction factor, F_c^*, is defined as [5]:

$$F_c^* = \frac{\int S_A(\lambda)\cdot s_r(\lambda)\cdot d\lambda}{\int S_A(\lambda)\cdot V(\lambda)\cdot d\lambda}\cdot\frac{\int S_{\mathrm{LED}}(\lambda)\cdot V(\lambda)\cdot d\lambda}{\int S_{\mathrm{LED}}(\lambda)\cdot s_r(\lambda)\cdot d\lambda}, \qquad (1)$$

where $S_A(\lambda)$ is the relative power spectrum for the CIE standard illuminant A [7]; $S_{\mathrm{LED}}(\lambda)$ is that for the LED under test; $V(\lambda)$ is the CIE photopic observer function [6]; and $s_r(\lambda)$ is the spectral responsivity for the photometric detector used to measure the LED total luminous flux.

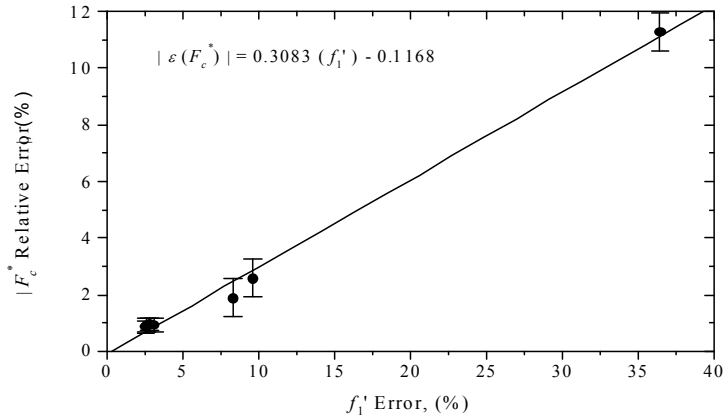

Fig.1. Spectral mismatch correction factor dependence on the photometric detector spectral responsivity.

This F_c^* highly influences LEDs sources total luminous flux measurements, thus affecting the corresponding luminous efficacy determination; and its impact increases when a photometric detector poorly reproducing the $V(\lambda)$ function is used, as shown in Fig. 1; where this effect is plotted for the averages of the F_c^* relative errors obtained for six high-intensity white LEDs, and seven photometric detectors having different f_1' errors, given by [5]:

$$f_1' = \frac{\int\left|\frac{\int S_A(\lambda)\cdot V(\lambda)\cdot d\lambda}{\int S_A(\lambda)\cdot s_r(\lambda)\cdot d\lambda}\cdot s_r(\lambda)\cdot V(\lambda)\right|\cdot d\lambda}{\int V(\lambda)\cdot d\lambda}, \qquad (2)$$

3. Conclusions

We have shown the dependence the spectral mismatch correction factor has on the spectral responsivity of the photometric detector; thus highlighting the importance of using a good quality photometric detector when LED sources are to be tested for its total luminous flux; otherwise the results deviation will in fact degrade the accuracy reached with the previously obtained uncertainty levels [3, 4]; thus affecting the test confidence or validity.

Acknowledgements

The authors wish to thank M. Appl. Tech. Juan Carlos Molina Vázquez, for measuring the spectral responsivities of the used photometric detectors.

MEXICAN OPTICS AND PHOTONICS MEETING
19 al 21 de septiembre del 2012
San Luis Potosí, México

Study of InGaAs/GaAs(001) growth with time-resolved reflectance difference spectroscopy

A. Armenta-Franco*, O. Núñez-Olvera, J. Ortega-Gallegos, R.E. Balderas-Navarro, L.F. Lastras-Martínez, A. Lastras-Martínez

Instituto de Investigación en Comunicación Óptica
Universidad Autónoma de San Luis Potosí. México
Av. Karakorúm 1470. Lomas 4ª. Secc. 78210. San Luis Potosí, SLP, México.

*Corresponding author: a2f_171084@hotmail.com

ABSTRACT:

We report on *in situ*, time resolved RD spectroscopy of MBE $In_{0.3}Ga_{0.7}$ As epitaxial growth on GaAs (001) substrates. A comparison between *in situ* RD spectra taken previously with a conventional spectrometer and those reported here, measured by a new rapid RD spectrometer, is discussed. We further report on time resolved RD spectroscopy of InAs MBE growth on GaAs (001). Simultaneous RD and RHEED measurements were taken during epitaxial growth in order to find correlations between the information provided by both techniques. We conclude that RD spectroscopy and RHEED are complementary probes to characterize the first stages of the epitaxial growth of InGaAs films.

Key words: Semiconductors, hetero-epitaxial growth, optical spectroscopy

---

REFERENCES AND LINKS

[1]O. Núñez Olvera, abstract submitted to this meeting.
[2] A. Lastras Martínez, C.I. Medel Ruíz, R.E. Balderas Navarro, S.L. Gallardo, V.H. Méndez García, J.M. Flores Camacho, A. Gaona Couto, L.F. Lastras Martínez, App. Surf. Sci. 222 (2004) 48-52.
[3] A. Lastras Martínez, R.E. Balderas Navarro, L.F. Lastras Martínez, M.A. Vidal, *Phys. Rev. 59,(1999) 10234*.
[4]L.F. Lastras Martínez, M. Chavira Rodriguez, A. Lastras Martínez, R.E. Balderas Navarro, Phys. Rev. B 66 (2002) 075315.

---

1. Introduction

Optoelectronic devices have played a central role in several technological advances; specifically, those based on III-V compounds, being GaAs, InAs and GaSb the most important. However, as the complexity of the devices based on those compounds increases, higher structural material quality is required in order to enhance device performance. Therefore, a precise *in situ* and real time control must be accomplished during the crucial stages of their growth. Optical probes are suitable for such control because they are easily implemented for remote sensing. Among used optical techniques, Reflectance Difference (RD) spectroscopy, which measures the optical anisotropies between two orthogonal in-plane eigenaxes, has been a valuable tool for the study of surface processes in cubic semiconductors. The principle of operation of RD is based on the fact that as the optical properties of bulk cubic semiconductors are

nominally isotropic, any breakdown of the symmetry occurring in the surface or interfaces renders the eigenaxes inequivalent, thus filtering out the dominating bulk signal. Therefore only the optical anisotropies associated to those regions near the interfaces are measured.

In this work we focus on the in situ, real time RD study of $In_x Ga_{1-x} As$ growth on GaAs (001). As the lattice constant of InGaAs is larger than that of GaAs, we expect that the first stages of epitaxial growth on GaAs the InGaAs film should experience a compressive biaxial strain, with no significant optical anisotropies. However, as the film approaches the critical thickness the growth mode changes forms 2D to 3D, eventually generating an anisotropic strain relaxation.

RD spectra reported in this work were measured with a rapid spectrometer based on a photoelastic modulator with the capability of acquiring 32-channel spectra with sub-second time resolution, in the spectral range from 1.9 eV-4 eV.

2. Section Title 2

2.c.- Subsection Title 3: Figures

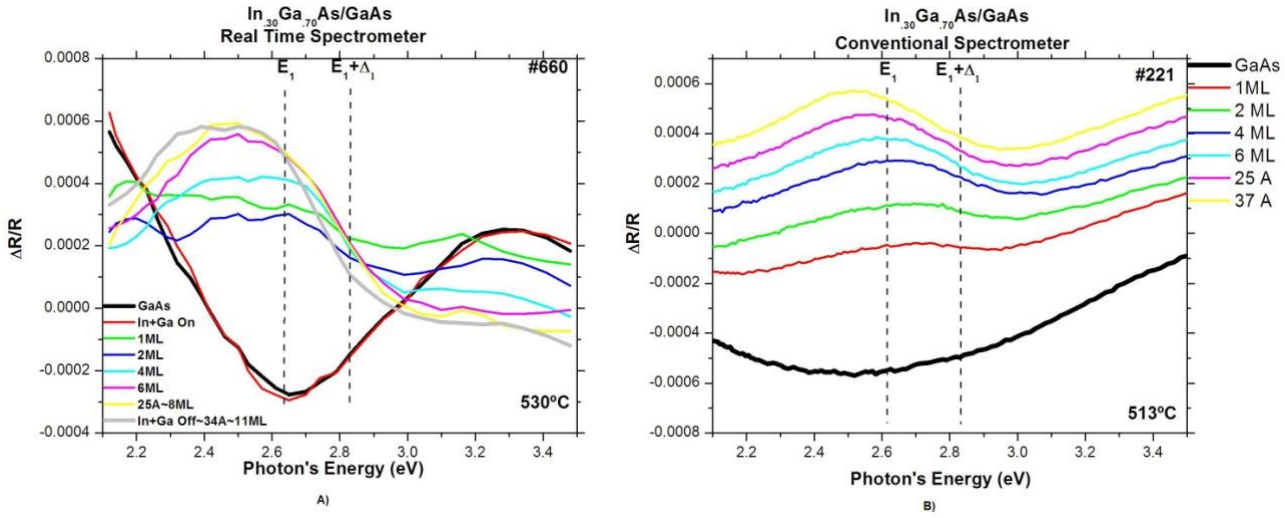

Figure 1. A) RD spectra of an InGaAs film deposited at once on a GaAs(001) substrate and taken with a time resolved spectrometer, B) RD spectra of InGaAs grown in steps over a GaAs(001) substrate and measured with a conventional spectrometer [1]. For both cases, intermedial thicknesses are shown.

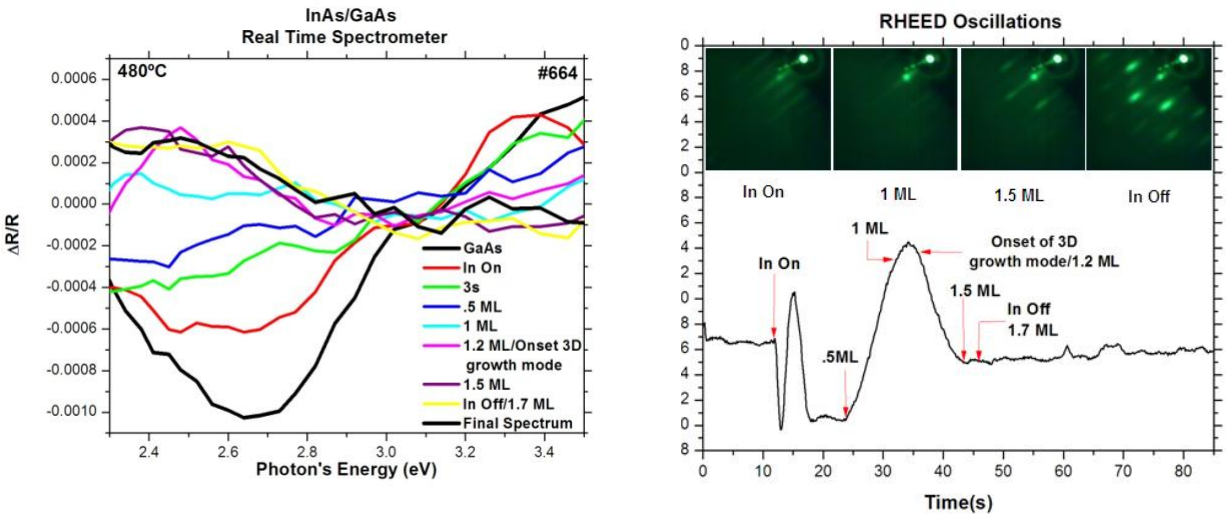

Figure 2. RD spectra of an InAs film deposited on GaAs (001) measured with the time resolved spectrometer (left) and their corresponding RHEED oscillations and intensities (right).

3. Conclusions

We have showed that there is a correlation between RHEED oscillations and RD spectrum evolution during the MBE growth of $In_{.30}Ga_{.70}As$ films on GaAs. To obtain time resolved RD spectra we employed a new rapid RD spectrometer with a acquisition time of 0.5 s. We conclude that time resolved RD spectroscopy is a useful complementary tool for the *in situ*, real-time monitoring of the hetero-epitaxial growth of $In_X Ga_{1-X} As$.

Acknowledgements

We thank the skilful technical assistance of Ezequiel Ontiveros Hernández, Francisco Ramírez Jacobo and Ismael Lara Velázquez. Work partially supported by Consejo Nacional de Ciencia y Tecnología under grant 81316. One of us (AAF) is supported by CONACyT fellowship.

MEXICAN OPTICS AND PHOTONICS MEETING
19 al 21 de septiembre del 2012
San Luis Potosí, México

Scorpion venom study by Raman Spectroscopy

Brenda Esmeralda Martínez Zérega[1,*]

1. Centro Universitario de los Lagos, Universidad de Guadalajara, Paseos de la Montaña s/n, Lagos de Moreno, Jal., México

[*] Corresponding author email: zerega@cio.mx

ABSTRACT:

In this work we study the venom of two scorpion species: Centrurorides elegans and Centruroides infamatus using Raman spectroscopy. The spectra analysis allows to determine the venoms composition and to establish the main differences among them. It is also shown that the use of Principal Component Analysis may help to tell apart between the two different scorpion species.

Key words: Raman spectra, scorpions.

REFERENCES AND LINKS

[1] L. D. Possani Posta, "El estudio de los componentes del veneno de alacranes en el contexto de la biología molecular, la farmacología y la medicina", *Una ventana al quehacer científico, Instituto de Biotecnología de la UNAM 25 aniversario* **cap 16,** 179–187 (2008).

[2] A. Torres-Larios et al., "Hadrurin, a new antimicrobial peptide from the venom of the scorpion Hadrurus aztecus", *Eur. J. Biochem* **267,** 5023–5031 (2000).

[3] B. Selisko, "An insect-specific toxin from Centruroides noxis Hoffmann. cDNA, primary structure, three-dimensional model and electrostatic surface potentials in comparison with other toxin variants", *Eur. J. Biochem* **242,** 235–242 (1996).

[4] C. García et al., Isolation, characterization and comparison of a novel crustacean toxin with a mammalian toxin from the venom of the scorpion Centruroides noxius Hoffmann, *Comp. Biochem. Physiol. B* **116,** 209– 216 (1997).

1. Introduction

Scorpion can bring benefice to humans, since some scorpion venom are known to have proteins that are now used in the creation of insecticides, vaccines, and protein engineering scaffolds.

In this work the attention is focus on Centruroides, a genus of scorpions belonging to the family Buthidae extensively found on Mexico, with several highly venomous species [1].

Nowadays one of the main problems is to identify and characterize different scorpions species. Since Raman spectra gives chemical information of almost any material (organic and inorganic), it can help to differentiate among several scorpions species analyzing their venom.

2. Results

Scorpions of Guerrero and Guanajuato where recollected and morphologically characterized and labeled to be studied. The venenom samples where obtained giving small electrical shocks near the scorpion telson, and subsequent analyzed on the LabRam HR800 microscope with a laser emitting at 830 nm.

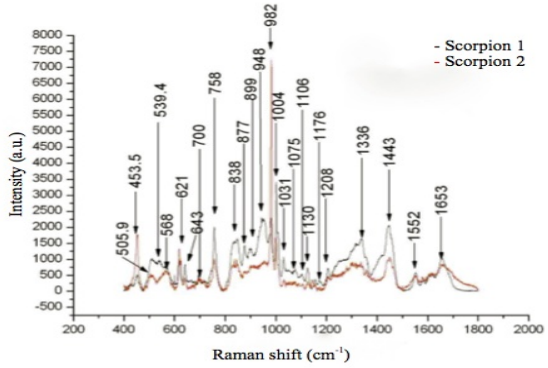

Fig. 1. Average Raman spectra of 5 venom samples of two scorpion species.

The equipment was calibrated by using silica with a characteristic pick at 520 cm^{-1}, and the exploded range cover from 400 to 1800 $cm^{-1}$with an exposition time of 80 seconds. The raman spectra obtained where studied to find similarities and difference between the two species venom (Figure 1), and also used to determine the biomolecules that conform the venoms, and to distinguish the main composition differences.

A mathematical procedure called Principal Component Analysis (PCA) was used to analyze the raman spectra from the two different scorpion species, it allows to tell apart between scorpions by using a small amount of their venom.

Recently some identified proteins were found to have enzymatic action, and some peptides as the hadrurin have antibiotic action [2]. Also, there are a few cancer treatments based on toxins extracted from scorpions venom, that can reduce tumorations and metastasis. Must of the scorpion toxins are not toxic for human beings, but insect and arthropods, in such a way that is becoming a potencial plage control source [3, 4], among many other applications.

3. Conclusions

Raman spectra of several samples of scorpions venom were analyzed. The studied species were Centruroides elegans and Centruroides infamatus, distributed on Guerrero and Guanajuato mexican states, respectively.

It was possible to identify composition differences between the two species by analyzing the spectra and also by using Principal Component Analysis.

We hope that this work can help to the better understanding of the scorpions neurotoxins and their posible pharmacological and medical applications.

Acknowledgements

The author would like to thank J.L. González Solís for his assistance with experimental advice, and to CONACyT (México) and Universidad de Guadalajara for their support.

MEXICAN OPTICS AND PHOTONICS MEETING
19 al 21 de septiembre del 2012
San Luis Potosí, México

Light-by-light polarization control in four-wave mixing in cubic crystals with optical Kerr effect.

G. A. Graciano-Armenta [(1)], A. V. Khomenko [(1)], J. H. Castro-Chacon [(2)], and M. A. García-Zárate [(1)]

1. Departamento de Óptica, Centro de Investigación Científica y de Educación Superior de Ensenada, Baja California, México
2. Instituto de Astronomía, Universidad Nacional Autónoma de México, Ensenada, Baja California, México

Corresponding author email: ggracian@cicese.mx

ABSTRACT:

We present numerical and experimental investigation of all-optical ultrafast polarization control and cross-polarized wave generation using Kerr-nonlinear Bragg gratings induced by a four-wave mixing process in cubic crystals. We show that full control of the diffracted light polarization can be performed by independent change of the recording beams polarization.

Key words: All-optical polarization control, optical Kerr effect, degenerate four-wave mixing, cubic crystal semiconductor, crosspolarized wave generation and beam propagation method.

REFERENCES AND LINKS

[1] R. L. Sutherland, *Handbook of Nonlinear Optics*, Marcel Dekker, New York (2003).

[2] A. Jullien, F. Auge-Rochereau, G. Cheriaux, J. P. Chambaret, P. d'Oliveira, T. Auguste, and F. Falcoz, "High-efficiency, simple setup for pulse cleaning at the milijoule level by nonlinear induced birefringence," Opt. Lett. **29,** 2184–2186 (2004).

[3] K. Sala, M. Richardson, and N. Isenor, "Passive mode locking of lasers with the optical Kerr effect modulator", IEEE J. Quantum Electron. **QE-13,** 915–924 (1977).

[4] Y. Prior, "Three-dimensional phase matching in four-wave mixing", Appl. Opt. **19**, 1741-1743 (1980).

[5] D. C. Hutchings, J. S. Aitchison, and J. M. Arnold, "Nonlinear refractive coupling and vector solitons in anisotropic cubic media", J. Opt. Soc. Am. B. **14**, 869-879 (1997).

[6] R. DeSalvo, M. Sheik-Bahae, A. A. Said, D. J. Hagan, and E. W. Van Stryland, "Z-scan measurements of the anisotropy of nonlinear refraction and absorption in crystals", Opt. Lett. **18**, 194-196 (1993).

---

1. Introduction

In recent years, nonlinear optical effects are attracting attention because they could be used in ultrafast light-by-light control devices [1]. It has been shown how to control the amplitude, phase, wavelength, and polarization of the light. It seems that in this list the polarization is the parameter, which is the most difficult for light-by-light control. Nonlinear ellipse rotation in single beam experimental arrangement has been used for cross-polarized wave generation (XPW) that is used for the contrast-improvement of femtosecond pulses and laser mode-locking [2, 3]. Nevertheless, XPW generation is an effect of self-action and cannot be used for all-optical polarization control.

In this work we study the anisotropic diffraction from Bragg gratings generated in CdTe crystal by picoseconds pulses due to optical Kerr effect. A large and fast nonlinear response of this crystal together with compatibility with many optoelectronic devices promise very fast and compact all-optical devices [1]. We show that anisotropic properties of the Bragg diffraction allow efficient XPW generation and controlling of the diffracted light polarization by changing the polarization of the beams that generate the grating in the crystal.

2. Experiments and numerical calculations

Our experimental setup has forward-box phase matching configuration for the three-pulse degenerate four-wave mixing. Two recording beams are propagated to corners of a three-dimensional phase-matching box and focused into nonlinear crystal. A pump pulse incidents onto the same crystal face with zero-time delay and diffracts from the grating generated by the two recording pulses. The laser source is a Nd:YAG laser (λ = 1064 nm) delivering pulses with a temporal FWHM 120 ps. The intensities and polarization of all three pulses were controlled independently by polarization beam splitters, polarizers, and $\lambda/2$-plates.

In theoretical part of our study we calculated the diffraction efficiency of the grating and the polarization of diffracted light using the vectorial two-dimensional beam propagation method (BPM) adapted for Kerr-nonlinear optical media. To describe the local nonlinearity of the media we use a coupled wave equations presented in the work of Hutchings *et al* [5]. The nonlinear refractive index n_2, two-photon absorption β, and anisotropy coefficient σ of our sample were measured by Z-scan method [6].

3. Results

Figure 1 shows the experimental and numerical results for diffraction efficiency, η, calculated as the ratio between the energy of the diffracted pulse and the energy of the probe beam behind the crystal when the grating is not recorded. The recording and probe beams have linear polarization and light propagates along [100] crystallographic axis. Based on these results we conclude that the polarization of the diffracted beam is linear and rotates almost synchronously with the recording beam polarization angle, θ. We have investigated other configurations and we found that combining the polarizations of incident beams we can obtain diffraction with practically any polarization. Combining the polarization and intensity of incident beams we have achieved a 55.5% of cross-polarized generation and 88.8% of diffracted light at the same polarization than the probe and recording beams.

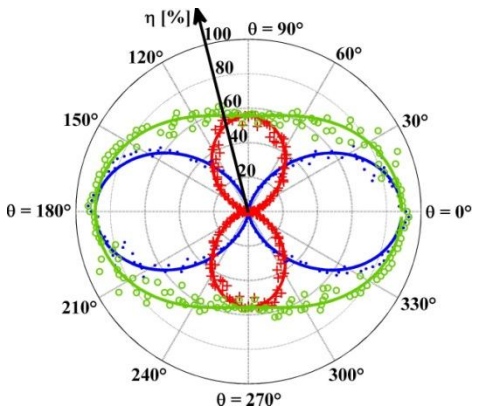

Fig.1. Diffraction efficiency, η, as a function of recording beam polarization angle θ. • is for the polarization component which is parallel to the polarization of probe beam, + is for orthogonal one, o is the overall efficiency. Solid lines are the numerical results.

4. Conclusions

We consider our results as a demonstration of fast all-optical control of short pulse polarization using a degenerate four-wave mixing in cubic nonlinear crystal. Overall efficiency, Γ, of the proposed scheme one can define as the ratio of the diffracted pulse energy and the sum of energies of the pumping and recording pulses. This definition does not include the reflection and linear absorption losses, and Γ is equal to 27.7% for XPW generation and reaches 44.4% for the parallel polarization.

MEXICAN OPTICS AND PHOTONICS MEETING
19 al 21 de septiembre del 2012
San Luis Potosí, México

Acousto-optic interaction in tapered fibers

M. Bello-Jiménez [(1)], A. Díez [(2)], J. L. Cruz [(2)], M. V. Andrés [(2)], A. Rodríguez-Cobos [(1)], G. Ramírez-Flores [(1)]

1. Universidad Autónoma de San Luis Potosí, Inst. de Invest. en Comun. Opt (IICO), S.L.P. 78210, México
2. Universidad de Valencia, Departamento de Física Aplicada, Burjassot, 46100, Valencia, España

Corresponding author email: m.bello@cactus.iico.uaslp.mx

ABSTRACT:

We report an experimental and theoretical study of the acousto-optic interaction in tapered fibers. We focus our attention on the effects of large tapered transitions on the spectral bandwidth. A 3 dB bandwidth of 32 nm is demonstrated in a fiber tapered down to 70 µm diameter and an overall length of 25 cm.

Key words: In-fiber acousto-optic devices, Acousto-optic interaction

REFERENCES AND LINKS

[1] T. A. Birks et. al., "The acousto-optic effect in single-mode fiber tapers and couplers," J. of light. Tech. **14**, 2519-2529 (1996).

[2] Q. Li et al., "Highly efficient acoustooptic tunable filter based on cladding etched single-mode fiber," IEEE Phot. Tech. Lett. **14**, 337-339 (2002).

[3] F. Abrishamian et al., "Design theory and experiment of acousto-optical tunable filter by use of flexural waves applied to thin opical fiber," Opt. Quant. Electron. **40**, 665-676 (2008).

1. Introduction

Tapered acousto-optic filters (TAOF) based on single-mode optical fibers (SMF) are very attractive devices with several applications in optical fiber technology. The operation principle of fiber TAOF relies on the intermodal coupling between the fundamental core mode and the cladding modes of a SMF [1]. When a flexural acoustic wave propagates along an uncoated SMF, it produces a periodical perturbation of the refractive index. As a result, intermodal coupling occurs between the fundamental core mode and some specific asymmetric cladding modes.

Previously, TAOF with long uniform waists have been reported, exhibiting an efficient intermodal mode coupling [2,3]. However, the specific effect of tapered transitions has not been investigated. Here, we investigate the effect of tapered transitions in the spectral response of TAOF. Experimental results demonstrate that TAOF can provide a broaden spectral response that depends on the shape and length of the adiabatic tapers. A spectral bandwidth of 32 nm is demonstrated in a fiber tapered down to 70 µm diameter.

2. Experimental results and discussion

A schematic view of the TAOF is shown in Fig. 1. It consists of a RF source, a piezoelectric disk (PD), an aluminum concentrator horn, and an uncoated tapered SMF. The tapers were prepared using a standard fusion and pulling technique.

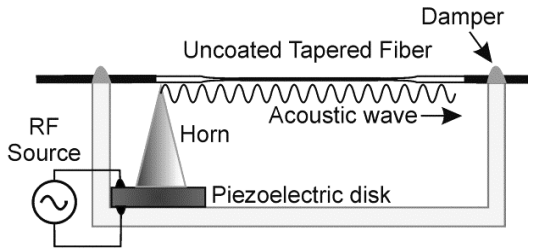

Fig. 1. Experimental setup of the tapered acoustooptic filter (TAOF).

The PD is excited by the RF source to produce an acoustic flexural wave that is transmitted to the fiber by the aluminum horn. At the output, only the light that remains guided by the core mode is transmitted, and the coupling between the fundamental core mode to one of the cladding modes results in the appearance of an attenuation notch in the spectrum.

In the experiments, three fibers were tapered down to a diameter of 90, 80, and 70 µm, respectively. The length of the tapered fiber is 25-cm long in each case, and the taper transition was fabricated with relatively long decaying-exponential profiles. The acoustic wave frequency is selected to produce the maximum transfer of energy between the LP_{01} core mode and the LP_{12} cladding mode. Fig. 2(a) shows the measured optical bandwidth corresponding to 70, 80, and 90 µm TAOF and a non-tapered SMF (125 µm fiber diameter). Fig. 2(b) shows the comparison between the transmission spectra of the non-tapered SMF and the 70 µm TAOF. For these particular cases the acoustic frequency was fixed at 2.37 and 1.125 MHz to obtain optical resonances around 1550 nm, respectively.

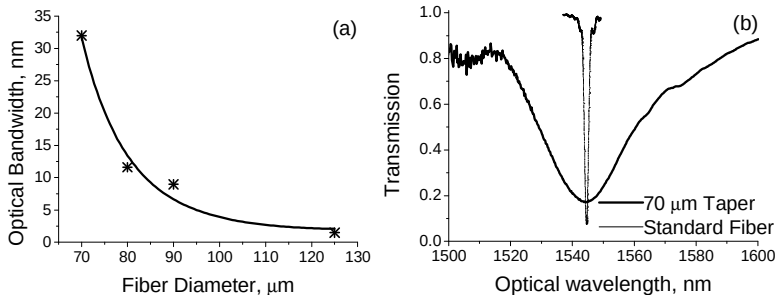

Fig. 2. (a) Measured optical bandwidth of TAOF corresponding to 70, 80, and 90 µm in conjunction with a non-tapered SMF of 125 µm. (b) Comparison of the spectral response between a non-tapered SM fiber and the 70 µm TAOF.

From the theoretical analysis it can be concluded that an important contribution to the spectral broadening is due to the transitions. The change in the fiber radius R produces a gradual variation of the acoustic wavelength, which determines the optical resonant wavelength λ_R. Hence, the tapered transitions can be used to produce a shift of λ_R along the device, broadening the spectral response.

3. Conclusions

We investigate the effect of taper transitions in the spectral response of tapered acousto-optic filters. Experimental results demonstrate that an important increase of the bandwidth can be achieved, which depends on the shape and length of the tapered transitions. From the analysis, we can attribute the enhancement of the optical bandwidth to the tapered transitions. We report a 70 µm TAOF with an enhanced optical bandwidth of 32 nm.

MEXICAN OPTICS AND PHOTONICS MEETING
19 al 21 de septiembre del 2012
San Luis Potosí, México

Noise and artifact characterization of in-vivo Raman spectroscopy skin measurements

Miguel G. Ramírez-Elías [(1)], Javier Alda[(2)] and Francisco J. González[(3)] .

1. Departamento de Estudios Multidisciplinarios, División de Ingenierías Campus Irapuato-Salamanca, Universidad de Guanajuato, C.P. 38940, Yuriria, Gto, Mexico

2. Grupo de óptica aplicada, Escuela de Óptica, Universidad Complutense de Madrid Av. Arcos de Jalón 118, 28037, Madrid, Spain.

3. Coordinación para la Innovación y la Aplicación de la Ciencia y la Tecnología, Universidad Autónoma de San Luis Potosí, Sierra Leona 550, Lomas 2da. Sección, 78210, San Luís Potosí, SLP, México

Corresponding author email: j.alda@opt.ucm.es

ABSTRACT: In this work the principal component analysis (PCA), is used to characterize the noise contribution of the experimental apparatus and two commonly used methods for fluorescence removal used in biomedical Raman spectroscopy measurements.

Key words: Raman spectroscopy; fluorescence; noise; principal components analysis; dermatology

---

REFERENCES AND LINKS

1. R. L. McCreery. Raman spectroscopy for chemical analysis. Wiley-Interscience, 2000.
2. F. J. González, J. Alda, B. Moreno-Cruz, M. Martínez-Escanamé, M. G. Ramírez-Elías, B. Torres-Álvarez, B. Moncada, "Use of Raman spectroscopy for the early detection of filaggrin-related atopic dermatitis". Skin Research and Technology. 2011. 17(1): 45–50.
3. J. T. Motz, S. J. Gandhi, O. R. Scepanovic, A. S. Haka, J. R. Kramer, R. R. Dasari, M. S. Feld, "Real-time Raman system for in vivo disease diagnosis". J. Biomed. Opt. 2005. 10, 031113.
4. E. B. Hanlon, R. Manoharan, T. W. Koo, K. E. Shafer, J. T. Motz, M. Fitzmaurice, J. R. Kramer, I. Itzkan, R. R. Dasari, M. S. Feld. "Prospects for in vivo Raman spectroscopy" Phys. Med. Biol. 2000, 45(2), R1.
5. M. G. Shim, B. C. Wilson. "Development of an In Vivo Raman Spectroscopy System for Diagnostic Applications". J. Raman Spectrosc. 1997. 28(2-3): 131-142.
6. Z. Huang, A. McWilliams, H. Lui, D. I. McLean, S. Lam, H. Zeng. "Near-infrared Raman spectroscopy of lung cancers". Int. J. Cancer. 2003. 107(6): 1047-1052.
7. Z. Huang, H. Lui, X. K. Chen, A. Alajlan, D. I. McLean, H. Zeng, "Raman spectroscopy of in vivo cutaneous melanin". J. Biomed. Opt. 2004. 9: 1198.
8. Z. Huang, H. Zeng, I. Hamzavi, D. I. McLean, H. Lui. "Rapid near infrared spectroscopy system for real-time in vivo skin measurements". Opt. Lett. 2001. 26(22), 1782-1784
9. J. Zhao, H. Lui, D. McLean, H. Zeng. "Automated Autofluorescence Background Subtraction Algorithm for Biomedical Raman Spectroscopy".Appl. Spectrosc. 2007. 61(11): 1225-1232 (2007).

---

1. Introduction

Raman Spectroscopy has been successfully used to analyze biological tissue [1-8], in the case of human skin the shape and position of Raman bands can be used to differentiate between healthy and diseased skin by detecting subtle changes at the molecular level.[2]. In order to simplify the analysis of spectral data this fluorescence background must be removed, the processes used to remove the fluorescence in Raman spectra are complicated due to the complex features associated to the biological Raman spectra. [10] Besides fluorescence, Raman spectroscopy also has a great deal of noise introduced by the equipment used.[1] In this work the noise generated by the instrumentation and the noise introduced by two polynomial fitting methods for fluorescence removal is explored.

2. Materials and methods

2.a Raman measurements

Raman measurements were performed using a portable Raman Systems R3000 spectrometer (Ocean Optics) with a 785-nm laser diode and a spectral nominal resolution of ~8 cm-1. In order to obtain the noise generated by the instrument forty measurements were taken on a Teflon standard. Also forty in-vivo measurements were performed on the skin of the right forearm of a healthy individual in order to evaluate the noise introduced by the fluorescence removal algorithm. All measurements were made under the same conditions, the power used was 90 mW with a 10s integration time. The data obtained from Raman spectroscopy is analyzed using PCA. The two methods for fluorescence removal used in this work were the Polynomial curve fitting (method 1) and the Vancouver Raman Algorithm proposed by Zhao et al. [9] (method 2).

3. Results and discussion

3.a.- Noise and artifacts from the measurement equipment

Figure 1 shows the spectral distribution of the independent principal components. PC#1 is strongly related to the Teflon spectrum (correlation coefficient r= 0.9999). PC#2 has a shape related to the spectral variation of PC#1, therefore this principal component describes the uncertainty in the wavenumber determination. This uncertainty is related with both the spectral line width and the spectral resolution of the experimental equipment. The spectral width defined as the distance between the maximum and the minimum of PC#2 around the locations of the spectral peaks of Teflon was obtained. This calculation shows that the difference is around 10 cm-1. This value is larger than the spectral resolution specified for the instrument (8 cm-1). This discrepancy is caused by the spectral linewidth of the Teflon lines. We may conclude that PCA estimates the uncertainty in the wavenumber determination of the system (sample + instrument) without prior knowledge of it.

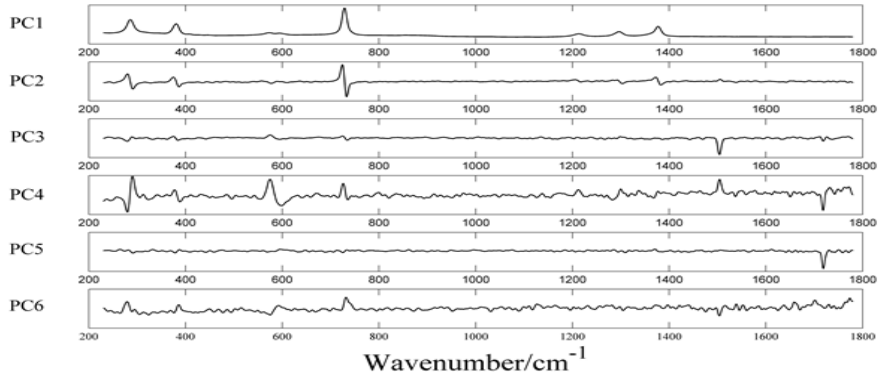

Figure 1. Independent PCs extracted from Teflon Raman spectra. PC#1 (99.94%), PC#2 (0.02%), PC#3 (0.01%), PC#4 (0.01%), PC#5 (0.01%), PC#6 (0.01%).

3.b.-Characterization of fluorescence removal algorithms

In figure 3 we are presenting the eigenvalues associated to the independent PCs. In both cases the first component explains most of the variance: 87.25% (method 1) and 90.94% (method 2). In method 1 only the first two principal components are statistically independent (indicated by a vertical line). In the method 2 the first four components are statistically independent (indicated by a vertical dotted line). These independent PCs explain the 87.35% (method 1) and the 93.94% (method 2) of the variance of the data.

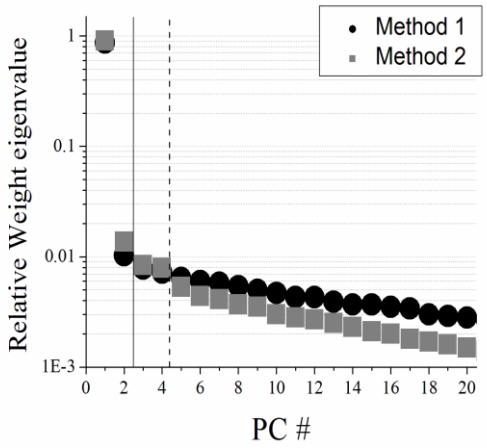

Figure 3. Semilog plot of the relative weight of the eigenvalues of the principal components. Method 1 (black circles) and Method 2 (gray squares).

4. Conclusions

The spectra obtained for the Teflon sample show a very high correlation and PCA extracts 6 independent components. PC#1 is related with the average spectrum of Teflon, PC#2 explains the measured linewidth. The spectral width of the peak is related to the intrinsic spectral linewidth of the Teflon lines, and also to the spectral resolution of the instrument. Comparing the two methods to remove fluorescence, PCA showed that the percentage of variance explained by the independent components in the Method 2 is greater (93.94%) than those of the Method 1 (87.35%). This is due to the percentage of explained variance by the first principal component, in the case of the Method 2 the first component explains the 90.94% of the variance of the data, in comparison to the 87.25% explained by the first component obtained from Method 1. This first principal component can serve as a parameter of how effective is the method to remove fluorescence without losing Raman signal information and to avoid artificial peaks created by the polynomial fit which contributes to the total noise. PCA identifies the additional variability by subtracting variance from the first independent PCs and grouping more PCs into the noise. Thus, from the results obtained in this work, we believe that Method 2 (Vancouver Raman Algorithm) can be considered better than Method 1 (polynomial fit) to remove fluorescence on Raman spectra of human skin.

Acknowledgements

This work was completed during a stay of Miguel Ramirez at the Universidad Complutense de Madrid (Spain). This stay has been funded by the Consejo Nacional de Ciencia y Tecnología (CONACYT) under Becas Mixtas 2010 program.

MEXICAN OPTICS AND PHOTONICS MEETING
19 al 21 de septiembre del 2012
San Luis Potosí, México

Classification of minerals using nonlinear correlation of Raman Spectrum data

José Luis Poom-Medina[(1)], Josué Álvarez-Borrego[(2)]

Depto. de Física Universidad de Sonora[1], Centro de Investigación Científica y de Educación Superior de Ensenada[2]
Corresponding author: josue@cicece.mx

ABSTRACT:
In this work a methodology to recognize minerals by using only phase information of the vectors, obtained for both the target and the problem spectrum vector, is used. In many classification problems of signals and automatic detection of objects, it is necessary to search in spectral database in order to identify objects to make decisions. This algorithm is computationally inexpensive and thus susceptible to be used like a part of the new information technology devices in the field of portable spectrometry or automatic scanning, particularly in the area of the mineralogy and crystallography because the nature of the spectra are of the type Raman.
Key words: Spectral image recognition, nonlinear correlation, spectral signatures, Fourier transform.

REFERENCES AND LINKS

[1] Downs R T (2006). The RRUFF Project: an integrated study of the chemistry, crystallography, Raman and infrared spectroscopy of minerals. Program and Abstracts of the 19th General Meeting of the International Mineralogical Association in Kobe, Japan. 000-13

[2] J. Lerma-Aragón, J. Álvarez-Borrego. "Vectorial signatures for invariant recognition of position, rotation and scale pattern recognition." *JMO*. 56: 1598-1606. (2009).

[3] B.V.K Vijaya-Kumar, L. Hassebrook . "Performance measures for correlation filters," *Appl. Opt.* 29: 2997–3006. (1990).

1. Introduction

In applied physics including digital optics and geosciences is necessary to build efficient data processing equipment to make use of algorithms for pattern recognition to detect objects or chemical compounds in spectrometry of minerals [1], with low cost computational, which is one of the main requirements in an automated computer vision scanning using autonomous machines[2-3]. In this work a method to classify different kind of minerals by using identity vectors signatures of spectra minerals is used. To facilitate the automatic identification of patterns in minerals, information from optical spectrometry useful for identification of different objects which has proved to be useful in pattern recognition is used. The algorithm uses non linear correlation applied to the identification of spectra minerals in a set of spectra, which can be extended to searches in a spectral database of N records.

2. Methodology

The procedure used in this work uses the phase of the reference data and is compared with the phase only of the data or vector of the mineral to be recognized. The nonlinear correlation can be expressed like

$$C_{NL} = \Im^{-1}\left[\exp\left[i\phi\right]\bullet\exp\left[-i\varphi\right]\right], \tag{1}$$

where ϕ is the phase of the vector of the mineral to be classified, φ is the phase of the mineral reference vector and $\Im^{-1}$ is the inverse Fourier transform.

2. a Identity vectors signatures.

The mineral to be recognized is denoted by $f(x)$ which is a vector representation or the Raman spectrum of the mineral (Fig. 1). Each mineral is represented by a unique Raman spectrum.

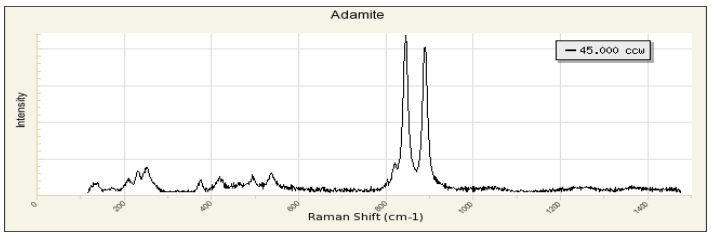

Fig. 1 Example of Raman spectrum of the mineral from RRUFF database

3. Results.

To evaluate the performance of this computational system, 10 test Raman spectra of different materials were used and downloaded from RRUFF project. The results for different instances of records used to recognize a spectrum target have a confidence level above 95.4% in all the cases. Each Raman spectrum used in the classification could be recognized above this confidence level.

4. Conclusion.

The system presented is an excellent alternative for the development embedded software in hardware vision devices for automatic recognition of spectra in site where the samples and information is processed. This work is addressed in the direction of applying the new information technologies to the traditional ways of processing information in important areas such as pattern recognition in mineralogy, particularly for the development of portable detection instruments that require autonomous high performance and low computational costs that allows the analysis at the site of the objects, allowing the identification and characterization of the environment immediately surrounding the sampling area.

Acknowledgement

The authors give thanks to RRUFF project by to permit get a set his collected data for identification of minerals both on earth and planetary exploration. This document is based on work partially supported by CONACyT under Grant No. 102007.

MEXICAN OPTICS AND PHOTONICS MEETING
19 al 21 de septiembre del 2012
San Luis Potosí, México

Nonlinear Optical Response of colloidal and films gold nanoparticles synthesized by Chitosan

A. Balbuena Ortega[1*], M.L. Arroyo Carrasco[1], V. L. Gayou[2], A. Orduña Díaz[2], R. Delgado Macuil[2] and M. D. Iturbe Castillo[3]

[1]Facultad de Ciencias Físico-Matemáticas, Benemérita Universidad Autónoma de Puebla, Av. San Claudio y 18 Sur. Col San Manuel, C.P. 72570, Puebla, Puebla, México.
[2]CIBA-IPN Tlaxcala, Km. 1.5 Carretera Estatal Tecuexcomac-Tepetitla. Tepetitla de Lardizabal, Tlaxcala, México. C.P. 90700.
[3]Instituto Nacional de Astrofísica, Óptica y Electrónica, Luis Enrique Erro # 1, C.P. 72840 Tonantzintla, Puebla, México.

**abalbuena1984@gmail.com*

ABSTRACT.
In this work Z-scan curves were obtained for colloidal and film samples of gold nanoparticles synthesized with chitosan. Under similar conditions the film samples showed a bigger response than the colloids. The results were reproduced and compared with a phenomenological model which takes into account the nonlocal character of the interaction, in order to estimate the refractive index change. Films were obtained adding hydroxypropyl methyl cellulose (HPMC) and sorbitol to the solution. Measures were done with an Argon-ion cw laser at a wavelength of 514 nm and powers of mW.
Keywords: Gold nanoparticles, nonlinear optics, z-scan.

REFERENCES AND LINKS

[1]. Esumi, K.; Takei, N.; Yoshimura, T. *Colloids Surf. B: Biointerfaces* **32**, 117 (2003),.
[2]. Bhumkar, Devika Joshi, Hrushikesh Sastry, Murali Pokharkar, Varsha Chitosan Reduced Gold Nanoparticles as Novel Carriers for Transmucosal Delivery of Insulin ,Pharmaceutical Research **24** 8 p1415-1426 (2007)
[3]. Sheik-bahae, A.A. Said and E.W. Van Stryland, "High-sensitivity, single-beam n2 measurements" Opt. Lett., **14** (17), 955-957 (1989).

1. Introduction

The synthesis of Nanoparticles with different chemical composition and size distribution is an important area of research in nanotechnology. Concerning the synthesis of metal nanoparticles, especially gold nanoparticles, many methods have been proposed in the literature [1]. In the latest years biomolecules and bioorganisms were also used in the synthesis of nanomaterials [2].
Chitosan is a derivative of chitin polyelectrolyte a linear polysaccharide chain composed of randomly distributed β-(1-4) D-glucosamine (deacetylated units) and N-acetyl-D-glucosamine (acetylated unit). This is a biodegradable polysaccharide obtained by deacetylation of chitin (66 to 95% deacetylation), which is the basic structure in the exoskeletons of crustaceans (crayfish, shrimp etc).
Disadvantages of the generation of chitosan-based supports are their mechanical properties, so that many times it has been tried to incorporate other elements for improvement. Within these elements is the hydroxypropyl methyl cellulose (HPMC).
In this work, employing the Z-scan technique and a phenomenological model [3], we measure the nonlinear refractive index change of gold nanoparticles in colloidal solutions and deposited in polymer films made from chitosan and HPMC.

2. Nanoparticles synthesis and film deposit

Chitosan, HPMC, Hydrochloroauric acid, Sorbitol and sodium phosphate pentabasic were purchased from sigma Aldrich while acetic acid and tribasic sodium phosphate were purchased from Baker. The stock solutions of chitosan 1%(w/v) in acetic acid 1%, gold solution at 1 mM, sodium phosphate pentabasic at 0.75mgr/ml, sorbitol at 1% and HPMC at 0.5% was prepared. The colloidal solution was prepared mixing the solutions of chitosan 1%, sodium phosphate pentabasic and gold solution. Then, this solution was heated to 70ºC under stirring at 500rpm using termomixer, and the reaction was carried out for another 90min after the color of the solution turned from yellow to red. For the preparation of polymeric films with the incorporation of gold nanoparticles, the procedure was as follows: obtained colloidal solution to be added HMPC and sorbitol at different concentrations stirred at 500rpm at 90ºC for 15 min. Once the mixture was completed with all

components is deposited a drop on a glass slide with a temperature of 70 ° C and remained there for 5 min to remove later and allow it to cools, and completely evaporate the liquid. The sample is easily removed from the surface of the glass slide

3. Phenomenological model

The model used to characterize the samples considers a Gaussian beam propagating in the *Z* direction, at some distance *z* it illuminates a thin nonlinear sample with a field amplitude $E(r,z)$, then the field at the exit of the medium can be written as;

$$E_{out} = E(r,z)\exp(-i\Delta\phi(r)) \ , \qquad (1)$$

where $\Delta\phi(r)$ is the nonlinear phase change and it is proposed as :

$$\Delta\phi(r) \approx \Delta\phi_0(z,m)\exp\left(-mr^2/w(z)^2\right), \qquad (2)$$

and

$$\Delta\phi_0(z,m) = \frac{\Delta\Phi_0}{(1+(z/z_0)^2)^{m/2}}, \qquad (3)$$

here, $\Delta\Phi_0$ is the maximum on axis photoinduced phase shift in the beam after the nonlinear medium located at $z=0$ and m can be any real positive number. The locality or non locality of the medium is implied in the m value, only for $m = 2$ the nonlinear phase change follows the intensity distribution and then the response of the material is considered as local.

4. Experimental Results

The change in the nonlinear index of refraction of the films and colloids were investigated with the Z-scan technique. Typical curves are shown in; figure 1.a) films and figure 1.b) colloids.

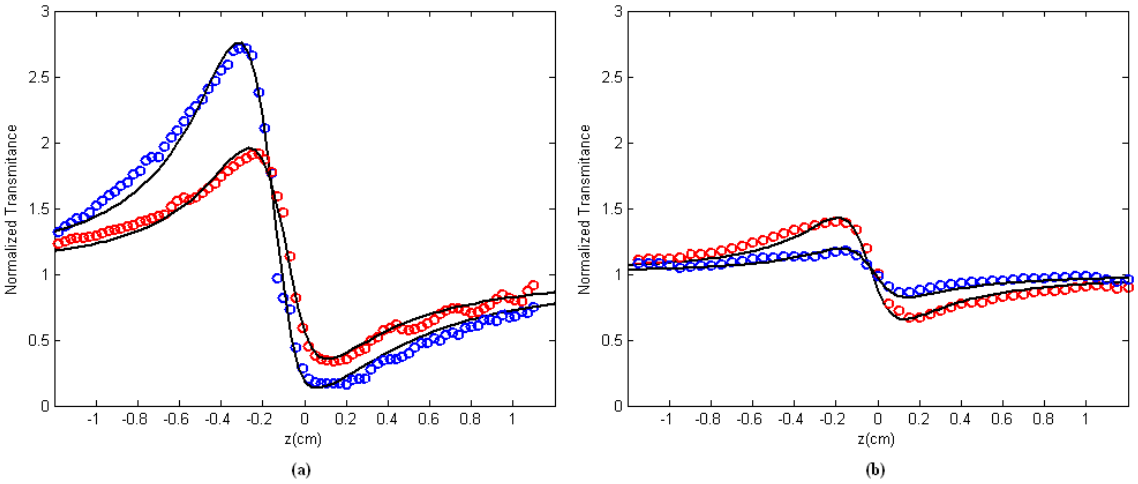

Figure1. Typical Z-scan curves for: a) films and b) colloids samples, with a power of 5 mW (blue) and 10 mW (red). Source Argon-ion CW laser, wavelength of 514 nm. Black line is the theoretical reproduction.

We can observe that the change in the nonlinear index of refraction of film is larger than in colloid, even when the thickness of the film (~ 500 μm) was lower than the colloid (~ 1 mm). It is interesting to observe that in film results a better response is obtained with a low power, it is indicative of a saturation behavior which is currently studied. The curves were reproduced with the phenomenological model described in [3], black lines in figure 1. The m value necessary for the reproductions was $m=0.5$. For the film with 5 mW, $\Delta\Phi_0 = -1.7\pi$ and for 10 mW, $\Delta\Phi 0 = -\pi$. For the colloid with 5 mW, $\Delta\Phi_0 = -0.25\pi$ and for 10 mW, $\Delta\Phi_0 = -0.4\ \pi$.

5. Conclusions

Gold nanoparticles were successfully synthesized using chitosan and polymer films were obtained with gold nanoparticles incorporated. From the m value of the curves reproductions we can conclude that the response has a non local character. It is obtained a larger nonlinear index change in films than in colloids. An interesting result in film is that the larger response is obtained with the low power.

MEXICAN OPTICS AND PHOTONICS MEETING
19 al 21 de septiembre del 2012
San Luis Potosí, México

Classification of Calcium Carbonate Minerals by Raman Spectroscopy and Principal Component Analysis

*M.A. Meneses-Nava[1], J. Robles-Camacho[2] , O. Barbosa-García[1], J.L. Maldonado[1], G. Ramos-Ortiz[1], I.R. Rosas-Román[1]

[1] Centro de Investigaciones en Óptica, León, Gto., México. [2] Laboratorio de Arqueometría del Occidente. Centro INAH Michoacán. Instituto Nacional de Antropología e Historia. * Corresponding author email: tono@cio.mx

ABSTRACT:

Calcium carbonate is the main component of a large variety of rocks used in sculpture and architecture along the human history. A large quantity of this objects are placed outdoors and suffer damage because acid rain, transforming the rock into calcium sulfate. The rate of damage varies, depending on the specific type of rock i.e. limestone, marble, travertine, etc., and a method for material identification is needed in order to give the proper treatment for preservation. Raman spectroscopy provides preparation less and rapid analysis of minerals; however, all calcium carbonate based objects present very similar spectra which are very difficult to differentiate. A methodology for classification based on Principal Component Analysis (PCA) is proposed, in order to accomplish better results

Key words: Raman Spectroscopy, Principal Component Analysis

REFERENCES AND LINKS

[1] Itzel Isunza Manrique, M.A. Meneses-Nava, J. Robles-Camacho, O. Barbosa-García, G. Ramos-Ortiz, J.L. Maldonado, Monitoreo del efecto de lluvia ácida en materiales calcáreos mediante espectroscopia Raman, IX Encuentro Participación de la Mujer en la Ciencia, León, Gto., México, Mayo 2012, ISBN: 978-607-95228-2-7

[2] Miroslav Morhac and Vladislav Matousek, Peak Clipping Algorithms for Background Estimation in Spectroscopic Data, Applied Spectroscopy, 2008, Vol. 62, Number 1, p91-106

1. Introduction

Carbonate minerals have as their anionic structure the anion CO_3^{-2}, where Calcium Carbonate $CaCO_3$, known as Calcite, is the most abundant. Depending of their paragenesis, this compound crystallizes in several structures, which have been employed in art and construction by many civilizations.

The deterioration in historical buildings and sculptures produced by acid rain is well known, transforming Calcium Carbonate in Calcium Sulfate, a water soluble compound. A previous study shows that Calcium Carbonate minerals, such as marble, travertine and limestone, show different degradation rates [1]. For this reason, a methodology that improves the classification is needed, in order to provide a tool that helps to schedule maintenance programs.

2.1 Experimental setup

The spectroscopic data has been acquired with a homemade Raman spectrometer build at CIO. It employs a 785 nm laser source, a Volume Phase Grating (VPG) spectrometer with a resolution of 6 cm-1, with a cooled CCD detector, as shown in figure 1, and the software for data processing has been also developed.

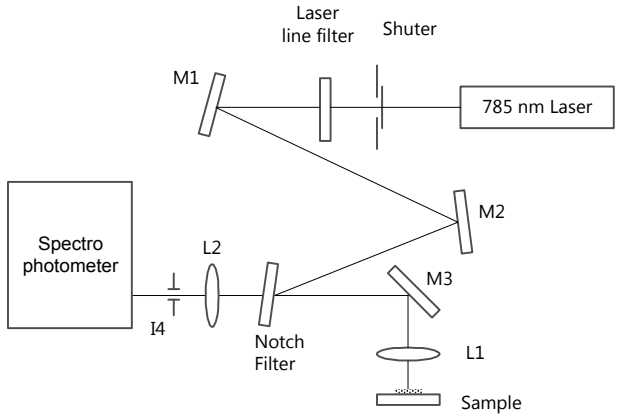

Figure 1. Raman Spectrometer Schematic.

2.2 Results

Several spectra at different regions of the same sample were taken, then the signals were smoothed and the background is eliminated using the SNIP algorithm [2]. Figure 2 shows the normalized spectra from marble, travertine and limestone. It can be seen that the spectra are nearly identical, and the small differences in peak widths and heights are difficult to quantify for proper material identification.

Principal Component Analysis (PCA) highlights subtle similarities and differences in data sets. Visual representations of the results are depicted in Figure 3, where the first two PCA's are plotted and it clearly shows regions where spectral data of the calcium carbonate minerals are grouped according to their paragenesis.

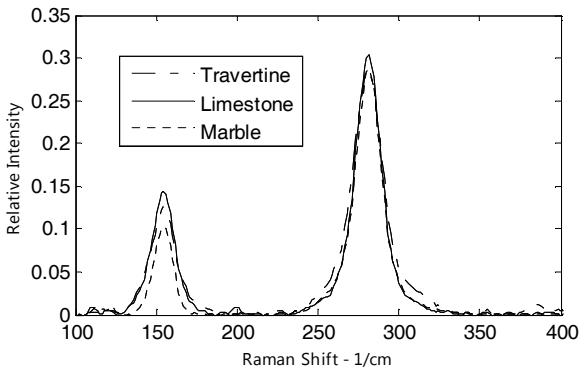

Figure 2. Travertine, Limestone and Marble spectra comparison.

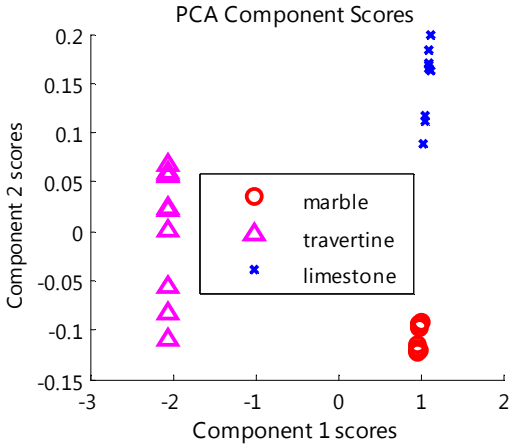

Figure 3. PCA analysis results.

3. Conclusions

Raman spectroscopy together with PCA analysis can effectively be used as a tool to differentiate minerals with same composition but different paragenesis, as has been shown for calcium carbonate based minerals.

MEXICAN OPTICS AND PHOTONICS MEETING
19 al 21 de septiembre del 2012
San Luis Potosí, México

Tinkerbell beam in a Ring Resonator

V. Aboites

Centro de Investigaciones en Optica
Loma del Bosque 115
Col. Campestre
Leon, Gto.
Mexico 37150
Corresponding author email: aboites@cio.mx

ABSTRACT:

In this article the dynamical behaviour of a beam that spatially behaves according to a Tinkerbell map (i. e. Tinkerbell beam), within a ring phase-conjugated resonator is modelled. The ABCD matrix of an optical device able to generate a two dimensional Tinkerbell map is found in terms of the map parameters, the state variables and the resonator parameters. For the first time to our knowledge the dynamics of a beam behaving according to a Tinkerbell map is found within an optical resonator.

Key words: resonator, Tinkerbell map, phase conjugated mirror

REFERENCES AND LINKS

[1] Aboites V *Int. J. of Pure and App. Math.* **36** (4) 345 (2007)

[2] Aboites V, Pisarchik A N, Kiryanov A and Gomez-Mont X *Opt. Comm.* **283**, 3328 (2010)

1. Introduction

In this work the dynamical behaviour of a beam that spatially behaves accordingly to a Tinkerbell map (i. e. Tinkerbell beam), within a ring phase-conjugated resonator is modelled. It is shown that the behaviour of a beam within a ring optical resonator may be well described by a Tinkerbell map and the necessary conditions for its occurrence are discussed. The state of the beam, as well as the iterative map, is determined by its previous state. In particular, it stands out that the introduction of a specific intracavity element within a ring phase-conjugated resonator may produce beams described by a Tinkerbell map, which we call from now on "Tinkerbell beams". The idea of describing chaotic optical resonators through the introduction of map generating elements from a mathematical viewpoint was already explored elsewhere [1,2]. The approach to the Tinkerbell map is taken into account due to its experimental viability, the final mathematical description for the Tinkerbell beams generator makes us think that it can be physically constructed.

2. Ring phase-conjugated resonator with Tinkerbell dynamics

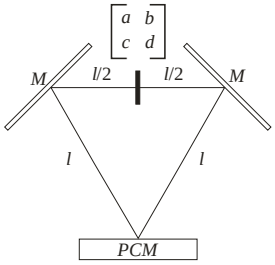

Figure 1. Ring phase conjugated laser resonator with a chaos generating element.

The total transformation ABCD matrix for a complete round trip is calculated as:

$$\begin{pmatrix} A & B \\ C & D \end{pmatrix} = \begin{pmatrix} 1 & 0 \\ 0 & -1 \end{pmatrix}\begin{pmatrix} 1 & l \\ 0 & 1 \end{pmatrix}\begin{pmatrix} 1 & 0 \\ 0 & 1 \end{pmatrix}\begin{pmatrix} 1 & l/2 \\ 0 & 1 \end{pmatrix}\begin{pmatrix} a & b \\ c & d \end{pmatrix}\begin{pmatrix} 1 & l/2 \\ 0 & 1 \end{pmatrix}\begin{pmatrix} 1 & 0 \\ 0 & 1 \end{pmatrix}\begin{pmatrix} 1 & l \\ 0 & 1 \end{pmatrix}. \quad (1)$$

The resulting matrix is:

$$\begin{pmatrix} A & B \\ C & D \end{pmatrix} = \begin{pmatrix} a+\dfrac{3cl}{2} & b+\dfrac{3l}{4}\left(2a+3cl+2d\right) \\ -c & -\left(d+\dfrac{3cl}{2}\right) \end{pmatrix}. \quad (2)$$

If one does want a particular map to be reproduced by a ray in the optical resonator, each round trip described by (y_n, θ_n), has to be considered as an iteration of the selected map. In order to obtain Tinkerbell beams, Eq. (11) must be equated to Eq. (13), that is:

$$a+\frac{3cl}{2} = \alpha + y_n, \quad (3)$$

$$b+\frac{3l}{4}\left(2a+3cl+2d\right) = \beta - \theta_n, \quad (4)$$

$$c = -\gamma - 2\theta_n, \quad (5)$$

$$d+\frac{3cl}{2} = -\delta, \quad (6)$$

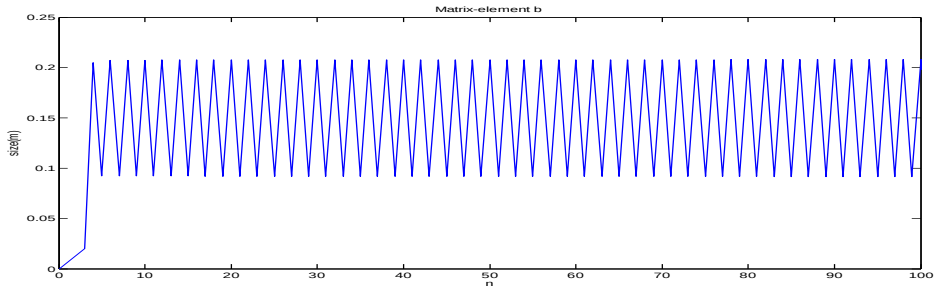

Figure 2. Computer calculation of the magnitude of matrix element b of the Tinkerbell map generating device for a resonator with l = 1 and Tinkerbell parameters α = 0, β = -0.6, γ = 0 and δ = -1 for the first 100 round trips.

5. Conclusions

This article shows how Tinkerbell beams can be produced if a particular device is introduced in a ring optical phase-conjugated resonator.

MEXICAN OPTICS AND PHOTONICS MEETING
19 al 21 de septiembre del 2012
San Luis Potosí, México

Real-time Anisotropic Reflectance Spectroscopy: MBE growth of $Al_xGa_{1-x}As$ on GaAs (001)

K. Hernández Vidales, L. E. Tapia Rodríguez, J. Ortega Gallegos, O. Núñez Olvera, A. Armenta-Franco, A. Lastras Martínez, L. F. Lastras Martínez and R. E. Balderas Navarro

Instituto de Investigación en Comunicación Optica, Universidad Autónoma de San Luis Potosí, Alvaro Obregón 64, San Luis Potosí, México
Corresponding author email: jortega@cactus.iico.uaslp.mx

ABSTRACT:

We report on an experimental study of the evolution of the reflectance anisotropy (RA) spectrum during the first stages of the molecular beam epitaxial growth of $Al_xGa_{1-x}As$ films on GaAs (001) substrates. To carry out real-time RD measurements we employed a 32-channel rapid reflectance anisotropy spectrometer with a spectrum acquisition time of 0.5 s. RA measurements were carried out simultaneously with Reflection High Energy Electron Diffraction (RHEED) measurements in order to establish a correlation between the information provided for each techniques. We show that RD spectroscopy constitutes a sensitive tool to characterize the epitaxial growth of $Al_xGa_{1-x}As$ on GaAs (001) substrates. Information provided for RD spectroscopy results complementary to that provided by RHEED.

Key words:

REFERENCES AND LINKS

[1] O. Nuñez Olvera *et al.*, to be published.

1. Introduction

The heterointerface GaAs-AlxGa1-xAs has played a fundamental role in the development of light-emitting semiconductors devices. AlxGa1-xAs alloys can be grown with direct energy gaps up to 1.9 eV. This permits the fabrication of red-emitting LED´s and lasers. Furthermore, interfaces between these two semiconductors can be grown with low roughness, thus allowing for the growth of ultrathin quantum wells. Understanding roughness formation and dynamics in MBE conditions is of crucial importance because it influences the optical emission properties of devices. As a matter of fact, in single quantum wells, two or more lines related to the same quantum level can occur, which can be accounted for the existence of bimodal interface roughness. In this work we report on a reflectance-anisotropy (RA) study of the first stages of the growth of AlxGa1-xAs on GaAs (001) substrates. We show that reflectance anisotropy spectroscopy (RAS) provides information on the evolution of the GaAs-AlxGa1-xAs heterointerface at submonolayer coverage.

2. Setup and Results

Experiments were carried out in a molecular beam epitaxy chamber (Riber 32) equipped with solid-source effusion cells. Attached to the growth chamber there are both a RHEED system and a rapid reflectance-anisotropy (RA) spectrometer. The RAS spectrometer allows us to measure real-time differential reflectance anisotropy spectra during epitaxial growth, thus providing real-time information on surface phenomena taking place during growth. RA and RHEED instruments can be operated simultaneously. The RA spectrometer [1] is based on a 10 cm focal length monochromator (Jobin Yvon MicroHR) with a spectral range from 150-450 nm, and a 32-channel photomultiplier

array (Hamamatsu H7260). The 32 outputs of the photomultiplier are multiplexed into the input of a lock-in amplifier (Stanford Research SR530). Channel multiplexing is carried out with two 16-channel analog multiplexor cards (MAXIM MAX306CPI). Both the analog input (R) and the analog output (ΔR) of the lock-in amplifier are digitized by a 16-bit data acquisition card (National Instruments NI-PCI 6221).

AlGaAs Epitaxial grow was carried out with As_4 on semi insulating GaAs (001) substrates. Prior to grow the oxide in the GaAs substrate was desorbed at 580 ^oC in the presence of an arsenic flux of 5×10^{-6} torr. After desorption, a 0.3μm -thick GaAs layer was grown at a temperature of 580 ^oC. The substrate temperature was then lowered to 530 ^oC to initiate experiments on $Al_xGa_{1-x}As$ deposition.

In figure 1 we show RD spectra taken during the epitaxial deposition of Al0.3Ga0.7As files on GaAs (001) substrates. Growth was carried out with a deposition rate of 0.4 ml/s. Al0.3Ga0.7As at t=13 s and ends at t=50 s for a final thickness of about 40 angstroms. As we can see from figure 1, previous to epitaxial growth, the RD spectrum shows the deep minimum around 2.6 eV that is characteristic of c(4x4) reconstructed surfaces. At the onset of the $Al_{0.3}Ga_{0.7}As$ epitaxial growth, the RD spectrum shows rapid changes. It first decreases in amplitude and almost flattens out as the GaAs surface reaches half $Al_{0.3}Ga_{0.7}As$ coverage. Afterwards, it shows a lower rate of change as it evolves toward the RD spectrum characteristic of the $Al_{0.3}Ga_{0.7}As$ surface. We note that RD line shape evolution does not stop with the end of epitaxial growth but it persists for about one more minute afterwards. We further note that, despite the fact that the light penetration depth (about 180 angstroms) is larger than the final $Al_{0.3}Ga_{0.7}As$ thickness, the GaAs RD spectrum does not show up at the end of the growth. This fact indicates that the GaAs-$Al_{0.3}Ga_{0.7}As$ interface is isotropic to a large extent.

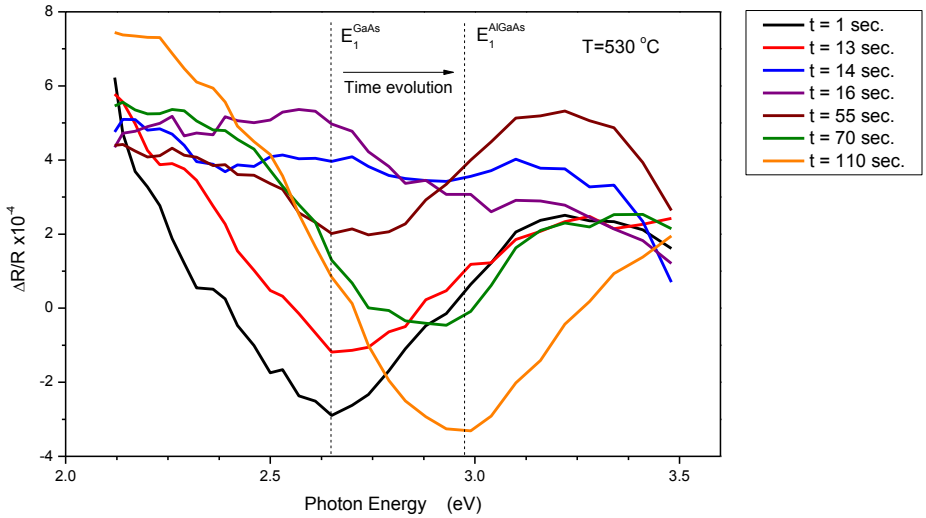

Fig.1. Different typical RA spectra measured during the deposition process of $Al_{0.3}Ga_{0.7}As$ / GaAs at a temperature of 530 ^oC. The deposition began at 13 sec., ending at 50 sec., at a growth rate of 0.4 mL/ s. Note that the remaining time accounts for the formation of a new feature related to surface reconstruction.

3. Conclusions

This paper shows that rapid RAS spectroscopy is a powerful tool for the in situ, real time monitoring of the first stages of the epitaxial growth of $Al_xGa_{1-x}As$ on GaAs (001). We expect it can be used to characterize the growth of $Al_xGa_{1-x}As$-GaAs interfaces, specifically to monitor interface roughness.

MEXICAN OPTICS AND PHOTONICS MEETING
19 al 21 de septiembre del 2012
San Luis Potosí, México

Thickness dependence of the nonlinear optical response of Ag nanoparticles embedded in SiO_2

Héctor Sánchez-Esquivel[(1)*], Raúl Rangel-Rojo[(1)], Alicia Oliver[(2)], Luis Rodríguez-Fernández[(2)]

1. Centro de Investigación Científica y de Educación Superior de Ensenada, Carretera Ensenada-Tijuana No. 3918, C.P. 22860, Ensenada, B.C., México
2. Instituto de Física, Universidad Nacional Autónoma de México,Circuito de la Investigación Científica S/N, Ciudad Universitaria,Distrito Federal, Mexico

hecsan@cicese.edu.mx

ABSTRACT:

We present the study of the third order nonlinear response in spherical Ag nanoparticles in silica with different thicknesses. The refractive and absorptive contributions to the nonlinearity were resolved using the z-scan technique with fs pulses

Key words: Third Order Nonlinearity, Silver Nanoparticles, Z-scan technique, ultrafast lasers

REFERENCES AND LINKS

[1] Rangel-Rojo, R., McCarthy, J., Bookey, H. T., Kar, A. K., Rodriguez-Fernandez, L., Cheang-Wong, J. C., Crespo-Sosa, A., et al. (2009). Anisotropy in the nonlinear absorption of elongated silver nanoparticles in silica, probed by femtosecond pulses. *Optics Communications*, *282*(9), 1909-1912. doi:10.1016/j.optcom.2009.01.048

[2] Meldrum, A., L_opez, R., Magruder, R., Boatner, L., y White, CStructure and properties of nanoparticles formed by ion implantation. Topics in Appl. Phys., 116, 255-285. (2010)

[3] Sheik-Bahae, M., Said, A. A., Wei, T. H., Hagan, D. J., & Van Stryland, E. W. (1990). Sensitive measurement of optical nonlinearities using a single beam. *IEEE Journal of Quantum Electronics*, *26*(4), 760-769. IEEE. doi:10.1109/3.53394

1. Introduction

Nanostructured materials have attracted attention for their potential applications in optical systems, particularly in the development of all optical switching devices, which are based on their nonlinear optical properties, particularly the third-order one. Metallic nanoparticles embedded in dielectric matrices such as SiO_2, have shown large nonlinearities with ps response times [1]. The size, shape, alignment and composition of the nanoparticles determine the third order susceptibility of the composite material [2]. The nonlinear properties of interest are both the real and imaginary parts of $\chi^{(3)}$, related to the nonlinear refractive index n_2 and the two photon absorption coefficient respectively. The z-scan technique with fs pulses allows us to resolve the absorptive and refractive contributions to the nonlinearity of a material.

Our samples are two Silica (SiO_2) substrates containing spherical Ag nanoparticles with different nanoparticle layer thicknesses. These samples are produced by ion implantation method, using a 3 MV Tandem accelerator (NEC9SDH-2 Pelletron) at the Institute of Physics at UNAM. For sample one, the ions were implanted at 4MeV resulting in a 500nm thick nanoparticle layer, while for sample two, three different implantations at 4MeV, 5MeV

and 6MeV were used, resulting in an approximately 1.4um thick nanoparticle layer. Both samples were thermically annealed at 600°C. Figure 1 shows the linear absorption spectra for both samples. In this work, we focused on the study of these samples using a Ti:Sapphire pulsed laser with a wavelength centered at 830nm, producing pulses with a duration of 73 fs at FWHM and a 94 MHz of pulse rate.

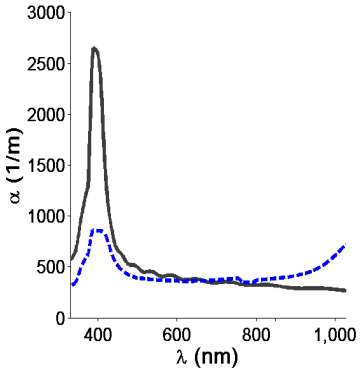

Figure 1:Absorption spectra for sample one with one implantation (solid) and sample two with multiple implantation (dashed)

2. Results

We observed saturable absorption in sample one, negligible nonlinear absorption for sample two and positive nonlinear refraction for both samples. We obtained enough data to estimate the n_2 of sample one, found to be 0.83cm^2/GW. The following traces were found (figure 2a and 2b) for sample one.

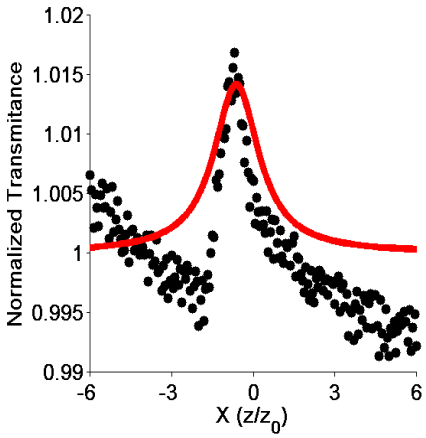

Figure 2a: Saturable absorption is clearly seen on open aperture trace

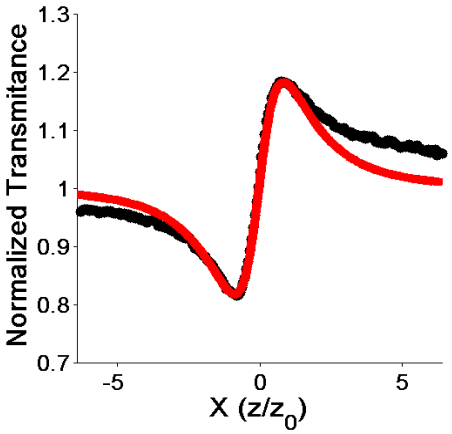

Figure 2b: Positive nonlinear refraction is clearly seen on closed aperture trace

3. Conclusions

We characterized the nonlinear optical properties of structured Ag nanoparticles in SiO_2. We found a positive n_2 for sample one and sample 2. We found saturable absorption for both samples.

MEXICAN OPTICS AND PHOTONICS MEETING
19 al 21 de septiembre del 2012
San Luis Potosí, México

Transient-Thermo-Reflectance for the study of surface carrier dynamics

B.G. Pérez-Hernández [(1)], J. Garduño-Mejía [(1)], C. J. Román-Moreno [(1)], O. G. Morales-Saavedra [(1)] and R. Ortega-Martínez [(1)].

CCADET-UNAM, Apdo. Postal 70-186, C.P. 04510. Coyoacán, Cd. Universitaria, México D. F.
Corresponding author email: jesus.garduno@ccadet.unam.mx.mx

ABSTRACT:

In this work we present a non-destructive examination (NDE) pump-probe technique known as Transient-Thermo-Reflectance (TTR) for the study of transient carrier dynamics in semiconductor and metal surfaces. The technique enables to monitor the change in reflectance at the sample surface as a function of time on the femtosecond time regime. Changes in reflectance can then be used to determine properties of the sample. Experimental results are compared with numerical model calculations.

Keywords: ultrafast optics, femtosecond time resolved spectroscopy.

REFERENCES AND LINKS

[1] P. M. Norris, A. P. Caffrey, R. J. Stevens, J. M. Klopf, J. T. McLeskey Jr. and A. N. Smith, "Femtosecond pump–probe nondestructive examination of materials". *Rev. Sci. Inst.* 74, (1), pp. 400-406, 2003.

[2] J. Garduño-Mejía, M. P. Higlett and S. R. Meech, "Modelling the influence of nonthermal electron dynamics in thin and ultrathin gold films". *Chemical Physics*, 341, pp. 276–284, 2007.

[3] C.K. Sun, F. Vallee, L.H. Acioli, E.P. Ippen and J.G. Fujimoto, Physical, "Femtosecond Tunable Measurement of Electron Thermalization in Gold". *Phys. Rev. B,* 50, (20), pp. 15337-15348, 1994.

[4] S. K. Sundaram and E. Mazur, "Inducing and probing non-thermal transitions in semiconductors using femtosecond laser pulses", *Nature*, 1, pp. 217-224, 2002

1. Introduction

Ultrashort pulsed lasers have been demonstrated as effective tools for the non-destructive examination (NDE) of energy transport properties in thin film samples, in particular for the investigation of transient dynamics as well as nonlinear optical properties in semiconductors and metals. A good alternative for the NDE pump-probe technique is known as Transient-Thermo-Reflectance (TTR) for the study of transient dynamics in semiconductor and metal materials [1]. The technique enables to monitor the change in reflectance at the sample surface as a function of time on a sub-picosecond time scale. Changes in reflectance can then be used to determine properties of the sample. In the case of metals, the change in reflectance is related to changes in temperature and strain. The transient temperature profile at the surface is then used to estimates the rate of energy transfer and coupling factor between the electron and phonon as well as the thermal properties of the material [1-3]. In the case of semiconductors, the change in the reflectance is related with local electronic state changes and temperature [4].

2. Experimental Setup

In TTR technique a femtosecond pulse is split into an intense heating pulse and a weaker probe pulse. The heating pulse is used to generate the transient event to be observed. Control of the optical path length of the probe pulse produces a variable time delay between the pump and probe pulses. The probe then takes a snapshot of the reflectance at a specific experimental time delay relative to the pump, with a temporal resolution on the order of the probe pulse duration. In our case delayed line is capable to produce time steps of 3 fs. Pulses from a self-mode-locked femtosecond Ti:sapphire laser delivering 200 fs, centered at 810 nm (Coherent MIRA-900) were divided in the pump and probe with a wedged window. The pump beam passes through a chopper, creating a modulated pulse train at a prescribed frequency of 2 KHz, which will drive the reference frequency an phase of a Lock-In amplifier. The non collinear pump and probe beams are focused to a spot size of about 5 μm at an incident angle of 45° from normal. Corresponding pump excitation fluence is up to 6 mJ/cm^2.

3. Results

Preliminary time resolved spectroscopy results using the TTR technique are presented using GaAs and Au sample with 5 nm thickness deposited on a glass substrate in figure 1.

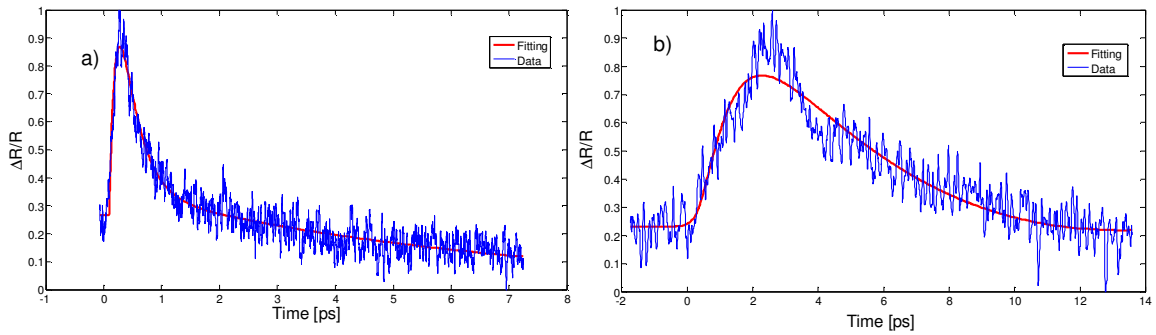

Figure 1. Transientent-Thermo-Reflectance results on (a) GaAs , (b) Au film with 5 nm thickness

In the case of Au sample, transient temperature, heat transfer parameters and coupling factor between electrons and phonons (energy rate transfer) were estimated with a numerical model.

4. Conclusions

Preliminary results based on a time resolved spectroscopy demonstrates transient behavior on the reflectance at the excitation focal point, which can be related with the change of population of excited carriers on both semiconductor and metal surfaces. Non-destructive examination (NDE) of energy transport technique has been demonstrated at low fluence regime of 6 mJ/cm^2. In the case of Au sample, transient temperature, heat transfer parameters and coupling factor related with energy transfer rate between electrons and phonons were corroborated with a numerical model.

Acknowledgements

The authors gratefully acknowledge sponsorship of this work by DGAPA-UNAM. PAPIIT project: IN113809, IB101212, IACOD-I1100611, CONACyT-Mexico project CB 131746.

MEXICAN OPTICS AND PHOTONICS MEETING
19 al 21 de septiembre del 2012
San Luis Potosí, México

High-Efficiency LEDs Luminous Intensity Spatial Measurement at CENAM

N. Vidal-Medina [(1)], E. Rosas [(1)], L. P. González-Galván [(1)], A. Estrada-Hernández [(1)], Juan B. Hurtado-Ramos [(2)]

1. Centro Nacional de Metrología, km. 4.5 carretera a Los Cués, 76246, El Marqués, Querétaro.
2. CICATA Unidad Querétaro, Instituto Politécnico Nacional, Cerro Blanco 141, 76090, Querétaro, Querétaro.

Corresponding author email: nvidal@cenam.mx

ABSTRACT:

Here we present results on the luminous intensity spatial distribution, and the corresponding total luminous fluxes and luminous efficacies measurements, carried out for high-intensity white LEDs currently under development to become the reference standards for such photometric quantities. The obtained values for the mentioned quantities showed a good agreement to the expected nominal values, which were selected in order to provide appropriate reference points to support the calibrations required in the Mexican regulation [1].

Key words: Solid-state lighting, luminous intensity spatial distribution, high-efficiency LEDs, total luminous flux.

REFERENCES AND LINKS

[1] Gobierno Federal Mexicano, *Proyecto de norma oficial mexicana. Eficacia luminosa de lámparas de diodos emisores de luz (LED) integradas para iluminación general. Límites y métodos de prueba*, Secretaría de Energía, PROY-NOM-030-ENER-2012, Mexico City, Mexico, (2007).

[2] A. Estrada-Hernández, L. P. González-Galván, H. Zárate-Hernández, R. Cardoso, E. Rosas, *Luminous flux and correlated color temperature determination for LEDs sources*, Proceedings of SPIE, **6422**(64220O), Bellingham, USA, (2007).

[3] A. Estrada-Hernández, L. P. González-Galván, E. Rosas, *New paradigms in LED photometry and colorimetry*, Proceedings of SPIE, **7499**(74990L), Bellingham, USA, (2009).

[4] N. Vidal, E. Rosas, J. B. Hurtado Ramos, *Illuminance spatial distribution based total luminous flux determination for white LEDs*, Proceedings of SPIE, **8011**(80111Z), Bellingham, USA, (2011).

[5] C. DeCusatis, *Handbook of applied photometry*, Springer-Verlag, Ney York, USA, (1997).

[6] Commission International de l'Eclairage, *The measurement of luminous flux*, Technical Report No. 84, Vienna, Austria, (1989).

1. Introduction

As part of the implementation of high accuracy radiometric and photometric capabilities for Solid-state lighting [2, 3], CENAM has recently installed a new facility for goniometric radiometry and photometry; which metrological characterization has begun by determining the luminous intensity spatial distribution of a set of high-intensity white LEDs, currently under development to become the reference standards for such a novel lighting technology. These luminous intensity spatial distributions allow the subsequent determination of the tested LEDs luminous fluxes and luminous efficacies, while still improving the previously reported uncertainty levels [4].

2. Results

The total luminous flux, Φ_v, can be obtained from the luminous intensity spatial distribution, $I_v(\theta, \phi)$, as [5]:

$$\Phi_v = \int_{\phi=0}^{2\pi} \int_{\theta=0}^{\pi} I_v(\theta,\phi) \cdot \sin(\theta) \cdot d\theta \cdot d\phi, \qquad (1)$$

where θ, ϕ are the so called polar (or elevation) and azimuth angles, which can be specifically considered among any of the standardized coordinate systems normally used in photometric measurements [6].

By using a photo-goniometer working under the C-γ geometry [6], it was possible to measure the luminous intensity spatial distribution of a high-intensity white LED, Fig. 1, and then use Eq. (1) to find its total luminous flux as 596.03 lm, once this has been properly corrected [3], while estimating an expanded uncertainty of U=3.18, (k=2), even lower than the previously reported value [4].

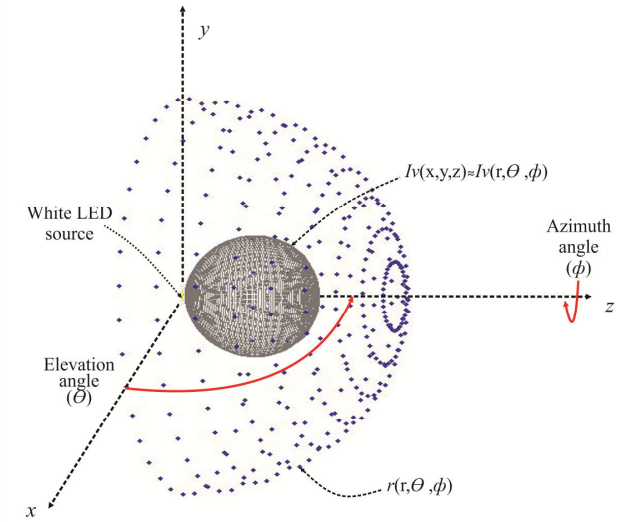

Fig.1. Typical luminous intensity spatial distribution patterns, for the studied high-intensity white LEDs.

Since the luminous efficacy η_v is defined by [1]:

$$\eta_v = \frac{\Phi_v}{P_{el}}, \qquad (2)$$

where P_{el} is the total electrical power consumed by the LED while producing the measured total luminous flux Φ_v. Therefore it was also possible to determine the luminous efficacy for the studied LED as 86.64 lm·W^{-1}; with an estimated expanded uncertainty of U=3.20, (k=2); thus qualifying this specimen as a high-efficiency LED source, according to the Mexican regulation [1].

3. Conclusions

We have successfully tested for total luminous flux and luminous efficacy, a specimen of the set of high-intensity white LEDs currently under development, to become the reference standards for Solid-state lighting in these quantities. The obtained values allowed this particular specimen, to be considered as a high-efficiency LED source [1]; while the expanded uncertainty for the total luminous flux was reduced with respect to a previous estimation [4].

MEXICAN OPTICS AND PHOTONICS MEETING
19 al 21 de septiembre del 2012
San Luis Potosí, México

Modeling and Simulation of Chaotic Behavior

Gilberto Sánchez Mares[(1)], Norman Andres Herrera Hernández[(1)]

1. Universidad Politécnica de Aguascalientes, Paseos de San Gerardo No. 207, 4421400 ext. 1441
gilberto_gsm@hotmail.com, norman_andres09@hotmail.com

ABSTRACT:

Chaos is a stationary behavior of a dynamical system and its main characteristic is the sensitivity to initial conditions. This type of system is being considered for various areas of knowledge such as optics, mathematics, physics, telecommunications, medicine and among others. This paper presents one of the most used electronic circuits for the study of chaotic oscillators, the so called Chua´s Circuit, proposed by Leon Chua, this oscillator wins popularity due to the large number of nonlinear behavior that occurs when the parameter values changes. The main objective is to analyze the above circuit, based on the mathematical modeling to understand how it works and some of its most important features, as the great sensitivity to the variation of initial conditions and the peculiar graph (attractor) illustrating the peculiar behavior.

Key words: Chaotic Attractor, Chua´s Circuit, Nonlinear System

REFERENCES AND LINKS

[1] Razminia, A., Sadrnira M. A., Chua´s Circuit Regulation Using a Nonlinear Adaptive Feedback Technique, World Academy of Science. 34, (2007).

1. Introduction

Chaos theory in control systems are defined as a stationary behavior of a dynamical system, behavior that isn´t an equilibrium point and isn´t periodical. The so called Chua´s Circuit is a nonlinear model representing dynamic behavior of the chaotic type. This circuit consists of four linear elements: inductor (L), resistor (R), two capacitors (C_1) and (C_2); and a nonlinear element: the Chua´s diode (Fig. 1 a)).

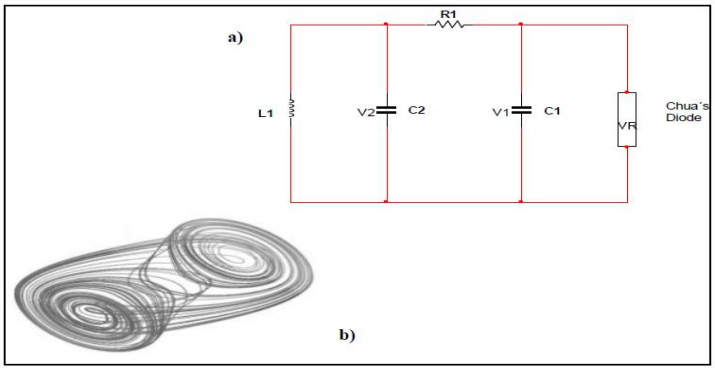

Fig. 1. a) Chua´s Circuit y b) Chua´s Attractor.

2. Development and Results

2.a. Development

The project has been developed in two sections; the first consist of modeling the circuit expressed in mathematical form, in the second part was carried out by a group of simulations in two specialized softwares: MATLAB™ and Multisim™, thus obtaining sources where we can check the attractor created by this system.

The system dynamics is determinate by applying the laws Kirchhoff´s voltage and current, as follows [1]:

$$C_1 \frac{dV_1}{dt} = \frac{(V_2 - V_1)}{R} - g(V_1) \tag{1}$$

$$C_2 \frac{dV_2}{dt} = -\frac{(V_2 - V_1)}{R} + I_L \tag{2}$$

$$L \frac{dI_L}{dt} = -V_2 \tag{3}$$

2.b. Results

Multisim. In this software was designed the Chua´s circuit. In the oscilloscope was simulated the behavior of the attractor "Double Scroll", which can be seen in Fig. 2 where we have the form that is displayed in XY format.

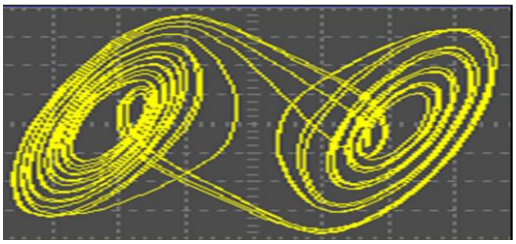

Fig. 2. Signal Chua Attractor.

MATLAB. Were programmed equations (1-3) to produce the attractor and visualized on 3 dimensions, this can be seen in Fig. 3.

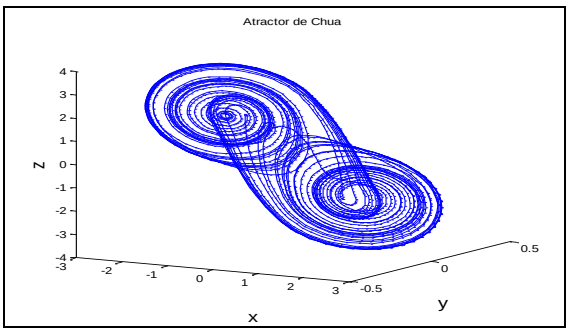

Fig. 7. MATLAB simulation of Chua´s attractor in 3 dimensions (*x*, *y* and *z*).

3. Conclusions

The development and study of such systems brings great contributions to areas such as optics, electronics, communications and even biomedical systems and economic, which remains an area of development leaving way to research projects on the subject.

MEXICAN OPTICS AND PHOTONICS MEETING
19 al 21 de septiembre del 2012
San Luis Potosí, México

Lasing properties of novel Fluorene Polymers

S. Romero-Servin [(1)], R. Carriles[(1)], G. Ramos-Ortíz[(1)], J.L. Maldonado[(1)] and M. G. Zolotukhin [(2)]

1. Centro de Investigaciones en Óptica, A. P: 1-948, 37000, León, Gto. México
2. Instituto de Investigación en Materiales, Universidad Nacional Autónoma de México

Corresponding author email: sromero@cio.mx

ABSTRACT:

Organic polymers with delocalized electrons can display large optical nonlinearities and high gain coefficients. Recently, several studies have reported the development of organic semiconductors with efficient two-photon activity; i.e. large two-photon absorption cross section and high fluorescence quantum yield. There is a growing interest in using these materials in two-photon pumped lasing systems emitting in the visible but pumped in the infrared. Here, we report on a novel fluorene polymer and its characterization as laser gain media.

Key words: Fluorene polymer, Two-photon pumped lasing, laser gain media.

REFERENCES AND LINKS

[1] Laura Aparicio-Ixta1, et. al.,"Two-photon excited fluorescence of silica nanoparticles loaded with fluorene-based monomer and its cross-conjugated polymer and their application to cell imaging",submitted.

[2] G. Ramos-Ortíz, et. al. "Synthesis, characterization and third-order non-linear optical properties of novel fluorene monomers and their cross-conjugated polymers", Polymer **51**,2351-2359 (2010).

[3] Silu Tao, et. al., "Highly Efficient non-doped blue organic light-emitting diodes based on fluorene derivatives with high thermal stability". Advanced Functional Materials **15**, 1716-1721 (2005).

1. Introduction

Fluorene-based derived compounds continue to be a subject of active research due to their nonlinear optical properties such as giant cross section for two-photon absorption [1], high fluorescence quantum yield, thermal and photochemical stability [2]. These properties make them attractive for applications in numerous areas, among others: organic light-emitting diodes, two photon microfabrication, multiphoton fluorescence, optical data storage and laser applications [3].

2. Experiment and Results

This work is based on the fluorene polymer PMC300. Its synthesis and structure have been discussed elsewhere [3]. The ultimate goal is to use this compound as a two-photon pumped laser medium.

2.a.- Linear Characterization

Figure 1(a) shows the linear absorption (black line) and the fluorescence (red line) spectra of PMC300 taken in solution with a concentration of 10^{-4} M. We used a commercial spectrophotometer for the absorption measurements while the fluorescence curve was measured by a spectrometer under UV light excitation. There are two absorption bands centered at 323 and 427 nm, PMC300 is transparent in the 750-850 nm range. Fluorescence exhibits a wide feature centered at 555 nm with a FWHM of 140 nm. The fluorescence quantum yield was determined to be around of 1[2].

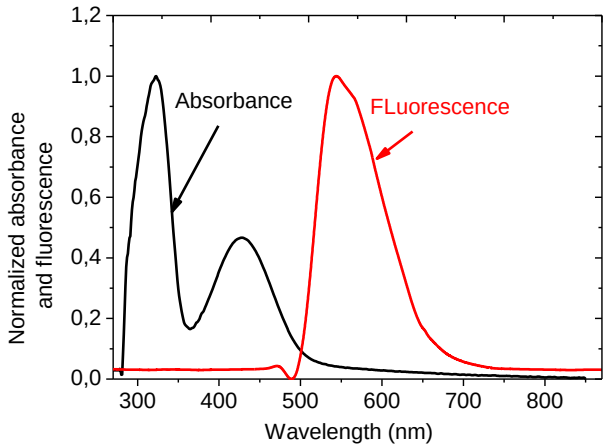

Figure 1. Absorption and fluorescence spectra of PMC300

2.b.- Lasing Measurements

We built a resonator consisting of a flat mirror and a diffraction grating with a 10 mm thick quartz cuvette containing the PMC300 solution inside this arrangement. We focused the output of an OPO at 425 nm with maximum energy of E_p 180 μJ using a 10 cm focal length cylindrical lens to transversely pump the PMC300. Figure 1(b) shows the emitted energy versus pumping energy, as seen in this figure the lasing threshold is at around 70 μJ. The inset clearly shows that the laser emission is tunable over at least 15 nm. This value for the lasing threshold positions PMC300 as a competitive laser material.

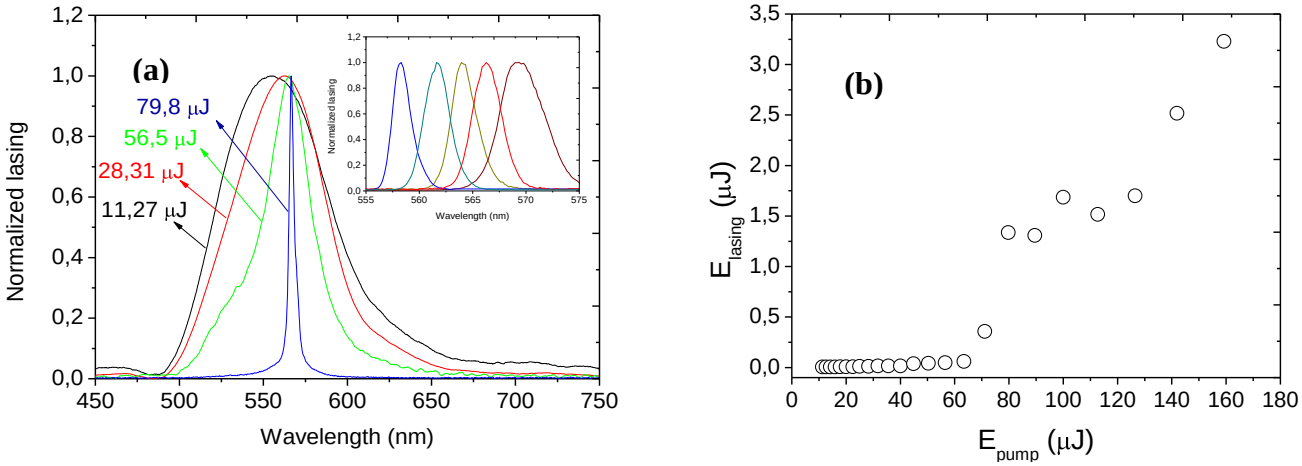

Figure 2. a) narrowing of the fluorescence spectrum generating laser emission due to pump energy, inset tenability of PMC300 and b) laser emission threshold.

3. Conclusions

We reported on the linear photophysical properties and stimulated emission of a new fluorene polymer derivative (PMC300). The observed linear spectral properties and its giant TPA cross section open the possibility of using PMC300 as a laser medium pumped by two photons in the infrared region.

MEXICAN OPTICS AND PHOTONICS MEETING
19 al 21 de septiembre del 2012
San Luis Potosí, México

Micro Reflectance Difference Spectrosopy

L. F. Lastras-Martínez, R. Herrera-Jasso, N. Ulloa-Castillo, R. E. Balderas-Navarro, J. Ortega-Gallegos and A. Lastras-Martínez.

Instituto de Investigación en Comunicación Óptica, Universidad Autónoma de San Luis Potosí, Álvaro Obregón 64 CP 78000, San Luis Potosí, SLP, México.

Corresponding author email: lflm@cactus.iico.uaslp.mx

ABSTRACT:

Micro reflectance difference (μ-RD) spectroscopy is a promising tool for the *in-situ* and *ex-situ* characterization of semiconductor surfaces and interfaces. This technique allows us to isolate the RD spectrum of specific areas of the sample under study; thus topographic maps of the surface or interface can be obtained. We report on measurement of μ-RD spectroscopy of several semiconductor systems and we illustrate the performance of our μ-RD setup.

Key words: Reflectance difference spectroscopy, microscopy, semiconductors, defects, surface strain.

REFERENCES AND LINKS

[1] D. E. Aspnes "Anisotropies in the Above-Band-Gap Qptical Spectra of Cubic Semiconductors", Phys. Rev. Lett. **54**, 1956-1959 (1985).

[2] L. F. Lastras-Martínez, "Microreflectance difference spectrometer based on a charge coupled device camera: surface distribution of polishing-related linear defect density in GaAs (001)", APPLIED OPTICS **48(30)**, 5713-5717 (2009).

[3] R. E. Balderas-Navarro, "Optical anisotropies of Si grown on step-graded SiGe (110) layers", APPLIED PHYSICS LETTERS **96**, 091904-1, 091904-3 (2010).

[4] L. F. Lastras-Martínez, "Micro reflectance difference techniques: Optical probes for surface exploration", Phys. Status Solidi B **249(6)**, 1119–1123 (2012).

---

1. Introduction

Reflectance difference (RD/RA) spectroscopy [1] is a powerful tool for the optical characterizations of surfaces and interfaces. The development of the RD spectroscopy as an optical probe for the characterization of surfaces and interfaces has suggested that an extension of the RD spectroscopy to a microscopic scale Micro reflectance difference (μ-RD) could further increase the potential of the technique [2]. In particular, the characterization of the strain induced by lineal defects [2-4].

In this work, we use μ-RD spectroscopy for the surface characterization in of several semiconductor systems. The experimental setup is illustrated in Fig. 1 [2]. The light coming from a Tungsten lamp is focused onto the entrance slit of a monochromator. The light beam at the output of the monochromator is directed through a polarizer prism and a photoelastic modulator (PEM) in tandem to the surface of the sample. The light reflected by the sample is

focused on the surface of a charge coupled device (CCD) used as a light detector. For each wavelength two images are obtained; one with the PEM turned on (un polarized image) and other with the PEM turned off (polarized image). The RD signal is obtained by subtracting both images and dividing by their sum.

2. Figures

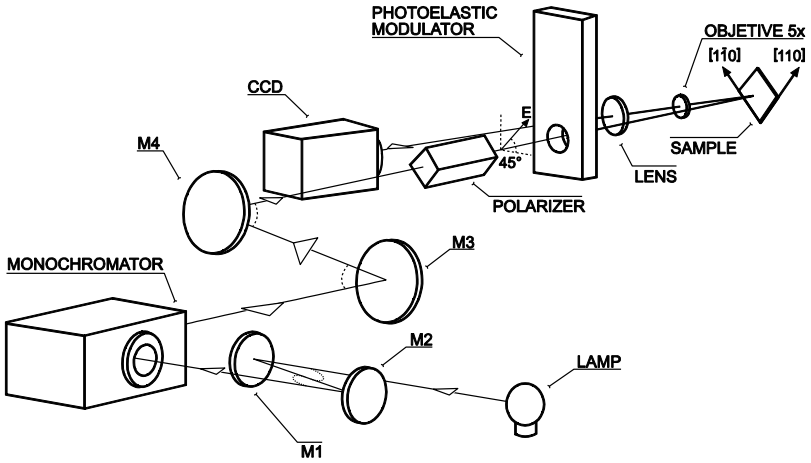

Fig.1. Experimental setup of the μRD spectrometer used in this work. The working spectral range is 1.1-5.5 eV.

3. Conclusions

We have used a m-RD spectrometer to map the surface distribution of anisotropies in different semiconductor systems. Our results show, that the μRD spectrometer constitutes a promising tool for the study and characterization of the distribution of the strain fields, surface electric fields, roughness of the surface of semiconductors and metals.

Acknowledgements

We would like to thank E. Ontiveros, F. Ramírez-Jacobo and J. Gonzalez-Fortuna for technical assistance. This work was supported by Consejo Nacional de Ciencia y Tecnología through grants Nos. 130009, 79635, and 81316.

MEXICAN OPTICS AND PHOTONICS MEETING
19 al 21 de septiembre del 2012
San Luis Potosí, México

Real time study of the evolution of a Arsenic-rich c(4x4) to a Gallium-rich GaAs(001) surface by Anisotropic Reflectance Spectroscopy

L. E. Guevara-Macías, A. Lastras-Martínez, J. Ortega-Gallegos, O. Núñez-Olvera, R. E. Balderas-Navarro and L. F. Lastras-Martínez

Instituto de Investigación en Comunicación Óptica, Universidad Autónoma de San Luis Potosí. Alvaro Obregón 64, San Luis Potosí, México
Corresponding author email: Liliana@cactus.iico.uaslp.mx

ABSTRACT:

This paper shows a study of the evolution of GaAs(001), from an (4x4) As-rich surface to a (4x2)-like Ga-rich surface as induced by the deposition of a few monolayers of GaAs by molecular beam without As flux. The evolution was traced by real-time Rapid Reflectance Anisotropic Spectroscopy (RRAS) and Reflection High Energy Electron Diffraction (RHEED).

Key words: GaAs(001); optical anisotropies; molecular beam epitaxy.

REFERENCES

[1] Akihiro Ohtake, Masashi Ozeki, Tetsuji Yasuda, Takashi Hanada, PRB **65**, 165315 (2002).

[2] Alvason Zhenhua Li, Zhiming M. Wang, Jiang Wu, Yanze Xie, Kim A. Sablon and Gregory J. Salamo, Crystal Growth and Design **9**, 2941 (2009).

[3] Qikun Xue, T. Hashizume, J. M. Zhou, T. Sakata, T. Ohno and T. Sakurai, Phys. Rev. Lett. **74**, 3177 (1995).

1. Introduction

The study of III-V semiconductor surfaces is of valuable importance, since they play a role during the manufacture of a variety of functional devices. In particular, optoelectronic devices call for multiple layers such as stacked quantum wells employed in laser technology. GaAs(001) surface is one of the most interesting situations because it has several types of reconstructions[1], depending on temperature, and on the arriving fluxes in molecular beam epitaxy. One of the less studied reconstructions is that one with Ga-rich [2]. In contrast to the As-rich surfaces, Ga-rich surfaces are more difficult to synthesize [3]. It is therefore interesting to have an understanding of the various processes and phenomena occurring on this surface. In this work we show a real-time reflectance anisotropic spectroscopy study to follow the evolution and formation of the gallium-rich surface on GaAs at 500 ºC.

2. Experimental Setup

Experiments were carried out in a molecular beam epitaxy chamber (MBE, Riber 32) equipped with solid-source effusion cells, and both RHEED and a rapid reflectance anisotropy spectrometer. After the growth of an undoped GaAs layer, the substrate temperature was lowered to 500 ºC. The arsenic cell was then closed resulting in a residual As pressure of 10^{-9} Torr. RA spectra were acquired each 500 milliseconds within the photon energy range of 2 to 4eV. Such a spectrometer is implemented using a commercial monochromator MicroHR with a range of 150 to 450 coupled to a Hamamatsu photomultiplier array (H7260) with 32 channels. Each of the 32 channels are time-multiplexed and fed to a single Lock-in amplificator and a digital acquisition card.

3. Results and Conclusions

Figure 1 shows the experimental results into two stages. In stage 1, by starting with a (4x4) surface reconstruction (t=0s), each subsequent spectrum was recorded at a time of 500 miliseconds. At t = 10s, the As cell is close and the surface begins to evolve until t = 63s, showing a reduction in the concavity in the energy range around 2.5- 3.0 eV. The large decrease in concavity is observed at t = 95s. Finally at t = 125s the spectrum undergoes an inversion at E_1 and $E_1+\Delta_1$ indicating that the surface, had became a Ga-rich.

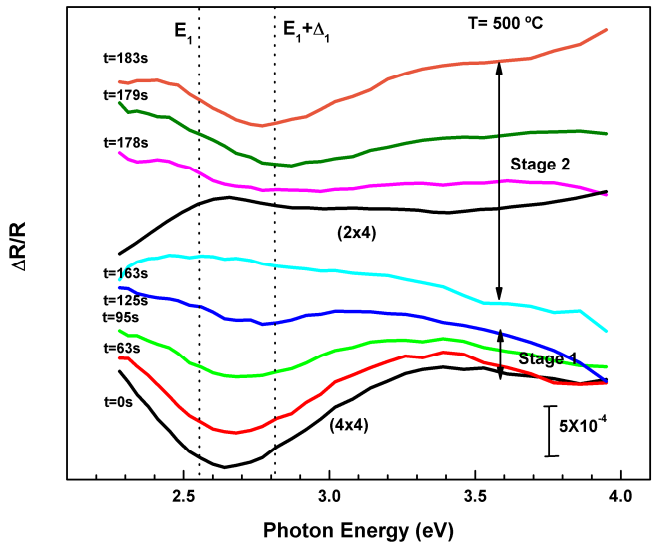

Fig.1. Stage 1: Surface process due to the lack of arsenic from a reconstruction (4x4) to a (2x4)-like because of the reduction of arsenic flux from $5x10^{-6}$ to $5x10^{-9}$ torr. Stage 2: Surface process due to the deposition of two monolayers of GaAs with a residual arsenic pressure of $5x10^{-9}$ torr.

In the stage 2 the RA spectrum, which still continues to evolve due to the absence of As flux, achieved a concavity change, becoming a (2x4)-like at time t = 163s. Afterwards, a deposition of two monolayers of Ga were done at t = 178s and immediately a change in the line shape occurs disappearing the (2x4) characteristic line shape and increasing the concavity on the spectrum. At the end of the experiments, however, RHEED shows that the (2x4) reconstruction renders diffuse.

In summary, this paper shows that RRAS/RHEED combination can be used to follow fine spectral details, in real time and *in situ*, of the conversion of GaAs(001) surface in As-deficient conditions in MBE. This knowledge should be useful for the tailoring of Ga-rich templates used in nanotechnology.

MEXICAN OPTICS AND PHOTONICS MEETING
19 al 21 de septiembre del 2012
San Luis Potosí, México

Numerical study the presence of two nonlinearities in a nonlinear medium by the Z-scan technique

I. Severiano Carrillo[1], M. M. Méndez Otero[1], M. L. Arroyo Carrasco[1], M. D. Iturbe Castillo[2]
1. Facultad de Ciencias Físico Matemáticas, BUAP, C.P. 72570 Puebla, Pue., México;
2. INAOE, Luis Enrique Erro # 1, 72840 Tonantzintla, Pue., México
Author e-mail address: isevecar@hotmail.com

ABSTRACT:
We analyze numerically the presence of more of a nonlinearity in a thin nonlinear material through of the Z-scan technique, where the material is considered as a set of thin lens which have a focal length F expressed as a constant *a* multiplied by the beam radius ω elevated to some power *m.*
Key words: Z-scan, focal length, nonlinear phenomena.

REFERENCES AND LINKS
[1] M. Sheik-Bahae, A. A. Said and E. W. Van Stryland, "High-sensitivity, single-beam n2 measurements", Optics letters, **14**, 955-957 (1989).
[2] Bing Gu, Jing Chen, Ya-Xian Fan, Jianping Ding, and Hui-Tian Wang, "Theory of Gaussian beam Z scan with simultaneous third- and fifth-order nonlinear refraction based on a Gaussian decomposition method", J. Opt. Soc. Am. B, **22**, 2651-2659 (2005).
[3] E. Reynoso Lara, Z. Navarrete Meza, M. David Iturbe Castillo, C. G. Treviño Palacios, E. Martí Panameño and M. Luis Arroyo Carrasco, "Influence of the photoinduced focal length of a thin nonlinear material in the Z-scan technique", Opt. Exp., **15**, 2517-2529 (2007).

1. Introduction

The Z-scan technique [1] is based on the principles of the space distortion of beam and it consists on displacing a nonlinear material, thin, along a region of the optical axis (Z direction) and around the minimum width of an intense beam, generally Gaussian, focused by a convergent lens. The power transmitted through of material is obtained as a function of the position of the sample, and it is measured by a photodetector in the far field. The Z-scan's curves are obtained by the powers detected depending on the position.
The studies of some papers of Z-scan shown the presence of different types of nonlinearities in the material [2], these use the theory of Gaussian beam and Gaussian decomposition method, the model proposed for us for different thicknesses of the material is regarded as a set of nonlinear thin lenses with focal lengths that depend of the beam radius, this is calculated using the q parameter, matrices ABCD and theory of Gaussian beams.
The Z-scan curves are obtained numerically considering more of a nonlinearity in the nonlinear medium.

2. Theoretical Model

2.a. Numerical Model

Considering that the thin nonlinear media is illuminated by a Gaussian beam, then the response of the medium can be obtained as the propagation of this Gaussian beam through a set of sections that form the thin nonlinear medium, each section is formed for linear medium-lens-linear medium-lens where the linear medium have a refractive index *n* and width *d.* The focal length for each thin lens is going to be considered as proportional to the incident beam radius ω to some power *m* multiplied by a constant a_m[3] equation (1):

$$F(z) = a_m \omega^m(z) \tag{1}$$

The intensity at the position of the photodetector can be obtained using the ABCD matrix for each optical element and the propagation using the q-parameter for Gaussian beams. A schematic representation of the model is shown in figure 1.

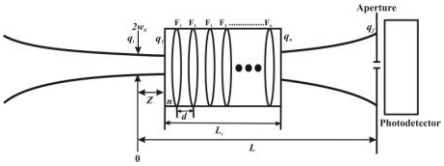

Figure 1. Z-scan arrangement with a thin medium.

3. Results

The incident beam have a beam waist ω_0=13 μm at λ=457nm (z_0=1.16 mm) and the linear refractive index of the nonlinear material was n=1.33 with thickness material of $0.5Z_0$.

We show in the figure 2 the curves obtained when it is considered a nonlinearity (a and b) and considering the two nonlinearities (c). It is observed in the curve (c that the negative nonlinearity (peak-valley) is obtained when we have a positive value in the constants a_3 and negative value in the constant a_4. Other difference in the curve (c is the value in transmittance, it decreases versus the curves that considered a nonlinearity, the distance of peak-valley are separated a distance proportional to the optical width of the medium.

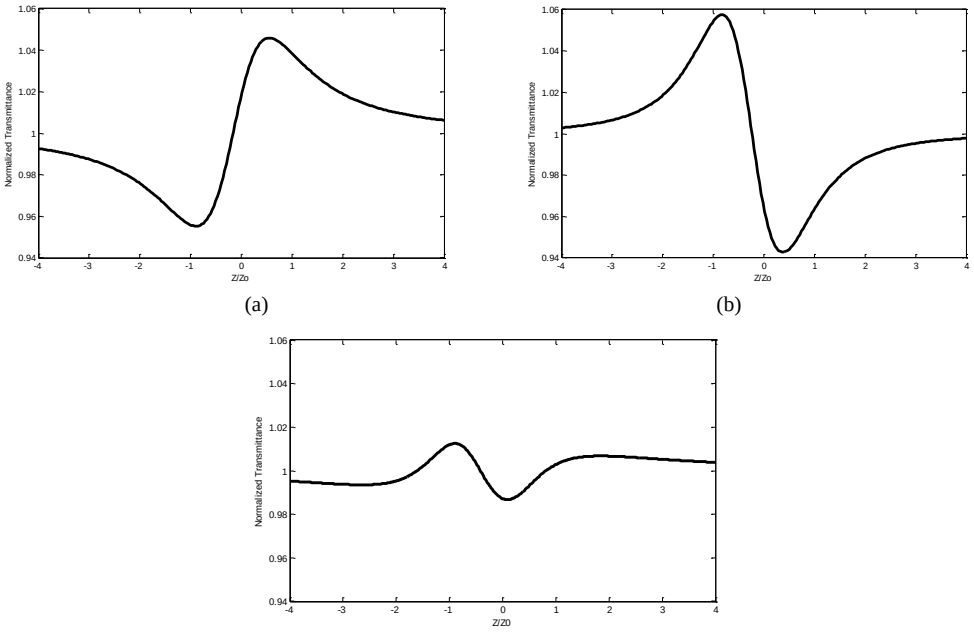

Figure 2. Numerical Z-scan curves for two nonlinearities and $0.5Z_0$ of thickness of the medium with: a) m_3= 3 (a_3= 4x10^{10}) and m_4= 4 (a_4= -2x10^{13}), b) m_3= 3 (a_2= 4x10^{10}), c) m_4= 4 (a_4= -2x10^{13}).

4. Conclusions

We presented a model to describe the z-scan curves obtained for thin nonlinear media and two different nonlinearities where the nonlinearity was considered as the focal length of the photoinduced lens dependent on the incident beam radius to some power *m*.

MEXICAN OPTICS AND PHOTONICS MEETING
19 al 21 de septiembre del 2012
San Luis Potosí, México

Design and implementation of a digital scanned laser light sheet microscope using spatially shaped beams

Jacob Licea-Rodriguez [(1)], Omar E. Olarte [(2)], Israel Rocha-Mendoza [(1)], Raul Rangel-Rojo [(1)] and Pablo Loza-Alvarez [(2)]

1. Centro de Investigación Científica y de Educación Superior de Ensenada, Carretera Ensenada-Tijuana, No 3918, Zona Playitas, 22860 Ensenada B.C., México
2. ICFO-Institut de Ciències Fotòniques, Av. Carl Friedrich Gauss, 3, 08860 Castelldefels (Barcelona), Spain.

jlicea@cicese.edu.mx

ABSTRACT:

We present the implementation of a combined digital scanned light sheet microscope (DSLM) able to work in the linear and nonlinear regimes under either Gaussian or Bessel beam excitation schemes. The design and characterization of each DSLM imaging modality is presented using *in vivo Caernohabditis elegans* samples. We obtained better results using Bessel beam and two-photon excitation.

Key words: Nonlinear microscopy; Medical and biological imaging; Fluorescence microscopy

REFERENCES AND LINKS

[1] J. Palero *et al.*, "A simple scanless two-photon fluorescence microscope using selective plane illumination," Opt. Exp. **18**, 8491-8498 (2010).

[2] T. V. Truong *et al.,* "Deep and fast live imaging with two-photon scanned light-sheet microscopy," Nat Meth. **8**, 757-760 (2011).

[3] P. J. Keller *et al.,* "Reconstruction of Zebrafish Early Embryonic Development by Scanned Light Sheet Microscopy," Science. **322**, 1065 -1069 (2008).

[4] O. E. Olarte *et al.,* "Image formation by linear and nonlinear digital scanned light-sheet fluorescence microscopy with Gaussian and Bessel beam profiles," Biom. Opt. Exp. **3**, 1492-1505 (2012).

1. Introduction

Recently Two-Photon Selective Plane Illumination Microscopy (2p-SPIM) was demonstrated [1]. Although this technique is ideal for accessing larger penetration depths, due to the involved reduced intensities, its implementation is not optimal in terms of efficiency of fluorescence excitation [2]. In order to overcome this limitation, we use a variant in which light is focused to produce a line that is scanned in one direction, forming a digitally scanned light sheet, the fluorescence signal is collected by a microscope objective oriented perpendicularly to the excitation [3]. In this work, we present a multimodal configuration of DSLM in which linear and nonlinear excitation modalities can be easily accessible. Furthermore, in both modalities, Gaussian or Bessel beams can be produced. The design and

characterization of each DSLM imaging modality is presented using *in vivo Caernohabditis elegans* (*C. elegans*) samples [4].

2. Results

In Fig 1a, a bright field image of a row of *C. elegans* aligned along the x direction is shown. Figs. 1c)-f) show the maximum intensity projections images for all the modalities available in our DSLM setup. Also the obtained excitation focal lines are depicted below each figure as an indication of the expected effective field of view (FOV). It is clearly appreciated the increase of the FOV in the x direction by using Bessel beam, in both the linear and nonlinear modalities. Note that this is remarkably extended in the nonlinear regime (see Figs. 1d and 1f). In terms of image contrast and resolution the 2p-DSLM-Bessel gives better results when compared to any other modality (see Fig. 1b). In Fig. 1e, the generated image is more blurry due to the side lobes characteristic of the Bessel beam and the nonlinear excitation.

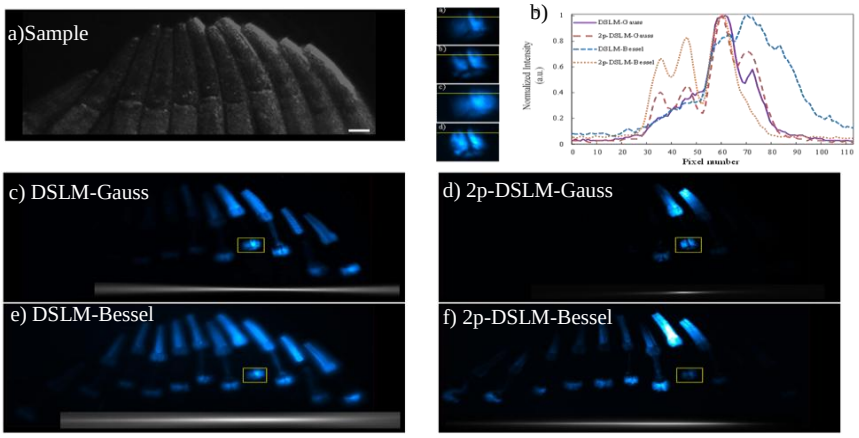

Fig.1. Fluorescent images of a row of *C. elegans* aligned along the *x* direction. a) Bright field image of the sample used. b) Normalized intensity profiles of a zone of the pharinx. Figs (c-f) are maximum intensity projections of *z* stacks taken with the four modalities available in our setup: c) DSLM-Gauss, d) 2p-DSLM-Gauss, e) DSLM-Bessel and f) 2p-DSLM-Bessel. The insets below each image indicate the position and extension of the excitation focal lines. All *z*-stacks are composed of 50 images taken in steps of 2 μm. Scale bar: 50 μm.

3. Conclusions

We have demonstrated a DSLM system with four different modalities using a single ultrashort-pulsed laser. Switching between linear and non-linear, or between Gaussian and Bessel beam can be done in a reliable way. This has enabled us to perform a complete characterization and comparison of the performance for imaging of the different modalities using the same living sample. The results are better for Bessel beam and two-photon excitation.

Acknowledgements

This research has been partially supported by Fundació Cellex Barcelona and has been conducted at ICFO's "Super-Resolution Light Microscopy and Nanoscopy Facility" (SLN@ICFO). J. Licea-Rodriguez acknowledges CONACYT México for supporting his stay at ICFO through a mixed fellowship.

MEXICAN OPTICS AND PHOTONICS MEETING
19 al 21 de septiembre del 2012
San Luis Potosí, México

Polarization selectable nonlinear response of elongated Ag nanoparticles embedded in SiO_2 studied by the Z-scan technique

Bonifacio Can-Uc[(1)], Raúl Rangel-Rojo[(1)], Luis Rodríguez-Fernández[(2)] and Alicia Oliver[(2)]

1. Centro de Investigación Científica y de Educación Superior de Ensenada, Carretera Ensenada-Tijuana No. 3918, Zona Playitas, C.P. 22860, Ensenada, B. C. México.
2. Instituto de Física, Universidad Nacional Autónoma de México, Circuito de la Investigación Científica S/N, Ciudad Universitaria, Distrito Federal, México.

bcan@cicese.mx

ABSTRACT:

We report the study of the nonlinear response of elongated silver nanoparticles embedded in SiO_2 substrates. The absorptive and refractive contributions to the nonlinearity response of the sample were studied by the z-scan technique using fs laser pulses as function of the intensity and the polarization angles of light used.

Key words: elongated nanoparticles, nonlinear absorption, nonlinear refraction.

REFERENCES

[1] R. Rangel-Rojo, J. McCarthy, H.T. Bookey, A.K. Kar, L. Rodriguez-Fernandez, J.C. Cheang-Wong, A. Crespo-Sosa, A. Lopez-Suarez, A. Oliver, V. Rodriguez-Iglesias, H.G. Silva-Pereyra, Anisotropy in the nonlinear absorption of elongated silver nanoparticlesin silica, probed by femtosecond pulses, Optics Communications 282: 1909–1912 (2009).

[2] Meldrum, A., López, R., Magruder, R., Boatner, L., y White, C. Structure and properties of nanoparticles formed by ion implantation. Topics in Appl. Phys., 116, 255-285. (2010).

[3] Mattei, G., Mazzoldi, P., y Bernas, H., Metal nanoclusters for optical properties. Topics in Appl. Phys., 117, (2010)

[4] Sheik-Bahae, M., Said, T. T., Wei, T., Hagan, D. J., y Van Stryland, E. W. Sensitive measurement of optical nonlinearities using a simple beam. IEEE Journal of Quantum Electronics, 26(4): 760-769,. (1990).

1. Introduction

Metallic nanoparticles embedded in dielectric substrates have showed several properties, such as large nonlinearities and response times in the ps regime [1]. The size, shape and type of metal of nanoparticles induced enhancement in the third order susceptibility, $\chi^{(3)}$, which it have been clearly observed [2]. Thereby these materials have attracted a considerable amount of attention for their application in optical systems. In particular, glass matrices embedding metal nanoparticles exhibit and enhanced optical susceptibility, $\chi^{(3)}$, whose real part is related to the n^2 coefficient of th intensity dependent refractive index [3]. Correspondingly, nonlinear absorpiton also takes place, which can be described by the intensity-dependent absorption coefficient β. These coefficients can be found with Z-Scan technique, which is based on the observation of change in the far field of a focused gaussian beam due to distortion in phase or amplitude, when the sample is scanned through focal plane along the optical axis [4].

In this work, we focuse in the study of nonlinear absorption (NLA) and refraction (NLR) coefficients by Z-Scan technique using a Ti:Sapphire pulsed laser whose wavelength is centred at $\lambda = 830$ nm and has 88 fs of duration pulse in FWHM to 94 Mhz of repetition frequency.

2. Results

The optical density of the spherical and elongated Ag nanoparticles are shown in the figure 1a and 1d respectively where we used linearity light polarized at 0º and 90º with respect to the long axis of the elongated nanoparticles. We have used open-aperture and closed-aperture Z-Scan technique for both polarizations in the samples with spherical and elongated nanoparticles. The results to spherical nanoparticles have shown a discernible NLA and closely positive NLR for both polarizations used. In samples with elongated nanoparticles, we observed two photon absorption process (TPA, $\beta > 0$) by 0º polarized light in open-aperture Z-Scan, and the other polarization used, there was not appreciable absorption. In the case of closed-aperture Z-Scan using the same polarizations, the scans performed exhibit a behavior of typical trace of positive NLR effect (self-focusing, $n_2 > 0$) at 0º polarized light used, while at 90º, the NLR response indicate a much weaker nonlinearity.

The nonlinear coefficients and the analisis about this result will be commented later.

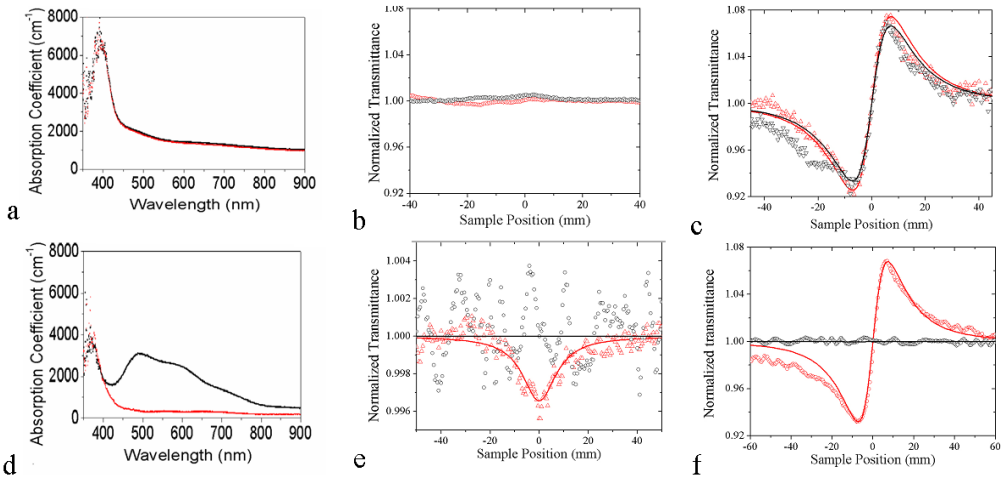

Fig. 1. 1a and 1d are the absorption spectra of spherical and elongated nanoparticles respectively, these were taken for mutually orthogonal linear polarizations, the black data correspond to polarization angle 0º and the red data 90º. 1b (open-aperture) and 1c (closed-aperture) are the Z-Scan traces to the spherical nanoparticles, the red data are to 0º and the black are to 90º. The red data and the continuos red line (fits) in 1e and 1f are traces of the TPA and NLR effects at 0º respectively and the others black are at 90º with the polarized light used.

3. Conclusions

In summary, we have studied the nonlinear optical response inspherical and aligned elongated Ag nanoparticles embedded in SiO2 by mean the z-scan technique where, we could see the NLR in spherical nanoparticles and NLA and NLR effects in eleongated nanoparticles with fs laser pulses. We have seen that the absorption spectra is directly dependent with the polarized light in the sample of elongated nanoparticles. Also we found a high anisotropy on NLR effect that is highly dependent of the polarization of the light used due to the changes on the absorption spectra at 830 nm.

MEXICAN OPTICS AND PHOTONICS MEETING
19 al 21 de septiembre del 2012
San Luis Potosí, México

LIBS SPECTROSCOPY FOR THE DETERMINATION OF CONTAMINANTS IN FRESHWATER FISH

Marcela Sosa Saldaña [1], Teresa Flores Reyes [2], Kriss Dialis Mejías [3], Luis Ponce Cabrera [4], Miguel Arronte Garcia [5], Eduardo de Posada Piñán [6].

Email. lponce@ipn.mx

ABSTRACT:

We present experimental results of the analysis by LIBS technique for the sampling of elements in freshwater fish tilapia species. As excitation source, we used a Nd: YAG laser emitting in multi-pulse Q: Switch regime.

Key words: LIBS, ND: YAG, MULTI-PULSE, Q: SWITCH, TILAPIA.

REFERENCES

[1] J. A. Anticamara*, et al.*, "Global fishing effort (1950–2010): Trends, gaps, and implications," *Fisheries Research,* vol. 107, pp. 131-136, 2011.

[2] P. Dumas*, et al.*, "Mud crab ecology encourages site-specific approaches to fishery management," *Journal of Sea Research,* vol. 67, pp. 1-9, 2012.

[3] D. A. Cremers and L. J. Radziemski, "Basics of the LIBS Plasma," in *Laser-Induced Breakdown Spectroscopy (LIBS): Fundamentals and Applications*, C. U. Press, Ed., ed New York: John Wiley & Sons, Ltd, 2006, pp. 23-50.

[4] Base de datos del Nist http://physics.nist.gov/PhysRefData/ASD/lines_form.html

1. Introduction

Fish are an excellent source of proteins and other nutrients, and make for a balanced and healthy diet [1]. However, pollution of the seas and rivers has been on the rise as a result of the toxic waste thrown into the water, giving rise to the accumulation of toxic matter on the scales and on parts of the skin of fish which, when eaten, is harmful to the health of human beings [2].

In this paper we undertake to monitor the contaminants present in fresh and frozen fish, utilizing the Analysis of Laser Induced Plasma (LIBS), a technique that is simple and easy to implement.

The LIBS technique is an emission spectroscopy technique that uses short pulses of laser radiation that are focused on a sample [5] to achieve material vaporization, plasma formation and the excitation of the latter at levels sufficient to generate a detectable emission[3].

2. MATERIAL AND METHOD

Young tilapia (*Oreochromis niloticus)* specimens from the Altamira, Tamaulipas, Mexico fish market, weighing an average of 25, 7 grams were used. The samples taken from the fresh fish, as well as from the frozen one, measure approximately 2x2 cm.

A pulsed Nd: YAG (λ = 1064 nm) laser is used for the ablation of the fish samples. The laser works in both Q-switched regime, producing light pulses with an energy of 300 mJ and a pulse time duration of 300 ns. The laser beam was focused using a 25 mm focal length lens to produce a 0.0019 cm^2 spot over the samples. A portion of the light emitted from the plasma was collected by a quartz optic fiber and delivered to an Ocean Optics USB2000 spectrometer. Although a trigger signal, coming from a fast photodiode, was used to command the spectra acquisition, no time delay was implemented. All spectra were integrated over 3 ms after the laser shot. The different line and band emissions were identified using the SpecLine software and database, from Ocean Optics, data reported at NIST database [4], as well as spectra recorded in our lab. The latter used the laser, with the same parameters used for this work to ablate high purity targets of C, Ca, K, and Fe, supplied by Kurt Lesker Corp.

3 RESULTS

Figure 1 compares the results of the relation of the normalized Cd and Pb with regard to the Fe line (373.71nm). The three series correspond to the branchiae, muscle and scales respectively. The purpose of this comparison is to determine by analyses carried out using different techniques if there is a change in the proportions of each element present. No changes in the proportions are detected which confirms the adequate behavior of the LIBS technique.

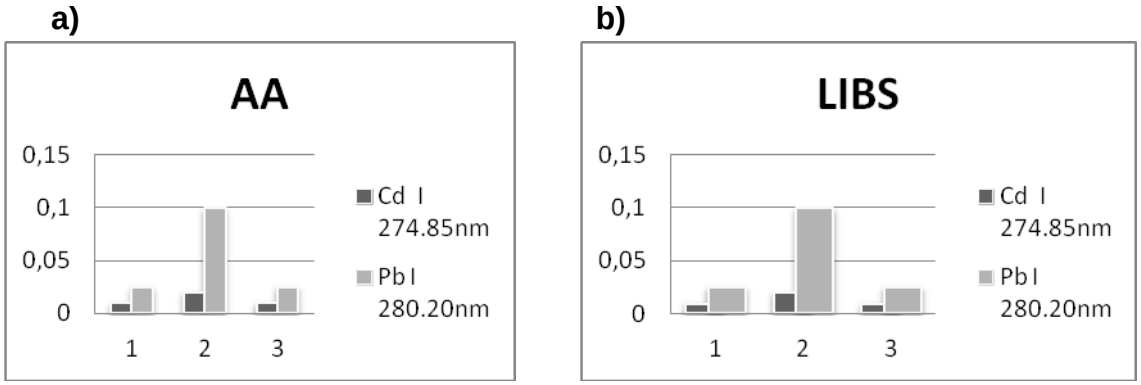

Figure 1. Qualitative analysis for two lines of Cd and Pb respectively normalized with regard to the Fe I peak (373.71nm). a) Analysis by atomic absorption spectrometry [4] b) Analysis by LIBS.

4. Conclusions

The paper confirms that the LIBS technique is an effective tool for qualitative and semi-quantitative monitoring of contaminants like heavy metals, which could be present in fish for human consumption.

The analysis of the scales showed that the intensity of the characteristic peaks associated with atomic elements was more intense, and Ca and H emissions, among others, were detected. The peaks have a significant intensity and could be used for a quantitative monitoring if compared to reference standards.

traditional analysis technique, the LIBS technique does not alter the proportions among the elements.

Acknoledgements: thank the CONACYT for supporting this project.

MEXICAN OPTICS AND PHOTONICS MEETING
19 al 21 de septiembre del 2012
San Luis Potosí, México

Nonlinear Optical Response of byosintethized Gold Nanoparticles

A. Balbuena Ortega[1*], M.L. Arroyo Carrasco[1], V. L. Gayou[2], A. Orduña Díaz[2], R. Delgado Macuil[2] and M. D. Iturbe Castillo[3]

[1]Facultad de Ciencias Físico-Matemáticas, Benemérita Universidad Autónoma de Puebla, Av. San Claudio y 18 Sur. Col San Manuel, C.P. 72570, Puebla, Puebla, México.
[2]CIBA-IPN Tlaxcala, Km. 1.5 Carretera Estatal Tecuexcomac-Tepetitla. Tepetitla de Lardizabal, Tlaxcala, México. C.P. 90700.
[3]Instituto Nacional de Astrofísica, Óptica y Electrónica, Luis Enrique Erro # 1, C.P. 72840 Tonantzintla, Puebla, México.
abalbuena1984@gmail.com

Abstract. In this work nonlinear index refraction of colloidal biosynthesized gold nanoparticles with latex of *Jatropha curcas* is investigated. Z-scan curves were obtained using a CW Argon ion laser, with an incident power of 20 mW and wavelength of 514 nm, for samples synthesized at different temperatures and latex concentrations. Experimental results are compared with a phenomenological model.
Keywords: nanoparticles, nonlinear optics, z-scan.

REFERENCES AND LINKS

1. Mandal D, Bolander M E, Mukhopadhyay D, Sarkar G and Mukherjee P 2006 *Appl. Microbiol. Biotechnol.* 69 485
2. E. V. García Ramírez, M.L Arroyo Carrasco, M. M. Méndez Otero, E Reynoso Lara, S. Chávez-Cerda and M. D. Iturbe. "Z-scan and spatial self-phase modulation of a Gaussian beam in a thin nonlocal nonlinear media", Journal of optics. 13, 085203 (2011).

1. Introduction.

As building blocks in nanotechnology, various methods have been developed to fabricate nanostructures of well defined compositions. However, conventional physical and chemical methods either are energy intensive or impose environmental hazards due to toxic solvents or additives as well as hazardous by products. Biosynthesis of nanoparticles has received considerable attention due to the growing need to develop environmentally benign technologies in material synthesis. The use of parts of whole plants in the biosynthesis of metal nanoparticles is an exciting possibility that is relatively unexplored and under exploited. The plant *Jatropha curcas* is commercially important one as biodiesel is extracted from its seeds on industrial scale. Though the jatropha latex has come ethno medical use like wound healing, coagulant activities of blood, it is acrid and irritable to the skin also.

In this work we characterized the nonlinear optical response of this kind of nanoparticles, which were synthesized with different concentration of gold and jatropha and using different temperatures. Employing the Z-scan technique and a recent theoretical model that takes into account the non local response of the media [2], the nonlinear refractive index of the medium was investigated.

2. Nanoparticle synthesis.

All the aqueous solutions were prepared using deionized water. For sample preparation, crude latex was obtained by cutting the green stem of jatropha curca plants. Milky white latex was stored at −20 ◦C until use. In a typical reaction procedure, crude latex was diluted to 100ml using deionized water to make it 1% in volume of this latex solution, different concentration of this latex solution was used and mixed with 5×10^{-3}M aqueous $AuHCl_4$ solution. All the mixtures were heated at different temperatures with constant stirring for 4 h the gold nanoparticles were obtained gradually. Jatropha plants were obtained from Huitzilan, Puebla, Mexico and the $AuHCl_4$ was purchased from Sigma–Aldrich.

3. Theoretical model.

The model used to characterize the samples is the established in [2], considers a Gaussian beam propagating in the *Z* direction, at some distance *z* it illuminates a thin nonlinear sample with a field amplitude $E(r,z)$, then the field at the exit of the medium can be written as;

$$E_{out} = E(r,z)\exp(-i\Delta\phi(r)) \ , \tag{1}$$

where φ(r) is the nonlinear phase change and it is proposed as :

$$\Delta\phi(r) \approx \Delta\phi_0(z,m)\exp\left(-mr^2/w(z)^2\right), \tag{2}$$

and

$$\Delta\phi_0(z,m) = \frac{\Delta\Phi_0}{(1+(z/z_0)^2)^{m/2}}, \quad (3)$$

here, $\Delta\Phi_0$ is the maximum on axis photoinduced phase shift in the beam after the nonlinear medium located at *z=0* and *m* can be any real positive number. The locality or non locality of the medium is implied in the *m* value, only for *m = 2* the nonlinear phase change follows the intensity distribution and then the response of the material is considered as local.

4. Experimental Results

UV–vis absorption spectra were measured using Thermo Scientific Evolution 600 spectrophotometer and are showed in Figure 1, we can observe that shift and increase in the peak of absorbance exist and it is depending of the latex concentration.

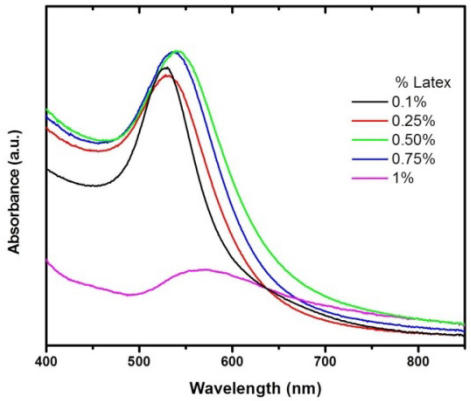

Figure 1. UV-vis curves for samples of gold nanoparticles synthesized by jatropha with different concentration 0.1 % (blue line), 0.25% (red line), 0.5% (magenta line) and 0.75% (green line).

The nonlinear optical properties of the colloid were investigated using the Z-scan technique in the CW regime for a wavelength at 514 nm using an Argon ion laser with an incident power of 20mW, Figure 2 shows the results.

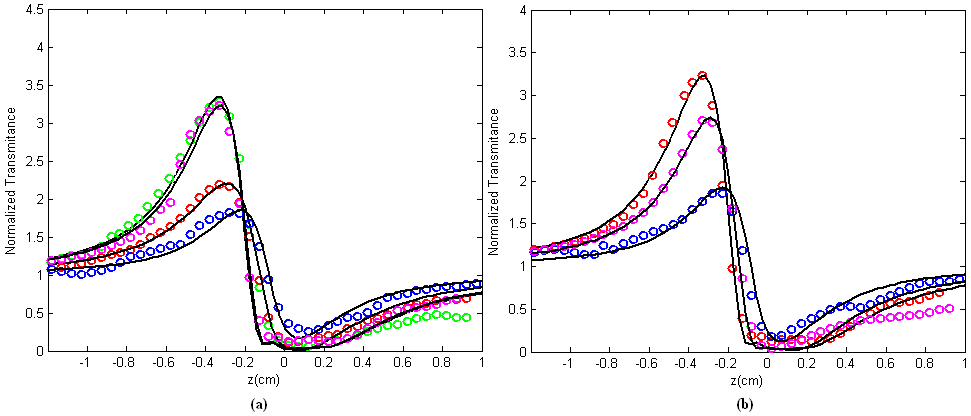

Figure 2. Z-scan curves for samples of gold nanoparticle synthesized by jatropha with a) different concentration: 0.1 % (blue line), 0.25% (red line), 0.5% (magenta line) and 0.75% (green line) at 80ºC b) different temperature: room temperature (blue line), 40º (red line), 80ºC (magenta line) with 0.5% of the latex concentration. The black line is the reproduction with the theoretical model.

We can observe that the sign of the nonlinear index refraction is negative for all the samples. In order to obtain a Z-scan numerical curve the field described in (1) is propagated using a Fast Fourier Transformer (FFT) algorithm and the on axis intensity at far field is obtained. The *m* value necessary for the reproduction at different concentration was *m=1.3* and $\Delta\Phi_0$=-1.1π for 0.1%, $\Delta\Phi_0$=-1.6π for 0.25%, $\Delta\Phi_0$=-3.3 for 0.5% and $\Delta\Phi_0$=-2.5π for 0.75%. While for a concentration of 0.5% solution of latex the value of *m* is the same and ΔΦ0=-1.2π for room temperature, $\Delta\Phi_0$=-3.3π for 40ºC and ΔΦ0=-3.3 for 80ºC.

5. Conclusions

Gold nanoparticles were successfully synthesized using different concentrations of jatropha and at different temperatures. From the reproduction of the z-scan experimental data we observed that the response depend of both, jatropha and temperature, also from the values of *m* we conclude that the response of the samples have a nonlocal character and the mechanis that generate the non linear response is the same.

AUTHORS INDEX

H

I

K

L

M

Sponsored by:

CENTRO DE INVESTIGACIONES EN OPTICA, A.C.

CICESE

INAOE

OSA Optical Society of America

SATEL SA MR

MOPM

MEXICAN OPTICS AND PHOTONICS MEETING 2012